



NRL/MR/6720--05-8862

# **Advanced Radiation Theory Support Annual Report 2004, Final Report**

*Radiation Hydrodynamics Branch  
Plasma Physics Division*

April 29, 2005

20050607 096

Approved for public release; distribution is unlimited.

REPORT DOCUMENTATION PAGE				Form Approved OMB No. 0704-0188	
Public reporting burden for this collection of information is estimated to average 1 hour per response, including the time for reviewing instructions, searching existing data sources, gathering and maintaining the data needed, and completing and reviewing this collection of information. Send comments regarding this burden estimate or any other aspect of this collection of information, including suggestions for reducing this burden to Department of Defense, Washington Headquarters Services, Directorate for Information Operations and Reports (0704-0188), 1215 Jefferson Davis Highway, Suite 1204, Arlington, VA 22202-4302. Respondents should be aware that notwithstanding any other provision of law, no person shall be subject to any penalty for failing to comply with a collection of information if it does not display a currently valid OMB control number. PLEASE DO NOT RETURN YOUR FORM TO THE ABOVE ADDRESS.					
1. REPORT DATE (DD-MM-YYYY) 29-04-2005		2. REPORT TYPE Memorandum report		3. DATES COVERED (From - To) 1 October 2003-30 September 2004	
4. TITLE AND SUBTITLE  Advanced Radiation Theory Support — Annual Report 2004, Final Report				5a. CONTRACT NUMBER	
				5b. GRANT NUMBER	
				5c. PROGRAM ELEMENT NUMBER	
6. AUTHOR(S)  J. Davis, J.P. Apruzese, Y. Chong, R.W. Clark, A. Dasgupta, J.L. Giuliani, P.C. Kepple, G.M. Petrov, R.E. Terry, J.W. Thornhill, and A. Velikovich				5d. PROJECT NUMBER	
				5e. TASK NUMBER	
				5f. WORK UNIT NUMBER	
7. PERFORMING ORGANIZATION NAME(S) AND ADDRESS(ES)  Naval Research Laboratory, Code 6720 4555 Overlook Avenue, SW Washington, DC 20375-5320				8. PERFORMING ORGANIZATION REPORT NUMBER  NRL/MR/6720--05-8862	
9. SPONSORING / MONITORING AGENCY NAME(S) AND ADDRESS(ES)  Defense Threat Reduction Agency 6801 Telegraph Road Alexandria, VA 22310				10. SPONSOR / MONITOR'S ACRONYM(S)	
				11. SPONSOR / MONITOR'S REPORT NUMBER(S)	
12. DISTRIBUTION / AVAILABILITY STATEMENT  Approved for public release; distribution is unlimited.					
13. SUPPLEMENTARY NOTES  This research was sponsored by Defense Threat Reduction Agency under JO title, "Advanced Concepts Theory Program," MIPR No. 2222M.					
14. ABSTRACT  This report describes the work of the Radiation Hydrodynamics Branch during FY 2004 in support of the DTRA's PRS and Sandia National Laboratories high energy density programs. It is a compilation of articles that were co-authored by Branch members. The titles are: (1) Controlling uniformity of gas-puff and wire array implosions with wire current-carrying structures, (2) Two- and three-wire loads for large current machines, (3) Enhanced energy coupling and X-ray emission in Z-pinch plasma implosions, (4) Spectroscopic diagnosis of nested-wire-array dynamics and interpenetration at 7 MA, (5) Characterization of on-axis plasma heating for keV X-ray production with Z-pinches, (6) Interferometric measurement of physical phenomena during the implosion phase of a puff-on-puff Z-pinch load on Double-EAGLE, and (7) Design of a multilayer mirror monochromatic X-ray imager for the Z accelerator.					
15. SUBJECT TERMS Decade; Enhanced energy dissipation; Flux compression; Large radius implosions; Transport coefficients; Long time implosions; Z-pinch physics; Rayleigh-Taylor instability; Plasma radiation source; Radiation MHD					
16. SECURITY CLASSIFICATION OF:			17. LIMITATION OF ABSTRACT  UL	18. NUMBER OF PAGES  122	19a. NAME OF RESPONSIBLE PERSON J. Ward Thornhill
a. REPORT Unclassified	b. ABSTRACT Unclassified	c. THIS PAGE Unclassified			19b. TELEPHONE NUMBER (include area code) (202) 404-4383

# CONTENTS

Executive Summary .....	v
Controlling Uniformity of Gas-Puff and Wire Array Implosions with Wire Current-Carrying Structures .....	1
Two- and Three- Wire Loads for Large Current Machines .....	51
Enhanced Energy Coupling and X-Ray Emission in Z-Pinch Plasma Implosions .....	62
Spectroscopic Diagnosis of Nested-Wire-Array Dynamics and Interpenetration at 7 MA .....	77
Characterization of On-Axis Plasma Heating for keV X-Ray Production with Z-Pinches .....	81
Interferometric Measurement of Physical Phenomena During the Implosion Phase of a Puff-On-Puff Z-Pinch Load on Double-Eagle .....	94
Design of a Multilayer Mirror Monochromatic X-ray Imager for the Z Accelerator .....	102



## EXECUTIVE SUMMARY

This report summarizes the activities of NRL Code 6720 in the areas of modeling, simulation, and diagnosis of multiple wire arrays and gas puff Z-pinches under the sponsorship of DTRA and Sandia National Laboratories. It is a compilation of articles that have been co-authored by Code 6720 Branch members and published, or submitted for publication, in professional journals. The papers reflect the work that has been performed as theory support for DTRA's Plasma Radiation Source (PRS) program carried out by NRL's Radiation Hydrodynamics Branch (Code 6720) in FY 2004. Included is work called for in DTRA MIPR 04-2222M - "Plasma Radiation Theory Support". This work was also partially supported by Sandia National Laboratories (Document 261344) as part of its high energy density physics campaign. The title and abstract for each article are given in the proceeding paragraphs, as follows:

(I) Controlling Uniformity of Gas-Puff and Wire Array Implosions with Wire Current-Carrying Structures - The magnetic field driving a gas-puff PRS implosion in a realistic load unit of a multi-MA current driver cannot be perfectly uniform. Sources of the non-uniformity include: a finite number of return current posts and the discrete structure of the anode and cathode grids. Analytical formulas have been derived to estimate the contribution of each of these factors to the total non-uniformity of the driving magnetic field. The non-uniformity is found to be substantial where the distance from the discrete current-carrying structure is less than the gap between the two neighboring elements of the structure, whether it be the anode/cathode spokes or the return current posts.

(II) Two- and Three- Wire Loads for Large Current Machines - Energetic implosions, using two or three load wires to create a focused axial stagnation of dense wire cores amidst the assembled precursor plasma, are examined with respect to the trade between the implosion mass loss to precursor ablation and the mass or kinetic energy available at stagnation. The calculated kinetic energy at stagnation serves as the primary source for the output x-radiation, which is estimated with a tabulated collisional radiative model.

(III) Enhanced Energy Coupling and X-Ray Emission in Z-Pinch Plasma Implosions - Recent experiments conducted on the Saturn pulsed-power generator at Sandia National Laboratories have

produced large amounts of x-ray output, which cannot be accounted for in conventional MHD calculations. In these experiments, the Saturn current has risetime of 180 ns in contrast to a risetime of 60 ns in Saturn's earlier mode of operation. In both aluminum and tungsten wire-array Z-pinch implosions, 2 to 4 times more x-ray output was generated than could be supplied according to one-dimensional magnetohydrodynamic calculations by the combined action of the  $\mathbf{j} \times \mathbf{B}$  acceleration forces and Ohmic heating (as described by a classical Braginskii resistivity). In this paper we reexamine the problem of coupling transmission line circuits to plasma fluid equations and derive expressions for the Z-pinch load circuit resistance and inductance that relate these quantities in a 1-D analysis to the surface resistivity of the fluid, and to the magnetic field energy that is stored in the vacuum diode, respectively. Enhanced energy coupling analysis, therefore, comes from enhancements to the surface resistivity, and we show that plasma resistivities approximately three orders of magnitude larger than classical are needed in order to achieve energy inputs that are comparable to the Saturn x-ray outputs. Large enhancements of the plasma resistivity increase the rate of magnetic field and current diffusion, significantly modify the qualitative features of the MHD, and raise important questions as to how the plasma fluid dynamics converts enhanced energy inputs into enhanced energy outputs. One-dimensional MHD calculations in which resistivity values are adjusted phenomenologically are used to illustrate how various dynamical assumptions influence the way enhanced energy inputs are channeled by the fluid dynamics. Variations in the parameters of the phenomenological model are made in order to determine how sensitively they influence the dynamics and the degree to which the calculated x-ray outputs can be made to replicate the kinds of large variations in the experimental x-ray power data that were observed in three nominally identical aluminum wire shots on Saturn.

(IV) Spectroscopic Diagnosis of Nested-Wire-Array Dynamics and Interpenetration at 7 MA - Nested-wire array experiments have been conducted at the 7 MA level with 150 ns implosion times from an outer diameter of 40 mm. Analysis of spectral data indicates that material from the outer array preferentially occupies the high temperature core of the stagnated pinch independent of the interwire gap in the range of 1.1 to 4.5 mm.

(V) Characterization of On-Axis Plasma Heating for keV X-Ray Production with Z-Pinches - We discuss a new opportunity of using Z-pinch plasma radiation sources for generating Ar K-shell

radiation and harder keV quanta. Our approach to keV x-ray generation is based upon an analogy with laser fusion, where the imploding shell compressionally heats the low-density inner mass. The suggested design of a Z-pinch load consist then of one or two heavy outer shell(s) with a lower mass on-axis fill (i.e., central gas jet) producing most of the radiation. The outer shell is not supposed to radiate and thus does not need to have high specific energy characterized by the large  $\eta$  parameter. Thus, the heavy outer shell does not need to have a very large initial diameter for its implosion to be matched to the amount of energy from the driver coupled to this shell by the moment when the shell collides with the low-density fill and eventually converts much of this energy to the thermal energy of the on-axis plasma. This configuration is investigated numerically in the framework of a one-dimensional radiation-magneto-hydrodynamics model for the case of Ar K-shell radiators. It is demonstrated that the argon fill is heated in two stages. The first stage corresponds to the shock heating and thermal conduction in an initially low-density fill, and it allows preheating the fill while avoiding significant losses in soft radiation. The fill radiator is then compressed quasi-adiabatically and is heated-up to the temperature optimum for K-shell quanta generation. Diffusion of the driving magnetic field is shown to always suppress the conductive heat losses from the hot on-axis plasma to the cold outer shell. Absorption of the K-lines emitted near the outer shell with a different gas (like N-on-Ar), which allows a substantial increase in the observed keV x-ray radiation yields.

(VI) Interferometric Measurement of Physical Phenomena During the Implosion Phase of a Puff-On-Puff Z-Pinch Load on Double-Eagle - Theoretical studies have predicted that the disruptive role of the Rayleigh-Taylor (R-T) instability on the current conduction and implosion characteristics of annular Z-pinch loads will be mitigated by mass accretion if uniform fill or multiple annular shell loads are used. Holographic interferometry was used to study these physical processes during the implosion phase of puff-on-puff loads on a terawatt accelerator. Both axial ( $r$ - $z$ ) density perturbation and azimuthal ( $r$  -  $\theta$ ) filamentation modes of the R-T instability were observed. Significant ionization ( $Z$  3 - 10) of the inner gas puff atoms were observed below the anode grid before the outer puff had imploded to this radial position. Radiation hydrodynamic calculations indicate that photoionization by radiation from the outer current carrying shell could not account for this ionization. Current flowing on the inner gas puff could be the source of this ionization. The effect of these physical processes on the radiation yield from z-pinches warrants further

investigation.

(VII) Design of a Multilayer Mirror Monochromatic X-ray Imager for the Z Accelerator - A time-resolved pinhole camera is being developed for monochromatic soft x-ray imaging of z-pinch plasmas on the Z accelerator at Sandia National Laboratories. Pinhole images will reflect from a planar multilayer mirror onto a microchannel plate detector. A W/Si or Cr/C multilayer reflects a narrow energy range (full width at half maximum  $< 10$  eV) centered at 277 eV with peak reflectivity up to 20 percent. This choice of energy will allow final implosion imaging of any wire-array z-pinch fielded on Z, as well as bench testing using a carbon K- $\alpha$  source. Aluminized parylene filters will eliminate optical and second harmonic reflection, and the 34 degree multilayer grazing angle will allow detector shielding from high energy x-rays. The beamline will also include a standard in-line pinhole camera, which can be filtered to obtain simultaneous higher-photon-energy images. Future instruments could use multiple mirrors to image at several energies, or operate at low grazing angle to image 1-10 keV K-shell emission.



# Controlling Uniformity of Gas-Puff and Wire Array Implosions with Wire Current-Carrying Structures

A. L. Velikovich<sup>1</sup> and L. I. Rudakov<sup>2</sup>

<sup>1</sup>*Code 6720, Plasma Physics Division, Naval Research Laboratory*

<sup>2</sup>*Berkeley Scholars, Inc.,*

## Abstract

The magnetic field driving a gas-puff plasma radiation source (PRS) implosion in a realistic load unit of a multi-MA current driver cannot be perfectly uniform. Sources of its non-uniformity (which is mainly azimuthal modulation whose amplitude depends on  $z$ ) include: a finite number of return current posts and the discrete structure of the anode and cathode grids. Analytical formulas have been derived to estimate the contribution of each of these factors to the total non-uniformity (relative modulation amplitude) of the driving magnetic field. The non-uniformity is found to be substantial where the distance from the discrete current-carrying structure is much less than the gap between the two neighboring elements of this structure, whether it be the anode/cathode grids or the return current posts.

For instance, the initial peak-to-valley amplitude of non-uniformity of magnetic pressure at the cylindrical surface of a Z-pinch plasma is given by  $4(r/R)^N$ , where  $r$  is the external plasma radius,  $R$  is the distance between the return current posts and the axis,  $N$  is the number of return current posts. Taking for the 12-cm Titan Pulse Sciences Division (TPSD) nozzle  $r = 7.3$  cm,  $R = 9$  cm, we estimate the non-uniformity of magnetic pressure at the pinch surface as 32% for  $N = 12$  return current posts and 2.6% for  $N = 24$ . A similar estimate for the 12-cm Alameda Applied Sciences Corporation (AASC) nozzle ( $r = 6.6$  cm,  $R = 7.7$  cm), yields an initial non-uniformity of 63% and

10% for  $N = 12$  and  $N = 24$  return current posts, respectively. These estimates suggest that under the conditions of the recent experiments, increasing the number of return current posts from 12 to 24 will make a big difference in terms of the initial azimuthal uniformity of magnetic pressure.

The same formula shows that by decreasing the number of return current posts and at the same time placing them farther from the axis to maintain the uniformity of the driving magnetic field constant, we gain in the minimum stand-off distance  $R_{\min}$  between the PRS and the test object (determined by the solid angle characteristic of the opening between the posts) as much as we lose in the load inductance. Since the x-ray fluence delivered to the object scales approximately as  $R_{\min}^{-2}$ , we can gain a factor of  $\sim 4$  in fluence at the test object at the expense of increasing the initial inductance of the load by a factor of  $\sim 2$ , which translates into adding up to  $\sim 2$  nH to initial inductance.

We have demonstrated that twisting of the anode/cathode wire grids can produce an axial magnetic field sufficiently high to stabilize the gas-puff implosion. It is certainly easier than introducing a Helmholtz coil into the load unit. The advantage of twisting the anode/cathode grids rather than the current return cage is that in the latter case we have to decrease the opening between the posts, and hence, the fluence at the surface of our test object. We have also described the force-free configuration of a twisted wire array load, which can help control the precursor plasma flow to the axis at the early stages of wire array implosions.

## 1. Introduction

The current-carrying structure producing the magnetic field that drives Z-pinch implosions in multi-MA-current facilities is schematically presented in Figure 1.

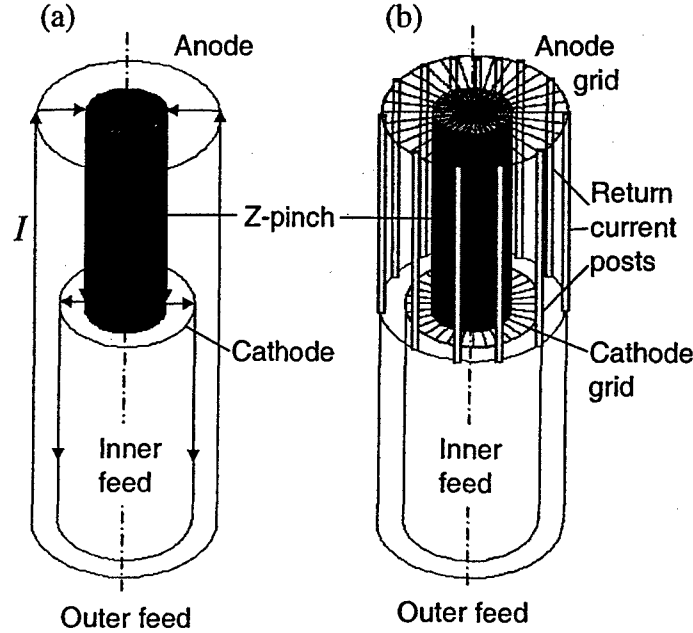


**Figure 1.** Schematic of a PRS gas-puff Z-pinch in a return current cage: idealized azimuthally-symmetric structure (a), and a realistic cage where a finite number of return current posts and the radial anode/cathode spokes violate the azimuthal symmetry (b).

In an azimuthally symmetric structure shown in Figure 1(a), the magnetic field that drives the Z-pinch implosion is azimuthal, independent of  $z$ , and its radial dependence is found using the Ampère's law:

$$B_{\theta}(r) = \frac{\mu_0 I}{2\pi r}, \quad (1)$$

where  $I$  is the current, and  $r$  is the distance from the axis of symmetry to the point where the magnetic field is measured.

Magnetic field given by Eq. (1) is exactly the same as produced by a straight current  $I$  flowing uniformly on an infinite cylindrical Z-pinch surface whose radius  $R_p$  is less than  $r$  (note that in Figure 1, the vertical current in the central pinch is actually

*negative*). In reality, however, this cylinder is never infinite, and the contribution of the vertical current through the plasma pinch cylinder to the magnetic field compressing the pinch is less than 100%. The difference is supplied by the currents flowing in the electrodes, as in Figure 1 – vertical coaxial cylinders (inner and outer feed) and planar horizontal rings, cathode and anode. We calculate each of these contributions separately. This will allow us to estimate the contributions to non-uniformity of the driving magnetic field due to real, discrete structure [Figure 1(b)], as opposite to the idealized [Figure 1(a)] structure of electrodes and return current cage. For this estimate, we subtract from the total in Eq. (1) the contributions of the planar cathode and/or anode rings and/or of the cylindrical section of the outer feed, and replace it with a contribution of the same current  $I$  equally distributed among a given number of either horizontal spokes or vertical return current posts. This approach is not exact: once either of the anode/cathode rings or the return current cylinder is replaced with a set of discrete linear conductors, the current density in the remaining azimuthally-symmetric elements of the structure (the cylindrical surfaces of the feeds and the pinch, the planar anode/cathode surfaces) is no longer azimuthally-symmetric, and acquires some azimuthal modulation, too. However, we have demonstrated that such modulation of the current has little effect on the magnetic field produced by this section far from it: e. g., magnetic field produced by a set of vertical return current posts [Figure 1(b)] at a distance from the posts exceeding the inter-post gap virtually coincides with the field produced by an azimuthally uniform current in a cylindrical return current can of the same length and radius. This justifies our “local” approximation almost everywhere, except, for instance, the corners, where the discrete anode/cathode spokes are connected to the return current posts.

Improved initial uniformity of the imploding plasma could result in a tighter pinch plasma column, and ultimately, in better radiative performance of the PRS. It has been experimentally demonstrated [1] that a substantial increase in the number of wires in a wire array, enhancing the azimuthal uniformity of the imploding plasma, leads to a substantial increase in radiative power. One can argue that improvement of the azimuthal symmetry of a gas-puff implosion achieved through improved design of the load unit can be similarly beneficial for PRS performance, see [2]. It remains to be established in experiments, whether or not this is indeed the case.

The purpose of the present work is to quantify the non-uniformity caused by the discrete anode/cathode and return current structures typical for gas-puff implosions, and thus to estimate the enhancement of uniformity that could possibly be achieved through design of the load unit.

In Section 2, the magnetic field created by finite azimuthally-symmetric elements of the current-carrying structures is calculated, and its contribution to the total driving magnetic field is evaluated. In Sections 3 and 4, we estimate the non-uniformity of the driving magnetic field due to the radial spoke structure of the anode/cathode grid and to the finite number of return current posts. In Section 5, we apply these estimates to the conditions of recent experiments with 12-cm nozzle diameter argon gas-puff loads on the Decade Quad (DQ) simulator at the Arnold Engineering Development Center. Section 6 presents estimates for a stabilizing axial magnetic field  $B_z$  that could be produced by twisting either the anode-cathode spoke structure or the return current cage. Section 7 contains a brief discussion of using twisted wire array loads to produce a collective magnetic field, which does not push the precursor plasma radially to the axis, as in a

straight wire array, or from the axis, as in a solenoid, but rather directs it to fill the gaps between the neighboring wires. Conclusions are summarized in Section 8.

## 2. Magnetic fields produced by finite and semi-infinite cylinders and rings

For this calculation, we use the Biot-Savart's formula

$$\mathbf{B} = \frac{\mu_0}{4\pi} \int \frac{\mathbf{j} \times \mathbf{R}}{R^3} dl, \quad (2)$$

where  $\mathbf{j}dl$  is a current element,  $\mathbf{R}$  is a vector from this current element's position to the observation point where the magnetic field is calculated. For a uniform vertical current flowing on the surface of a cylinder whose radius is  $R_0$

$$\mathbf{j}dl = \{0, 0, 1\} \frac{Idz d\theta}{2\pi}, \quad (3)$$

$$\mathbf{R} = \{r \cos \phi - R_0 \cos \theta, r \sin \phi - R_0 \sin \theta, z - z_0\},$$

$$R^3 = [r^2 + R_0^2 - 2rR_0 \cos(\theta - \phi) + (z - z_0)^2]^{3/2}, \quad (4)$$

where  $x = r \cos \phi$ ,  $y = r \sin \phi$ ,  $z$ , and  $x = R_0 \cos \theta$ ,  $y = R_0 \sin \theta$ ,  $z_0$  are coordinates of the observation point and of the current element, respectively. Substituting (3), (4) into (2), we find:

$$\mathbf{B} = \frac{\mu_0 I}{8\pi^2} \int dz_0 \int d\theta \frac{\{-r \sin \phi + R_0 \sin \theta, r \cos \phi - R_0 \cos \theta, 0\}}{[r^2 + R_0^2 - 2rR_0 \cos(\theta - \phi) + (z - z_0)^2]^{3/2}}, \quad (5)$$

or

$$B_x = \frac{\mu_0 I}{8\pi^2} \int dz_0 \int_0^{2\pi} d\theta \frac{-r \sin \phi + R_0 \sin \theta}{[r^2 + R_0^2 - 2rR_0 \cos(\theta - \phi) + (z - z_0)^2]^{3/2}}, \quad (6)$$

$$B_y = \frac{\mu_0 I}{8\pi^2} \int dz_0 \int_0^{2\pi} d\theta \frac{r \cos \phi - R_0 \cos \theta}{[r^2 + R_0^2 - 2rR_0 \cos(\theta - \phi) + (z - z_0)^2]^{3/2}}, \quad (7)$$

$$B_z = 0. \quad (8)$$

Since in cylindrical coordinates

$$B_r = B_x \cos \phi + B_y \sin \phi, \quad B_\theta = -B_x \sin \phi + B_y \cos \phi, \quad (9)$$

we find:

$$B_r = \frac{\mu_0 I}{8\pi^2} \int dz \int_0^{2\pi} d\theta \frac{\sin(\theta - \phi)}{[r^2 + R_0^2 - 2rR_0 \cos(\theta - \phi) + (z - z_0)^2]^{3/2}} = 0. \quad (10)$$

Therefore, any azimuthally-symmetric vertical (axial) current contributes only to the azimuthal magnetic field:

$$B_\theta = \frac{\mu_0 I}{8\pi^2} \int dz_0 \int_0^{2\pi} d\theta \frac{r - R_0 \cos(\theta - \phi)}{[r^2 + R_0^2 - 2rR_0 \cos(\theta - \phi) + (z - z_0)^2]^{3/2}}. \quad (11)$$

The integral (11) is easily calculated if the cylinder is infinite, extending from  $-\infty$  to  $+\infty$ . Then, changing the variables of integration to  $\theta' = \theta - \phi$  and  $z' = z_0 - z$

$$\begin{aligned} B_\theta &= \frac{\mu_0 I}{8\pi^2} \int_0^{2\pi} d\theta' (r - R_0 \cos \theta') \int_{-\infty}^{+\infty} dz' [r^2 + R_0^2 - 2rR_0 \cos \theta' + z'^2]^{3/2} \\ &= \frac{\mu_0 I}{4\pi^2} \int_0^{2\pi} d\theta' \frac{r - R_0 \cos \theta'}{r^2 + R_0^2 - 2rR_0 \cos \theta'} = \frac{\mu_0 I}{2\pi r} \Theta(r - R_0), \end{aligned} \quad (12)$$

where  $\Theta(x)$  is the Heaviside step function:  $\Theta(x) = 1$  for  $x > 0$  and  $\Theta(x) = 0$  for  $x < 0$ .

We have thus reproduced (1).

The next step is calculating the magnetic field produced by a half-infinite cylinder extending either from  $-\infty$  to  $z = z_1$  or from  $z = z_1$  to  $+\infty$ . Denote the corresponding contributions to  $B_\theta$  by  $B(r, z; r' = R_0, -\infty < z' < z_1)$  and  $B(r, z; r' = R_0, z_1 < z' < +\infty)$  (here and below the primed variables indicate the current-carrying contour). Then we obviously have

$$B(r, z; r' = R_0, -\infty < z' < z_1) + B(r, z; r' = R_0, z_1 < z' < +\infty) = \frac{\mu_0 I}{2\pi r} \Theta(r - R_0). \quad (13)$$

Therefore we need to calculate only one of these two integrals; the other complements it to the right-hand side of (13). The result is:

$$B(r, z; r' = R_0, z_1 < z' < +\infty) = \frac{\mu_0 I}{2\pi r} \left\{ \frac{1}{2} \Theta(r - R_0) + \frac{z - z_1}{2\pi(r + R_0)\sqrt{(r + R_0)^2 + (z - z_1)^2}} \times \right. \\ \left. \left[ (r + R_0)K\left(2\sqrt{\frac{rR_0}{(r + R_0)^2 + (z - z_1)^2}}\right) + (r - R_0)\Pi\left(\frac{4rR_0}{(r + R_0)^2}, 2\sqrt{\frac{rR_0}{(r + R_0)^2 + (z - z_1)^2}}\right) \right] \right\}, \quad (14a)$$

$$B(r, z; r' = R_0, -\infty < z' < z_1) = \frac{\mu_0 I}{2\pi r} \left\{ \frac{1}{2} \Theta(r - R_0) - \frac{z - z_1}{2\pi(r + R_0)\sqrt{(r + R_0)^2 + (z - z_1)^2}} \times \right. \\ \left. \left[ (r + R_0)K\left(2\sqrt{\frac{rR_0}{(r + R_0)^2 + (z - z_1)^2}}\right) + (r - R_0)\Pi\left(\frac{4rR_0}{(r + R_0)^2}, 2\sqrt{\frac{rR_0}{(r + R_0)^2 + (z - z_1)^2}}\right) \right] \right\}, \quad (14b)$$

where  $K(\varphi)$  and  $\Pi(\alpha, \varphi)$  are complete elliptic integrals of the first and third kind, respectively [3].

Equations (14a, b) allow us to calculate the contribution to the azimuthal magnetic field from a finite cylinder of radius  $R_0$  extending from  $z = z_1$  to  $z = z_2$ , which we denote by  $B(r, z; r' = R_0, z_1 < z' < z_2)$ . Obviously,

$$B(r, z; r' = R_0, z_1 < z' < z_2) + B(r, z; r' = R_0, -\infty < z' < z_1) \\ + B(r, z; r' = R_0, z_2 < z' < +\infty) = \frac{\mu_0 I}{2\pi r} \Theta(r - R_0). \quad (15)$$

Substituting (14) into (15), we obtain the azimuthal magnetic field of a finite cylinder:



$$\begin{aligned}
B(r, z; r' = R_0, z_1 < z' < z_2) = & \frac{\mu_0 I}{4\pi^2 r(r+R_0)} \left\{ \frac{z-z_1}{\sqrt{(r+R_0)^2 + (z-z_1)^2}} \times \right. \\
& \left[ (r+R_0)K\left(2\sqrt{\frac{rR_0}{(r+R_0)^2 + (z-z_1)^2}}\right) + (r-R_0)\Pi\left(\frac{4rR_0}{(r+R_0)^2}, 2\sqrt{\frac{rR_0}{(r+R_0)^2 + (z-z_1)^2}}\right) \right] \\
& - \frac{z-z_2}{\sqrt{(r+R_0)^2 + (z-z_2)^2}} \left[ (r+R_0)K\left(2\sqrt{\frac{rR_0}{(r+R_0)^2 + (z-z_2)^2}}\right) \right. \\
& \left. \left. + (r-R_0)\Pi\left(\frac{4rR_0}{(r+R_0)^2}, 2\sqrt{\frac{rR_0}{(r+R_0)^2 + (z-z_2)^2}}\right) \right] \right\}. \quad (16)
\end{aligned}$$

Now we can calculate the azimuthal magnetic field of the horizontal electrodes, anode and cathode. To begin, we find the azimuthal magnetic field  $B(r, z; R_0 < r' < +\infty, z' = z_1)$  produced by a negative radial current flowing in an infinite plane with a circular hole of the radius  $R_0$  near the origin. Obviously, for the top-hat current configuration (current flowing inward radially on the plane  $z = z_1$ , and then in the positive  $z$  direction on the surface of a half-infinite cylinder whose radius is  $r = R_0$ ),

$$\begin{aligned}
& B(r, z; R_0 < r' < +\infty, z' = z_1) + B(r, z; r' = R_0, z_1 < z' < +\infty) \\
& = \frac{\mu_0 I}{2\pi r} \Theta(r-R_0)\Theta(z-z_1). \quad (17)
\end{aligned}$$

Equation (17) means that the magnetic field is the same as given by (1) outside the half-infinite vertical cylinder and above the horizontal electrode plane, and zero elsewhere.

Substituting (14a) into (17), we find:

$$\begin{aligned}
B(r, z; R_0 < r' < +\infty, z' = z_1) = & \frac{\mu_0 I}{2\pi r} \left\{ \frac{1}{2} \Theta(r-R_0)[2\Theta(z-z_1)-1] \right. \\
& - \frac{z-z_1}{2\pi(r+R_0)\sqrt{(r+R_0)^2 + (z-z_1)^2}} \times \left[ (r+R_0)K\left(2\sqrt{\frac{rR_0}{(r+R_0)^2 + (z-z_1)^2}}\right) \right. \\
& \left. \left. + (r-R_0)\Pi\left(\frac{4rR_0}{(r+R_0)^2}, 2\sqrt{\frac{rR_0}{(r+R_0)^2 + (z-z_1)^2}}\right) \right] \right\}. \quad (18)
\end{aligned}$$

Now we are able to calculate the azimuthal magnetic field produced by a current flowing in the negative radial direction through a planar ring that extends between  $r = R_1$  and  $r = R_2$ . We denote this field by  $B(r, z; R_1 < r' < R_2, z' = z_1)$ . Obviously,

$$\begin{aligned} & B(r, z; R_1 < r' < R_2, z' = z_1) + B(r, z; R_2 < r' < +\infty, z' = z_1) \\ & = B(r, z; R_1 < r' < +\infty, z' = z_1), \end{aligned} \quad (19)$$

and therefore

$$\begin{aligned} B(r, z; R_1 < r' < R_2, z' = z_1) = & \frac{\mu_0 I}{2\pi r} \left\{ \left[ \Theta(z - z_1) - \frac{1}{2} \right] [\Theta(r - R_1) - \Theta(r - R_2)] \right. \\ & - \frac{z - z_1}{2\pi(r + R_1)\sqrt{(r + R_1)^2 + (z - z_1)^2}} \left[ (r + R_1)K\left(2\sqrt{\frac{rR_1}{(r + R_1)^2 + (z - z_1)^2}}\right) \right. \\ & \left. \left. + (r - R_1)\Pi\left(\frac{4rR_1}{(r + R_1)^2}, 2\sqrt{\frac{rR_1}{(r + R_1)^2 + (z - z_1)^2}}\right) \right] \right. \\ & + \frac{z - z_1}{2\pi(r + R_2)\sqrt{(r + R_2)^2 + (z - z_1)^2}} \left[ (r + R_2)K\left(2\sqrt{\frac{rR_2}{(r + R_2)^2 + (z - z_1)^2}}\right) \right. \\ & \left. \left. + (r - R_2)\Pi\left(\frac{4rR_2}{(r + R_2)^2}, 2\sqrt{\frac{rR_2}{(r + R_2)^2 + (z - z_1)^2}}\right) \right] \right\}. \end{aligned} \quad (20)$$

Assigning dimensions to the idealized current configuration of Figure 1(a), as shown in Figure 2, we express the contributions to the azimuthal magnetic field as

$$\begin{aligned} B_{\theta}^{\text{inner feed}}(r, z) &= B(r, z; r' = R_1, -\infty < z' < 0), \\ B_{\theta}^{\text{outer feed}}(r, z) &= -B(r, z; r' = R_2, -\infty < z' < h), \\ B_{\theta}^{\text{Z-pinch}}(r, z) &= B(r, z; r' = R_p, 0 < z' < h), \\ B_{\theta}^{\text{cathode}}(r, z) &= B(r, z; R_p < r' < R_1, z' = 0), \\ B_{\theta}^{\text{anode}}(r, z) &= -B(r, z; R_p < r' < R_2, z' = h); \end{aligned} \quad (21)$$

to obtain the correct sign of magnetic field we should take into account the negative direction of the current  $I$  (Figures 1, 2) in Eqs. (14), (16) and (20), as indicated above.

From (14), (16), (20) we obtain the expression for the total azimuthal magnetic field in the idealized configuration of Figure 2:

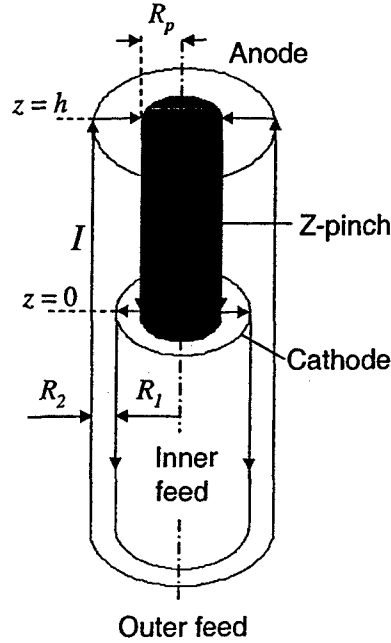


Figure 2. Dimensions assigned to the idealized configuration of Figure 1(a): Z-pinch radius  $R_p$ , its height  $h$ , radii of the inner and the outer coaxial feed electrodes are  $R_1$  and  $R_2$ , respectively.

$$\begin{aligned}
 & B_{\theta}^{\text{inner feed}}(r, z) + B_{\theta}^{\text{outer feed}}(r, z) + B_{\theta}^{\text{Z-pinch}}(r, z) + B_{\theta}^{\text{cathode}}(r, z) + B_{\theta}^{\text{anode}}(r, z) \\
 &= \frac{\mu_0 I}{2\pi r} \left\{ [\Theta(r - R_2) - \Theta(r - R_p)] \Theta(z - h) - [\Theta(r - R_1) - \Theta(r - R_p)] \Theta(z) + \Theta(r - R_1) - \Theta(r - R_2) \right\}
 \end{aligned}
 \tag{22}$$

This is the correct generalization of Eq. (1) for the geometry of Figures 1(a), 2. Due to the factor in braces, the magnetic field coincides with Eq. (1) between the Z-pinch column or the inner feed and the outer feed cylinder, below the anode plane, and is zero above the anode, outside of the outer feed or inside the inner. The magnetic field near the pinch surface, that drives the implosion, is expressed by Eq. (1), as it should be.

Figures 3-5 illustrate the relative contributions to the azimuthal magnetic field.

These figures are plotted for  $R_p = 6$  cm,  $R_1 = 7$  cm,  $R_2 = 8$  cm,  $h = 4$  cm, which

resembles the parameters of the DQ load unit. Figures 3 and 4 show the radial profiles of  $B_\theta$  and various contributions to it, at mid-section ( $z = 2$  cm) and 1 mm above the cathode ( $z = 0.1$  cm), respectively. The magnetic fields are normalized with respect to the maximum value of  $B_\theta$  at the pinch surface. At the mid-section (Figure 3), 67% of the total  $B_\theta$  near the pinch plasma surface is produced by the current flowing in the z-pinch, 83% - by the z-pinch and the coaxial feed, and the remaining 17% - by the horizontal electrodes, cathode and anode.

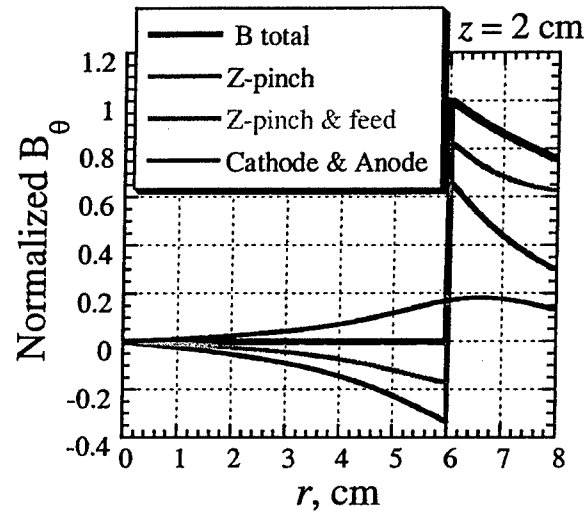


**Figure 3.** Radial profiles of the azimuthal magnetic field and three separate contributions to it in the mid-section of the pinch.

The electrodes' contribution is higher in the vicinity of the cathode and anode. Figure 4 shows the same radial profiles as Figure 3 at 1 mm above the cathode, where the electrodes contribute 30% of the total. The radial profiles at  $z = 3.9$  cm, 1 mm below the anode, look very similar to those shown in Figure 4, the electrodes' contribution being 28% of the total.

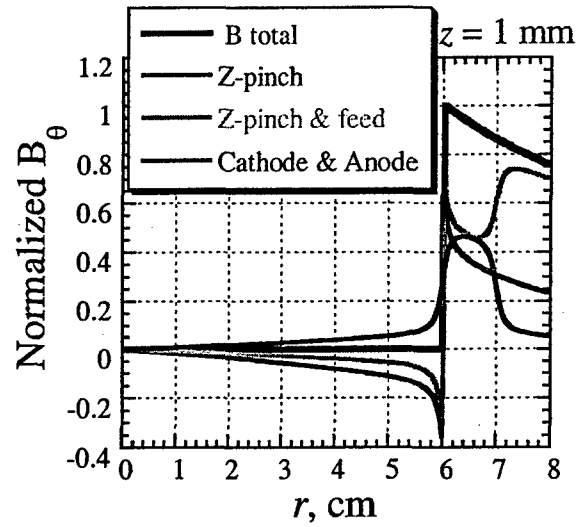


**Figure 4.** Radial profiles of the azimuthal magnetic field and three separate contributions to it 1 mm above the cathode.

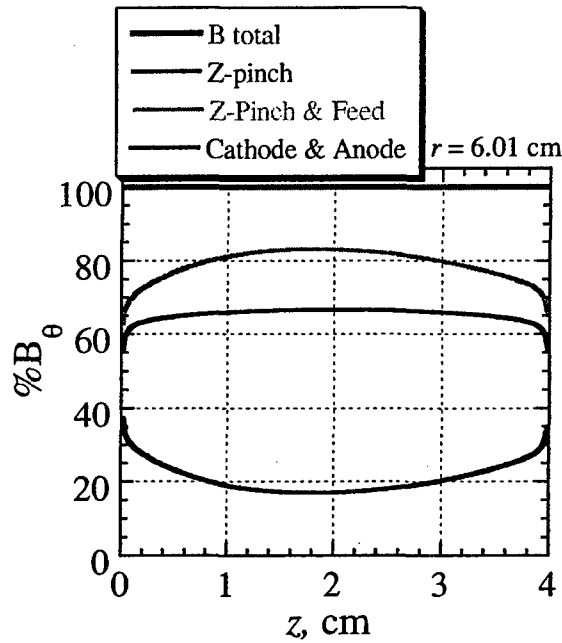


**Figure 5.** Axial profiles of the azimuthal magnetic field and three separate contributions to it near the pinch surface.

The axial dependence of the magnetic field near the pinch surface ( $r = 6.01$  cm) is shown in Figure 5. The maximum electrode contributions seen in Figure 5 are 37% near the cathode and 34% near the anode. The actual limits of these contributions at

$R_p = 6.01$  cm,  $z = \varepsilon$  cm and  $z = h - \varepsilon$  and  $\varepsilon \rightarrow 0$  are even higher, 55% and 53%, respectively, but these are reached at extremely small distances from the electrodes,  $\varepsilon \sim 10^{-4}$ . The limit could also be taken differently, assuming additionally  $R_p = 6 + \varepsilon$  cm. In the latter case, the corresponding limiting values are 42% and 40% respectively.

### 3. Contribution to the non-uniformity due to the radial anode/cathode spokes

Let us estimate the non-uniformity of the driving magnetic field due to the discreteness of the anode/cathode sets of radial spokes. The magnetic field is calculated in the same way from the integral in Eq. (2). The spokes are assumed to be thin wires whose diameters are small compared to all the other characteristic distances. The integration in (2) is thus reduced to a line integral calculated for each spoke, which extends from  $r = R_1$  to  $r = R_2$  at  $z = z_0$  and the azimuthal angle  $\theta_j = 2\pi j / N_s$ , where  $N_s$  is the number of radial spokes [see Figure 1(b)], and  $j = 0, 1, \dots, N_s - 1$ . Each wire carries  $1/N_s$  of the total current  $I$ , which is assumed to flow in the negative radial direction. Then the summation over  $j$  is performed. The result is:

$$B_\theta \equiv \tilde{B}_\theta(r, \phi, z; R_1 < r' < R_2, z' = z_0, N_s) \\ = \frac{\mu_0 I (z - z_0)}{4\pi N_s} \sum_{j=0}^{N_s-1} \frac{\cos(\theta_j - \phi)}{r^2 \sin^2(\theta_j - \phi) + (z - z_0)^2} \times [G_j(r, \phi, z, R_2, z_0) - G_j(r, \phi, z, R_1, z_0)] \quad (23)$$

$$B_r \equiv \tilde{B}_r(r, \phi, z; R_1 < r' < R_2, z' = z_0, N_s) \\ = -\frac{\mu_0 I (z - z_0)}{4\pi N_s} \sum_{j=0}^{N_s-1} \frac{\sin(\theta_j - \phi)}{r^2 \sin^2(\theta_j - \phi) + (z - z_0)^2} \times [G_j(r, \phi, z, R_2, z_0) - G_j(r, \phi, z, R_1, z_0)] \quad (24)$$

$$B_z \equiv \tilde{B}_z(r, \phi, z; R_1 < r' < R_2, z' = z_0, N_s) \\ = \frac{\mu_0 I r}{4\pi N_s} \sum_{j=0}^{N_s-1} \frac{\sin(\theta_j - \phi)}{r^2 \sin^2(\theta_j - \phi) + (z - z_0)^2} \times [G_j(r, \phi, z, R_2, z_0) - G_j(r, \phi, z, R_1, z_0)], \quad (25)$$

where

$$G_j(r, \phi, z, R, z_0) = \frac{R - r \cos(\theta_j - \phi)}{[r^2 + R^2 - 2rR \cos(\theta_j - \phi) + (z - z_0)^2]^{1/2}}. \quad (26)$$

The magnetic field produced by the set of spokes has all three components, in contrast with the magnetic field of a planar ring, which has only the azimuthal component given by (20). The radial and axial components, however, oscillate and both vanish at the angular positions of the spokes,  $\phi = \theta_j$  or exactly between them,  $\phi = \theta_j + \pi/N_s, j = 0, 1, \dots, N_s - 1$ , due to symmetry [the terms of equal magnitude and opposite signs containing  $\sin(\theta_j - \phi)$  in the sums (24), (25) cancel each other in both cases]. We can expect that the radial and azimuthal components of the field vanish with either increased distance from the set of spokes and the observation point or increased number of the spokes  $N_s$ . In any case, the magnetic field produced by the set of spokes should tend to that generated by a planar ring, (20):

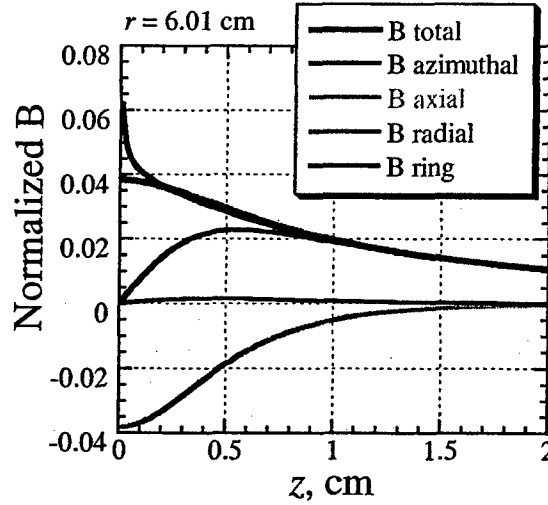


**Figure 6.** Axial profiles of the three components of magnetic field produced by a set of 16 spokes and the azimuthal field produced by an equivalent planar ring.

$$\begin{aligned}
\tilde{B}_\theta(r, z, \phi; R_1 < r' < R_2, z' = z_0, N_s) &\rightarrow B(r, z; R_1 < r' < R_2, z' = z_0), \\
\tilde{B}_r(r, z, \phi; R_1 < r' < R_2, z' = z_0, N_s) &\rightarrow 0, \\
\tilde{B}_z(r, z, \phi; R_1 < r' < R_2, z' = z_0, N_s) &\rightarrow 0.
\end{aligned} \tag{27}$$

Figures 6 and 7 demonstrate this limiting transition. They are both plotted for  $r = 6.01$  cm, the other parameters being the same as taken for the cathode ring in Figures 3-5:  $R_1 = 6$  cm,  $R_2 = 7$  cm. Figure 6 is plotted for  $N_s = 16$  spokes and the angular position is  $\phi = \pi/2N_s$ , exactly in the middle between the positions  $\phi = 0$  and  $\phi = \pi/N_s$ , where both radial and axial components of the magnetic field vanish. The magnetic field is normalized with respect to the factor  $\mu_0 I / 2\pi$  (in these units the magnetic field of an infinite cylinder is  $1/r \approx 0.166$ ). Figure 6 presents the axial dependence of magnetic field. For  $z < 5$  mm, there is noticeable difference between the fields produced by the set of spokes and an equivalent ring. This is not surprising, since the inter-spoke gap at  $r = 6.01$  cm is  $2\pi/N_s = 2.3$  cm, and at the distance from the cathode plane much less than that, the private field of the closest spoke dominates. It is rather surprising that at  $z > 1$  cm, which is still less than the inter-spoke gap, the private magnetic field is already small compared to the collective field produced by all the other spokes, the magnetic field there being almost undistinguishable from that of a ring.

Figure 7 demonstrates the same limiting transition with increased number of the spokes. Here, we increase the number of the spokes  $N_s$  from 16 to 1024, keeping fixed  $z = 2$  mm and choosing  $\phi = \pi/2N_s$  for each  $N_s$ . Again, we see that the field produced by the set of spokes approaches the continuum limit between  $N_s = 2^6 = 64$  and



$N_s = 2^7 = 128$ , as the ratio of the inter-spoke gap  $2\pi r / N_s$  to the height  $z$  decreases from  $\sim 3$  to  $\sim 1.5$ , still remaining greater than unity.

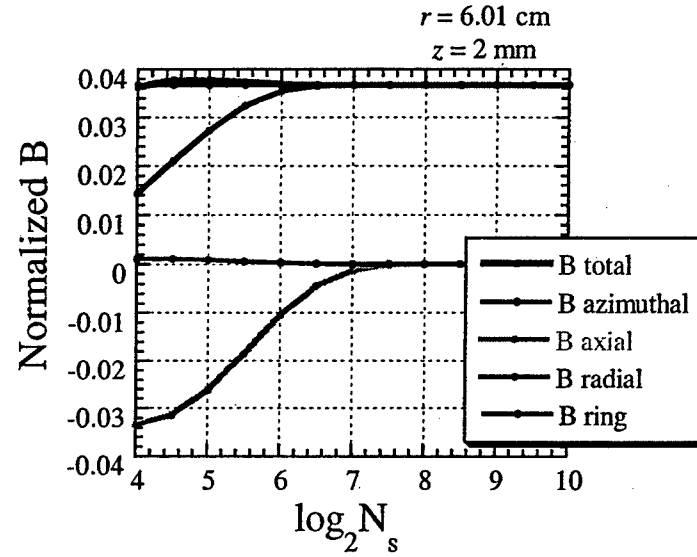


Figure 7. Dependence of the three components of magnetic field produced by a set of  $N_s$  spokes on the number of spokes varied between 16 and 1024.

Figures 8-12 illustrate the profiles of magnetic field near the pinch surface calculated for the same parameters as in Figures 3-5:  $R_p = 6$  cm,  $R_1 = 7$  cm,  $R_2 = 8$  cm,  $h = 4$  cm. Both the cathode and the anode grids are assumed to consist of radial spokes, the number of which is varied from  $N_s = 16$  (Figures 8 to 10) to  $N_s = 32$  (Figures 11, 12), which corresponds to the inter-spoke gap at the pinch surface varied from 2.36 cm to 1.18 cm. The magnetic fields at the given radius  $r = 6.01$  cm and height  $z$  are shown vs. the angular position. As before,  $z = 0$  corresponds to the cathode surface. The angle  $\phi$  is expressed in degrees and varied between  $\phi = 0^\circ$  and  $\phi = 360^\circ / N_s$ , which corresponds to the angular positions of two neighboring wires. In the legends, the black curve labeled "B symmetric" stands for the azimuthal (=total) magnetic field (1) produced by the

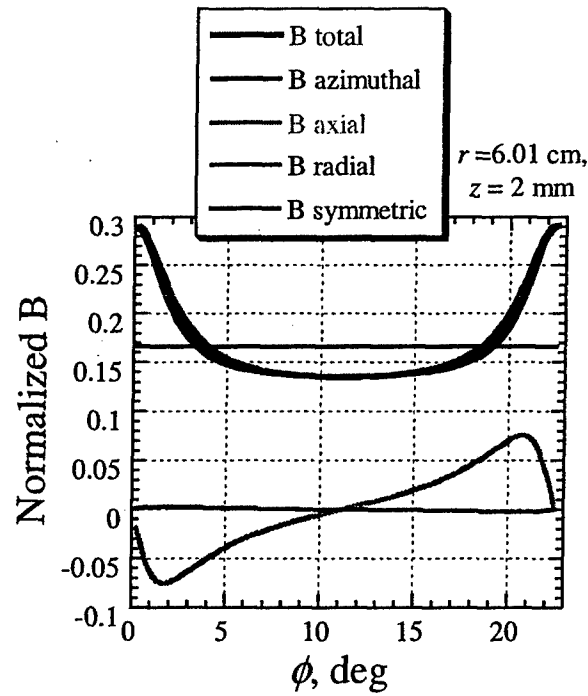


Figure 8. Magnetic field profiles for  $N_s = 16$ ,  $r = 6.01$  cm,  $z = 2$  mm.

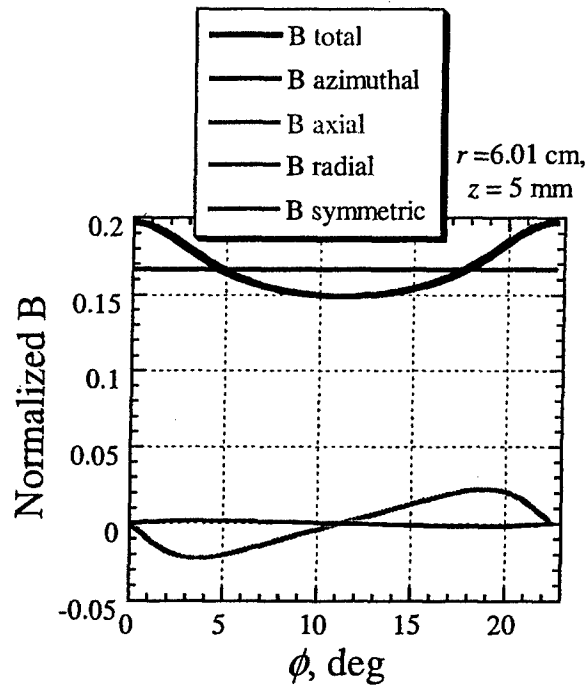


Figure 9. Magnetic field profiles for  $N_s = 16$ ,  $r = 6.01$  cm,  $z = 5$  mm.

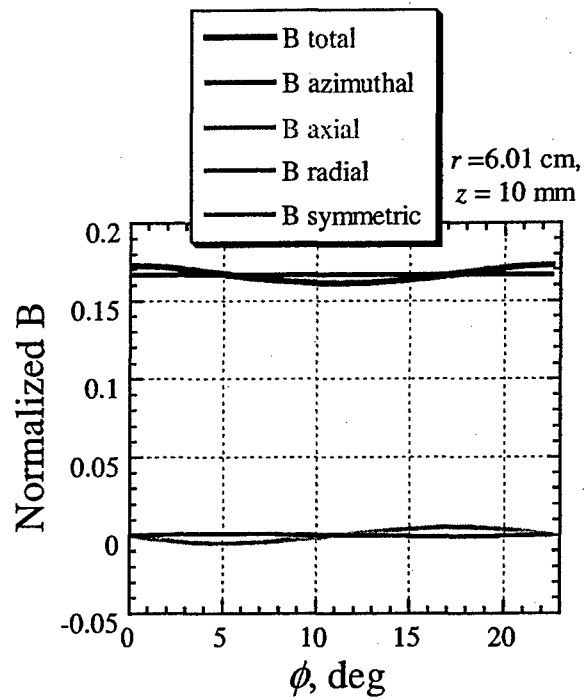


Figure 10. Magnetic field profiles for  $N_s = 16$ ,  $r = 6.01$  cm,  $z = 1$  cm.

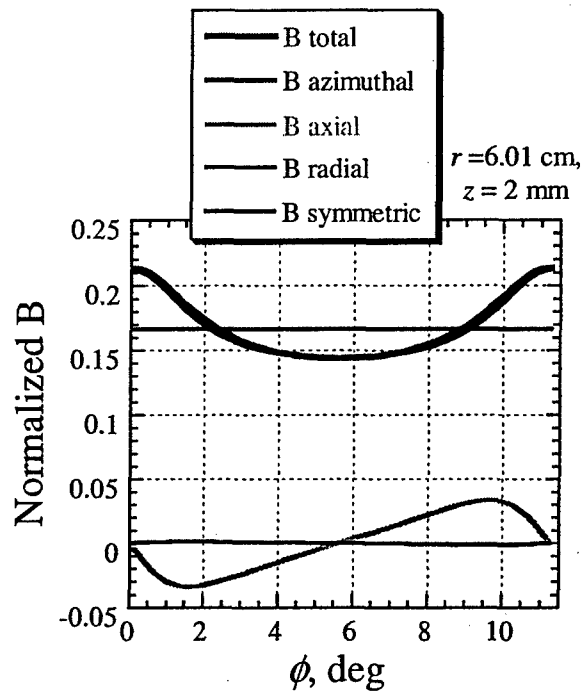


Figure 11. Magnetic field profiles for  $N_s = 32$ ,  $r = 6.01$  cm,  $z = 2$  mm.

symmetric structure of Figure 1(a) and thereby independent of  $\phi$ . Magnetic field is normalized with respect to  $\mu_0 I / 2\pi$ , as before.

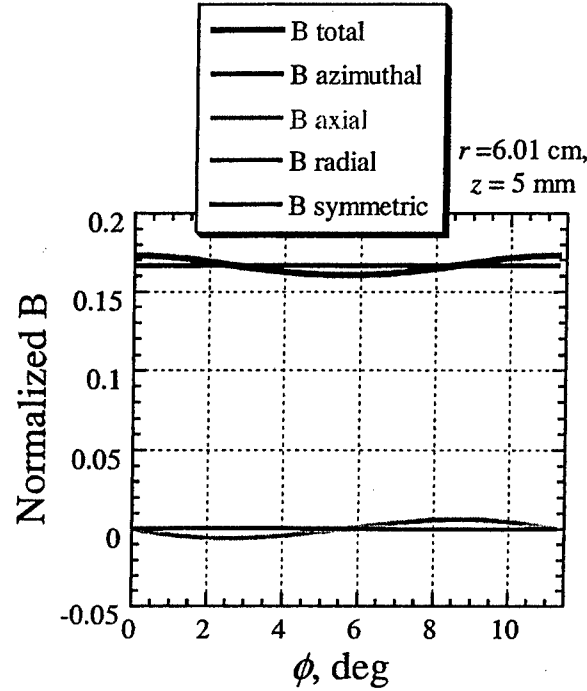


Figure 12. Magnetic field profiles for  $N_s = 32$ ,  $r = 6.01$  cm,  $z = 5$  mm.

For  $N_s = 16$ , the relative peak-to-valley variation of the magnetic pressure  $B^2 / 2\mu_0$  decreases from 237% at  $z = 2$  mm (Figure 8) to 60% at  $z = 5$  mm (Figure 9) to 14% at  $z = 1$  cm (Figure 10).

Doubling the number of spokes to make  $N_s = 32$  - that is, reducing the inter-spoke gap by a factor of 2, - we decrease the relative peak-to-valley variation of the magnetic pressure to 89% at  $z = 2$  mm (Figure 11) and 14% at  $z = 5$  mm (Figure 12).

The axial dependence of the non-uniformity is summarized in Figure 13, where the profiles of the azimuthal component of the magnetic field are presented vs.  $z$  for both cases of 16 and 32 spokes, for the angles corresponding to the maximum and minimum values of the azimuthal and total magnetic field (see Figures 8-12): exactly above the

spokes, at  $\phi = 0^\circ$ , and exactly in the middle between the spokes, at  $\phi = 180^\circ / N_s$ . We conclude that the discreteness of the anode and cathode grids translates into an appreciable non-uniformity of the driving magnetic field only at the distances much smaller than the inter-spoke gap. For  $R_p = 6$  cm,  $R_1 = 7$  cm,  $R_2 = 8$  cm,  $h = 4$  cm, the peak-to-valley variation of magnetic pressure is significant at distances from the cathode and anode planes less than  $\frac{1}{2}$  of the inter-spoke gap, which means less than 1.2 cm for 16 spokes, or less than 0.6 cm for 32 spokes.

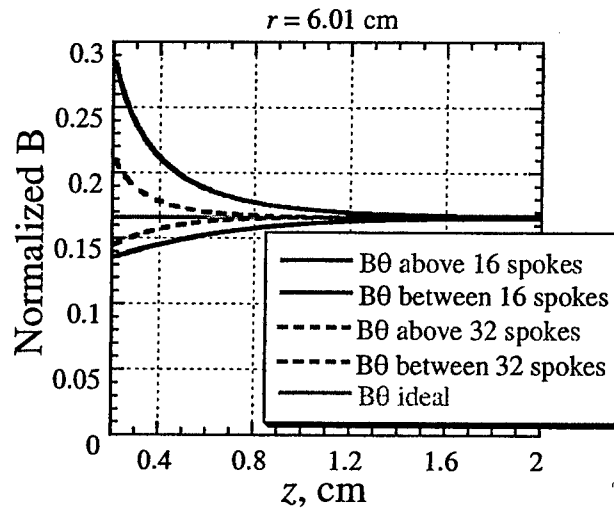


Figure 13. Axial profiles of the azimuthal magnetic field for ideal cylindrically-symmetric case (green line), for 16 and 32 spokes (solid and dashed lines, respectively), at angular locations exactly above the spokes  $\phi = 0^\circ$  and in the middle between the spokes  $\phi = 180^\circ / N_s$  (red and blue lines, respectively).

If the radial spoke structure is replaced with a rectangular or hexagonal mesh with a 2 mm cell size, the driving magnetic field should be undistinguishable from that of the ideal structure (Figure 1) at distances from the cathode and the anode exceeding 1 mm.

#### 4. Contribution to non-uniformity due to the finite number of return current posts

There is a simple way of estimating the modulation amplitude of magnetic pressure due to a finite number of return current posts. To do this, we note that the discreteness of the set of the vertical return current posts should only be noticeable at distances much less than the inter-post gap  $\Delta r_p = 2\pi R_2 / N_p$ , where  $N_p$  is the number of return current posts. Indeed, as explained below, the variation of the magnetic pressure at  $r = R_2 - \Delta r_p$  is estimated as  $4\exp(-2\pi) \cong 0.7\% \ll 1$ . Therefore one can estimate this non-uniformity assuming the return current posts to have infinite length and neglecting the contributions to the non-uniformity coming from all other sources.

Then, assuming that the pinch current  $I$  flowing through the load in  $z$ -direction is cylindrically-symmetric, the return current is equally divided between the  $N_p$  return current posts located at  $r = R_2$  and  $\theta = \theta_j = 2\pi j / N_p$ ,  $j = 0, 1, \dots, N_p - 1$ , and the magnetic field depends only on  $x$  and  $y$ , we find that the vector potential has only a  $z$ -component, which can be written as

$$\begin{aligned} A_z(r, \phi) &= -\frac{\mu_0 I}{2\pi} \left[ \ln r - \frac{1}{N_p} \sum_{j=0}^{N_p-1} \ln |\mathbf{r} - \mathbf{r}_j| \right] \\ &= -\frac{\mu_0 I}{2\pi} \left[ \ln r - \frac{1}{2N_p} \ln \prod_{j=0}^{N_p-1} \left( r^2 - 2rR_2 \cos \left( \phi - \frac{2\pi j}{N_p} \right) + R_2^2 \right) \right]. \end{aligned} \quad (28)$$

Using complex representation on the  $(x, y)$  plane,  $\hat{z} = x + iy = r \exp(i\phi)$ , we can reduce the product in (28) to

$$\begin{aligned}
& \prod_{j=0}^{N_p-1} \left( r^2 - 2rR_2 \cos \left( \phi - \frac{2\pi j}{N_p} \right) + R_2^2 \right) = \prod_{j=0}^{N_p-1} |\hat{z} - \hat{z}_j|^2 \\
& = \prod_{j=0}^{N_p-1} (\hat{z} - \hat{z}_j) \times \prod_{j=0}^{N_p-1} (\bar{\hat{z}} - \bar{\hat{z}}_j) = (\hat{z}^{N_p} - R_2^{N_p}) (\bar{\hat{z}}^{N_p} - R_2^{N_p}) \\
& = (r^{N_p} \cos N_p \phi - R_2^{N_p} + ir^{N_p} \sin N_p \phi) (r^{N_p} \cos N_p \phi - R_2^{N_p} - ir \sin N_p \phi) \\
& = r^{2N_p} - 2r^{N_p} R_2^{N_p} \cos N_p \phi + R_2^{2N_p}.
\end{aligned} \tag{29}$$

This transformation could be performed because the positions  $(x_j, y_j)$  of the return current posts on the  $(x, y)$  plane exactly correspond to the  $N_p$  complex roots  $\hat{z}_j$ ,  $j = 0, 1, \dots, N_p - 1$ , of the equation  $\hat{z}^{N_p} = R_2^{N_p}$  on the complex plane  $\hat{z}$  [4, 5]. Therefore,

$$A_z(r, \phi) = -\frac{\mu_0 I}{2\pi} \left[ \ln r - \frac{1}{2N_p} \ln (r^{2N_p} - 2r^{N_p} R_2^{N_p} \cos N_p \phi + R_2^{2N_p}) \right], \tag{30}$$

and we find the magnetic field:

$$\begin{aligned}
B_\theta(r, \phi) &= -\frac{\partial A_z}{\partial r} = \frac{\mu_0 I}{2\pi} \left[ \frac{1}{r} - \frac{r^{2N_p-1} - r^{N_p-1} R_2^{N_p} \cos N_p \phi}{r^{2N_p} - 2r^{N_p} R_2^{N_p} \cos N_p \phi + R_2^{2N_p}} \right] \\
&= \frac{\mu_0 I}{2\pi} \times \frac{R_2^{N_p} (R_2^{N_p} - r^{N_p} \cos N_p \phi)}{r (r^{2N_p} - 2r^{N_p} R_2^{N_p} \cos N_p \phi + R_2^{2N_p})},
\end{aligned} \tag{31}$$

$$B_r(r, \phi) = \frac{1}{r} \frac{\partial A_z}{\partial \phi} = \frac{\mu_0 I}{2\pi} \times \frac{r^{N_p-1} R_2^{N_p} \sin N_p \phi}{r^{2N_p} - 2r^{N_p} R_2^{N_p} \cos N_p \phi + R_2^{2N_p}}. \tag{32}$$

The magnetic pressure is

$$p_M = \frac{1}{2\mu_0} (B_\theta^2 + B_r^2) = \frac{\mu_0 I^2}{8\pi^2} \times \frac{R_2^{2N_p}}{r^2 (r^{2N_p} - 2r^{N_p} R_2^{N_p} \cos N_p \phi + R_2^{2N_p})}. \tag{33}$$

For a given  $r$ , the magnetic pressure (33) is an oscillating function of the azimuthal angle  $\phi$  with a period of  $2\pi/N_p$ . Its maximum and minimum values are achieved at positions where  $\cos N_p \phi = 1$  and  $\cos N_p \phi = -1$ , respectively:

$$p_{M,\max} = \frac{\mu_0 I^2}{8\pi^2} \times \frac{R_2^{2N_p}}{r^2 (R_2^{N_p} - r^{N_p})^2}, \quad p_{M,\min} = \frac{\mu_0 I^2}{8\pi^2} \times \frac{R_2^{2N_p}}{r^2 (R_2^{N_p} + r^{N_p})^2}. \quad (34)$$

The average value of magnetic pressure could be estimated in two ways: either

$$\bar{p}_M = \frac{1}{2} (p_{M,\max} + p_{M,\min}) = \frac{\mu_0 I^2}{8\pi^2} \times \frac{R_2^{2N_p} (R_2^{2N_p} + r^{2N_p})}{r^2 (R_2^{2N_p} - r^{2N_p})^2}, \quad (35a)$$

or

$$\langle p_M \rangle = \frac{1}{2\pi} \int_0^{2\pi} p_M d\phi = \frac{\mu_0 I^2}{8\pi^2} \times \frac{R_2^{2N_p}}{r^2 (R_2^{2N_p} - r^{2N_p})}. \quad (35b)$$

Peak-to-valley modulation amplitude of magnetic pressure is

$$\delta p_M = p_{M,\max} - p_{M,\min} = \frac{\mu_0 I^2}{8\pi^2} \times \frac{4R_2^{3N_p} r^{N_p-2}}{(R_2^{2N_p} - r^{2N_p})^2}. \quad (36)$$

The relative peak-to-valley amplitude of pressure modulation at the pinch surface due to a finite number of return current posts can thus be estimated either as

$$\frac{\delta p_M}{\bar{p}_M} = 4 \frac{(r/R_2)^{N_p}}{1 + (r/R_2)^{2N_p}} \quad (37a)$$

or as

$$\frac{\delta p_M}{\langle p_M \rangle} = 4 \frac{(r/R_2)^{N_p}}{1 - (r/R_2)^{2N_p}}. \quad (37b)$$

For most typical conditions of practical interest, the denominator in both cases only introduces a small correction:  $(r/R_2)^{2N_p} \ll 1$ . Therefore we can use the simple estimate

$$\frac{\delta p_M}{p_M} = 4 \left( \frac{r}{R_2} \right)^{N_p} \quad (38)$$



in all cases. In particular, substituting into (38)  $r = R_2 - \Delta r_p = R_2(1 - 2\pi/N_p)$ , and taking into account that  $\lim_{N \rightarrow \infty} (1 - x/N)^N = \exp(-x)$ , we confirm the above statement that the peak-to-valley variation of the driving magnetic field is less than  $4\exp(-2\pi) \cong 0.7\% \ll 1$ , or negligible at a distance from the return current posts equal to the inter-post gap  $\Delta r_p$ .

For a finite length of the return current posts, we can test the accuracy of the above approximate expressions by calculating the magnetic field produced by the set of  $N_p$  vertical posts in exactly the same way as in Section 3 for the anode/cathode spokes (here again, the posts are considered to be thin linear conductors). The result for the conditions of Figure 2 is:

$$B_\theta \equiv \tilde{B}_\theta(r, \phi, z; r' = R_2, 0 < z' < h, N_p) \\ = -\frac{\mu_0 I}{4\pi N_p} \sum_{j=0}^{N_p-1} \frac{r - R_2 \cos(\theta_j - \phi)}{r^2 + R_2^2 - 2rR_2 \cos(\theta_j - \phi)} \times [Q_j(r, \phi, z, R_2) + Q_j(r, \phi, h - z, R_2)], \quad (39)$$

$$B_r \equiv \tilde{B}_r(r, \phi, z; r' = R_2, 0 < z' < h, N_p) \\ = -\frac{\mu_0 I R_2}{4\pi N_p} \sum_{j=0}^{N_p-1} \frac{\sin(\theta_j - \phi)}{r^2 + R_2^2 - 2rR_2 \cos(\theta_j - \phi)} \times [Q_j(r, \phi, z, R_2) + Q_j(r, \phi, h - z, R_2)], \quad (40)$$

$$B_z = 0, \quad (41)$$

where

$$Q_j(r, \phi, z, R_2) = \frac{z}{[r^2 + R_2^2 - 2rR_2 \cos(\theta_j - \phi) + z^2]^{1/2}}. \quad (42)$$

Here, we assume that each of the  $N_p$  finite-length posts carries the same fraction of the return current,  $-I/N_p$ .

Replacing the cylindrical segment of the outer feed with the return current structure consisting of  $N_p$  finite-length posts, we find the exact expression for the magnetic field inside the cage:

$$B_\theta(r, \phi, z) = \frac{\mu_0 I}{2\pi r} + \tilde{B}_\theta(r, \phi, z; r' = R_2, 0 < z' < h, N_p) + B(r, z; r' = R_2, 0 < z' < h), \quad (43)$$

$$B_r(r, \phi, z) \equiv \tilde{B}_r(r, \phi, z; r' = R_2, 0 < z' < h, N_p), \quad (44)$$

where  $\tilde{B}_\theta(r, \phi, z; r' = R_2, 0 < z' < h, N_p)$ ,  $\tilde{B}_r(r, \phi, z; r' = R_2, 0 < z' < h, N_p)$  and  $B(r, z; r' = R_2, 0 < z' < h)$  are given by Eqs. (39), (40), and (16), respectively.

Figure 14 presents the profiles of magnetic field vs. azimuthal angle  $\phi$  for a fixed radius  $r = 6.6$  cm,  $h = 4$  cm and  $N_p = 12$  return current posts located at  $R_2 = 7.7$  cm, as appropriate for the 12-cm AASC nozzle on DQ. The approximate expressions for the components of magnetic field independent of  $z$  are given by Eqs. (31), (32). We see that these represent a very good approximation for the magnetic field near the mid-section of the pinch ( $z = 2$  cm). At locations closer to the cathode or anode, a greater fraction of the azimuthal magnetic field is produced by the horizontal current in the cathode/anode, hence the angular modulation of the azimuthal magnetic field and the radial magnetic field are less than predicted by Eqs. (31), (32). Still, the latter are shown to be accurate estimates of the non-uniformity of magnetic field due a finite number of return current posts. Therefore, Eq. (38) is a reliable estimate of the non-uniformity of the driving magnetic field from above.

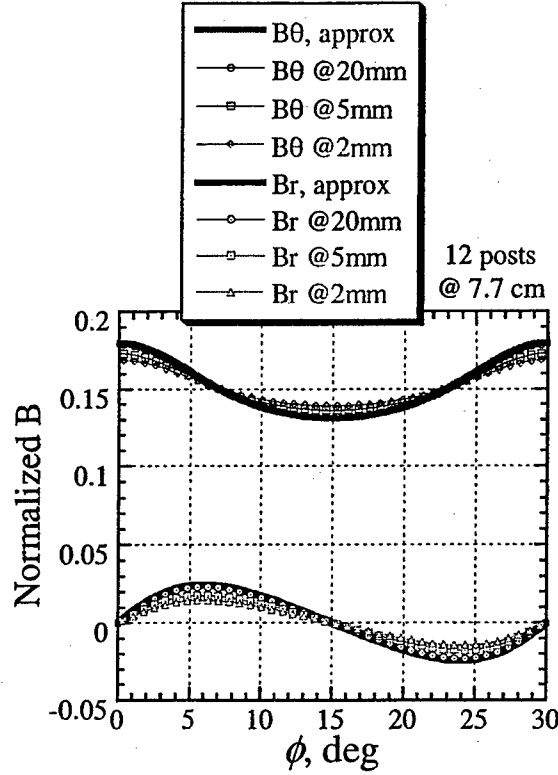


**Figure 14.** Magnetic field profiles at  $r = 6.6$  cm for  $N_p = 12$  return current posts located at  $R_2 = 7.7$  cm and varied distance from the cathode plane. Thick red and blue curves show approximate results given by Eqs. (31), (32), respectively.

##### 5. Azimuthal non-uniformity estimated for 12-cm diameter nozzles on DQ

Assuming for the TPSD nozzle used in recent experiments  $r = 7.3$  cm,  $R_2 = 9$  cm (Figure 15), we estimate the initial peak-to-valley non-uniformity of magnetic pressure at the pinch surface from (38) as 32% for  $N_p = 12$  return current posts and 2.6% for  $N_p = 24$ . The estimates (37a), (37b) for these cases would vary from 32.4% to 32.6% and from 2.6301% to 2.6303%, respectively, thus confirming the accuracy of the simple estimate (38). For the AASC nozzle in the same experimental campaign, we take  $r = 6.6$  cm,  $R_2 = 7.7$  cm, and find the amplitude of the initial non-uniformity: 63% for  $N_p = 12$  return current posts and 10% for  $N_p = 24$ .

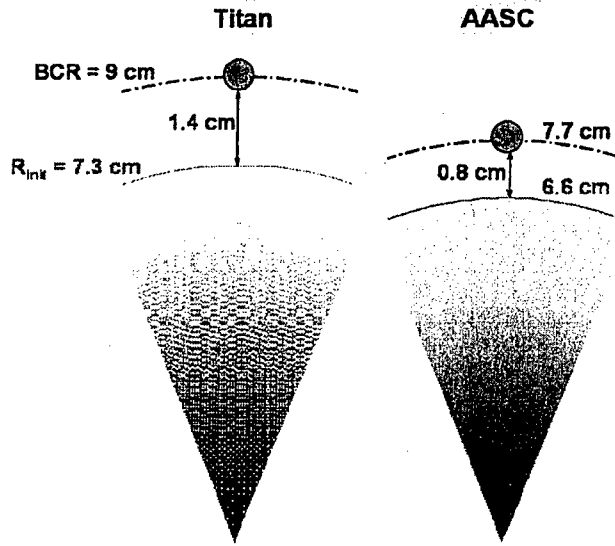


**Figure 15.** Geometry of the pinch – return current posts for 12-cm TPSD and AASC nozzles on DQ.

Let us suppose that the PRS irradiates a test object through the gap between the return current posts. Then, in order to deliver more of the radiation produced by the PRS to the test object, it is preferable to have a larger opening between the return current posts, which means that their number should be smaller. For the given transverse dimension  $\sqrt{S}$  of the test object (where  $S$  is its surface area), the minimum stand-off distance  $R_{\min}$  between the on-axis PRS and the test object is largely determined by the solid angle characteristic of the opening between the posts. A simple estimate is

$$R_{\min} = \frac{\sqrt{S}}{2 \tan(\pi / N_p)} \cong \frac{N_p \sqrt{S}}{2\pi}, \quad (45)$$

since  $N_p \gg 1$ . Then the peak x-ray fluence at the surface of the test object is estimated as

$$F_{\max} = \frac{\eta Y}{4\pi R_{\min}^2} \cong \frac{\pi \eta Y}{N_p^2 S}, \quad (46)$$

where  $Y$  is the x-ray yield in the desired spectral range,  $\eta < 1$  is the filter transmission of the debris mitigation system. For  $Y = 60$  kJ,  $S = 1000$  cm<sup>2</sup>,  $\eta = 70\%$ ,  $N_b = 12$ , we find that  $F_{\max} = 0.22$  cal/cm<sup>2</sup> at a distance of  $R_{\min} = 60$  cm. According to (46), increasing the number of return current posts from 12 to 24 would decrease  $F_{\max}$  by a factor of 4, to 0.05 cal/cm<sup>2</sup>. This estimate demonstrates that the price for improving azimuthal uniformity of the driving magnetic pressure by increasing the number  $N_b$  of return current posts is very steep [6]. If the azimuthal non-uniformity needs to be decreased, we should try the alternative way of moving the return current posts farther from the axis. But, this would improve the uniformity at the expense of increasing the inductance of the load.

Equation (38) allows us to evaluate the trade-off between load inductance and the opening between the return current posts. Suppose we decrease their number from  $N_p = N_1$  to  $N_p = N_2$ , and at the same time move them farther from the axis, from  $r = R_2$  to  $r = R'_2$ , so that the non-uniformity estimated from (38) does not change. Therefore,

$$\left(\frac{R_2}{r}\right)^{N_1} = \left(\frac{R'_2}{r}\right)^{N_2}, \quad (47)$$

where  $r$  is the outer radius of the gas puff load. The inductance of the load is thereby increased from  $L_1 = (\mu_0 h / 2\pi) \ln(R_2 / r)$  to  $L_2 = (\mu_0 h / 2\pi) \ln(R'_2 / r)$ . Using (47), we find that

$$\frac{L_2}{L_1} = \frac{N_1}{N_2}. \quad (48)$$

In other words, by decreasing the number of return current posts while keeping the non-uniformity of the driving magnetic field constant, we gain in the viewing factor (the solid

angle characteristic of the opening between the posts) as much as we lose in the initial load inductance. Whether or not this loss translates into a commensurate decrease in the radiation yield depends on the stiffness of the current driver.

For example, consider the azimuthal non-uniformity characteristic of the AASC 12-cm nozzle shots on DQ with  $N_p = 12$  return current posts. Increasing the number of posts to  $N_p = 24$  would reduce the non-uniformity to 10% at the expense of decreasing the fluence by a factor of 4. Alternatively, the same 10% level of non-uniformity can be achieved by moving these 12 return current posts to  $R_2 = 9$  cm – same location as in the shots with the TPSD nozzle, but doubling the initial inductance of the load, 1.2 nH.

To decrease the initial non-uniformity even further, to the same level <3% as in Shots DQ 548, 549 with the TPSD nozzle and  $N_p = 24$  return current posts, while keeping  $r = 6.6$  cm,  $R_2 = 7.7$  cm and all the other parameters the same as in Shots DQ 546, 547, one should increase the number of return current posts to  $N_p = 24 \times \ln(9/7.3)/\ln(7.7/6.6) \cong 32$ , that is, by a factor of 8/3. This would result in a ~7-fold decrease of the fluence at the test object. Alternatively, one can achieve the same uniformity by moving the  $N_p = 12$  return current posts farther out to  $R_2 = 10$  cm. As explained above, this would increase the initial inductance of the load by the same factor of 8/3, from 1.2 nH to 3.2 nH. For Decade Quad, an increase in inductance of this magnitude seems to be a much lower price to be paid for ensuring azimuthal uniformity of the driving magnetic field.

6. Axial magnetic field  $B_z$  produced by a twisted anode/cathode structure and return current cage

It is well known that an axial magnetic field  $B_z$  can effectively stabilize implosion of an annular gas-puff shell against the Rayleigh-Taylor (RT) instability [7]. To mitigate the RT instability,  $B_z$  should be sufficiently strong, which translates into the condition [8]

$$B_{z0} > 10 \frac{I_{\max}(\text{MA})}{R_0(\text{cm})} \text{ kG.} \quad (49)$$

As demonstrated in numerous experiments, the price paid for the stabilization of annular shells with high  $B_z$  field satisfying (49) is pretty steep: a large part of the energy of implosion is spent on compression of the axial magnetic field, the thermal energy coupled to the stagnated plasma column is less, and the radiative yields decrease.

A double-shell configuration helps stabilize the implosion with a smaller initial magnetic field than given by (1). Stabilization in this case may be due to formation of a “magnetic interlayer” between the two shells, see [9]. Recent DTRA sponsored experiments [10] have demonstrated that the stabilization criterion (49) for the shell-on-fill structured load could be relaxed to

$$B_{z0} > 5 \frac{I_{\max}(\text{MA})}{R_0(\text{cm})} \text{ kG,} \quad (50)$$

which implies four times less energy spent on compressing  $B_z$ . Increase in K-shell radiation yield and power due to stabilization was reported in [10] for neon.

In most experiments [7, 9, 10] the initial axial magnetic field was generated by adding a specially designed Helmholtz coil to the load unit. In some early experiments at Maxwell Laboratories, and later at HCEI [11], a twisted or helical return current cage was

used to add some  $B_z$  field produced directly by the load current. In the experiment [11], a full stabilization of krypton single-shell and argon shell-on-fill implosions was achieved when the external axial magnetic field produced by Helmholtz coils was supplemented by the  $B_z$  field from the helical return current structure.

Here we would like to attract attention to another opportunity for generating axial magnetic field that was suggested recently by L. I. Rudakov. Instead of (or in addition to) twisting the return current cage, we can twist a part of the anode/cathode structure, creating an effective azimuthal current that produces the  $B_z$  field. Since the radial current in the anode and cathode flows in the opposite directions, the twisting should be made in opposite directions, too, as shown in Figure 16. Recall that, in order to be consistent with Figures 1 and 2, we have labeled the top and bottom electrodes "anode" and "cathode" respectively, although the current between these electrodes is supposed to flow in positive  $z$  direction, in agreement with (1), thus reversing their roles. Assuming that the "cathode" current flows radially inward, we see that its twisting in the positive (counter-clockwise) direction produces a loop of azimuthal current in the negative (clockwise) direction, which contributes to a negative  $B_z$  field above the cathode. Conversely, the anode current flows radially outward, and its counter-twisting in the negative direction produces a loop of azimuthal current in the same negative direction, which adds to a negative  $B_z$  field below the anode.

The wires between  $r = R_1$  and  $r = R_2$  can be twisted by any angle  $\psi$  in the range  $-\psi_{\max} < \psi < \psi_{\max}$ , where the maximum angle

$$\psi_{\max} = \arccos(R_1 / R_2) \quad (51)$$



corresponds to the twisted spokes tangent to the smaller ring  $r = R_1$ . Figure 16 is plotted for  $R_1 / R_2 = 3/4$ ,  $\psi = \pm\psi_{\max} = \pm 41.4^\circ$ , where the upper and lower signs correspond to the cathode and anode, respectively.

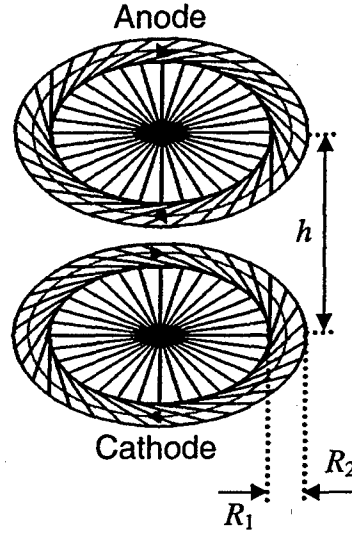


Figure 16. Schematic of a twisted anode/cathode wire structure equivalent to a Helmholtz coil. Red lines show the direction of azimuthal current loops.

Calculation of the magnetic field produced by a twisted part of a single  $N_s$ -spoke grid yields:

$$B_\theta \equiv \tilde{B}_\theta(r, \phi, z; R_1 < r' < R_2, z' = z_1, N_s, \psi) \\ = \frac{\mu_0 I (z - z_1)}{4\pi N_s (R_1^2 + R_2^2 - 2R_1 R_2 \cos \psi)^{3/2}} \sum_{j=0}^{N_s-1} [R_2 \cos(\theta_j + \psi - \phi) - R_1 \cos(\theta_j - \phi)] \times S_j \quad (52)$$

$$B_r \equiv \tilde{B}_r(r, \phi, z; R_1 < r' < R_2, z' = z_1, N_s, \psi) \\ = \frac{\mu_0 I (z - z_1)}{4\pi N_s (R_1^2 + R_2^2 - 2R_1 R_2 \cos \psi)^{3/2}} \sum_{j=0}^{N_s-1} [-R_2 \sin(\theta_j + \psi - \phi) + R_1 \sin(\theta_j - \phi)] \times S_j \quad (53)$$

$$B_z \equiv \tilde{B}_z(r, \phi, z; R_1 < r' < R_2, z' = z_1, N_s, \psi) \\ = \frac{\mu_0 I}{4\pi N_s (R_1^2 + R_2^2 - 2R_1 R_2 \cos \psi)^{3/2}} \sum_{j=0}^{N_s-1} [r R_2 \sin(\theta_j + \psi - \phi) - r R_1 \sin(\theta_j - \phi) - R_1 R_2 \sin \psi] \times S_j, \quad (54)$$

where

$$\begin{aligned}
S_j(r, \phi, z, R_1, R_2, \psi) &= \frac{1}{v^2} \left[ \frac{\zeta + 1}{\sqrt{v^2 + (\zeta + 1)^2}} - \frac{\zeta}{\sqrt{v^2 + \zeta^2}} \right], \\
\zeta &= \frac{-rR_2 \cos(\theta_j + \psi - \phi) + rR_1 \cos(\theta_j - \phi) + R_1 R_2 \cos \psi - R_1^2}{R_1^2 + R_2^2 - 2R_1 R_2 \cos \psi}, \\
v^2 &= \frac{r^2 + R_1^2 - 2rR_1 \cos(\theta_j - \phi) + (z - z_1)^2}{R_1^2 + R_2^2 - 2R_1 R_2 \cos \psi} - \zeta^2.
\end{aligned} \tag{55}$$

For zero twisting angle  $\psi = 0$ , Eqs. (52)-(54) are reduced to Eqs. (23)-(25), respectively, valid for radial spokes, as they should.

Therefore the axial magnetic field produced by the two twisted sets of spokes shown in Figure 16 is given by

$$B_z \equiv \tilde{B}_z(r, \phi, z; R_1 < r' < R_2, z' = 0, N_s, \psi) - \tilde{B}_z(r, \phi, z; R_1 < r' < R_2, z' = h, N_s, -\psi), \tag{56}$$

and similar expressions are valid for both other components of the magnetic field.

Obviously, there must be an optimal ratio  $R_1 / R_2$  that maximizes the axial magnetic field produced by the twisted structure of Figure 16: in the limit  $R_1 / R_2 \rightarrow 1$  the length of the twisted spokes tends to zero, whereas in the opposite limit  $R_1 / R_2 \rightarrow 0$  the twisted spokes become radial.

In Figure 17, the normalized values of  $B_z$  (normalization is almost the same as above, with respect to the factor  $-\mu_0 I / 2\pi$ , so that the values of  $B_z$  shown in the figure are positive) are plotted vs.  $R_1$  for a double set of 32 twisted wires as shown in Figure 16 (only the contribution to  $B_z$  from the twisted parts of the wires is plotted here), fixed value of  $R_2 = 7$  cm and  $h = 4$ . The axial field is slightly greater at  $r = 0$ , as it should be, and in each case peaks at some optimum ratio  $R_1 / R_2$ .

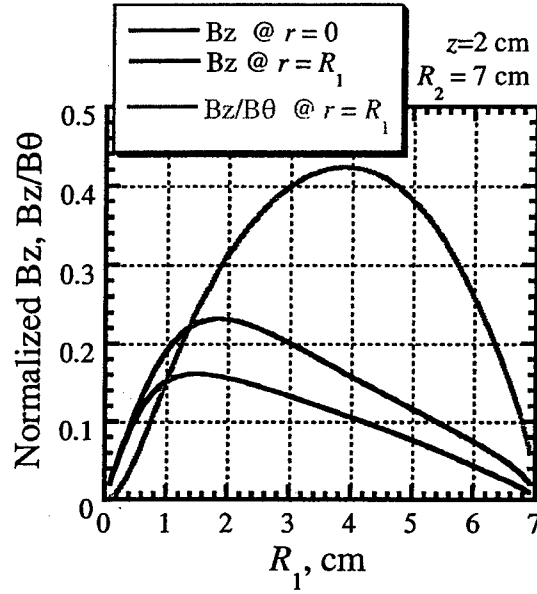


Figure 17.  $B_z$  at  $r=0$  and  $r=R_1$  and the ratio of  $B_z(r=R_1)/B_\theta(r=R_1)$ , where  $B_\theta$  is given by (1), for  $N_s = 32$ ,  $h = 4$  cm,  $R_2 = 7$  cm.

In a real configuration of Figure 1b with twisted anode and cathode structure, the axial magnetic field on axis will not be the same as shown in Figure 17, because the azimuthal current loops will cause an azimuthal diamagnetic current to flow on the surface of the pinch column, thus effectively screening the inner region of the pinch from penetration of  $B_z$ . Moreover, we do not need  $B_z$  to be substantial where the radiating plasma is compressed, and might want to enhance the effect of excluding the axial field from the stagnation area by replacing the central parts of the cathode and anode structures in Figure 16 by conducting rings, as in [11]. However, the main contribution to the axial field outside the pinch with the anode/cathode structure of Figure 16 is correctly estimated by (56) since the contribution of the azimuthal diamagnetic current in the pinch column outside of this column is small. We see that for the smaller radius of the twisted

ring  $R_1$  no less than 6/7 of the outer radius  $R_2$ , the axial magnetic field near the surface of the pinch is about 25% of the driving magnetic field:

$$B_z \sim 50 \frac{I(\text{MA})}{R_p(\text{cm})} \text{ kG.} \quad (57)$$

This estimate shows the  $B_z$  field produced by the anode/cathode structure of Figure 16 to be sufficient for stabilization with a large margin. Indeed, consider the stabilization of DQ implosions according to (50): for  $I_{\max} = 6$  MA and initial outer radius  $R_0 = 6$  cm, we need the initial axial field  $B_{z0} = 5$  kG for stabilization. According to (57), the axial magnetic field of this magnitude is produced by the twisted anode-cathode structure when the pinch current reaches 0.6 MA, that is, pretty early in the implosion, before most of the plasma starts moving. The later increase of  $B_z$  with increased current would contribute to magnetic shear near the accelerated plasma surface, which is precisely what is needed to mitigate the RT instability [8].

Figure 18 presents the axial profiles of the magnetic field for a configuration of Figure 2, with anode and cathode grids structured as in Figure 16. We see that near the mid-section of the pinch the axial magnetic field is about 25% of the driving magnetic field, in agreement with Eq. (57). Azimuthal modulation of all the components of the magnetic field is seen to be weak everywhere except the vicinity of the anode and the cathode grids, as it should be. The azimuthal magnetic field, which constitutes the main contribution to the driving field near the mid-section, is very uniform and close to (1) along the pinch length. The total driving field, however, is noticeably larger near the anode and cathode due to axial and radial components of magnetic field. This might give rise to an unusual kind of zippering, with top and bottom of the pinch imploding before

the mid-section. However, this effect may turn out to be beneficial: the higher axial magnetic field frozen into the plasma near the anode and cathode might stop its implosion earlier, thus helping concentrate most of the energy coupled to the plasma near the mid-section.

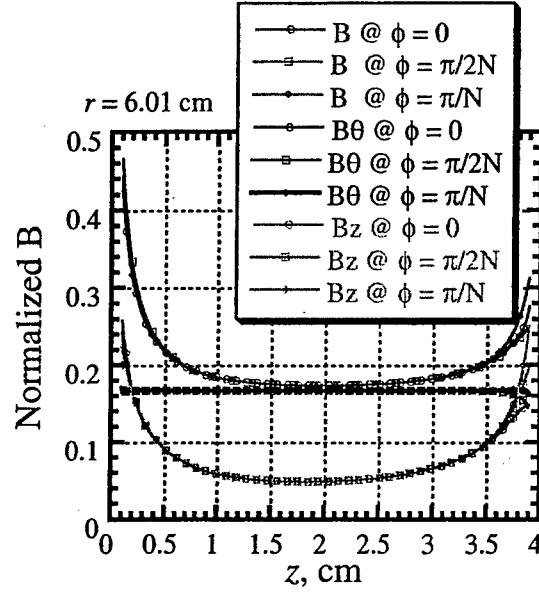


**Figure 18.** The axial profiles of the absolute value of magnetic field  $B$ , its azimuthal  $B_\theta$  and axial  $B_z$  components at  $r = 6.01$  cm for three angular positions:  $\phi = 0, \pi/2N_s$ , and  $\pi/N_s$ . Number of spokes is  $N_s = 32$  in both anode and cathode grids. The twisted part of the cathode extends from  $R_p = 6$  cm to the inner feed,  $R_1 = 7$  cm, and the twisting angle is  $\psi_{\max} = 31^\circ$ . The counter-twisted part of the anode extends from  $R_p = 6$  cm to the outer feed/return current posts,  $R_2 = 8$  cm, and the twisting angle is the same,  $\psi = -31^\circ$ .

For completeness, we present here the formulas describing the magnetic field produced by a twisted set of return current posts. The twisting angle  $\psi$  is defined as the azimuthal angle between the angular positions of the ends of the posts at the cathode,  $\theta$ , and the anode,  $\theta + \psi$ . The return current posts are inclined at the angle

$$\chi = \arctan \left[ \frac{2R}{h} \sin \left( \frac{\psi}{2} \right) \right] \quad (58)$$

with respect to the vertical pinch axis. A simple calculation yields the magnetic field produced by the twisted set of return current posts:

$$B_\theta \equiv \tilde{B}_\theta(r, \phi, z; r' = R, 0 < z' < h, N_p, \psi) \\ = \frac{\mu_0 I}{4\pi N_p [4R^2 \sin^2(\psi/2) + h^2]^{3/2}} \sum_{j=0}^{N_p-1} \{ -hr - R[(z-h)\cos(\theta_j - \phi) - z\cos(\theta_j + \psi - \phi)] \} \times T_j \quad (59)$$

$$B_r \equiv \tilde{B}_r(r, \phi, z; r' = R, 0 < z' < h, N_p, \psi) \\ = \frac{\mu_0 IR}{4\pi N_p [4R^2 \sin^2(\psi/2) + h^2]^{3/2}} \sum_{j=0}^{N_p-1} \{ (z-h)\sin(\theta_j - \phi) - z\sin(\theta_j + \psi - \phi) \} \times T_j \quad (60)$$

$$B_z \equiv \tilde{B}_z(r, \phi, z; r' = R, 0 < z' < h, N_p, \psi) \\ = -\frac{\mu_0 IR}{4\pi N_p [4R^2 \sin^2(\psi/2) + h^2]^{3/2}} \sum_{j=0}^{N_p-1} \{ R\sin\psi + r[\sin(\theta_j - \phi) - \sin(\theta_j + \psi - \phi)] \} \times T_j \quad (61)$$

where

$$T_j(r, \phi, z, R, \psi) = \frac{1}{v^2} \left[ \frac{\zeta + 1}{\sqrt{v^2 + (\zeta + 1)^2}} - \frac{\zeta}{\sqrt{v^2 + \zeta^2}} \right], \\ \zeta = \frac{-rR\cos(\theta_j + \psi - \phi) + rR\cos(\theta_j - \phi) - hz - 2R^2 \sin^2(\psi/2)}{4R^2 \sin^2(\psi/2) + h^2}, \\ v^2 = \frac{r^2 + R^2 - 2rR\cos(\theta_j - \phi) + z^2}{4R^2 \sin^2(\psi/2) + h^2} - \zeta^2. \quad (62)$$

For zero twisting angle  $\psi = 0$ , Eqs. (59)-(61) are reduced to Eqs. (39)-(41), respectively, valid for vertical return current posts, as they should.

Twisting the return current posts is no less efficient in generating a  $B_z$  field than twisting of the anode/cathode rings, see below. However, in view of the discussion of Section 5, we note that twisting brings the posts closer to each other, approximately by a factor of  $\cos\chi$ , where  $\chi$  is the angle between the posts and the vertical axis given by (58). The corresponding loss of fluence  $F$  at the test object, according to (45), (46), is

given by a factor of  $\cos^2 \chi$ . Figure 19 shows this fluence factor and the angle  $\chi$  vs. the ratio of the  $B_z$  field to the driving field at the pinch surface  $r = 6$  cm, for 12 return current posts located at  $R_2 = 8$  cm and the pinch height  $h = 4$  cm. We see that the same 25% ratio of the axial field to the driving azimuthal field as above (cf. Figures 17, 18) is achieved for  $\chi = 40^\circ$  (which corresponds to the twisting angle  $\psi = 24^\circ$ ) and at the expense of a ~40% loss of the fluence at the test object. This is a disadvantage of twisting the return current cage.

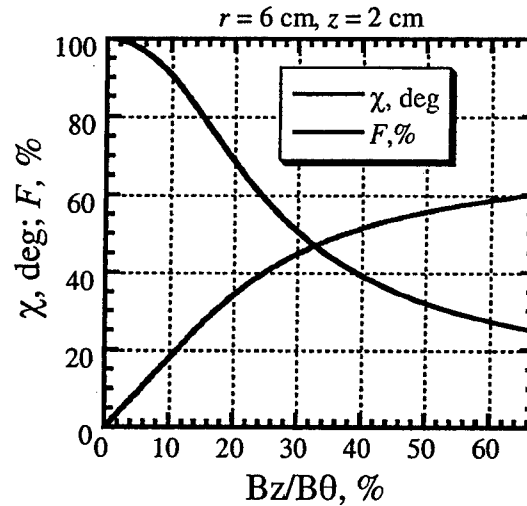


**Figure 19.** The angle  $\chi$  between the twisted return current posts and the pinch axis, and the fluence at the surface of a test object of the given size normalized with respect to the fluence at  $\chi = 0^\circ$  vs. the ratio of the axial magnetic field at  $r = 6$  cm,  $z = 2$  cm to the driving magnetic field (1). The twisting angle  $\psi$  is varied between 0 and  $51^\circ$ , which corresponds to variation of  $\chi$  between 0 and  $60^\circ$ .

### 7. Solenoid wire implosion?

Here we discuss the problem of making an annular plasma shell load from a wire array. It is not certain that 2D implosion of an annular load will work better (e. g., generate a higher x-ray power) than a wire array, with its inherent variety of 3D phenomena. Nevertheless, it will certainly not hurt to try.

There is a little known theoretical recipe of producing an annular shell of a single wire (or plasma filament) [12]. Put the wire into a cylindrical return current can and impose an axial magnetic field. Due to the kink instability of a straight current in a  $B_z$  field, the wire will first form a helix, then a helical ribbon, and then evolve into the equilibrium shape, a thin-walled cylindrical shell, whose inner magnetic field  $B_z$  provides a pressure equilibrium with the outer magnetic field, which is a combination of the external  $B_z$  field and the azimuthal  $B_\theta$  field generated by the current in the wire. This sounds nice (see the reference [12]), but the question is, could it actually be done?

Geometry of magnetic field of a wire array with wires parallel to the axis is such that the azimuthal magnetic field pushes the current-carrying wires to the axis. Before they start moving, the precursor plasma evaporated from the wires flows in this direction. On the other hand, the magnetic field produced inside a cylindrical load in the form of a multi-turn solenoid acts differently: it would push the solenoid walls outside, increasing its radius (and if there is any precursor plasma, it would be pushed outside). One can expect that there is a middle ground: for some shape of a helical wire load, the magnetic field at the wires would be force-free, that is, the Ampère force would not be pushing the wire(s) neither inside nor outside. Consequently, the preferential flow direction for the precursor plasma would be in the axial direction. If the load is a multi-wire solenoid, it implies that the precursor plasma would tend to fill the gaps between the wires, the load thus evolving to the annular shell structure. This is very much like the process described by Kadomtsev [12]: from a current filament to a helical ribbon, and then to a thin-walled cylindrical shell. The helical shape sought for is something intermediate between a conventional wire array (pitch angle  $\chi = 0^\circ$ ) and a multi-turn solenoid (pitch angle



$\chi \cong 90^\circ$ ). A natural first guess for the pitch angle of a force-free solenoid is something in the middle between these two extremes (Figure 20)

$$\chi = 45^\circ. \quad (63)$$

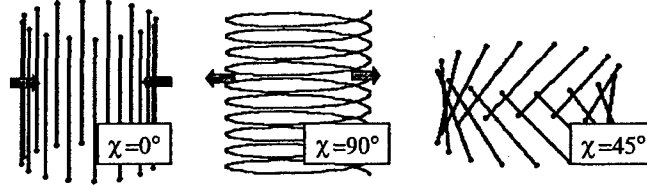


**Figure 20.** Wire array ( $\chi = 0^\circ$ ), multi-turn solenoid ( $\chi \cong 90^\circ$ ) and a force-free wire array load twisted by the angle  $45^\circ$ .

Surprisingly, (63) provides an almost exact result. Let us calculate the angle  $\alpha$  between the collective magnetic field produced at the middle of wire #1, where  $r = R \cos(\psi/2)$ ,  $\phi = \psi/2$ ,  $z = h/2$ , by all the other wires in the twisted array except wire #1; here,  $R$  is the radius of the wire array,  $\psi$  is the twisting angle defined in the same way as for twisted return current posts. The collective magnetic field is found from our Eqs. (59)-(62), where the summation over  $j$  should now start from  $j = 1$ , and the number of wires  $N_w$  replaces the number of posts  $N_p$ . The calculation is performed for certain values of  $N_w$  and the ratio  $h/R$ . The result, however, turns out to be independent of these values [13]:

$$\alpha = \frac{\pi}{2} - 2\chi, \quad (64)$$

where  $\chi$  is the angle between the wires and the pinch axis, related to the twisting angle  $\psi$  by (58). This formula is obvious when there are only  $N_w = 2$  wires: Then the magnetic field of wire #2 is always perpendicular to its own direction, and (64) follows from

elementary geometry. In particular, the two-wire array is force-free when the opposite wires are perpendicular to each other. We found this to be the case for arbitrary  $N_w$ .

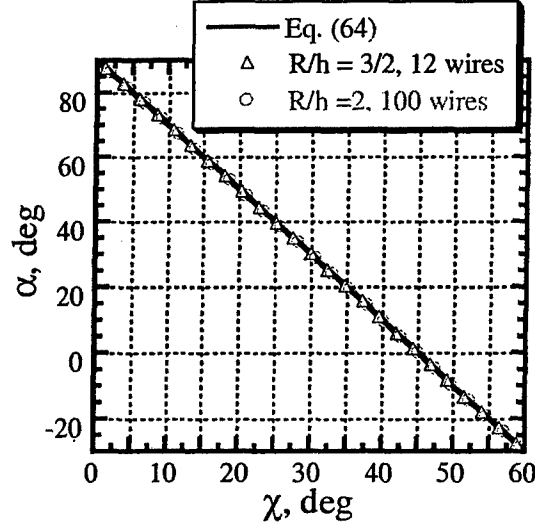


Figure 21. The angle between the collective magnetic field of a twisted wire array and the wire is found to be independent of  $N_w$  and  $h/R$  and expressed by (64).

The force-free field means angle  $\alpha = 0$ , which corresponds to  $\chi = \pi/4 = 45^\circ$ .

The twisting angle  $\psi$  depends on the ratio  $h/R$  and is found from (58), where  $\tan \chi = 1$  is substituted:

$$\psi = 2 \arcsin \frac{h}{2R}. \quad (65)$$

Eq. (65) demonstrates that not every combination of  $h$  and  $R$  is suitable for twisting the array to produce a force-free field: The wire array height should be less than its diameter. For example, typical DQ parameters  $R = 6$  cm,  $h = 4$  cm correspond to a twisting angle of  $39^\circ$ . The experiments on Z are mostly performed with  $R = 2$  cm and  $h$  varied between 1 and 2 cm, which corresponds to variation of the twisting angle between  $29^\circ$  and  $60^\circ$ .

Note that our formulas (63)-(65) only account for the magnetic field produced by current in the wires – this is the reason why they are *almost* exact. To make them exact, we need to account for the contributions from the cathode, anode, return current posts and the coaxial feed to the magnetic field. If neither the cathode/anode nor the return current cage is twisted, then their contribution is mainly to the azimuthal field, and it is not insignificant when  $h/2R < 1$ , cf. Figure 5. Therefore, in order to compensate for the addition to the azimuthal field, the twisted wire array should generate a larger axial magnetic field, which requires twisting by a larger angle than (65). Alternatively, the extra  $B_\theta$  field at the wires could be compensated by a properly adjusted extra  $B_z$  field produced through twisting either the anode/cathode grid or the return current cage. The formulas needed to calculate the twisting angle are found in Sections 2 and 6.

Let us discuss another approach. Instead of using a twisted array formed by straight wires (for which the force-free condition could only be satisfied at the midsection), we can twist the wires into a helical shape and require the collective magnetic field to be force-free at any point of any wire. The simplest load of this sort is a long multi-turn solenoid. The axial magnetic field produced inside the solenoid is expressed as

$$B_z = \mu_0 \frac{N}{h} I, \quad (66)$$

where  $h$ , as above, is the height of the solenoid, and  $N$  is the number of turns. The contribution of this field to the inductance of the solenoid load equals

$$L_z = \mu_0 \pi N^2 \frac{R^2}{h}. \quad (67)$$

If the solenoid is mounted in a cylindrical return current can, then the azimuthal magnetic field outside of it is given by

$$B_\theta = \frac{\mu_0 I}{2\pi R}, \quad (68)$$

and the corresponding contribution to the inductance is

$$L_\theta = \frac{\mu_0 h}{2\pi} \ln \frac{R_b}{R}, \quad (69)$$

where  $R_b$  is the radius of the return current can.

Assuming equilibrium between the magnetic pressure of the axial magnetic field inside the solenoid, which pushes its walls outward, and the azimuthal magnetic field outside the solenoid, which tries to implode it,  $B_z = B_\theta$ , we find from (66), (68):

$$R = R_{eq} = \frac{h}{2\pi N}. \quad (70)$$

Since the pitch angle for a helical wire is expressed by  $\chi = \arctan(h/2\pi RN)$ , (70) leads to (63). The same result would be found from the requirement that  $\partial L/\partial R = 0$ , where  $L$  is the total inductance:

$$L = L_\theta + L_z = \mu_0 \left( \pi R^2 \frac{N^2}{h} + \frac{h}{2\pi} \ln \frac{R_b}{R} \right). \quad (71)$$

We see that the inductance  $L$  as a function of  $R$  has a minimum at  $R = R_{eq}$ .

Physically, it means that the equilibrium in question is unstable (a stable equilibrium requires a maximum of inductance). This is not surprising, given that the pressure of the axial field (66) is independent of  $R$ , whereas the pressure of the azimuthal field (68) is a decreasing function of  $R$ . In other words, if we allow the solenoid to expand radially beyond the equilibrium radius (70), it will keep exploding under the pressure of the axial

field, exhibiting a solenoid-like behavior. If it we allow it to contract, then it will keep imploding like a conventional wire array.

For a short coil with a small number of turns, the expression (67) requires a correction that takes account of the effects of the ends. This correction is given by the so-called Nagaoka's formula [14]. We will use Lundin's approximation to this formula [15], which for  $R < h/2$  reads:

$$L_z = \mu_0 \pi N^2 \frac{R^2}{h} \times K\left(\frac{R}{h}\right), \quad (72)$$

where the correction factor is given by

$$K(z) = \frac{1 + k_1 z^2 + k_2 z^4}{1 + k_3 z^2} - \frac{8}{3\pi} z, \quad (72)$$

$$k_1 = 1.535604, \quad k_2 = 0.273728, \quad k_3 = 1.035808.$$

Substituting (72) instead of (67) into (71) and minimizing this expression with respect to  $R$ , we obtain the equilibrium condition to determine  $z = R/h$  for a given  $N$ :

$$N^2 z \frac{d}{dz} [z^2 K(z)] = \frac{1}{2\pi^2}. \quad (74)$$

For  $N = 1, 2$  and  $3$ , solving (74) numerically, we obtain the values of  $z = z_{eq} = 0.1774, 0.08387$ , and  $0.05492$ . The simple approximation (70) for the same values of  $N$  gives  $z = z_{eq} = 0.1592, 0.07958$ , and  $0.05305$ , respectively. The corrected values of the pitch angle  $\chi$  are  $41.9^\circ, 43.5^\circ$ , and  $44.0^\circ$ , respectively, very close to (63) even for  $N = 1$ .

Although (70) is not a good approximation for a single wire (it lacks the contribution to the self-inductance proportional to  $\ln R_w$ , where  $R_w$  is the radius of the wire), the estimate is still reasonable.

To facilitate the formation of the annular shell, it would be natural to make a solenoid of more than one wire, so that the neighboring wires are closer to each other. This does not change the above formulas because each of the  $N_w$  identical wires carries  $1/N_w$  fraction of the total current, and the contribution to inductance is the same as above, each with the weight  $1/N_w$ . Moreover, these formulas are more reliable in this case, as the relative contribution of the terms describing the discrete wires vs. a cylindrical shell/solenoid decreases with increased number of the wires as  $(1/N_w)\ln(R_w/N_w)$ .

For example, consider a 2-cm high single-turn ( $N = 1$ ) solenoid of 8 wires. Its equilibrium diameter is  $20 \text{ mm} \times 0.1774 \times 2 \cong 7 \text{ mm}$ , and the gap between the neighboring wires is  $h/N_w = 1.86 \text{ mm}$ . For a 2-turn solenoid, the equilibrium diameter is 3.3 mm, and the inter-wire gap 0.9 mm.

## 8. Conclusions

We have estimated the non-uniformity of the driving magnetic field due to the parts of the current-carrying structure that violate azimuthal symmetry – the radial anode and cathode spokes and the vertical return current posts. We have demonstrated that the non-uniformity is substantial where the distance from the anode, cathode, or return current cage is much less than the gap between the two neighboring elements of these structures. This conclusion appears to be quite general, and is independent of the cylindrical nature of the coaxial feed shown in Figures 1-2 – all the present results are valid for an arbitrary azimuthally-symmetric feed, including the more realistic conical shape. While not directly applicable to the case of a rectangular or hexagonal

anode/cathode mesh, our results nevertheless indicate that the non-uniformity of magnetic field produced by such a grid would not extend farther from its plane than half of the grid cell.

Applying these estimates for conditions of recent experiments on DQ with 12-cm diameter argon gas-puff nozzles, we have shown that the initial azimuthal non-uniformity of the driving magnetic field is substantial for shots using TPSD and AASC nozzles and 12 return current posts. The price for improving the uniformity through increasing the number of return current posts at the same distance from the axis is a substantial decrease of x-ray fluence at the surface of a test object irradiated through a gap between the posts. A better way of improving the uniformity is moving the return current posts farther from the axis, the penalty for this being an increase in initial load inductance by  $\sim 2$  nH.

We have demonstrated that twisting of the anode/cathode wire grids can produce an axial magnetic field that is sufficiently high to stabilize the gas-puff implosion. It is certainly easier than introducing a Helmholtz coil into the load unit. The advantage of twisting the anode/cathode grids, rather than the current return cage, is that in the latter case we have to decrease the opening between the posts, and hence, the fluence at the surface of our test object. We have also described the force-free configuration of a twisted wire array load, which can help control the precursor plasma flow to the axis at the early stages of wire array implosions.

#### Acknowledgements

The authors are grateful to J. Davis, J. W. Thornhill, R. Commisso, R. Davis and I. Vitkovitsky for stimulating discussions. This work was performed for the U. S. Defense Threat Reduction Agency under MIPR 04-2222M.

## References

1. T. W. L. Sanford, R. C. Mock, T. J. Nash, K. G. Whitney, P. E. Pulsifer, J. P. Apruzese, D. Mosher, D. L. Peterson, M. G. Haines, Phys. Plasmas **6**, 1270 (1999).
2. D. Mosher, "Plasma radiation source implosion limits due to azimuthal asymmetries," in Proceedings of the 10<sup>th</sup> International Conference on High Power Particle Beams 20-24 June 1994, San Diego, CA, p. 159. Copies may be ordered from NTIS, Springfield, VA 22161 [National Technical Information Service Document No. PB95-144317].
3. *Handbook of Mathematical Functions with Formulas, Graphs, and Mathematical Tables*, edited by M. Abramowitz and I. A. Stegun (National Institute of Standards and Technology, 1972), Chapter 17 "Elliptic Integrals".
4. E. M. Waisman, J. Appl. Phys. **50**, 23 (1979).
5. A. L. Velikovich, I. V. Sokolov and A. A. Esaulov, Phys. Plasmas **9**, 1366 (2002).
6. M. Krishnan, private communication.
7. R. B. Baksht, A. L. Velikovich, B. A. Kablambaev, M. A. Liberman, A. V. Luchinskii, and N. A. Ratakhin, Sov. Phys. Tech. Phys. **32**, 145 (1987); F. S. Felber, F. J. Wessel, N. C. Wild, H. U. Rahman, A. Fisher, C. M. Fowler, M. A. Liberman, and A. L. Velikovich, J. Appl. Phys. **64**, 3831 (1988); F. S. Felber, M. M. Malley, F. J. Wessel, M. K. Matzen, M. A. Palmer, R. B. Spielman, M. A. Liberman, and A. L. Velikovich, Phys. Fluids **31**, 2053 (1988); L. I. Rudakov, in *Dense Z-Pinches*, 2<sup>nd</sup> International Conference on Dense Z-Pinches, Laguna Beach, CA 1989, edited by N. R. Pereira, J. Davis, and N. Rostoker, AIP Conf. Proc. Vol. 195 (AIP, New York, 1989), p. 290.
8. A. B. Bud'ko, F. S. Felber, A. I. Kleev, M. A. Liberman, and A. L. Velikovich, Phys. Fluids B **1**, 598 (1989).



9. R. E. Terry and R. W. Clark, in , in *Dense Z-Pinches*, 4<sup>th</sup> International Conference on Dense Z-Pinches, Laguna Beach, CA 1989, edited by N. R. Pereira, J. Davis, and P. E. Pulsifer, AIP Conf. Proc. Vol. 409 (AIP, Woodbury, New York, 1989), p. 601. S. A. Sorokin and S. A. Chaikovskii, J. of X-Ray Science and Technology **5**, 307 (1995); S. A. Sorokin and S. A. Chaikovskii, Plasma Phys. Rept. **22**, 897 (1996).
10. A. V. Shishlov, R. B. Baksht, S. A. Chaikovsky, A. Y. Labetsky, V. I. Oreshkin, A. G. Roussikh, and A. V. Fedyunin, in *Dense Z-Pinches*, 5<sup>th</sup> International Conference on Dense Z-Pinches, Albuquerque, NM 2002, edited by J. Davis, C. Deeney and N. R. Pereira, AIP Conf. Proc. Vol. 651 (AIP, Melville, New York, 2002), p. 117; S. A. Chaikovsky, A. Yu. Labetsky, V. I. Oreshkin, A. V. Shishlov, R. B. Baksht, A. V. Fedunin, A. G. Roussikh, Laser and Particle Beams **21**, 255 (2003).
11. S. A. Sorokin, S. A. Chaikovsky, in *Dense Z-Pinches*, 3<sup>rd</sup> International Conference on Dense Z-Pinches, United Kingdom, 1993, edited by M. Haines and A. Knight, AIP Conf. Proc. Vol. 299 (AIP, New York, 1994), p. 83.
12. B. B. Kadomtsev, "Hydrodynamic Stability of a Plasma," § 9 "Screw Instability", in *Reviews of Plasma Physics*, edited by M. A. Leontovich, Vol. 2 (Consultants Bureau, New York, 1966), p. 153.
13. A. L. Velikovich, R. E. Terry, J. Davis and L. I. Rudakov, "Precursor and Shell Formation, Nesting, Twisting and Magnetic Flux Compression in Wire Arrays," presented at the 2nd Annual Workshop on the Physics of Wire-Array Z-Pinch Plasmas, Taos, NM, April 3-7, 2000.
14. F. W Grover, *Inductance Calculations* (D. Van Nostrand Company, New York, 1946).

15. R. Lundin, "A Handbook Formula for the Inductance of a Single-Layer Circular Coil," *Proc. IEEE* **73**, 1428 (1985).

# Two- and Three- Wire Loads for Large Current Machines

Robert E. Terry, *Member, IEEE*, and John P. Apruzese

**Abstract**—Energetic implosions, using two or three load wires to create a focused axial stagnation of dense wire cores amidst the assembled precursor plasma, are examined with respect to the trade between the implosion mass lost to precursor ablation and the mass or kinetic energy available at stagnation. The calculated kinetic energy at stagnation serves as the primary source for the output x-radiation which is estimated with a tabulated collisional radiative model.

**Index Terms**—Plasma Radiation Sources, X-ray production, Z-pinches, wire arrays, wire ablation, fluid particle methods.

## I. INTRODUCTION

THE use of a single wire load on large machines like "Z" is usually avoided due to an excessive initial inductance and subsequent high voltages on upstream components. There is however a middle ground where a few larger wires can start well off axis and present much less initial inductance. Such loads will provide the lower inductance at the expense of more precursor plasma involvement.

In contrast to closed arrays with hundreds of fine wires, this relatively unexplored path to energetic implosions would use two or perhaps three load wires of appropriately heavier mass and aims to create a focused axial collision of dense wire cores amidst the assembled precursor plasma. The precursor, not confined by many wires, would presumably not soften this collision.

Hence we must examine the trade between the implosion mass lost to precursor ablation and the mass available to deliver the wire core's kinetic energy.

A clear consequence of this load choice is a quite open geometry for which the transition to a highly conducting annular MHD plasma is neither an early nor a necessarily dominant feature of the electrodynamics. Generalizing slightly beyond MHD, we use a Lorentz gauge direct field solver to treat the TEM to TM mode set transition in the pinch region. The problem is formulated using a scalar potential  $\Phi$  and an axial vector potential  $A_z$  as unknowns, with the radial vector potential  $A_r$  being determined by the gauge constraint.

In contrast to earlier wire dynamic model (WDM) formulations with inductance matrix elements good only in the thin wire limit[1], the present work will make use of a new analytic Green's function for  $A_z$  that accounts for proximity effects among the wire cores and the return current structure.

Manuscript received September 30, 2003. This work was supported by the Defense Threat Reduction Agency.

The authors are with the Radiation Hydrodynamics Branch, Plasma Physics Division, Naval Research Laboratory, Washington, DC 20375 USA (email: terry@ccs.nrl.navy.mil)

The Green's function provides a first estimate for the axial vector potential solution  $A_z(x, y)$  at the pinch midplane and the net load inductance arising among the heavy wire filaments. That solution is further refined by a current density source term representing the extended coronal plasma conductivity and flow.

The use of empirical mass source terms[2], for estimating the precursor mass ejection rate, ablative cooling rate, and ablation velocity, is then introduced to complete the picture.

## II. MATHEMATICAL FORMULATION

There are two required innovations to carry out the desired calculations. First, we must go beyond the thin wire inductance limit, which is fine for wire core dynamics and current sharing, but starts to break down when the tenuous corona plasma jackets the wires and entrains current. Moreover, in the larger wires used for the loads we consider, proximity effects become noticeable as the wires approach one another. Hence a means of describing the extended conduction medium of the corona while maintaining contact with the lowest order inductive picture enforced by the wire cores is key to a versatile picture.

Second, we require a fluid description that admits a large adaptability in scale lengths in order to track the history of coronal plasma elements that drift radially to form the axial precursor. A smooth generalization of the discrete wire filaments into fluid particles allows a large dynamic range in mesh size for the field solver. The new fluid particle methods used here adapt easily to such grids because the projection of the fluid particle variables like density, velocity, and energy onto the Eulerian grid is virtually exact. The resulting errors in working with the tabular collisional radiative equilibrium (TCRE) algorithms will also be minimized.

### A. Energy Transfer in a Circuit Model

For the original WDM the direct interaction among an ensemble of current elements is equivalent to a potential energy defined by the array inductance. Within the ensemble are symmetry groups of multiplicity  $S$ , e.g.

$$I = \sum_{i,s=1,1}^{N,S} J_{i,s} = I \sum_{i=1}^N S \alpha_i, \quad (1)$$

where  $\alpha_i$  is any  $S$ -wise invariant current fraction contained in any particular wire path represented by a series resistance and inductance.

By construction then the sum of all  $\alpha_i$  is one. Since the wire paths are in parallel, the voltage seen by each path  $\alpha_i$  is equal in the absence of (small) wave transit time effects.

If we examine the voltage  $V_e(t)$  impressed at the entrance or feed of a wire array cage, the resolution of the set  $\alpha_i$  and the total current  $I$  admitted to the array are seen to be two distinct problems. From the view of the external generator  $V_g(t)$ , the array is a two terminal device and the energy into it must be the same for all sets  $\alpha_i$  that show the same net impedance.

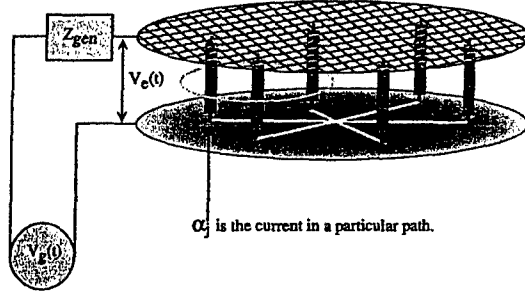


Figure 1. WDM circuit elements can decompose into symmetry groups, with each element representing a resistance and inductance.

As illustrated in Fig. 1, maintaining equal voltage at each circuit element, the equations fixing the current fractions  $\alpha_i$  for any given  $I$  and  $V_e(t) = V_g(t) - Z_{gen}I$  can be written as,

$$V_e(t) = R_i(t)\alpha_i I + \left( \frac{d}{dt} L_{ij} \cdot \alpha_j \right), \quad (2)$$

and then integrated over a time interval  $\delta \equiv (V_e(t))/(dV_e/dt)$  to eliminate the time derivative. Let  $\Delta\Psi_e$  be the change in flux over this interval, the matrix relation

$$\frac{\Delta\Psi_e}{I} \mathbf{u}_i = \delta R_j L_{ij} \cdot \alpha_j + L_{ij} \cdot \alpha_j \quad (3)$$

emerges, with  $L_{ij}$  the diagonal identity matrix,  $\mathbf{u}_i$  a unit vector over the local group.

In the limit of vanishing inductance, or slow timescales ( $\delta \gg L_i/R_i$ ), it is easy to see that the  $\alpha_i = Z_{||}/R_i(t)$  and thus they clearly add up to unity.

The use of time dependent inductances also shows that radial displacements are self healing insofar as any excursion of a filament to the interior of an array increases that filaments inductance, lowers the current to it, and allows the others to catch up. Such behavior is still true for low count loads (down to three such filaments), and is of course a moot point for two wires. In contrast with an earlier analysis[3] the stabilization arises from the generalization to a self consistent description of forces and inductances.

### B. Field Methods for Open Geometries

Loads with fewer wires using larger initial wire diameters and load radii will present a lower initial inductance at the expense of more precursor plasma involvement. In contrast to closed arrays with hundreds of fine wires, this very open field geometry can be addressed with only marginal validity by a conventional inductance and MHD picture due to the large dynamic range in scale lengths and magnetic Reynolds number. The limit of spatially constant voltage throughout the corona is probably pretty good but by no means certain.

1) *Mode Transitions from TEM to TM:* With  $Z_o = \sqrt{\epsilon_o/\mu_o} = 367.7\Omega$ , a coaxial inlet TEM boundary condition on the scalar potential  $\Phi(r, z, t)$

$$V_{in} = Z_L I_c = \left[ \frac{Z_o}{2\pi} \ln\left(\frac{r_>}{r_<}\right) \right] I_c, \quad (4)$$

determines all the fields near the inlet, where  $A_z \rightarrow 0$ .

Elsewhere, where the TM mode set is selected by the axial and radial currents of the diode, the time integral of the scalar potential forms a useful generalization of the familiar inductive "flux function", viz. let  $\Psi(r, z, t) = \int^t dt_1 \Phi(r, z, t_1)$ , and

$$\Psi(r_>) - \Psi(r_<) = \int_{r_<}^{r_>} A_r(z_c, r_1, t) dr_1, \quad (5)$$

$$\Psi(z_>) - \Psi(z_<) = \int_{z_<}^{z_>} A_z(z_1, r_c, t) dz_1, \quad (6)$$

on radial  $z_c$  and axial  $r_c$  conductor boundaries will ensure that the tangential component of electric field vanishes. Here ( $r_<$ ,  $r_>$ ) are any two points on a plane conductor  $z_c$ ; ( $z_<$ ,  $z_>$ ), any two points on an axial conductor  $r_c$ .

2) *Utility of the Lorentz Gauge:* The Lorentz gauge condition choice

$$r^{-1} \partial_r(r A_r) + \partial_z A_z + c^{-2} \partial_t^2 \Phi \equiv 0, \quad (7)$$

allows the dynamics to concentrate on the solution of  $A_z(z, r, t)$  only. One may in fact examine only two coupled wave equations for the needed fields

$$\nabla^2 \Phi - c^{-2} \partial_t^2 \Phi = 0, \quad (8)$$

$$\nabla^2 A_z - c^{-2} \partial_t^2 A_z = -\mu_o J_z, \quad (9)$$

with the axial current density near the wires given by

$$\mathbf{J}_z = \sigma_{\perp} [\mathbf{E}_z + \mathbf{V}_r \times \mathbf{B}_{\theta}(A)] . \quad (10)$$

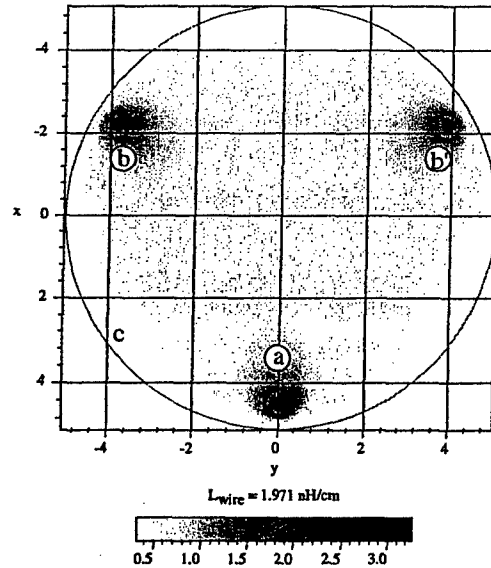


Figure 2. Three 1000  $\mu\text{m}$  Wire Vector Potential  $A_z(x, y)$

For the inhomogeneous wave equation involving  $A_z(x, y)$ , a Green's function can be developed for the problem at the diode mid-plane, shown in Fig. 2, which captures the proper boundary conditions on the outer return current surface and on the finite size conducting wire cores. The function can be built up piecewise from image currents generated by a source cylinder (a), any number of floating cylinders (b, b', ...) and the return cylinder (c),

$$\mathcal{G}(x, y|s = a, b, b' \dots) = g_a(x, y) + g_b(x, y) + g_{b'}(x, y) + g_{bb'}(x, y) + g_{xb'}(x, y) + \dots, \quad (11)$$

and over the symmetry groups  $A_z(x, y) = \Sigma_s \mathcal{G}(x, y|s)$ . This  $A_z$  "diagonalizes" the inductance matrix. For the example of Fig. 2 with quite large wires close to the return current, the thin wire inductance would be inaccurate. The details of the Green's function are covered in the Appendix. Similar Green's functions were examined in earlier work[4], but were specialized to strict rotational symmetry and never obtained in the closed form used here to help accelerate the convergence of the general field solver or offer a fast implosion solution.

3) *Variational Form of the Field Problem:* Dimensionless spatial variables are based on a characteristic time  $t_0$  of the input pulse line,  $\lambda_0 = ct_0$ , and a skin depth  $\delta_0 = \sqrt{2t_0/\mu_0\sigma}$ .

With  $\mathcal{E}_z = t_0 E'_z$ , action integrals advance all fields,

$$\mathcal{L}(\Phi) = \int d\tau dA [(\nabla\Phi)^2 - (\partial_\tau\Phi)^2], \quad (12)$$

$$\mathcal{L}(A_z) = \int d\tau dA \left[ (\nabla A_z)^2 - (\partial_\tau A_z)^2 - A_z \left( \frac{2\lambda_0}{\delta_0} \right)^2 \mathcal{E}_z \right]. \quad (13)$$

Our finite element (FE) representation employs value and time derivative degrees of freedom, e.g.  $\tilde{\Phi} = [\Phi, \partial_\tau\Phi]$ . Representing the action integral of (12) with such variables, the scalar potential variational constraint

$${}_{i+1}W_{i+1} \cdot {}^{i+1}\tilde{\Phi} + {}_{i+1}W_i \cdot {}^i\tilde{\Phi} + {}_{i+1}W_{i-1} \cdot {}^{i-1}\tilde{\Phi} \equiv 0, \quad (14)$$

is equivalent to solving that PDE problem. The symmetric positive definite weight matrices have the general form,  ${}^iW_m = T_{lm} \otimes (G_x + G_y) - T'_{lm} \otimes V$  with integrals of squared time values  $T$ , time derivatives  $T'$ , spatial gradients  $G$ , and spatial values  $V$  taken over each cell. A similar formulation resolves (13).

The weight matrices are essentially quadrature factors for integrals performed on finite element domains and then assembled over an entire mesh. Several element options exist to construct the weight matrices, but a common requirement, easily seen from (10), is that of continuity in both interpolant values and first derivatives across the element boundaries, viz.  $C^1$  continuity. Elements meeting this requirement on both triangular and quadrilateral meshes have been developed.

### C. Particle Methods

An early formulation[5] of fluid particles, similar to those we want here, used freely drifting particles only and focused on particle annihilation and creation rules to track emerging features.

The novel particle solutions used here are drift kinetic fluid particles (DKFP) and track precisely the distribution function evolving under the action of the drift velocity  $C$  and acceleration  $A$  which are functions of local position  $x$ ,  $C = V + x \cdot \delta/h$ ,  $a = A + x \cdot \alpha/h$ . Here  $h$  is an initial width parameter, and the gradient scale parameters  $\delta \equiv h\partial_x C$  and  $\alpha \equiv h\partial_x a$  are independently specifiable for each spatial dimension of a particle.

These DKFP contain three common factors which represent the dilation of the initial size (due to the shear in the velocity and acceleration), and the (asymmetric) movement of the initial domain boundaries. For a 1D particle class these are:

$$D(t) = \left(1 + \frac{t\delta}{h} + \frac{1}{2} \frac{t^2\alpha}{h}\right), \quad (15)$$

$$h_{\pm}(t) = \pm h + (V \pm \delta)t + \frac{1}{2}(A \pm \alpha)t^2. \quad (16)$$

The expected profile for number density (per unit length, area, or volume)  $n(X, t) \equiv \langle N \rangle / \ell$  is then:

$$n(X, t) = \frac{N}{2hD(t)} \left( \text{erf} \left( \frac{(h_+(t) - X)}{\sqrt{2}Ut} \right) + \text{erf} \left( \frac{(X - h_-(t))}{\sqrt{2}Ut} \right) \right) \quad (17)$$

with similar expressions for momentum and enthalpy. The fluid properties, needed by the electrodynamics to support the evaluation of a magnetic Reynolds number ( $\mathcal{R}_m = 2\ell_B t_0 V_r / \delta_0^2$ ) and the source term above, are then easily projected into each node or cell of the field solution grid with virtually no error.

1) *Source Boundary Conditions at the Wire Core:* The detailed accounting of material phase changes as the wires vaporize and ionize is left to future refinements. A reasonably simple and apparently accurate approximation is to balance the force of the wire core attraction with a "rocket" force due to the inward flow of coronal plasma[2]. Here a strict balance is too specialized, for what is needed is a path to account for wire loads that do not hang at the initial radius until they virtually disintegrate. From earlier work[6] we know that Al foil switches exhibit an areal mass loss rate that scales directly with the surface magnetic energy density, viz.  $\partial_t m = -\kappa(B^2/8\pi)$ , and a flow velocity determined by a sound speed[7] or, as seen for switch foils, an Alfvén speed characterized by local field or "private flux" near the wire. Such considerations lead to a mass loss estimate, for a wire of length  $\ell$  and radius  $r_{\text{wire}}$ , that scales like

$$\dot{m} \approx 10\kappa(\ell/r_{\text{wire}})I_{[MA]}^2 [\mu\text{g/ns}]. \quad (18)$$

Typical values for  $\kappa$  are (5-25) [ $\mu\text{g cm/erg s}$ ] and we find that, in keeping with the other models cited here, only a small fraction of the wire current ( $\approx 10^{-2}$ ) can be viewed as directly participating in this erosion process. The larger current fraction must be concentrated outside the core in the vapor and plasma emitted by the wire. If the material outside the wire tends to a state such that  $\mathcal{R}_m \approx 1$ , then a similar analysis reveals that

$$\dot{m} \approx (\ell/41.09Z \ln \Lambda \alpha_{\perp}(Z, \omega\tau))I_{[MA]}^2 T_e^{3/2} [\mu\text{g/ns}]. \quad (19)$$

2) *Magnetoplasma Conductivity*: The Epperlein-Haines[8] formulation for the required skin depth  $\delta_o$  in the wire corona can be written

$$1/\sigma_{\perp} \equiv \eta_{\perp} = \eta_0 \alpha_{\perp}(Z, \omega\tau) \quad (20)$$

with,  $\alpha_{\perp}(Z, \omega\tau)$  a rational function, and

$$\eta_0 \equiv \left[ \frac{m_e}{e^2 n_e \tau_e} \right] = 1.147519 \cdot 10^{-14} \frac{Z \ln \Lambda}{T_{[eV]}^{3/2}} [s]. \quad (21)$$

As needed in the  $A_z$  source term, for a time  $t_o$ ,

$$\left( \frac{\lambda_o}{\delta_o} \right)^2 = 1.218472 \cdot 10^{-2} \frac{\lambda_o^2}{2t_o \ln \Lambda Z \alpha_{\perp}(Z, \omega\tau)} T_{[eV]}^{3/2} \quad (22)$$

is the (dimensionless) equivalent.

3) *Simplified Model*: In the studies reported below we have employed a simplified load model, pending the full development and testing of the general formulation outlined thus far. The simple model treats the electrodynamic problem inductively but uses the more precise Green's function to establish that inductance. The material model treats each wire core as a single macroparticle, equipped with an EOS based on the total absorbed enthalpy. This wire core heats ohmically and viscously at stagnation, cools radiatively using the TCRE model, and shares current self consistently with a Spitzer corona. Mass ablation is allowed, scales with the wire size and wire core current, but is subject to an approximate rate factor  $\kappa$  in (18).

### III. EARLY INDUCTANCE AND ENERGY AT STAGNATION

First we have examined the question of initial inductances for loads that might be contemplated on larger machines like "Z". For 1, 2, and 3 wire loads set at 0.9 of the return current radius (5 cm), one sees quite favorable inductances for diameters near or above 100  $\mu\text{m}$ . The subscripts on the inductance denote the number of wires. The loads in Table I above 100  $\mu\text{m}$  would require hollow or otherwise thinned tube loads to meet the cited mass and wire diameter. In addition to a lower inductance, the advantages of larger wire radius are reflected in a lower mass ablation.

TABLE I. INITIAL INDUCTANCES AND MASSES FOR ONE-, TWO-, OR THREE-WIRE LOADS

Dia. $\mu\text{m}$	$L_1$ $\frac{nH}{cm}$	$L_2$ $\frac{nH}{cm}$	$L_3$ $\frac{nH}{cm}$	Mass $\mu g$
1000.	5.88	2.95	1.97	$\leq 375$
500	7.27	3.64	2.43	$\leq 375$
200	9.11	4.56	3.05	$\leq 375$
100	10.49	5.25	3.51	357
50	11.98	5.95	3.97	89.2
20	13.71	6.86	4.58	14.26
10	15.10	7.55	5.04	3.57

A second figure of merit with respect to early inductance issues is the ratio of peak inlet or port voltage during rundown  $V_{e,r}$  to that peak inlet voltage developed at stagnation  $V_{e,s}$ .

Whatever the details of the driving machine voltage, if the early inductance of a low wire number load doesn't erect a port voltage competitive with the port voltage at stagnation, then upstream pulse power components won't see an excessive voltage. For typical "Z" parameters this ratio is shown in Table II, as a function of the wire number, diameter, and ratio of initial radius  $R$  to current return radius  $C$ . In only one case does the ratio exceed one. Generally, for  $R/C \geq 0.6$  the effects of early inductance are minimal. The more inductive loads do diminish the peak load current, but not very strongly. The increase of the voltage ratio with radius reflects the proximity of wire to the return current cylinder, and would be absent in the thin wire limit.

TABLE II. RATIO OF RUN-DOWN TO STAGNATION VOLTAGE

Number @ Dia. $\mu\text{m}$	( $R/C$ ) 0.60	0.75	0.90
2 @ 1000	0.557	0.611	0.732
2 @ 500	0.633	0.811	0.964
2 @ 200	0.711	0.850	1.305
3 @ 1000	0.246	0.267	0.336
3 @ 500	0.296	0.330	0.409
3 @ 200	0.366	0.423	0.507

With regard to energy coupling some straightforward scalings emerge with wire number. Considering a load mass  $m_i$  in  $\mu\text{gm}$  per wire, an inductance  $L$  in  $nH$ , a (constant) driver voltage  $V$  in  $MV$ , and pinch dimensions of length  $\ell$ , and radius  $r_0$  in  $cm$ , the available wire core energy at stagnation becomes,

$$K_{imp,2} = 522.4 \left( r_0 (m_i \ell)^{1/2} V/L \right) [kJ]. \quad (23)$$

One expects,  $K_{imp,3} = \sqrt{4/3} K_{imp,2}$  for the three wires, although the greater inductive reduction of the peak current for two wires tends to spoil this rule somewhat, allowing more energy into the three wire case than suggested by (23).

As an initial survey of the expected behavior of these loads, the simple model was used first in the very approximate case of small, fixed wire resistance and a fixed mass erosion constant so that for given current histories smaller diameter wires would lose a higher mass fraction. The results with this simple ablation model are shown in Table III.

TABLE III. KINETIC ENERGY TRANSFERS [KJ] FOR TI LOADS

Dia. & Case $\mu\text{m}$ Z,DE	$H_2$ kJ	$H_3$ kJ	Mass $\mu g$
1000 on Z	428.2	591.6	1,125
500 on Z	552.6	802.2	1,125
200 on Z	631.8	1,017	1,125
100 on Z	662.4	1,004	1,125
100 on DE	78.8	94.47	180

The two- and three-wire loads were centered at 0.8 of the return current radius (5 cm), and run for a fixed mass erosion coefficient that offered mass losses comparable to experiments. Under these test constraints, the lower masses lose available stagnation kinetic energy due to mass ablation, while the larger masses are bit too large for optimal coupling to the generator. Hence, on Z the 3 wire case optimized for the 200  $\mu\text{m}$  diameter load. On DE the wires were placed at 0.6 of the return current radius and the energy delivery is modest. Similar calculations for DE varying the initial radius infer energies in the same range.

Using the complete simple model, viz. TCRC radiation losses[9], an explicit calculation of the stagnation heating with viscous drag forces slowing the model wire cores, and a time dependent wire resistance and ablation model, the re-examination of kinetic energy transfer (shown in Table IV) again establishes large available stagnation enthalpies. The mass was changed with each value of  $R/C$  to maintain a roughly constant implosion time, but is at about the same value as before for similar conditions, viz. 1125  $\mu\text{gm}$  for three wires at  $R/C=0.75$ . The use of a larger return current radius (6 cm) also allowed a longer implosion time for similar values of  $R/C$  and hence the kinetic energy transfers are a bit higher than before.

TABLE IV. PEAK KINETIC ENERGY TRANSFER [KJ] ON Z WITH TI

Number @ Dia. [ $\mu\text{m}$ ]	( $R/C$ ) 0.60	0.75	0.90
2 @ 1000	590.7	641.9	714.7
2 @ 500	518.1	590.0	664.4
2 @ 200	418.7	445.9	555.8
3 @ 1000	864.0	917.6	979.9
3 @ 500	815.8	864.5	926.9
3 @ 200	724.5	775.1	811.3

The radiation yield and power accessible in a high density stagnation are seen to extract over half the available energy (0.57) and show net cooling rates clearly comparable to expected stagnation heating rates. However the more detailed ablation model shows only a monotone decay of available stagnation enthalpy with decreasing wire diameter, mostly because the mass loss tends to strengthen late in the implosion, bleeding off accumulated kinetic energy but not starting soon enough to get down to a more favorable mass for the generator.

#### IV. SUMMARY AND CONCLUSIONS

The use of loads consisting of hundreds of fine wires on large current drivers like Z at Sandia National Laboratories has resulted in better implosion quality, reduced X-ray pulsewidths, and correspondingly higher X-ray powers. However, with the well established presence of precursor plasma on axis and the near complete ablation of the wire mass before any compression begins, there is a strong possibility

that even these implosions are also softened by the precursor plasma and do not gain access to the powers and pulsewidths inferred from detailed 1-D models.

One means of overcoming this barrier is the use of fewer heavy wires of larger diameter which might collide on axis with most of the mass still in the wire core and little parasitic energy or mass entrained in a thin coronal plasma. The high velocity collision of dense wire cores should in principle provide extremely rapid ionization to high Z and rapid stagnation to even higher X-ray powers.

To examine this possibility we have modified our wire dynamic model (WDM) to calculate kinetic energy transfer to low wire number loads on both Double Eagle and "Z" class drivers. and assessed the load energy and upstream voltages.

For DE any initial mounting of two or three 50 to 200  $\mu\text{m}$  Ti wire loads at radii in excess of 0.6 of the return current radius will easily preclude early voltages near the insulator stack from rising above one half the open circuit voltage as the load initiates and starts to run in. The best available kinetic energies are about 80 kJ for two wire loads, and about 100 kJ for three wire loads. The (60-80  $\mu\text{g/cm}$ ) masses required are typical for DE, the inductive current "bite" is clear.

For "Z" again initial mounting of similar wire loads at radii in excess of 0.6 of the return current radius will also keep early voltages in bounds. The best available kinetic energies are about 600 kJ for two wire loads, and about 1000 kJ for three wire loads. The (250-375  $\mu\text{g/cm}$ ) masses used are an excellent match in "Z". In both cases the result of too much mass erosion is to degrade the available kinetic energy at stagnation.

Finally the sharp dependence of delivered energy on the wire ablation rate clearly shows the need to keep this as a focus area in future work.

#### ACKNOWLEDGEMENTS

The authors wish to acknowledge discussions with A. Velikovich and M. Haines. Maple software was instrumental in this research.

#### REFERENCES

- [1] R. E. Terry, *et al*, "Current Switching and Mass Interpenetration Offer Enhanced Power from Nested Array Z Pinches", *Phys.Rev.Lett.*, 83(21), pp.4305-4308,1999.
- [2] S. V. Lebedev, *et al*, "Effect of discrete wires on the implosion dynamics of wire array Z pinches", *Phys.Plasmas*, 8(8),pp.3744-3747,2001.
- [3] F. S. Felber, *et al*, "Kink and Displacement Instabilities in Imploding Wire Arrays", *Phys. Fluids*, 24(6), pp.1049-1055,1981.
- [4] E. Waisman, "The magnetostatic field of a periodic cylindrical array of perfect conductors of arbitrary x-y cross section", *J. Appl. Physics*, 50(1), pp.23-29,1979.
- [5] W. Bateson and D. Hewett, "Grid and Particle Hydrodynamics", *J. Comp. Phys.* 144, pp.358-378,1998.
- [6] J. E. Brandenburg, R. E. Terry, N. R. Pereira, "Mass Erosion in Foil Switches", *Fourth Int'l Conf on Megagauss Fields*, Plenum Press, New York, 1986, pp.543-550.
- [7] M. G. Haines, "A Three Dimensional Model of Wire Array Instability, Ablation, and Jetting", *IEEE Trans. Plasma Sci.*, 30(2), pp.588-592,2002.
- [8] E. M. Epperlein and M. G. Haines, "Plasma transport coefficients in a magnetic field by direct numerical solution of the Fokker Planck equation", *Phys. Fluids*, 29(4), pp.1029-1041,1986.
- [9] J. W. Thornhill, *et al*, "An efficient tabulated collisional radiative equilibrium radiation transport model suitable for multidimensional hydrodynamics calculations", *Phys.Plasmas*, 8(7), pp.3480-3489,2001.

PLACE  
PHOTO  
HERE

Robert E. Terry (M'04) received the B.S. degree in physics from the Massachusetts Institute of Technology, Cambridge, MA, and the Ph.D. degree from Johns Hopkins University, Baltimore, MD, in 1968 and 1978, respectively. He is currently a research physicist with the Radiation Hydrodynamics Branch of the Plasma Physics Division, Naval Research Laboratory (NRL). From 1979 to 1984 he worked with the theoretical physics division of Jaycor, Inc in Alexandria, VA. Joining NRL in 1985, he has worked on PRS dynamics, power flow, plasma flow and reflex triode switches, magnetic interlayer pinches, gyrokinetic flows and microturbulence, RF discharge theory, plasma chemistry, and specialized wire z-pinch models. His current research activities include PRS wire array dynamics, radiation models, and precursor physics.

PLACE  
PHOTO  
HERE

John P. Apruzese received the B.S. degree in Physics from Yale University in 1970, and the Ph.D. in 1974 from the University of Wisconsin, Madison. Dr. Apruzese then pursued a NSF Postdoctoral Fellowship at the Naval Research Laboratory where his research focused on x-ray emission, diagnostics, and transport in laboratory plasmas. In 1976 he joined Science Applications International Corporation of McLean, Virginia. Dr. Apruzese coordinated numerical wave optics modeling of laser propagation. In 1982, Dr. Apruzese joined the Naval Research Laboratory in Washington, D.C. where he is currently Head of the Radiation Dynamics Section in the Plasma Physics Division. While at NRL, his scientific contributions have centered on plasma spectroscopy, short-wavelength lasers, radiation transport theory, and high power x-ray sources.



# APPENDIX I DEVELOPMENT OF THE GREEN'S FUNCTION

For a return current cylinder of radius  $C$  we develop here the components of (11) in the main text. The primary source is located within  $C$  along the  $x$  axis at position  $P$ . Since the cylinder is of finite size (radius  $A$ ), the center of current within  $A$  is shifted to

$$S(P, A, C) = \frac{C^2 + P^2 - A^2 - (C + P)(C - P)\sqrt{1 + A^2 \frac{A^2 - 2C^2 - 2P^2}{((C - P)^2(C + P)^2)}}}{2P}, \quad (24)$$

so  $S/P$  is the primary measure of proximity effects for cylinders that are separated by distances of a few diameters.

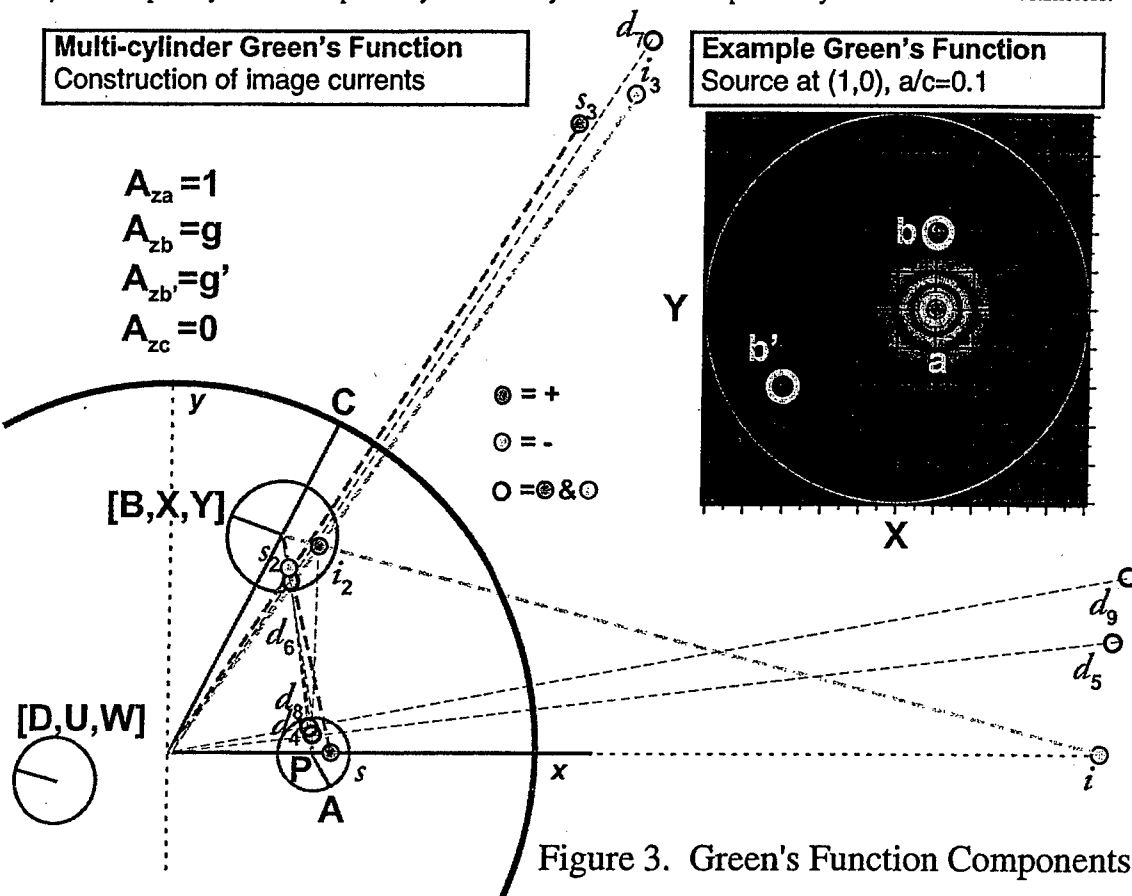


Figure 3. Green's Function Components

The method is readily extended to more participating cylinders and more image currents in the sequence. Despite the complexity of these expressions the maintenance of the proper boundary conditions on the cylinder surfaces to errors on the order of  $10^{-5}$  or better requires this level of detail.

In Fig. 3 is shown the sequence of image currents required to construct the required Green's function and the boundary conditions it must meet on the cylinder surfaces. The term sequence is divided into sets of sources and images, color coded as shown. An example Green's function is also shown in the insert. Recasting (11) slightly, decompose the complete expression as

$$G = G_A + G_B + G_D + G_{xB} + G_{xD}. \quad (25)$$

Now the source (numerator) and image (denominator) terms for the potential from this primary current are

$$G_A = \frac{1}{2} \ln \left( \frac{y^2 + (x - S)^2}{y^2 + (x - \frac{C^2}{S})^2} \right). \quad (26)$$

### A. Direct Terms

The direct term for the cylinder  $[B, X, Y]$  is given by a source group and an image group

$$G_B = G_{Bs} - G_{Bi} \quad (27)$$

and for the source group with the common terms,

$$T1 = Y^2 + \left(\frac{C^2}{S} - X\right)^2 \quad T2 = Y^2 \left(1 - \frac{B^2}{T1}\right)^2 + \left(P - X - \frac{B^2 \left(\frac{C^2}{S} - X\right)}{T1}\right)^2 \quad T3 = Y^2 + (S - X)^2,$$

$$G_{Bs} = \frac{1}{2} \ln \left( \left( \left( y - Y \left(1 - \frac{B^2}{T1}\right) \right)^2 + \left( x - X - \frac{B^2 \left(\frac{C^2}{S} - X\right)}{T1} \right)^2 \right) \right.$$

$$\left( \left( y - \frac{C^2 Y \left(1 - \frac{B^2}{T3}\right)}{Y^2 \left(1 - \frac{B^2}{T3}\right)^2 + \left(X + \frac{B^2 (S - X)}{T3}\right)^2} \right)^2 + \left( x - \frac{C^2 \left(X + \frac{B^2 (S - X)}{T3}\right)}{Y^2 \left(1 - \frac{B^2}{T3}\right)^2 + \left(X + \frac{B^2 (S - X)}{T3}\right)^2} \right)^2 \right) \left( \right.$$

$$\left( y - \frac{A^2 Y \left(1 - \frac{B^2}{T3}\right)}{Y^2 \left(1 - \frac{B^2}{T3}\right)^2 + \left(P - X - \frac{B^2 (S - X)}{T3}\right)^2} \right)^2$$

$$+ \left( x - P + \frac{A^2 \left(P - X - \frac{B^2 (S - X)}{T3}\right)}{Y^2 \left(1 - \frac{B^2}{T3}\right)^2 + \left(P - X - \frac{B^2 (S - X)}{T3}\right)^2} \right)^2 \left( \right.$$

$$\left. \left( y - \frac{C^2 A^2 Y \left(1 - \frac{B^2}{T1}\right)}{\frac{A^4 Y^2 \left(1 - \frac{B^2}{T1}\right)^2}{T2^2} + \left( P - \frac{A^2 \left( P - X - \frac{B^2 \left(\frac{C^2}{S} - X\right)}{T1} \right)}{T2} \right)^2} \right)^2 \right)$$

$$+ \left( x - \frac{C^2 \left( P - \frac{A^2 \left( P - X - \frac{B^2 \left( \frac{C^2}{S} - X \right)}{T_1} \right)}{T_2} \right)}{\frac{A^4 Y^2 \left( 1 - \frac{B^2}{T_1} \right)^2}{T_2^2} + \left( P - \frac{A^2 \left( P - X - \frac{B^2 \left( \frac{C^2}{S} - X \right)}{T_1} \right)}{T_2} \right)^2} \right)^2 \right)$$

With the common terms,

$$T_1 = Y^2 + (S - X)^2 \quad T_2 = Y^2 \left( 1 - \frac{B^2}{T_1} \right)^2 + \left( P - X - \frac{B^2 (S - X)}{T_1} \right)^2 \quad T_3 = Y^2 + \left( \frac{C^2}{S} - X \right)^2$$

the image group subtracted above becomes

$$G_{Bi} = \frac{1}{2} \ln \left( \left( (y - Y \left( 1 - \frac{B^2}{T_1} \right))^2 + \left( x - X - \frac{B^2 (S - X)}{T_1} \right)^2 \right) \right. \\ \left. \left( \left( y - \frac{C^2 Y \left( 1 - \frac{B^2}{T_3} \right)}{Y^2 \left( 1 - \frac{B^2}{T_3} \right)^2 + \left( X + \frac{B^2 \left( \frac{C^2}{S} - X \right)}{T_3} \right)^2} \right)^2 + \left( x - \frac{C^2 \left( X + \frac{B^2 \left( \frac{C^2}{S} - X \right)}{T_3} \right)}{Y^2 \left( 1 - \frac{B^2}{T_3} \right)^2 + \left( X + \frac{B^2 \left( \frac{C^2}{S} - X \right)}{T_3} \right)^2} \right)^2 \right) \right. \\ \left. \left( y - \frac{A^2 Y \left( 1 - \frac{B^2}{T_3} \right)}{Y^2 \left( 1 - \frac{B^2}{T_3} \right)^2 + \left( P - X - \frac{B^2 \left( \frac{C^2}{S} - X \right)}{T_3} \right)^2} \right)^2 \right. \\ \left. + \left( x - P + \frac{A^2 \left( P - X - \frac{B^2 \left( \frac{C^2}{S} - X \right)}{T_3} \right)}{Y^2 \left( 1 - \frac{B^2}{T_3} \right)^2 + \left( P - X - \frac{B^2 \left( \frac{C^2}{S} - X \right)}{T_3} \right)^2} \right)^2 \right) \right) \\ \left( y - \frac{C^2 A^2 Y \left( 1 - \frac{B^2}{T_1} \right)}{\left( \frac{A^4 Y^2 \left( 1 - \frac{B^2}{T_1} \right)^2}{T_2^2} + \left( P - \frac{A^2 \left( P - X - \frac{B^2 (S - X)}{T_1} \right)}{T_2} \right)^2 \right) T_2} \right)^2 \right)$$

$$+ \left( x - \frac{C^2 \left( P - \frac{A^2 (P - X - \frac{B^2 (S - X)}{T_1})}{T_2} \right)}{\frac{A^4 Y^2 (1 - \frac{B^2}{T_1})^2}{T_2^2} + \left( P - \frac{A^2 (P - X - \frac{B^2 (S - X)}{T_1})}{T_2} \right)^2} \right)^2 \right)$$

A similar development is done for a second cylinder at  $[D, U, W]$ ,

$$G_D = G_{Ds} - G_{Di} \quad (28)$$

with the substitutions  $X \rightarrow U$ ,  $Y \rightarrow W$ , and  $B \rightarrow D$ , in the previous expression.

### B. Exchange Terms

There are exchange terms for images of B in D and vice versa. With the common terms,

$$T1 = Y^2 + (\frac{C^2}{S} - X)^2 \quad T2 = (Y(1 - \frac{B^2}{T1}) - W)^2 + \left( X + \frac{B^2(\frac{C^2}{S} - X)}{T1} - U \right)^2 \quad T3 = Y^2 + (S - X)^2$$

the exchange source term for B in D is

$$G_{Bx} = G_{Bxs} - G_{Bxi} \quad (29)$$

$$G_{Bxs} = \frac{1}{2} \ln \left( \left( \left( y - W - \frac{D^2 (Y(1 - \frac{B^2}{T3}) - W)}{(Y(1 - \frac{B^2}{T3}) - W)^2 + (X + \frac{B^2(S - X)}{T3} - U)^2} \right)^2 + \left( x - U - \frac{D^2 (X + \frac{B^2(S - X)}{T3} - U)}{(Y(1 - \frac{B^2}{T3}) - W)^2 + (X + \frac{B^2(S - X)}{T3} - U)^2} \right)^2 \right) \left( \left( y - \frac{C^2 \left( W + \frac{D^2 (Y(1 - \frac{B^2}{T1}) - W)}{T2} \right)}{\left( W + \frac{D^2 (Y(1 - \frac{B^2}{T1}) - W)}{T2} \right)^2 + \left( U + \frac{D^2 \left( X + \frac{B^2(\frac{C^2}{S} - X)}{T1} - U \right)}{T2} \right)^2} \right)^2 \right)$$

$$+ \left( x - \frac{C^2 \left( U + \frac{D^2 \left( X + \frac{B^2 \left( \frac{C^2}{S} - X \right) - U \right)}{T_1} \right)}{T_2} \right)}{\left( W + \frac{D^2 \left( Y \left( 1 - \frac{B^2}{T_1} \right) - W \right)}{T_2} \right)^2 + \left( U + \frac{D^2 \left( X + \frac{B^2 \left( \frac{C^2}{S} - X \right) - U \right)}{T_2} \right)^2} \right)^2 \right)$$

With the common terms and the corresponding image, the final term is

$$T_1 = Y^2 + (S - X)^2 \quad T_2 = \left( Y \left( 1 - \frac{B^2}{T_1} \right) - W \right)^2 + \left( X + \frac{B^2 (S - X)}{T_1} - U \right)^2 \quad T_3 = Y^2 + \left( \frac{C^2}{S} - X \right)^2$$

$$G_{Bxi} = \frac{1}{2} \ln \left( \left( \left( y - W - \frac{D^2 \left( Y \left( 1 - \frac{B^2}{T_3} \right) - W \right)}{\left( Y \left( 1 - \frac{B^2}{T_3} \right) - W \right)^2 + \left( X + \frac{B^2 \left( \frac{C^2}{S} - X \right)}{T_3} - U \right)^2} \right)^2 + \left( x - U - \frac{D^2 \left( X + \frac{B^2 \left( \frac{C^2}{S} - X \right)}{T_3} - U \right)}{\left( Y \left( 1 - \frac{B^2}{T_3} \right) - W \right)^2 + \left( X + \frac{B^2 \left( \frac{C^2}{S} - X \right)}{T_3} - U \right)^2} \right)^2 \right) \right)$$

$$+ \left( y - \frac{C^2 \left( W + \frac{D^2 \left( Y \left( 1 - \frac{B^2}{T_1} \right) - W \right)}{T_2} \right)}{\left( W + \frac{D^2 \left( Y \left( 1 - \frac{B^2}{T_1} \right) - W \right)}{T_2} \right)^2 + \left( U + \frac{D^2 \left( X + \frac{B^2 (S - X)}{T_1} - U \right)}{T_2} \right)^2} \right)^2 + \left( x - \frac{C^2 \left( U + \frac{D^2 \left( X + \frac{B^2 (S - X)}{T_1} - U \right)}{T_2} \right)}{\left( W + \frac{D^2 \left( Y \left( 1 - \frac{B^2}{T_1} \right) - W \right)}{T_2} \right)^2 + \left( U + \frac{D^2 \left( X + \frac{B^2 (S - X)}{T_1} - U \right)}{T_2} \right)^2} \right)^2 \right)$$

Finally the exchange for D in B,

$$G_{Dx} = G_{Dxs} - G_{Dxi} \quad (30)$$

is formed from the previous expression with the exchanges  $X \leftrightarrow U$ ,  $Y \leftrightarrow W$  and  $B \leftrightarrow D$ .

## Enhanced energy coupling and x-ray emission in Z-pinch plasma implosions

K. G. Whitney,<sup>a)</sup> J. W. Thornhill, J. P. Apruzese, and J. Davis  
*Radiation Hydrodynamics Branch, Plasma Physics Division, Naval Research Laboratory,  
 Washington, DC 20375*

C. Deeney and C. A. Coverdale  
*Sandia National Laboratories, P. O. Box 5800, Albuquerque, New Mexico 87185*

(Received 10 February 2004; accepted 14 April 2004; published online 21 June 2004)

Recent experiments conducted on the Saturn pulsed-power generator at Sandia National Laboratories [R. B. Spielman *et al.*, in *Proceedings of the Second International Conference on Dense Z Pinches*, Laguna Beach, CA, 1989, edited by N. R. Pereira, J. Davis, and N. Rostoker (American Institute of Physics, New York, 1989), p. 3] have produced large amounts of x-ray output, which cannot be accounted for in conventional magnetohydrodynamic (MHD) calculations. In these experiments, the Saturn current had a rise time of  $\sim 180$  ns in contrast to a rise time of  $\sim 60$  ns in Saturn's earlier mode of operation. In both aluminum and tungsten wire-array Z-pinch implosions, 2–4 times more x-ray output was generated than could be supplied according to one-dimensional (1D) magnetohydrodynamic calculations by the combined action of the  $\mathbf{j} \times \mathbf{B}$  acceleration forces and ohmic heating (as described by a classical Braginskii resistivity). In this paper, we reexamine the problem of coupling transmission line circuits to plasma fluid equations and derive expressions for the Z-pinch load circuit resistance and inductance that relate these quantities in a 1D analysis to the surface resistivity of the fluid, and to the magnetic field energy that is stored in the vacuum diode, respectively. Enhanced energy coupling in this analysis, therefore, comes from enhancements to the surface resistivity, and we show that plasma resistivities approximately three orders of magnitude larger than classical are needed in order to achieve energy inputs that are comparable to the Saturn experiment x-ray outputs. Large enhancements of the plasma resistivity increase the rate of magnetic field and current diffusion, significantly modify the qualitative features of the MHD, and raise important questions as to how the plasma fluid dynamics converts enhanced energy inputs into enhanced x-ray outputs. One-dimensional MHD calculations in which resistivity values are adjusted phenomenologically are used to illustrate how various dynamical assumptions influence the way enhanced energy inputs are channeled by the fluid dynamics. Variations in the parameters of the phenomenological model are made in order to determine how sensitively they influence the dynamics and the degree to which the calculated x-ray outputs can be made to replicate the kinds of large variations in the experimental x-ray power data that were observed in three nominally identical aluminum wire shots on Saturn. © 2004 American Institute of Physics. [DOI: 10.1063/1.1760093]

### I. INTRODUCTION

The short-circuit current rise time of the Saturn generator at Sandia National Laboratories<sup>1</sup> was recently increased from  $\sim 60$  to  $\sim 180$  ns in order to investigate the effect of current rise time on the implosion dynamics of Z pinches. The effect was large. In both aluminum and tungsten wire experiments, significant increases in total x-ray output were observed<sup>2–4</sup> compared to the earlier outputs that were seen in short current-rise time Saturn experiments. Present magnetohydrodynamic (MHD) calculations are unable to generate such yields because the amount of x-ray energy radiated in the experiments is significantly larger than the sum of the  $\mathbf{j} \times \mathbf{B}$  work and ohmic heating calculated using the Saturn circuit model. Such energy discrepancies between Z-pinch cal-

culations and experiment have existed for some time,<sup>5–8</sup> but not to the degree seen in these experiments. The energy inputs calculated for these experiments in a one-dimensional (1D) MHD are in deficit by factors of 2 to 4. Such energy discrepancies pose serious theoretical challenges even as they offer new possibilities for increasing x-ray extraction efficiencies.

In early work on imploding Z pinches, it was observed that the total radiation yield could exceed the zero-dimensional (0D) or 1D estimates of radial kinetic energy by roughly 50%. Giuliani *et al.*<sup>9</sup> suggested that enhanced or anomalous resistivity could explain this discrepancy. Peterson *et al.*<sup>10</sup> subsequently showed that two-dimensional (2D) MHD calculations could increase the coupled energy over 0D and 1D kinetic energy couplings by accounting for mass distributions in the radial and axial directions that lead to reduced peak radial kinetic energy but significantly more

<sup>a)</sup>Berkeley Scholars, P. O. Box 852, Springfield, VA, 22150; electronic mail: whitney@ppdu.nrl.navy.mil

*pdV* work. As discussed by Peterson *et al.*,<sup>10</sup> two-dimensional MHD calculations of imploding shells indicated that instability development reduced the peak radial implosion energy but additional energy was added via *pdV* work as some of the stagnated plasma was compressed, and there was ohmic heating on axis. The combination of these heating mechanisms resulted in the plasma radiating 30% more x rays than the estimated zero-dimensional kinetic energy. These 2D calculations do not account for the actual dynamics of wire arrays, i.e., mass ablating from wires, precursor streams, and an implosion trajectory delayed from the 0D case, but they should include some of the physical mechanisms that do occur in wire arrays that have a more three-dimensional (3D) structure. The 2D calculations were also capable of reproducing the x-ray powers and total yields from foil implosions, where the x-ray yield was again greater than the 0D kinetic energy. However, attempts to reproduce the x-ray yield using 2D MHD calculations for the tungsten equivalent<sup>2</sup> of the aluminum long pulse shots described in this paper were unsuccessful.<sup>11</sup> These calculations could not reproduce the peak x-ray powers and rise times but could not explain the long duration emissions after peak x-ray power.

Evidence for energy input into Z pinches over and above radial implosion kinetic energy and *pdV* energy inputs exists in other Z-pinch configurations as well. In particular, experiments with exploding single wires on the Double-EAGLE generator<sup>12</sup> indicated that a single wire could radiate as much total energy as in a similarly massed wire array implosion. The recorded pinch sizes were comparable in all cases. Clearly, very little, if any,  $\mathbf{j} \times \mathbf{B}$  or *pdV* energy was imparted to this on-axis, single wire plasma by means of the conventional view of the thermalization of radial kinetic energy.

A theoretical mechanism was recently proposed in which energy coupling to a Z pinch is increased through the generation and storage of additional amounts of magnetic field energy in the Z-pinch plasma. The dissipation of this energy then increases the energy coupling to the plasma.<sup>7,8</sup> It was hypothesized that tubes of magnetic flux build up within a pinch as an additional effect of Rayleigh–Taylor or  $m=0$  instability growth at the surface of the plasma. If tubes of magnetic flux were to form and be trapped within the plasma, the currents that produce them would decouple from the circuit current and effectively increase the energy coupling between the Z pinch and the generator transmission line. In this paper, however, a different approach to enhanced energy coupling is investigated. First, the problem of coupling transmission lines to Z-pinch plasmas is analyzed. In a 1D hydrodynamics calculation, this analysis relates the strength of the energy coupling to the plasma's surface resistivity. Hence, enhanced coupling occurs because of increased surface resistivity.

A mechanism for increasing the electron collision frequency at the surface of a pinch was proposed in Ref. 13; namely, that currents flowing in the low density plasma at the pinch surface acquire drift velocities that can greatly exceed the sound speed. This event leads to the buildup of microinstabilities that increase the plasma's resistance to the current flow and that inhibit further growth in the drift velocity. How

this mechanism operates in detail has yet to be worked out. Consequently, the approach adopted in this paper was to increase energy coupling by phenomenologically increasing the strength of the surface resistivity. The kind of increases that could be applied were guided entirely by the x-ray data obtained in the Saturn experiments.

These data were obtained from three identically configured aluminum wire experiments and are presented in Sec. II. While the three aluminum shots were ostensibly identical, the x-ray data they produced were not. Large shot-to-shot variations were seen indicating (1) possible small differences in the wire loads or in the Saturn machine operation, or (2) a high level of randomness or sensitivity to the wire breakdown conditions in the experiments, or (3) a high level of sensitivity to the onset of the resistivity changes. In one shot, the total radiated yield was a factor of 2 larger than in the other two shots, and, in all three shots, significantly more energy was radiated than could be accounted for by conventional MHD resistivity theory.

In Sec. III, the problem of coupling circuit equations to fluid equations is investigated. Under the assumption that the fluid dynamics is one dimensional, we show that an analytic expression for the circuit resistance and inductance is derivable in terms of surface fluid quantities. The resistance is found to depend on both the surface resistivity and the surface current density of the pinch. Because increases in resistivity increase the rate of current diffusion, the current density at the surface, on which the energy coupling also depends, is lowered. Thus, the energy coupling problem is nonlinear, and MHD calculations are needed to quantitatively assess how increases in circuit resistance actually affect the fluid dynamics. These calculations are described in Sec. IV. Two of the problems investigated in Sec. IV concern (1) the time history of circuit resistance needed to approximately model the Saturn experiments and (2) the sensitivity of the calculations to variations of this time history.

The Saturn experiments manifest enhanced energy coupling because they produced enhanced x-ray outputs. Thus, fluid calculations must also demonstrate this capability. Some of the modeling issues that this energy channeling raises are investigated in Sec. IV. It is found that, under certain dynamical assumptions, the calculations can convert substantially all of the input energy into x rays, but not otherwise. Moreover, the x-ray pulses observed in the Saturn experiments, both as to their energy content and the presence or absence of sizable amounts of emission following the main x-ray pulse, are found to correlate well with the assumed behavior of the circuit resistance. Thus, the calculations serve to identify a variety of important issues related to the modeling of Z-pinch dynamics.

Finally, a formula for enhanced resistivity produced by the growth and saturation of a hybrid drift-wave instability<sup>13</sup> is tested in Sec. V by postprocessing the principal calculation described in Sec. IV. In this one case, the resistivity increases predicted by the formula do not support the resistivity assumptions that were made in the calculations. By a significant amount, they are neither large enough nor do they occur early enough to offer support to the resistivity assumptions

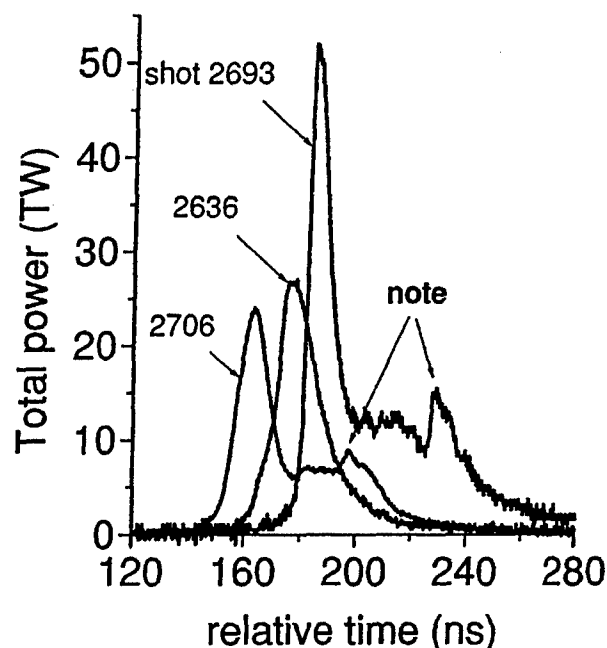


FIG. 1. Measured total x-ray output for the three identical shots identified in the figure. The measured times to peak power output were 163 ns for shot 2706, 162 ns for shot 2693, and 175 ns for shot 2636. However, the x-ray pulses have been slightly shifted in the figure relative to each other in order to make them more distinguishable.

that were built into the calculations. This work is then summarized in Sec. VI.

## II. EXPERIMENTAL DATA

Saturn generates sufficient current to drive large wire-number aluminum loads with small interwire gap spacings from radii of two or more centimeters when it is operated in a long current-rise time mode. Small gap spacings, in principle, allow plasma shells to form prior to wire implosion, and these shells implode with greater azimuthal symmetry than when gaps remain present during the run-in.<sup>14</sup> For the aluminum wire shots performed on Saturn in this long current-rise time mode of operation, a gap spacing that produced the most symmetric shell, and thus the most x-ray output, was first empirically determined. This was done by selecting a wire number that maximized the total x-ray power output from a series of aluminum wire experiments in which only the wire number and wire diameter of the arrays were varied while the array mass was kept fixed.<sup>3,4</sup> In these shots, the arrays were 2 cm long, 4 cm in diameter, each contained approximately 616  $\mu\text{g}/\text{cm}$ , and the wire numbers were 32, 56, 70, 126, 180, and 282. The highest x-ray power was obtained from the 180 wire load. This load was chosen for our 1D analysis since (1) the pinch had the largest compression and hence, it was the closest to 1D like, i.e., it had a minimum of wire array dynamics and (2) the short x-ray pulse minimized errors in inferring an implosion time. However, this power was highly variable. When the 180 wire shot was repeated two more times, large variations in the total x-ray power were observed (Fig. 1). The shots had nearly

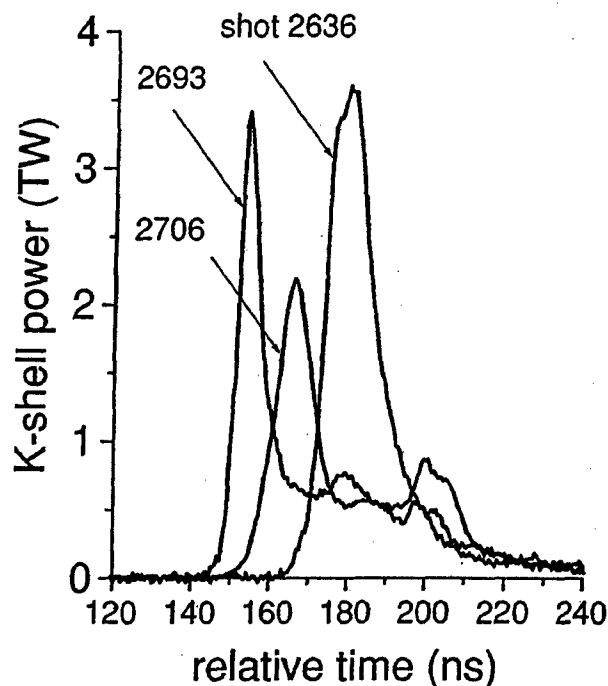


FIG. 2. Measured K-shell x-ray output for the same three identical shots as in Fig. 1. The measured times to peak K-shell power output were 165 ns for shot 2693, 163 ns for shot 2706, and 175 ns for shot 2636. The x-ray pulses have been shifted in the figure relative to each other in order to make them more distinguishable.

identical implosion times (to within 12 ns), but the x-ray pulses have been shifted in Fig. 1 for clarity. As seen in this figure, the peak x-ray intensity for shot 2693 was twice that measured in the other two shots, and the power pulse had a substantial late-time tail. Shot 2706 also had a late-time tail; however, shot 2636 did not. Similar variations in time were evident in the recorded K-shell emissions, which are shown in Fig. 2. The total x-ray powers in Fig. 1 are x-ray diode traces normalized to bare bolometer data to produce powers; likewise, the K-shell powers in Fig. 2 are photo-conducting detector (PCD) traces that were normalized to filtered bolometer data.

Running time integrations of the Fig. 1 powers, which are shown in Fig. 3, produced equally large variations in the total energy radiated, both during and after the main pulse. Twice the energy was radiated in shot 2693 than in the other shots, but half of this energy was late time. Shot 2706, on the other hand, had half the energy in its main pulse as shots 2693 and 2636, although eventually the same total amount of energy was radiated as in shot 2636. Approximately the same amount of energy ( $\sim 500$  kJ) was radiated in the main x-ray pulse of shot 2636 as in the main pulse of shot 2693, but shot 2636 produced essentially no late-time emission.

In some of the experiments, time-resolved pinhole cameras captured the dynamics of the on-axis plasma after the time of peak power. In Fig. 4, the total radiated and K-shell powers are plotted along with the K-shell emitting plasma diameter. After peak power, the on-axis plasma expands, while the x-ray emissions remain significant. In addition, time-resolved spectroscopy<sup>3</sup> would indicate that the plasma



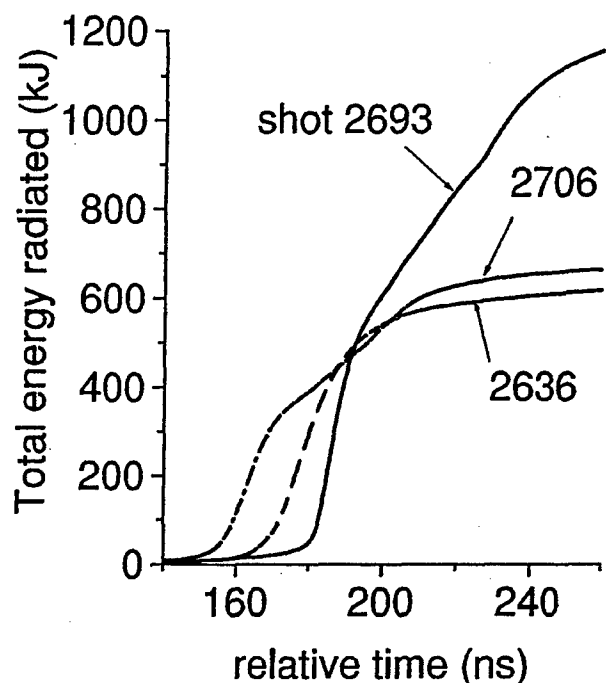


FIG. 3. The running time integrals for the three x-ray pulses shown in Fig. 1 are plotted as a function of the integration time.

electron temperature is relatively constant during this time. Also, based on the spectroscopic analysis, the estimated internal energy of the plasma is of the order of 1 kJ. At the measured 10 TW power level, this amount of internal energy is radiated in 0.1 ns. Clearly the plasma was being continuously heated on axis. The fact that the pinhole images indicate that the plasma was expanding (or in some shots, had a constant diameter) would indicate that gross plasma com-

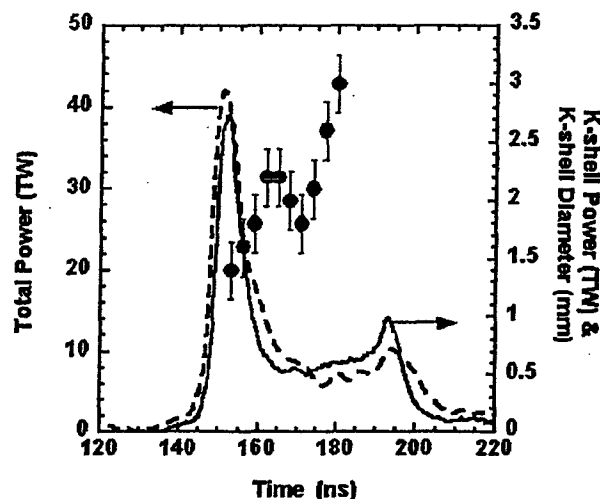


FIG. 4. The measured size of the K-shell emitting region at different times is plotted relative to the measured total and K-shell power outputs for Saturn shot 2633. The array in this shot was 40 mm in diameter and 2 cm in length; it contained 126 aluminum wires of 15.2  $\mu\text{m}$  diameter for a total array mass of 1235  $\mu\text{g}$ .

pression is not responsible for adding the radiated energy at late times.

Initially, when an analysis of Saturn shots 2636, 2693, and 2704 was carried out using a conventional 1D MHD calculation based on classically calculated transport coefficients<sup>15</sup> and the Saturn circuit model, 2–4 times more energy was found to be radiated in the experiments than had been supplied in the calculation. The large energies radiated in the experiments imply that even larger amounts of energy had coupled to the pinch. As our analysis will show, the pinches had to have higher impedances than conventional 1D calculations predict.

A direct measurement of impedance that was made in experiments conducted on the Tomsk IMRI-IV generator<sup>16</sup> had confirmed that large increases in resistivity, and therefore in energy coupling, had taken place late in the pinch implosion as it began to assemble on axis. The calculations described in Sec. IV of this paper are guided by this observation as well as by the x-ray data in Figs. 1–3. Large increases in the resistance of the plasma as seen by the circuit were introduced into these calculations slightly in advance of pinch assembly, and the turn-on time was taken to be relatively short in accord with the Tomsk experiments and with the Saturn x-ray data. How these resistance increases were made in the calculation is explained in the following section, where the problem of coupling a set of 1D fluid equations to a transmission line is examined and a formula relating the circuit resistance to the surface values of the plasma resistivity and current density is derived.

### III. ENERGY COUPLING THEORY

The coupling of pulsed-power generators to Z pinches is usefully addressed by separately considering the dynamics of the generator, the diode region, and the Z pinch. Maxwell's equations imply that transmission line energy couples to a pinch at its outer boundary. The location,  $b(z,t)$ , of this boundary as a function of time is, therefore, an important coupling parameter even though it may not be an easily definable, physical variable. Most theoretical analyses, however, assume it to be well defined. In a nonfluid, slug model description of Z-pinch implosions,<sup>17</sup> for example, the pinch boundary is the only variable employed. It is also an important variable in the definition of self-similar solutions, which are used in a variety of approximate hydrodynamics descriptions of Z-pinch dynamics.<sup>18–21</sup> It was also the important variable in a recent analysis of the free surface dynamics of an ideal fluid consisting of imploding wire-like plasmas.<sup>22</sup> It was used to describe the radiative collapse of hydrogen and helium Z pinches,<sup>23</sup> and it is the key variable in the original work of Bennett,<sup>24</sup> Pease,<sup>25</sup> and Braginskii<sup>26</sup> in their early treatment of Z-pinch equilibria. It is less well defined in more recent treatments of this problem, such as the work on gas-embedded Z pinches<sup>27</sup> or on Bennett equilibria as modified once microturbulence limits are set on the current flow.<sup>13</sup> Most importantly, the outer pinch boundary is sharply defined (minus the presence of coronal plasmas) in all MHD

computer calculations of Z-pinch plasma implosions, and it will be assumed to be equally well defined in the analysis that follows.

### A. Generator

The Saturn generator is a voltage-source driven transmission line in which electromagnetic energy flows to, couples to, and reflects from the Z-pinch load. Generally, however, the generator is modeled as a lumped circuit in which a voltage,  $V(t)$ , with a given (measured) time history drives a time varying inductance,  $L(t)$ , and a time varying resistance,  $R(t)$

$$\frac{d(LI)}{dt} + RI = V(t). \quad (1)$$

The inductance and the resistance are sums of time-independent line impedances and time-dependent load impedances:  $L(t) = L_{\text{line}} + L_{\text{load}}(t)$  and  $R(t) = R_{\text{line}} + R_{\text{load}}(t)$ .

The energy equation for this simple circuit equation is found by multiplying Eq. (1) through by  $I$

$$\begin{aligned} VI &= \frac{d}{dt} (U_B^{\text{line}} + U_B^{\text{diode}}) + \left( R_{\text{line}} + R_{\text{load}} + \frac{1}{2} \frac{dL_{\text{load}}}{dt} \right) I^2 \\ &= \frac{d}{dt} (U_B^{\text{line}} + U_B^{\text{diode}}) + R_{\text{line}} I^2 + P^{\text{load}}. \end{aligned} \quad (2)$$

Here,  $U_B^{\text{line}} \equiv (1/2) L_{\text{line}} I^2$  and  $U_B^{\text{diode}} \equiv (1/2) L_{\text{load}} I^2$  are the magnetic field energies stored in the transmission line and in the diode region between the pinch and return current circuitry, respectively. This equation describes how initially stored generator energy is converted into the growth of line and diode magnetic field energy, ohmic heating losses in the line, and a power flow into the Z-pinch load, as described by  $P^{\text{load}}$

$$P^{\text{load}} = \left( \frac{1}{2} \frac{dL_{\text{load}}}{dt} + R_{\text{load}} \right) I^2. \quad (3)$$

### B. Diode

The transmission line terminates at the Z-pinch diode. In principle, therefore, the diode's impedance is difficult to compute accurately, and it must be determined empirically. However, if it is assumed that the diode has perfect cylindrical symmetry and perfectly conducting walls, that the region between the pinch and the return current is a vacuum, and that displacement currents within the diode can be neglected, then an approximate evaluation of the electromagnetic fields in the diode can be made.<sup>28</sup> These fields are needed to determine the flow of electromagnetic energy into the diode and into the pinch, and thus, they relate to the load impedance. Under the above diode assumptions, Maxwell's equations can be solved subject to the boundary conditions that the current in the Z pinch,  $I(t)$ , and the voltage drop across the entry surface to the diode,  $V_p(t) \equiv -\int_b^{R_0} dr E_r(r, z=\ell)$ , are known functions of the time. The B field, in this case, has only an azimuthal component,  $B_\theta$ , which is determined by applying Stokes' theorem

$$\mathbf{B} = B_\theta \hat{u}_\theta = \frac{2I(t)}{cr} \hat{u}_\theta,$$

$$\text{for } b \leq r \leq R_0 \text{ and } 0 \leq z \leq \ell, \quad (4)$$

where the vacuum diode geometry is defined by:  $b$ , the outer boundary of the pinch,  $R_0$ , the radius of the diode region and of the return current path, and  $\ell$ , both the length of the plasma and the diode region. Maxwell's equations then require that the E field has a component along the  $z$  direction of the pinch,  $\hat{u}_z$ , and one along the radial direction,  $\hat{u}_r$ :  $\mathbf{E} = E_r \hat{u}_r + E_z \hat{u}_z$ , where (from Ref. 25)

$$\begin{aligned} E_r &= -\frac{V_p}{\ell \ln[R_0/b(t)]} \frac{z}{r} < 0, \\ E_z &= \left( \frac{V_p}{\ell \ln[R_0/b(t)]} - \frac{2I}{c^2} \right) \ln(R_0/r) > 0 \end{aligned} \quad (5)$$

and  $I \equiv \partial_t I$ . Since the walls of the return current path have infinite conductivity, the voltage drop across the entrance to the diode region also appears as a voltage drop across the load. The full voltage drop  $\int dz E_z(r=b, z)$  across the load, however, includes a back electromotive force and is given by

$$\int_0^\ell dz E_z(r=b, z) = V_p - \frac{2\ell}{c^2} \ln(R_0/b) \dot{I} = V_p - L_{\text{load}} \dot{I}, \quad (6)$$

where

$$L_{\text{load}} = \frac{2\ell}{c^2} \ln\left(\frac{R_0}{b(t)}\right). \quad (7)$$

The neglect of the displacement current is based on the assumption that the electric field energy density,  $u_E^{\text{diode}} \equiv E^2/(8\pi)$ , is negligible relative to  $u_B^{\text{diode}} \equiv B^2/(8\pi)$  in the diode. In this case, energy conservation is expressed locally by  $\partial_t u_B^{\text{diode}} + \nabla \cdot \mathbf{S} = 0$ , where  $\mathbf{S}$  is the Poynting vector,  $\mathbf{S} = [c/(4\pi)] \mathbf{E} \times \mathbf{B}$ ; an integration of this equation over the volume of the diode region then yields a global equation for energy conservation of the form

$$P^{\text{diode}} = \partial_t U_B^{\text{diode}} + P^{\text{load}} + P^{\text{wall}}, \quad (8)$$

where  $P^{\text{diode}}$  is the energy flux into the diode across its entry surface at  $z = \ell$

$$\begin{aligned} P^{\text{diode}} &= - \int_{\text{surface}} dA \mathbf{S} \cdot \hat{u}_z \\ &= - \int_b^{R_0} 2\pi r dr \frac{c}{4\pi} [E_r(r, z=\ell) B_\theta(r)] = V_p I \end{aligned} \quad (9)$$

and

$$U_B^{\text{diode}}(t) \equiv 2\pi \int_0^\ell dz \int_{b(t)}^{R_0} dr r u_B^{\text{diode}} = \frac{1}{2} L_{\text{load}}(t) I^2. \quad (10)$$

Power losses into the return current walls,  $P^{\text{wall}}$ , are found by integrating the Poynting flux over the walls of the return current can. They are zero in this analysis (because perfectly conducting return current walls were assumed) but not necessarily in experiments. Power flow into the Z pinch,

$P^{\text{load}}$ , has two parts, one coming from an integration of the Poynting flux across the surface of the pinch,  $P^L$ , and the other, from the magnetic field energy density, or pressure, acting on the moving boundary of the pinch

$$P^{\text{load}} = 2\pi b \dot{b} \ell \frac{[B_\theta(r=b)]^2}{8\pi} + P^L = -\frac{1}{2} \frac{dL_{\text{load}}}{dt} I^2 + P^L, \quad (11)$$

where  $\dot{b} \equiv \partial_t b$ .  $P^{\text{load}}$  cannot be determined from this diode analysis alone. The fields of Eqs. (4) and (5) satisfy Eq. (8) tautologically. To determine  $P^{\text{load}}$ , one must turn to an analysis of the plasma fluid equations, which govern the main characteristics of an idealized Z-pinch dynamics, i.e., of the dynamics that begin after the wires have broken down and plasma has fully formed.

### C. Z-pinch fluid theory

Z pinches have been described by one-, two-, or three-dimensional fluid dynamic models, which must, in each case, be coupled to a generator circuit equation self-consistently. Plasmas contain four kinds of fluid energy: kinetic,  $u_{\text{KE}} \equiv (1/2)\rho v_f^2$ , ion thermal,  $u_{\text{th}}^i \equiv (3/2)n_i k_B T_i$ , electron thermal,  $u_{\text{th}}^e \equiv (3/2)n_e k_B T_e$ , and an internal energy of ionization and excitation,  $u_{\text{ion}}$ . The full set of fluid equations describe the various ways that these energies are either partitioned within the plasma or radiated away. Their coupling to a circuit equation is carried out so as to maintain power flow continuity and overall energy conservation. However, while fluid dynamic models are much more detailed than a 0D model; they are nevertheless idealized and approximate as well, since, as noted, they do not treat the early-time dynamics by which solid wires explode, break down, and become plasmas or by which gases break down. In addition, computer solutions to fluid equations are resolution limited.

Equations that describe the buildup and decay of electron and ion energy densities are derivable directly by taking energy moments of the electron and ion kinetic equations<sup>15</sup>

$$\partial_t u_{\text{Tot}}^e + \nabla \cdot (u_{\text{Tot}}^e \mathbf{v}_e + \mathbf{P}_e \cdot \mathbf{v}_e + \mathbf{q}_e) = -n_e e \mathbf{E} \cdot \mathbf{v}_e + Q_e + \mathbf{R}_{ei} \cdot \mathbf{v}_e + Q_e^{\text{inel}} - p_{\text{brems}}, \quad (12)$$

$$\partial_t u_{\text{Tot}}^i + \nabla \cdot (u_{\text{Tot}}^i \mathbf{v}_i + \mathbf{P}_i \cdot \mathbf{v}_i + \mathbf{q}_i) = n_i Z e \mathbf{E} \cdot \mathbf{v}_i + Q_i + \mathbf{R}_{ie} \cdot \mathbf{v}_i, \quad (13)$$

where  $u_{\text{Tot}}^e \equiv 1/2 \rho_e v_e^2 + u_{\text{th}}^e$  is the sum of electron kinetic and thermal energies,  $\mathbf{v}_e$  is the electron fluid velocity,  $\mathbf{P}_e \equiv p_e \mathbf{I}_2 + \Pi_e$  is the electron pressure tensor,  $\mathbf{q}_e$  is the electron heat flux vector,  $\mathbf{E}$  is the electric field,  $Q_e$  is the elastic-collision energy transfer rate between electrons and ions,  $\mathbf{R}_{ei}$  is the elastic-collision momentum transfer rate between electrons and ions,  $Q_e^{\text{inel}}$  is the inelastic-collision energy transfer rate between electrons and ions, and  $p_{\text{brems}}$  is the bremsstrahlung energy loss rate. The quantities,  $u_{\text{Tot}}^i$ ,  $\mathbf{v}_i$ ,  $\mathbf{P}_i \equiv p_i \mathbf{I}_2 + \Pi_i$ ,  $\mathbf{q}_i$ ,  $Q_i$ , and  $\mathbf{R}_{ie}$  are similarly defined for the ions. The term,  $Q_e^{\text{inel}}$ , describes the rate of increase in the ion excitation and ionization energy density,  $u_{\text{ion}}$ , which is given by

$$\partial_t u_{\text{ion}} + \nabla \cdot (u_{\text{ion}} \mathbf{v}_i) = Q_e^{\text{inel}} - p_\ell - p_\pi. \quad (14)$$

Here  $p_\ell$  and  $p_\pi$  are line and recombination radiation energy density loss rates, respectively.

The fluid equations of a plasma are defined in terms of locally defined center of mass and relative (or drift) velocities,  $\mathbf{v}_f$  and  $\mathbf{v}_d$ , respectively, in terms of which the electron and ion fluid velocities are given by

$$\mathbf{v}_e = \mathbf{v}_f + \frac{\rho_i}{\rho} \mathbf{v}_d \equiv \mathbf{v}_f + \mathbf{v}_d, \quad \mathbf{v}_i = \mathbf{v}_f - \frac{\rho_e}{\rho} \mathbf{v}_d \equiv \mathbf{v}_f, \quad (15)$$

where  $\rho \equiv \rho_e + \rho_i \equiv \rho_i$ . An equation describing total energy conservation can then be derived in terms of  $\mathbf{v}_f$  and  $\mathbf{v}_d$  by adding Eqs. (12) and (13) and using the condition,  $Q_e + \mathbf{R}_{ei} \cdot \mathbf{v}_e = -Q_i - \mathbf{R}_{ie} \cdot \mathbf{v}_i$ , for energy conservation in elastic collisions

$$\partial_t u_{\text{Tot}} + \nabla \cdot (u_{\text{Tot}} \mathbf{v}_f + \mathbf{P} \cdot \mathbf{v}_f + \mathbf{q} + u_{\text{Tot}}^e \mathbf{v}_d + \mathbf{P}_e \cdot \mathbf{v}_d) = \mathbf{j} \cdot \mathbf{E} - p_{\text{rad}}, \quad (16)$$

where,  $u_{\text{Tot}} \equiv u_{\text{Tot}}^e + u_{\text{Tot}}^i + u_{\text{ion}}$ ,  $\mathbf{q} \equiv \mathbf{q}_e + \mathbf{q}_i$ ,  $\mathbf{j} \equiv -n_e e \mathbf{v}_d$  is the electric current density, and  $p_{\text{rad}} \equiv p_\ell + p_\pi + p_{\text{brems}}$  is the total radiation loss rate.

The plasma couples to the electromagnetic field by way of the  $\mathbf{j} \cdot \mathbf{E}$  term in Eq. (16), which also appears in the energy equation derived from Maxwell's equations. Since displacement currents are small in a plasma, the left hand side of this equation has the same form as the energy equation in the diode

$$\partial_t u_B^{\text{pl}} + \nabla \cdot \mathbf{S}^{\text{pl}} = -\mathbf{j} \cdot \mathbf{E}, \quad (17)$$

where  $u_B^{\text{pl}} \equiv B^2/(8\pi)$  is the magnetic field energy density stored within the plasma. Finally, the addition of Eq. (17) to Eq. (16) produces an equation expressing local total energy conservation

$$\partial_t (u_{\text{Tot}} + u_B^{\text{pl}}) + \nabla \cdot (u_{\text{Tot}} \mathbf{v}_f + \mathbf{P} \cdot \mathbf{v}_f + \mathbf{q} + u_{\text{Tot}}^e \mathbf{v}_d + \mathbf{P}_e \cdot \mathbf{v}_d + \mathbf{S}^{\text{pl}}) = -p_{\text{rad}}. \quad (18)$$

The coupling of the plasma fluid to the generator is now accomplished by integrating Eq. (18) over the volume of the plasma. The resulting equation connects the buildup of energy within the plasma to the flow of energy into the plasma from the diode

$$P^{\text{load}} = \frac{d}{dt} (U_{\text{Tot}}^{\text{pl}} + U_B^{\text{pl}}) + P_{\text{rad}} \quad (19)$$

and thus to the flow of energy into the diode from the generator when combined with Eq. (8), where

$$U_{\text{Tot}}^{\text{pl}} = 2\pi \int_0^\ell dz \int_0^{b(z)} r dr u_{\text{Tot}} \quad (20)$$

and  $U_B^{\text{pl}}$  and  $P_{\text{rad}}$  are similarly defined integrations over  $u_B^{\text{pl}}$  and  $p_{\text{rad}}$ , respectively.

When the surface of the integration volume is taken to lie just inside of the plasma boundary, the fluid variables are nonzero and, in particular, the electric field satisfies an Ohm's law, which, in a cylindrically symmetric plasma, is given by

$$E_z = -\frac{v_f}{c} B_\theta + \frac{1}{n_e e} \left\{ \alpha_\perp \frac{j_z}{n_e e} + \beta_\Lambda \partial_r (k_B T_e) \right\} \Big|_{r=b-\epsilon} \quad (21)$$

Then, because

$$2\pi \int_0^\ell dz \int_0^{b(r)} dr r \{ \partial_r (u_{\text{Tot}}^p) + \nabla \cdot (u_{\text{Tot}}^p \mathbf{v}_f) \} = \frac{dU_{\text{Tot}}^p}{dt} \quad (22)$$

and because the current flows parallel to the surface of the integration volume, whose normal is in the radial direction, it follows from Eqs. (18) and (19) that

$$\begin{aligned} & \frac{d}{dt} (U_{\text{Tot}}^p + U_B^p) + P_{\text{rad}} \\ &= \lim_{\epsilon \rightarrow 0+} \left[ +2\pi b \dot{b} \ell \frac{B_\theta^2}{8\pi} \right. \\ & \quad \left. -2\pi b \ell \left( q_r + (\mathbf{P} \cdot \mathbf{v}_f)_r - \frac{c}{4\pi} E_z B_\theta \right) \right] \Big|_{r=b-\epsilon} \quad (23) \end{aligned}$$

Taken together, therefore, Eqs. (3), (19), and (23) imply that

$$\begin{aligned} P_{\text{load}} &= \left( \frac{1}{2} \frac{dL_{\text{load}}}{dt} + R_{\text{load}} \right) I^2 \\ &= + \lim_{\epsilon \rightarrow 0+} \left[ 2\pi b \dot{b} \ell \frac{B_\theta^2}{8\pi} \right. \\ & \quad \left. -2\pi b \ell \left( q_r + (\mathbf{P} \cdot \mathbf{v}_f)_r - \frac{c}{4\pi} E_z B_\theta \right) \right] \Big|_{r=b-\epsilon} \quad (24) \end{aligned}$$

Equation (24) can be used to determine  $R_{\text{load}}$  and  $L_{\text{load}}$  provided that the plasma boundary is located where pressure forces make a negligible contribution to the equation. On physical grounds,  $q_r$  is strictly zero at the plasma outer surface; however, one cannot, in principle, set the surface pressure to zero unless one sets  $n_e = 0$  and  $n_i = 0$ . However, the current density would then go to zero unless one allows  $v_d$  at the surface to become infinitely large. In Ref. 13, it is this behavior that argues for the growth of microinstabilities and anomalous resistivity near to and at the plasma surface. This behavior also illustrates one of the ambiguities associated with producing a physically meaningful definition of an outer Z-pinch boundary. However, on setting  $(\mathbf{P} \cdot \mathbf{v}_f)_r = 0$ , one finds first that

$$\begin{aligned} & \frac{1}{2} \frac{dL_{\text{load}}}{dt} I^2 + R_{\text{load}} I^2 \\ &= + \lim_{\epsilon \rightarrow 0+} \left[ 2\pi b \dot{b} \ell \left( \dot{b} \frac{B_\theta^2}{8\pi} - \frac{c}{4\pi} E_z B_\theta \right) \right] \Big|_{r=b-\epsilon}; \quad (25) \end{aligned}$$

then, on substituting Eqs. (4) and (21) into this equation, one infers that

$$\frac{dL_{\text{load}}}{dt} = -\frac{2\ell}{c^2 b} \frac{db}{dt} \quad (26)$$

and

$$R_{\text{load}} I^2 = 2\pi b \ell \left\{ \frac{I}{2\pi b} \frac{1}{n_e e} \left[ \alpha_\perp \frac{j_z}{n_e e} + \beta_\Lambda \partial_r (k_B T_e) \right] \right\} \Big|_{r=b} \quad (27)$$

Equation (26) for  $L_{\text{load}}$  is consistent with Eq. (7), while Eq. (27) can be used to express  $R_{\text{load}}$  in a more physically meaningful form through the definition, first of all, of two areas,  $A_j$  and  $A_{\text{th}}$ , and a thermal velocity,  $v_{\text{th}}$

$$A_j \equiv \frac{I}{j_z(r=b)}, \quad A_{\text{th}} \equiv \frac{I}{j_{\text{th}}(r=b)}, \quad v_{\text{th}} \equiv \sqrt{2k_B T_e / m}, \quad (28)$$

and then, of a thermal current density

$$j_{\text{th}} \equiv n_e e v_{\text{th}} \equiv n_e e \sqrt{2k_B T_e / m}, \quad (29)$$

dimensionless transport coefficients,  $\hat{\alpha}_\perp$  and  $\hat{\beta}_\Lambda$ , by Ref. 15

$$\alpha_\perp = \frac{m n_e}{\tau_e} \hat{\alpha}_\perp, \quad \beta_\Lambda = n_e \hat{\beta}_\Lambda \quad (30)$$

and a dimensionless temperature gradient

$$x_{\text{tr}} \equiv \frac{v_{\text{th}} \tau_e}{T_e} \partial_r T_e \Big|_{r=b} \quad (31)$$

One then finds that

$$R_{\text{load}} = \left\{ \frac{\ell \hat{\alpha}_\perp \eta_0}{A_j} + \frac{1}{2} x_{\text{tr}} \hat{\beta}_\Lambda \frac{\ell \eta_0}{A_{\text{th}}} \right\} \Big|_{r=b}, \quad (32)$$

where the resistivity,  $\eta_0$ , is defined by<sup>15</sup>

$$\eta_0 \equiv m / (n_e e^2 \tau_e). \quad (33)$$

The Eq. (32) expression for  $R_{\text{load}}$  has an added benefit: it guarantees the continuity of  $E_z$  across the pinch boundary. Thus, one finds, on combining Eqs. (4), (6), and (21), that

$$\begin{aligned} E_z(r=b+\epsilon) &= \frac{1}{\ell} (V_p - L_{\text{load}} \dot{I}) \\ &= -\frac{\dot{b}}{c} \left( \frac{2I}{cb} \right) + \frac{1}{n_e e} \left[ \alpha_\perp \frac{j_z}{n_e e} \right. \\ & \quad \left. + \beta_\Lambda \partial_r (k_B T_e) \right] \Big|_{r=b-\epsilon} \\ &= E_z(r=b-\epsilon). \quad (34) \end{aligned}$$

Using Eq. (26), this equation can be rewritten as

$$V_p = \frac{d}{dt} (L_{\text{load}} I) + \frac{1}{n_e e} \left[ \alpha_\perp \frac{j_z}{n_e e} - \beta_\Lambda \partial_r (k_B T_e) \right] \Big|_{r=b} \quad (35)$$

However, by definition of  $V_p$ , the circuit equation [Eq. (1)] can also be rewritten as

$$V(t) = L_{\text{inc}} \frac{dI}{dt} + R_{\text{inc}} I + V_p, \quad (36)$$

which identifies  $V_p$  as

$$V_p = \frac{d}{dt} (L_{\text{load}} I) + R_{\text{load}} I. \quad (37)$$

The comparison of Eq. (35) with Eq. (37) provides an expression for  $R_{\ell\text{oad}}$  that is identical to Eq. (32).

Finally, a third expression for  $R_{\ell\text{oad}}$  can be derived, which provides an important check on the accuracy of Z-pinch fluid dynamics calculations when it is compared to the calculation of  $R_{\ell\text{oad}}$  from Eq. (32). To obtain this expression, one integrates Eq. (17) over the volume of the Z-pinch plasma to find [using Eq. (11)] that

$$\frac{dU_B^{\ell}}{dt} - P^{\ell\text{oad}} = -2\pi\ell \int_0^{b(n)} r dr j_z E_z. \quad (38)$$

One can then substitute Eq. (3) into Eq. (38) and solve for  $R_{\ell\text{oad}}$

$$R_{\ell\text{oad}} = \frac{1}{I^2} \left\{ \frac{dU_B^{\ell}}{dt} + 2\pi\ell \int_0^{b(n)} r dr j_z E_z \right\} - \frac{1}{2} \frac{dL_{\ell\text{oad}}}{dt}. \quad (39)$$

In this equation, the volume integral over  $j_z E_z = \mathbf{j} \cdot \mathbf{E}$  includes both  $\mathbf{v}_j \cdot \mathbf{j} \times \mathbf{B}$  work and ohmic heating by virtue of Ohm's law [Eq. (21)].

#### IV. MHD MODELING

The number of approximations built into the above analysis indicates the phenomenological nature of Z-pinch modeling (even when computers are used to solve sets of nonlinearly coupled, energy conserving circuit and fluid equations). It is not to be found entirely surprising, therefore, when such calculations contain insufficient resistive coupling to reproduce the energy coupling inferable from the Saturn experiments. Based on the above analysis, this coupling deficiency can be overcome in 1D modeling through the introduction of an additional (anomalous) surface resistivity

$$\alpha_{\perp} \eta_0|_{r=b} \rightarrow \alpha_{\perp} \eta_0|_{r=b} + \eta_{\text{Anomalous}}|_{r=b}. \quad (40)$$

The magnitude and temporal characteristics of  $\eta_{\text{Anomalous}}$  within the plasma, however, are not determined by coupling considerations; they must be inferred indirectly, if possible, from the influence that  $\eta_{\text{Anomalous}}$  has on the stagnation dynamics of a Z pinch and from the ability of this dynamics to replicate the x-ray output trends seen in experimental data. In this section, some results are presented from a phenomenological study of the Saturn data contained in Figs. 1–3 within the context of 1D MHD calculations.

This study addressed issues such as: how much energy actually couples to a pinch when prescribed additions to the circuit resistance are made, how large an increase in circuit resistance is needed in order to double the amount of coupled energy, when and how rapidly can this resistance be applied during the course of the implosion, how sensitive is the calculation to variations in the required enhanced resistivity, and, finally, what rate of energy transport is required within a plasma for enhanced energy inputs to show up as enhanced x-ray outputs? These questions were investigated within the context of a 1D radiative hydrodynamics calculation by (1) specifying a functional form for the anomalous circuit resistance, (2) varying the parameters of the functional form, and (3) comparing the calculated x-ray emission to the experimental x-ray pulses shown in Fig. 1.

One learns by this procedure that the circuit resistance cannot be sizably increased until the pinch nears assembly since otherwise observable amounts of soft x rays are emitted earlier than when they are seen experimentally. This finding is consistent with the impedance measurement reported in Ref. 16. One also finds limits on the rate at which energy can be coupled effectively to the plasma because of the large impact that this rate has on the hydrodynamics. These limits are set by both the rate at which energy is transported into the plasma and on the rate at which it is radiated from the plasma. Only when these two rates are sufficiently large does the calculated x-ray output move in the direction of the data presented in Figs. 1–3.

The calculations described in this section were computer intensive; the aluminum model contained 136 energy levels, 22 K-shell states, 77 L-shell states, 125 K-shell lines, and 202 L-shell lines, and the calculations employed a tabular lookup, escape probability method to carry out both the kilovolt and subkilovolt photon transport.<sup>29</sup> Nevertheless, 77 states do not provide an accurate description of the multiplet structure of the L-shell ionization stages; thus, L-shell emissions are not as accurately transported within the plasma as they should be. The transport of soft x rays is more diffusive than that of kilovolt x rays, making escape probability methods more appropriate for kilovolt emissions than subkilovolt. For this reason, two parameters were introduced into our calculations in order to phenomenologically increase and vary the rates of soft x-ray energy transport and partially compensate for the missing atomic structure. A multiplier,  $\alpha$ , on the electron heat flux was introduced as a way of approximately simulating the influence of soft x-ray diffusive transport on the pinch dynamics, and a multiplier,  $\beta$ , was included in the calculation of L-shell emissivities to compensate for missing distributions of L-shell oscillator strength.

In all, four modifications to the MHD were made in this investigation of enhanced energy coupling. The load impedance, the rate of diffusive energy transport, and the rate of soft x-ray emission were all increased as described above. In addition, the value of the anomalous resistivity was specified throughout the plasma. For lack of specific theoretical guidance, we assumed a fixed, gradual, linear reduction (by roughly two orders of magnitude from its surface value) in the value of  $\eta_{\text{Anomalous}}$  throughout the plasma interior. By this assumption, resistivity levels remained anomalously high throughout the plasma, which produced increases in the rate of magnetic field and current diffusion and, therefore, in the amount of ohmic heating interior to the plasma. The impact that this resistivity assumption had on x-ray conversion efficiencies was, therefore, positive, since it aided in the energy transport into the plasma, i.e., any steepening of the resistivity gradient at the surface of the pinch only serves to reduce the degree of current diffusion and ohmic heating within the plasma. Energy must then be transported by secondary means into the plasma (by pressure forces, electron heat conduction, or soft x-ray transport) in order to be radiated efficiently. The impact that varying the resistivity profile has on the calculations was not addressed in this work. The resistivity was reduced from zone to zone as described above, and

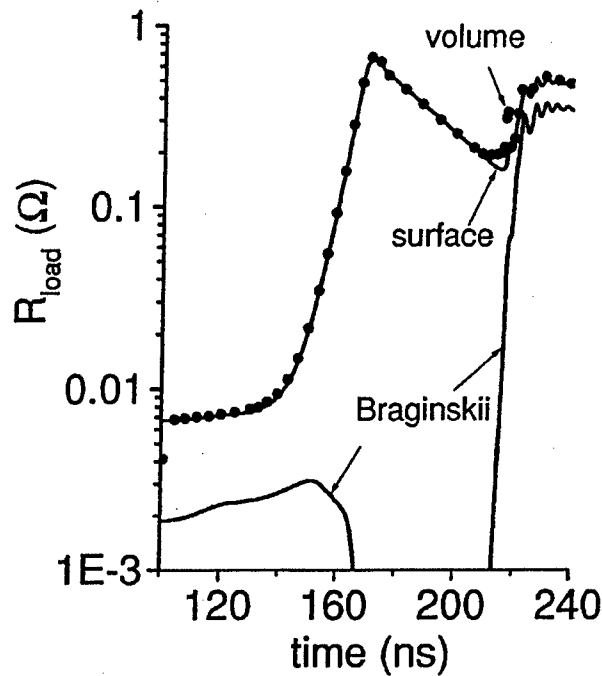


FIG. 5. A circuit resistance, which produces a comparable energy coupling as seen experimentally, is plotted as a function of time. It consists of a part derived from Eq. (32), using Braginskii's formula for electrical resistivity, and another part that is prescribed. The dotted points represent the circuit resistance that was calculated using Eq. (39).

this contouring was then kept the same in all of our calculations.

By applying the above phenomenology, we were able to replicate several important features of the Figs. 1–3 Saturn data. For example, when the resistance time history shown in Fig. 5 was employed in a 100 zone 1D calculation, it produced the total x-ray output pulse shown in Fig. 6. This pulse approximates both the early- and late-time features of the x-ray pulses shown in Fig. 1. The heat flux multiplier,  $\alpha$ , had a value of 600 and  $\beta$ , a value of 3 in this calculation. The sensitivity of the calculation to, and the validity of, the  $\alpha$  value used are discussed later in this section. The resistance in Fig. 5 is composed of two parts. One (labeled Braginskii in the figure) was calculated from the surface value of the classical resistivity,  $\hat{\alpha}_1 \eta_0$ , using Eq. (33), while the other was a prescribed input to the calculation. The prescribed resistance was taken to rise exponentially with a rise time of 5 ns, to peak at 172 ns at a value of 0.658  $\Omega$ , and to fall exponentially with a fall time of 30 ns. The surface value of  $\eta_{\text{Anomalous}}$  that was used in the fluid equations was calculated from the prescribed resistance using Eqs. (32) and (40).

Because the circuit resistance had an extended decay, a substantial amount of energy coupled to the plasma following the main x-ray pulse, and this late-time coupling produced the foot (or tail) to the main pulse seen in Fig. 6. The emission spike at the end of the tail was produced by a secondary, late-time implosion, an event often seen in 1D calculations. In this instance, the presence of this spike correlates with the more subdued late-time spiking seen in the x-ray pulses of the (3D) shots 2693 and 2706 (and noted in

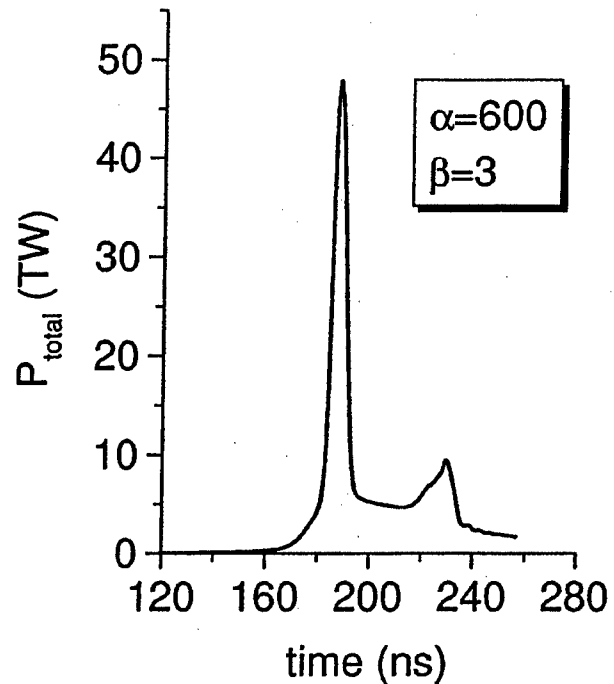


FIG. 6. Total x-ray pulse calculated using the circuit resistance shown in Fig. 5. The multipliers on heat conductivity and L-shell emissivity that were used in the calculation are listed in the figure.

Fig. 1). In this 100 zone, fiducial calculation, 671 kJ coupled to the pinch in 245 ns; 369 kJ of this coupled energy was emitted in the main x-ray pulse, and 292 kJ, in the tail. Overall, therefore, 661 of the 671 kJ input was radiated. It was divided into 143 kJ of kilovolt and 518 kJ of subkilovolt emissions. Thus, in the 245 ns time interval over which the calculation was performed substantially all of the energy that coupled to the pinch was radiated, and it had to be in order to be comparable to the total x-ray output measured in shots 2636 and 2706 (Fig. 3). For the calculation to produce this result, however, a nearly three order of magnitude increase in the circuit resistance was needed, in agreement with the resistance increases predicted by the 0D calculations described in Ref. 30. Finally, we note that, while a comparable amount of energy coupled to the pinch in this calculation as in the experiments, there was much less K-shell emission (by a factor  $\sim 2.5$ ) in the experiments than in the calculation. Moreover, the calculated K-shell pulse had less late-time structure than was seen experimentally in shots 2693 and 2706 (Fig. 2).

Figure 5 contains two plots of  $R_{\text{load}}(t)$ . The one labeled surface calculation was obtained from Eqs. (32) and (40) with  $\eta_{\text{Anomalous}}$  derived from the prescribed part of  $R_{\text{load}}$ . The dotted curve, labeled volume calculation, was calculated from Eq. (39). When these two calculations are in close agreement at a given time, they indicate that an accurate spatial integration of the magnetic field diffusion equation has been carried out at that time. This accuracy depends on the zoning in the calculation, and deviations between the curves temporarily occurred in the calculation late in time because irregular spacings between zones had been gener-

ated within the Lagrangian fluid dynamics. Thus, the quality of the agreement between the surface and volume calculated values of  $R_{\text{load}}$  (which was generally excellent for all of the calculations described in this section) can be degraded when the number of zones used in the calculation is too small or when their spacing becomes too irregular.

The above, fiducial, calculation was constructed so that the MHD would couple, transport, and radiate energy at comparable rates, and thus, retard expansion of the plasma following stagnation. Under these conditions, the plasma continues to radiate while the coupling remains strong, producing a tail on the x-ray pulse as seen in Fig. 6. On the other hand, when the enhanced resistance is taken to fall as fast as it rises (by replacing the resistance of Fig. 5 by a comparably fast rising and falling Gaussian pulse, for example), only a single x-ray pulse is generated, similar to the one observed in shot 2636 (Fig. 1). X-ray emission cuts off once the energy coupling enhancements are terminated. In this case, the inductive coupling between pinch and diode is reversed as the pinch maintains an outward expansion following assembly.

The x-ray emission generated in this fiducial calculation depended critically on four parameters: the magnitude of the heat flux multiplier, the magnitude of the L-shell emissivity multiplier, the maximum value of  $R_{\text{load}}$ , and the time relative to plasma assembly at which  $R_{\text{load}}$  achieved its maximum value. We determined the sensitivity of the calculation to each of these parameters, therefore, by varying each parameter in turn about the value it had in the fiducial calculation. The effects of these single parameter variations on energy coupling and x-ray output are presented in Figs. 7–15.

In order to determine the dependence of x-ray production on the strength of diffusive energy transport, a physically based range over which  $\alpha$  can be varied needed to be determined. This was done by comparing the heat flux,  $q_{\text{rad}} = -\kappa_R \partial_r T_e$ , due to blackbody radiation to the electron heat flux,  $q_e = -\kappa_e \partial_r T_e$ , where  $\kappa_e = \hat{\kappa}_e (n_e k_B^2 T_e \tau_e) / m_e$  and  $\kappa_R = 16\sigma T_e^3 / (3\rho K_R)$ . Here,  $\hat{\kappa}_e$  is a dimensionless transport coefficient,<sup>15</sup>  $\rho$  is the plasma density,  $\sigma$  is the Stefan-Boltzmann constant, and  $K_R$  is the Rosseland mean opacity per unit mass density. The Rosseland mean for aluminum was recently calculated<sup>31</sup> and found to have values ranging between  $10^3$  and  $10^4$  cm<sup>2</sup>/g at the plasma densities and temperatures that were present in our calculations prior to Z-pinch assembly. When employed in our calculations, these temperature and density values predicted blackbody heat fluxes that were more than four orders of magnitude larger than the electron heat flux. Consequently, we varied  $\alpha$  up to values of 2000.

In all the calculations in which  $\alpha$  was varied, the energy that coupled to the pinch in 200 ns was only slightly affected, ranging narrowly between 500 and 550 kJ. The ability of the plasma to radiate this energy, however, depended sensitively on its ability to conduct the coupled energy into its interior. The three energy curves shown in Figs. 7 and 8 demonstrate this point. The curve labeled 180 ns in Fig. 7 shows the total x-ray energy radiated in the main pulse, which terminated at 180 ns in these calculations. The other curves in Figs. 7 and 8 show how the total and K-shell x-ray outputs varied, re-

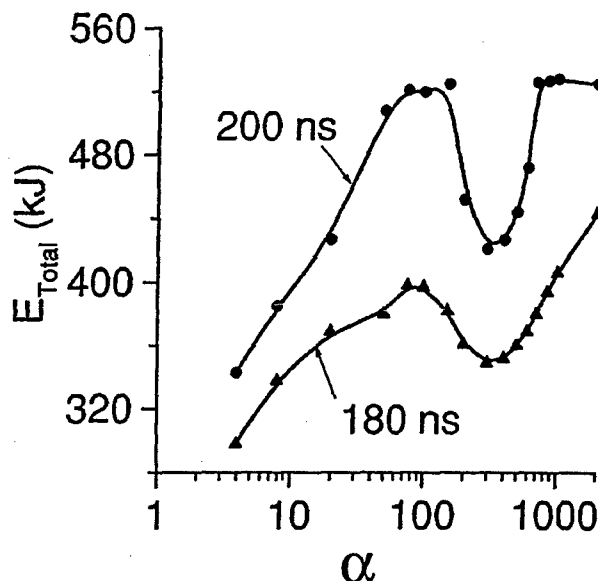


FIG. 7. The variation in the total energy radiated in 180 ns (in the main pulse) and in 200 ns as a function of the heat flux multiplier. The circuit resistance and  $\beta$  multiplier are the same as in Figs. 5 and 6. Spline fits are drawn to the calculated points.

spectively, over a 200 ns period. At first, the total emission rises as more energy is conducted into the plasma, but then it falls because sufficient energy has been conducted inwards to ionize the plasma into He-like ground states. At this point,

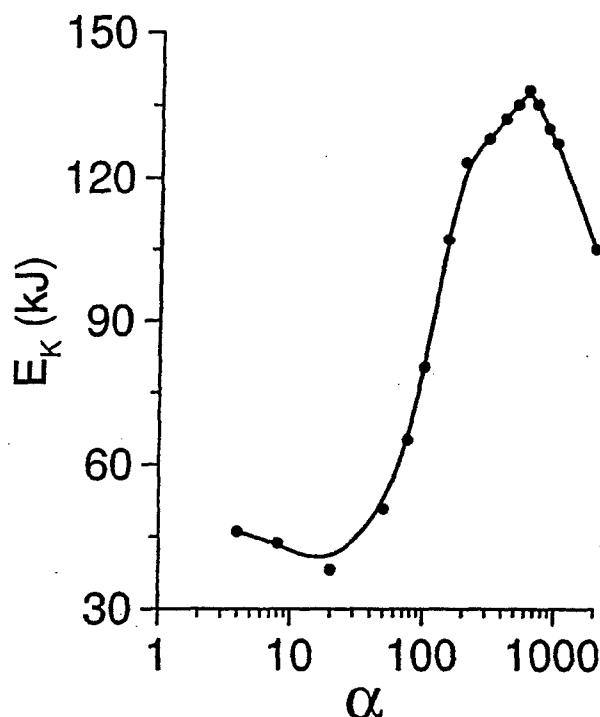


FIG. 8. The variation in the K-shell energy radiated in 200 ns as a function of the heat flux multiplier. The circuit resistance and  $\beta$  multiplier are the same as in Figs. 6 and 7. The calculated K-shell pulse had negligible amounts of emission following the main pulse. A spline fit is drawn to the calculated points.

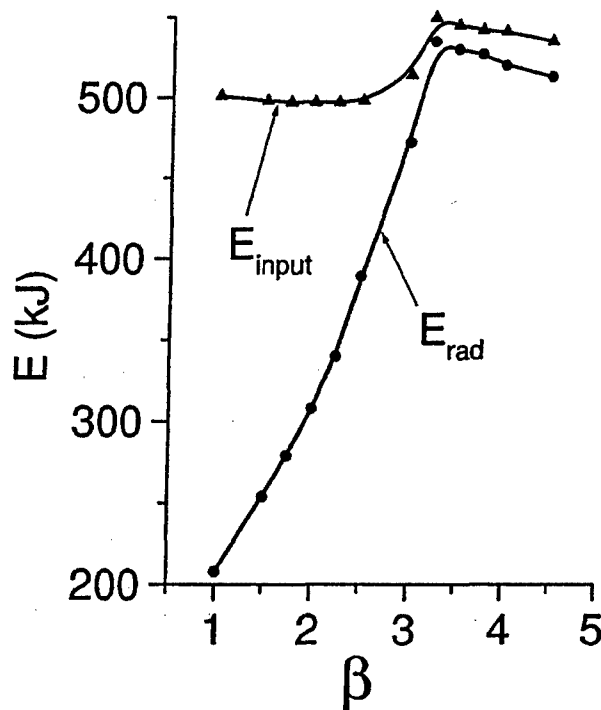


FIG. 9. Variations in the total energy coupled to the pinch and in the total energy radiated from the pinch in 200 ns are shown as a function of the L-shell emissivity multiplier. The circuit resistance and  $\alpha$  multiplier are the same as in Figs. 5 and 6. Spline fits are drawn to the calculated points.

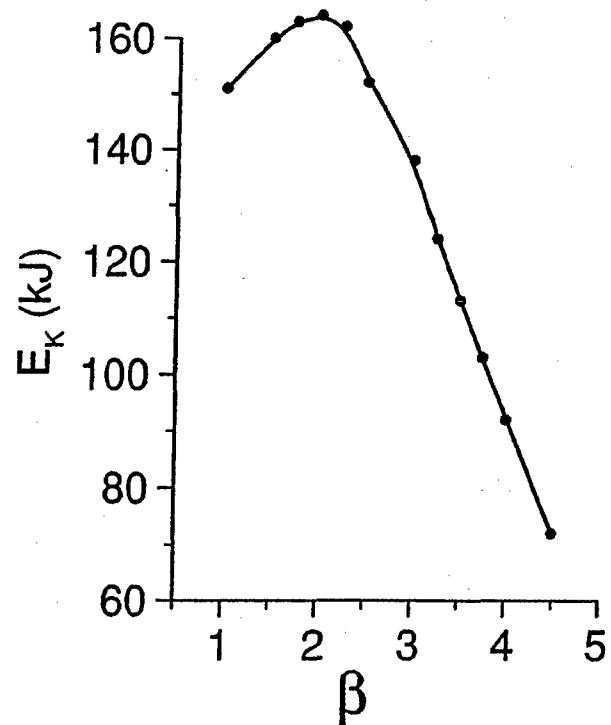


FIG. 10. Variation in the K-shell energy radiated from the pinch in 200 ns is shown as a function of the L-shell emissivity multiplier. The circuit resistance and  $\alpha$  multiplier are the same as in Figs. 5 and 6. A spline fit is drawn to the calculated points.

L-shell emissions turn down while K-shell emissions continue to rise. Once these K-shell emissions slow their rise, saturate, and then fall for  $\alpha \geq 600$ , subkilovolt emissions begin to move towards their peak values.

The influence of the L-shell emission rate on x-ray outputs is shown in Figs. 9 and 10. The energies plotted are emissions that were calculated over the first 200 ns of the pinch dynamics. Up to a  $\beta$  level of 2, both K- and L-shell emissions increase with  $\beta$  because an increased cooling rate moderates the fluid dynamics during plasma assembly and inhibits the regeneration of kinetic energy. However, as  $\beta$  becomes larger than 2, K-shell emissions decrease rapidly because a growing amount of L-shell cooled plasma is unable to ionize into the K shell. Throughout these variations in L-shell cooling rate, energy coupling to the plasma remains relatively unchanged.

As alluded to earlier, both the shape and the magnitude of the measured x-ray pulses place severe restrictions on the time history of the load resistance that is needed to replicate these pulses. When too much heating occurs too early in the implosion, the plasma emits x rays prematurely and produces a pulse with an early-time foot, which was not seen in the experiments. Moreover, too much early-time heating causes the plasma to overheat during run in, reducing its compressibility during assembly and, in turn, its x-ray conversion efficiency. Thus, if large and rapid increases in pinch resistance occurred in the experiments, these increases must have taken place near the time of pinch assembly.

Given these considerations, two sets of calculations were

carried out to determine the sensitivity of energy coupling and the accompanying x-ray production to the size and timing of circuit resistance increases. The results of these calculations are shown in Figs. 11–15. In them, the shape of the resistance pulse was kept the same as in Fig. 5, i.e., the rise and fall times were kept unchanged, while variations were made to the resistance's peak value and to the time at which it reached this value. In all of these calculations,  $\alpha$  and  $\beta$  were held at values of 600 and 3, respectively.

In one set of calculations, the maximum value of the load resistance,  $R_{\text{load}}^{\text{max}}$ , was varied while the rise and fall times and the time to peak resistance remained unchanged. The energy coupling and radiative outputs calculated during the first 200 ns of the pinch dynamics are shown in Figs. 11–13. The total energy coupled to the plasma, which is shown in Fig. 11, has been broken into an inductive and a resistive part. The inductive part is defined by

$$E_{\text{ind}}(t) \equiv \int_0^t dt' \left( \frac{1}{2} \frac{dL_{\text{load}}(t')}{dt'} I(t')^2 \right) \quad (41)$$

and the resistive part by

$$E_{\text{res}}(t) \equiv \int_0^t dt' R_{\text{load}}(t') I(t')^2. \quad (42)$$

Initially both of these couplings, and thus the total coupling, increase with  $R_{\text{load}}^{\text{max}}$ . However, once  $R_{\text{load}}^{\text{max}}$  becomes larger than  $0.3 \Omega$ , the inductive coupling falls at roughly the same rate as the resistive coupling rises, so that the total



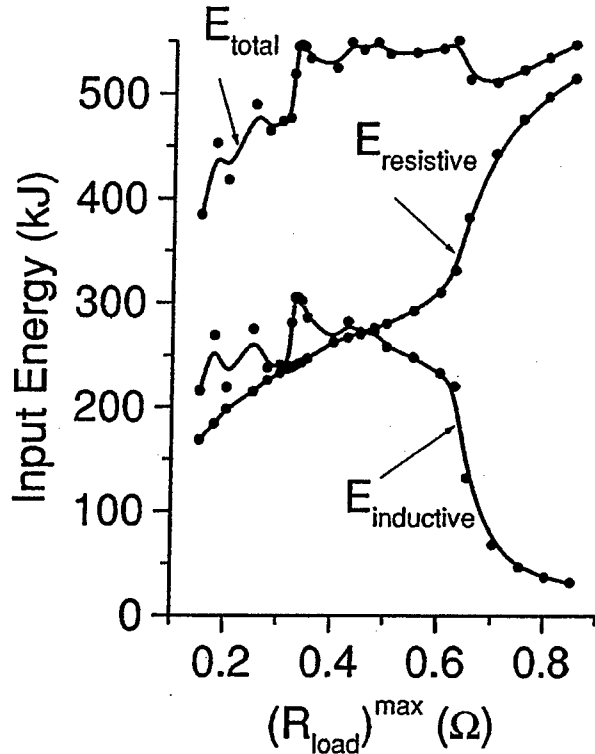


FIG. 11. The total, resistive, and inductive energies coupled to the Z-pinch load are shown as a function of variations in the maximum value of the Fig. 5 circuit resistance. Spline fits are drawn to the calculated points. The oscillations in the inductive coupling at small values of  $R_{load}^{max}$  represent numerical error.

coupled energy remains relatively flat. Beyond a peak of 0.6  $\Omega$ , the rise and fall rates of  $E_{res}$  and  $E_{ind}$ , respectively, increase, and this change correlates with the decline in the calculated x-ray emissions, both total and K shell that are shown in Figs. 12 and 13. This behavior shows that, when the amount of resistive heating is too large, the plasma cannot radiate coupled energy fast enough to prevent its late-time conversion into kinetic energy.

Finally, the sensitivity of coupled and radiated energy to the time at which the load resistance reaches its maximum value is illustrated in Figs. 14 and 15. In these calculations,  $R_{load}^{max}$  was held at a value of 0.653  $\Omega$ , and the time to peak resistance,  $t_0 + \Delta t$ , was varied around its Fig. 5 value in which  $t_0 = 172$  ns. The total and resistive energies that were coupled in these calculations over 200 ns are plotted in Fig. 14 as a function of  $\Delta t$ . Figure 15 contains similar plots of the calculated, total and K-shell, radiated energies. These figures again demonstrate that too much heating too soon in the implosion reduces the plasma's compressibility and its radiative cooling at assembly. Extra energy inputs are converted instead into kinetic energy. Hence, the radiative output rises rapidly as  $\Delta t \rightarrow 0$ , and K-shell emission is maximized at  $\Delta t = 0$ . When  $\Delta t = 2$  ns, the circuit resistance peaks at the time of peak emission, causing the K-shell emission to fall to half of its maximum value. We note finally that the extreme sensitivity, which is seen in all of the above calculations, to small changes in the size, shape, and timing of the enhanced

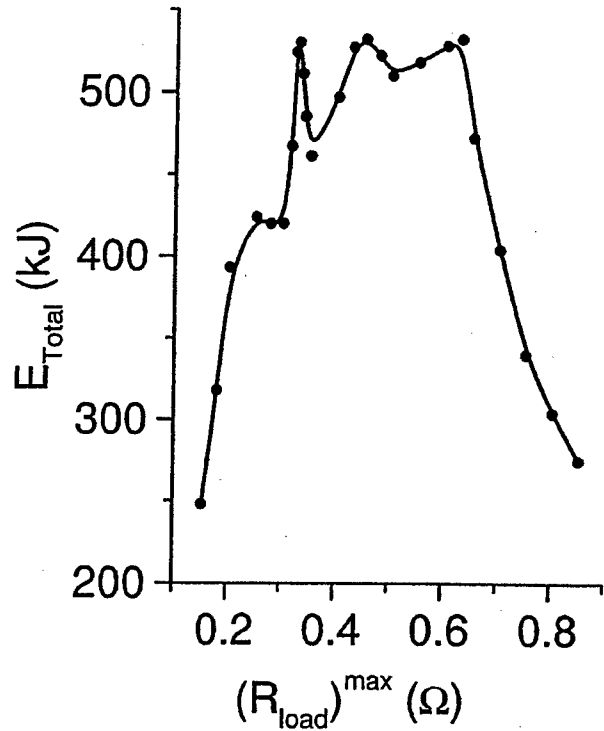


FIG. 12. The total energy radiated from the Z pinch is shown as a function of variations in the maximum value of the Fig. 5 circuit resistance. A spline fit is drawn to the calculated points.

circuit resistance is consistent with the large shot-to-shot variations seen experimentally (Fig. 1) in the x-ray data.

## V. PLASMA COLLISIONALITY

In Ref. 13, a resistivity formula based on the growth and saturation of lower-hybrid drift wave microinstabilities at the surface of a pinch was proposed and its effects on the equilibrium states and the radiative collapse of Z pinches was investigated. This formula was written in the form of a classical resistivity with an enhanced collision frequency,  $\nu^*$ , produced by an electron drift-wave interaction

$$\eta^* = \frac{m \nu^*}{n_e e^2}, \quad \nu^* = \left( \frac{\pi}{8} \right)^{1/2} \left( \frac{v_d}{v_{th}^i} \right)^2 \sqrt{\omega_{ce} \omega_{ci}} \text{ (s}^{-1}\text{)}, \quad (43)$$

where  $\omega_{ce}$  and  $\omega_{ci}$  are the electron and ion plasma frequencies, respectively,  $v_d = j_e / (n_e e)$  is the electron drift velocity, and  $v_{th}^i = \sqrt{2 k_B T_i / m_i}$  is the average ion thermal speed. This resistivity is temperature insensitive, and it increases as the surface density decreases in contrast to Spitzer resistivity, which is essentially density independent and which decreases with temperature increases. As electromagnetic energy couples to a pinch, its surface temperature rises and its surface density falls. Consequently, as these changes take place, Spitzer resistivity decreases, while drift-wave resistivity increases.

Because a drift-wave resistivity has properties in common with the surface resistivity employed in the above calculations, it was of interest to determine how closely they would compare in, for example, the above, fiducial calcula-

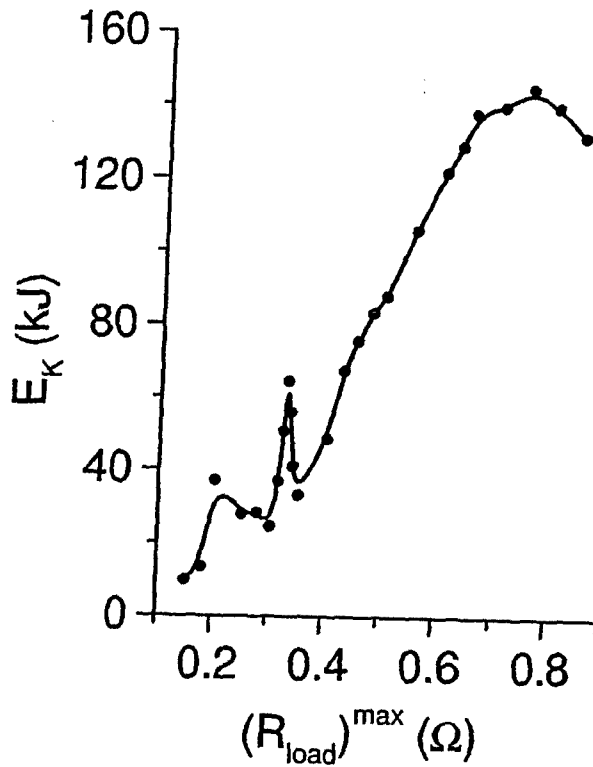


FIG. 13. The K-shell energy radiated from the Z pinch is shown as a function of variations in the maximum value of the Fig. 5 circuit resistance. A spline fit is drawn to the calculated points.

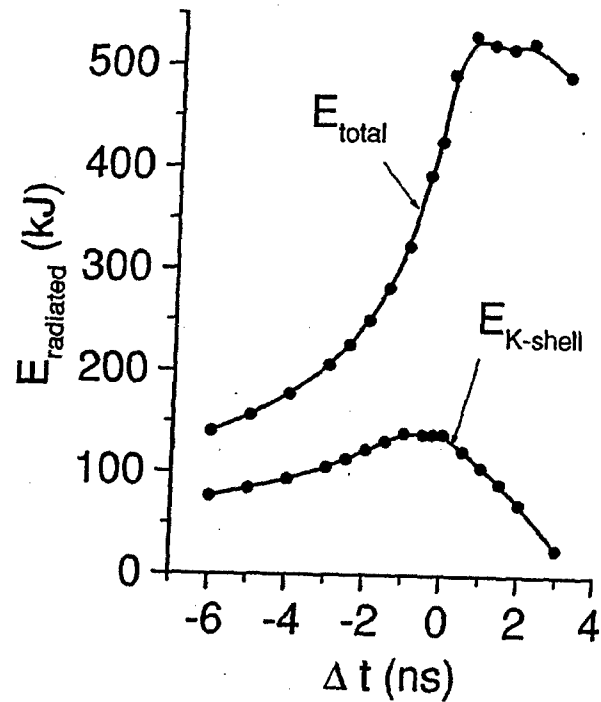


FIG. 15. The total and the K-shell energies that are radiated from the Z pinch are shown as a function of variations in the time to peak resistance of the Fig. 5 circuit resistance. Spline fits are drawn to the calculated points.

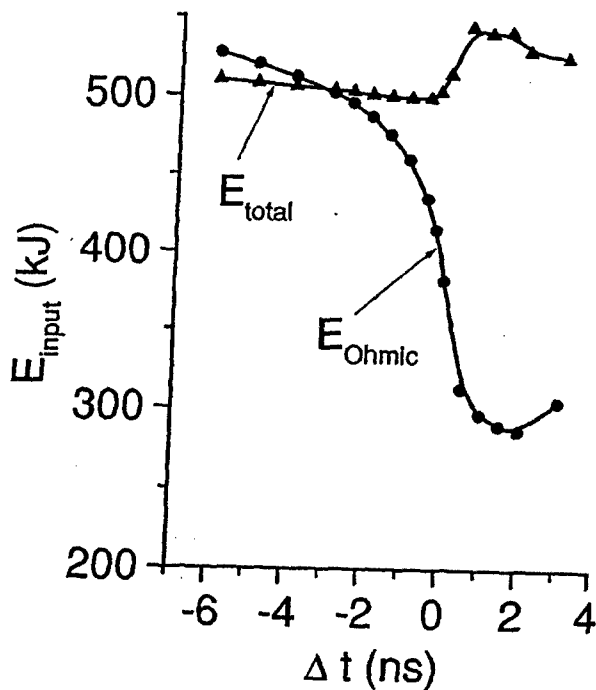


FIG. 14. The total and resistive energies that couple to the Z pinch are shown as a function of variations in the time to peak resistance of the Fig. 5 circuit resistance. Spline fits are drawn to the calculated points.

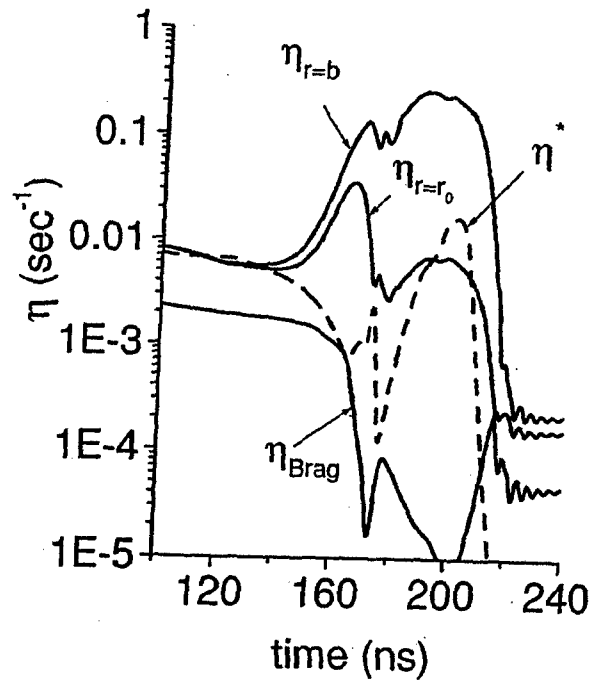


FIG. 16. Four calculated resistivities are shown as functions of time for the Figs. 5 and 6 calculation. The one, labeled  $\eta_{Brag}$ , is derived from  $\partial_t \eta_0$  [  $\eta_0$  from Eq. (32)]. The dashed curve is derived from the drift-wave formula, Eqs. (43). The one, labeled  $\eta_{r=b}$ , is derived from  $R_{load}$  using Eqs. (32) and (40), and the one labeled  $\eta_{r=r_0}$  is linearly extrapolated down from  $\eta_{r=b}$ . The term  $r_0$  is the inner surface location of the imploding plasma shell.

tion. This comparison is made in Fig. 16. It shows the time evolution of four resistivities. The resistivity at the plasma outer boundary, labeled  $\eta_{r=b}$  in Fig. 16, was calculated from  $R_{\text{load}}: \eta_{r=b} = R_{\text{load}} / [\ell j_z(r=b)]$ . The curve labeled  $\eta_{r=r_0}$  shows the resistivity at the nominal inner boundary of the shell-like imploding plasma. It illustrates the resistivity contouring that was employed in the calculation. The classical resistivity, labeled  $\eta_{\text{Brag}}$ , was calculated at the plasma outer boundary using the formula,  $\eta_{\text{Brag}} = \alpha_1 \eta_0|_{r=b}$ .<sup>15</sup> Finally, the resistivity, labeled  $\eta^*$ , was calculated at the outer boundary of the plasma using the drift-wave formula [Eq. (43)]. As anticipated, it did rise more than two orders of magnitude; however, its rise occurred late in time, well after the rise in  $\eta_{r=b}$  that was needed to produce the x-ray output shown in Fig. 6.

## VI. SUMMARY

Because Maxwell's equations and fluid equations describe local flows of energy, Z-pinch to pulsed-power generator coupling is determined by the continuity of the transmission line energy flow across the outer boundary of the pinch. Increases in Z-pinch resistance, therefore, are related to increases in the plasma's surface resistivity (and to its surface area). Resistivity increases can occur when surface conditions are set up during a pulsed-power discharge that stimulates the growth of plasma microinstabilities (which increase the plasma's surface collisionality) as well as the growth of Rayleigh–Taylor or other implosion instabilities (which are calculated to increase a pinch's surface area). In this paper, the impact on the fluid dynamics of augmenting the surface collisionality was investigated both to increase the energy coupling and to evaluate how well such augmentations are able to replicate the x-ray behavior seen in a set of identically designed Saturn experiments. A phenomenological approach to modeling this coupling was adopted for lack of a first-principles theory that accurately describes how microinstability growth, for example, affects a Z-pinch's surface resistivity.

Four things were learned from this 1D analysis. One, three orders of magnitude increases in resistance were needed to produce comparable amounts of energy coupling as were seen experimentally. Two, the rate at which energy is transported within the plasma and the rate at which it is radiated had to be comparable to the energy coupling rate for the added energy inputs to end up as added x-ray outputs. Three, for the calculations to approximately replicate the time history of a given measured x-ray pulse, only a highly restricted choice of resistance enhancement could be employed. In particular, the presence or absence of late-time x-ray emission depended on the decay rate of the enhanced resistance. And four, the extreme sensitivity of the calculations to variations in (1) the rates of energy transport and loss, (2) the peak value of the enhanced resistance, and (3) the onset time of the rapid increase of the resistance was consistent with the large shot-to-shot variations seen in the Saturn experiments.

Our calculations showed that significant changes in the fluid dynamics occur when the resistive coupling to a Z

pinch becomes competitive with the inductive coupling. As resistive coupling is increased, ohmic heating in the outer regions of the plasma is increased. If this energy is not transported into the plasma fast enough, the energized surface simply blows away in a 1D calculation. Thus, the analysis of the Saturn aluminum-wire shots presented in this paper has suggested that L-shell emissions have a significant influence on energy transport within the plasma. It is already known experimentally that they have an increasingly negative effect on K-shell emissions as the atomic number of the Z pinch is increased.<sup>32</sup> However, as a caveat, kinetic energy generation is different in one-dimensional fluid dynamics than in two or three dimensions. Recent work on the early-time dynamics of wire arrays has shown that plasma does not blow away when there are gaps between the wires. It flows into the gaps instead. If similar two-dimensional behavior persists late time, it may play a role in the energy coupling problem. In this case, a gap dependent coupling should be determinable experimentally.

Other issues need to be addressed before a more definitive understanding of the Saturn experiments can be worked out. More needs to be learned about the strength of surface microinstabilities and about their influence on current flow. If enhanced energy coupling is related to the multidimensional character of Z-pinch implosions, it should be detectable in both wire array and gas puff experiments. On the other hand, if it is more prominent in wire array than in gas puff experiments, it may be related more specifically to the way wires break down in time, generating a different implosion dynamics than is predicted by 0D Z-pinch calculations.<sup>33</sup> In all cases, however, the different fluid dynamic mechanisms that move energy about the plasma and that aid in converting enhanced energy couplings into x rays need to be investigated and better understood quantitatively.

## ACKNOWLEDGMENTS

This work was supported in part by Sandia National Laboratories and in part by DTRA. Sandia is a multiprogram laboratory operated by the Sandia Corporation, a Lockheed Martin Company, for the U.S. DoE under Contract No. DE-AC04-94AL85000.

<sup>1</sup>R. B. Spielman, R. J. Dukart, D. L. Hanson, B. A. Hammel, W. W. Hsing, M. K. Matzen, and J. L. Porter, in *Proceedings of the Second International Conference on Dense Z Pinches*, Laguna Beach, CA, 1989, edited by N. R. Pereira, J. Davis, and N. Rostoker (American Institute of Physics, New York, 1989), p. 3.

<sup>2</sup>C. Deeney, C. A. Coverdale, M. R. Douglas, K. W. Struve, R. B. Spielman, W. A. Stygar, D. L. Peterson, N. F. Roderick, M. G. Haines, F. N. Beg, and J. Ruiz-Camacho, *Phys. Plasmas* **6**, 3576 (1999).

<sup>3</sup>J. P. Apruzese, J. W. Thornhill, K. G. Whitney, J. Davis, C. Deeney, and C. A. Coverdale, *Phys. Plasmas* **8**, 3799 (2001).

<sup>4</sup>C. A. Coverdale, C. Deeney, M. R. Douglas, J. P. Apruzese, K. G. Whitney, J. W. Thornhill, and J. Davis, *Phys. Rev. Lett.* **88**, 065001 (2002).

<sup>5</sup>J. C. Riordan, J. S. Pearlman, M. Gersten, and J. E. Rauch, in *Sub-Kilovolt X-ray Emission from Imploding Wire Plasmas*, AIP Conf. Proc. No. 75, edited by D. Attwood and B. Henke (AIP, New York, 1981), p. 35.

<sup>6</sup>M. Krishnan, C. Deeney, T. Nash, P. D. LePell, and K. Childers, in *Dense Z-Pinches, Second International Conference*, AIP Conf. Proc. No. 195, edited by N. R. Pereira, J. Davis, and N. Rostoker (AIP, New York, 1989), p. 17.

- <sup>7</sup>L. I. Rudakov, A. L. Velikovich, J. Davis, J. W. Thornhill, J. L. Giuliani, Jr., and C. Deeney, Phys. Rev. Lett. **84**, 3326 (2000).
- <sup>8</sup>A. L. Velikovich, J. Davis, J. W. Thornhill, J. L. Giuliani, Jr., L. I. Rudakov, and C. Deeney, Phys. Plasmas **7**, 3265 (2000).
- <sup>9</sup>J. L. Giuliani, Jr., J. E. Rogerson, C. Deeney, T. Nash, R. R. Prasad, and M. Krishnan, J. Quant. Spectrosc. Radiat. Transf. **44**, 471 (1990).
- <sup>10</sup>D. L. Peterson, R. L. Bowers, K. D. McLenithan, C. Deeney, G. A. Chandler, R. B. Spielman, M. K. Matzen, and N. F. Roderick, Phys. Plasmas **5**, 3302 (1998).
- <sup>11</sup>D. L. Peterson (private communication).
- <sup>12</sup>C. Deeney, T. Nash, R. R. Prasad, L. Warren, K. G. Whitney, J. W. Thornhill, and M. C. Coulter, Phys. Rev. A **44**, 6762 (1991).
- <sup>13</sup>A. E. Robson, Phys. Fluids B **3**, 1461 (1991).
- <sup>14</sup>T. W. L. Sanford, R. C. Mock, R. B. Spielman, M. G. Haines, J. P. Chittenden, K. G. Whitney, J. P. Apruzese, D. L. Peterson, J. B. Greenly, D. B. Sinars, D. B. Reisman, and D. Mosher, Phys. Plasmas **6**, 2030 (1999).
- <sup>15</sup>S. I. Braginskii, *Reviews of Plasma Physics*, edited by M. A. Leontovich (Consultants Bureau, New York, 1965), p. 205.
- <sup>16</sup>A. Y. Labetsky, R. B. Baksht, V. I. Oreshkin, A. G. Roussikh, and A. V. Shishlov, IEEE Trans. Plasma Sci. **30**, 524 (2002).
- <sup>17</sup>J. Katzenstein, J. Appl. Phys. **52**, 676 (1981).
- <sup>18</sup>A. B. Bud'ko and M. A. Liberman, Zh. Prikl. Mekhaniki i Tekhnicheskoi Fiziki **30**, 3 (1989).
- <sup>19</sup>N. A. Bobrova and T. L. Razinkova, Sov. J. Plasma Phys. **13**, 53 (1987), trans. from Fiz. Plazmy **13**, 92 (1987).
- <sup>20</sup>D. W. Scudder, Phys. Fluids **26**, 1330 (1983).
- <sup>21</sup>M. Coppins, I. D. Culverwell, and M. G. Haines, Phys. Fluids **31**, 2688 (1988).
- <sup>22</sup>A. L. Velikovich, I. V. Sokolov, and A. A. Esaulov, Phys. Plasmas **9**, 1366 (2002).
- <sup>23</sup>A. E. Robson, Phys. Rev. Lett. **63**, 2816 (1989); A. E. Robson, Phys. Fluids B **1**, 1834 (1989).
- <sup>24</sup>W. H. Bennett, Phys. Rev. **45**, 890 (1934).
- <sup>25</sup>R. S. Pease, Proc. Phys. Soc. London, Sect. B **70**, 11 (1957).
- <sup>26</sup>S. I. Braginskii, Sov. Phys. JETP **6**, 494 (1958).
- <sup>27</sup>C.-G. Falthammer, Phys. Fluids **4**, 1145 (1961).
- <sup>28</sup>W. M. Manheimer, Phys. Fluids **17**, 1767 (1974).
- <sup>29</sup>J. W. Thornhill, J. P. Apruzese, J. Davis, R. W. Clark, A. L. Velikovich, J. L. Giuliani, Jr., Y. K. Chong, K. G. Whitney, C. Deeney, C. A. Coverdale, and F. L. Cochran, Phys. Plasmas **8**, 3480 (2001).
- <sup>30</sup>K. G. Whitney, J. W. Thornhill, C. Deeney, C. A. Coverdale, J. P. Apruzese, J. Davis, A. L. Velikovich, and L. I. Rudakov, in *Dense Z-Pinches, Fifth International Conference*, AIP Conf. Proc. No. 651, edited by J. Davis, C. Deeney, and N. R. Pereira (AIP, New York, 2002), p. 358.
- <sup>31</sup>J. Zeng and J. Yuan, Phys. Rev. E **66**, 016401 (2002).
- <sup>32</sup>C. Deeney, C. A. Coverdale, M. R. Douglas, T. J. Nash, R. B. Spielman, K. W. Struve, K. G. Whitney, J. W. Thornhill, J. P. Apruzese, R. W. Clark, J. Davis, F. N. Beg, and J. Ruiz-Camacho, Phys. Plasmas **6**, 2081 (1999).
- <sup>33</sup>S. V. Lebedev, F. N. Beg, S. N. Bland, J. P. Chittenden, A. E. Dangor, M. G. Haines, K. H. Kwek, S. A. Pikuz, and T. A. Shelkovenko, Phys. Plasmas **8**, 3734 (2001); S. V. Lebedev, R. Aliaga-Rossel, S. N. Bland, J. P. Chittenden, A. E. Dangor, M. G. Haines, and I. H. Mitchell, *ibid.* **6**, 2016 (1999).

## Spectroscopic Diagnosis of Nested-Wire-Array Dynamics and Interpenetration at 7 MA

C. Deeney,<sup>1</sup> J. P. Apruzese,<sup>2</sup> C. A. Coverdale,<sup>1</sup> K. G. Whitney,<sup>3</sup> J. W. Thornhill,<sup>2</sup> and J. Davis<sup>2</sup><sup>1</sup>Sandia National Laboratories, P.O. Box 5800 Albuquerque, New Mexico 87185, USA<sup>2</sup>Plasma Physics Division, Naval Research Laboratory, 4555 Overlook Avenue, Washington, D.C. 20375, USA<sup>3</sup>Berkeley Scholars, Inc., Springfield, Virginia 22150, USA

(Received 26 January 2004; published 4 October 2004; publisher error corrected 8 October 2004)

Nested-wire array experiments have been conducted at the 7 MA level with 150 ns implosion times from an outer diameter of 40 mm. Analysis of spectral data indicates that material from the outer array preferentially occupies the high temperature core of the stagnated pinch independent of the interwire gap in the range of 1.1 to 4.5 mm.

DOI: 10.1103/PhysRevLett.93.155001

PACS numbers: 52.58.Lq, 52.59.Qy

The recent demonstration of Z-pinch wire array implosions as a method to produce high x-ray powers has revitalized Z-pinch applications. Whether it be laboratory experiments relevant to astrophysics [1], inertial confinement fusion [2,3] or high-photon-energy x-ray production [4], these applications all rely on the ability of Z pinches to produce copious x-rays at high powers. One method to increase the radiated power from implosions is to use nested shells [5,6]. The nested-wire array concept was developed independently following two different assumptions on wire array dynamics. One approach assumed that the wire array remained an array of localized wires during the implosion phase (wire model) [7,8]; the other assumed that the inner and outer arrays would both expand to form shells (shell model) [9]. Although nested arrays were effective at increasing x-ray powers, the concepts were flawed in explaining the data. The wire model did not explain why the x-ray power would increase. In the shell model case, a radiation burst is expected when the two shells collide, resulting from the need to dissipate energy to conserve momentum: The observed radiation burst was never as pronounced as predicted from the two-dimensional calculations thus indicating a more transparent collision [10]. Calculations also suggested that the plasmas ablating from the outer array could be heating and evaporating the inner array. The magnitude of the flux from the precursors is determined by the wire material and wire number [11].

Experiments have shed light on the different models of nested-wire array experiments on a 1-MA Z-pinch driver called MAGPIE [12]. The data showed evidence in the implosion trajectories for both wirelike, i.e., delayed trajectories, and shell-like behavior, depending on the magnitude of the current flowing in the inner array. In the wirelike case, the outer array appeared to pass through the inner array as had been seen in some wire dynamic calculations. However, the low currents do not allow experiments with wire numbers greater than 64. In addition, the low currents also limit spectroscopic diagnostics since 1 MA is insufficient to achieve ionization of a significant fraction of the imploded mass into the

K-shell, where spectroscopic techniques can be used to relate the implosion dynamics to the plasma parameters of the stagnated pinch. In experiments where K-shell ionization can be achieved then tracer spectroscopy can be readily used to relate the location of the plasma during the implosion to its location in the pinched plasma [13].

We report on the first use of spectroscopic dopants to characterize the implosion of nested-wire arrays by inferring the radial gradients in the stagnated plasma for two wire numbers. By employing pure wire and alloys alternately in the two arrays, it is possible to trace the relative location of the mass in each array in the stagnated pinch, thus to determine the degree of interpenetration.

A wire number scan on Saturn with 40 mm diameter single arrays had identified regions where the wire numbers were high enough to minimize the pulse width, and where the wire numbers were so low as to produce very broad pulses [14]. These interwire gaps formed the basis for the nested array shots. Table I lists the parameters for the 150 ns implosion time shots. The inner array had half the wire number of the outer, as in Ref. [5]. To perform the tracer spectroscopy, aluminum 5056 alloy was employed which contains 5% magnesium. Each array condition was tested with the Al 5056 on the outer and pure aluminum (Al 1100) on the inner or vice versa. One shot, #2832, was performed with Al 5056 in both the inner and outer arrays to establish a baseline.

Table I compares the radiation parameters including: the K-shell radiated powers and yields; the K-shell full-width-at-half-maximum (FWHM); plus the total x-ray power and K-shell x-ray power rise times. As far as the powers, rise times and yields are concerned, there was significant variability in these parameters. However, on average, the high-wire number nested arrays and the low-wire number nested arrays produced similar results. The high-wire number nested arrays produce 40% longer rise time x-ray pulses than the equivalent high-wire number single arrays [14]. On the other hand, the low-wire number nested arrays produce x-ray pulses with rise times a factor of 3 less than single arrays with an equivalent

TABLE I. The configurations for the 40 mm diameter, total mass of 840  $\mu\text{g}/\text{cm}$  nested arrays.

Shot	Outer wire no.	Outer wire material	Inner wire material	K-shell power (TW)	K-shell yield (kJ)	K-shell FWHM (ns)	K-shell rise (ns)	Total rise (ns)
2832	116	5056	5056	$1.2 \pm 0.2$	$60 \pm 10$	7.5	8.0	7.6
2833	116	5056	1100	$0.7 \pm 0.2$	$60 \pm 10$	18.0	9.5	9.5
2838	116	1100	5056	$1.5 \pm 0.2$	$70 \pm 10$	10.0	5.5	6.0
2834	28	5056	1100	$0.6 \pm 0.2$	$70 \pm 10$	10.0	14.0	10.8
2835	28	1100	5056	$1.0 \pm 0.2$	$60 \pm 10$	11.0	7.5	8.8
2839	28	5056	1100	$1.0 \pm 0.2$	$85 \pm 10$	6.0	6.3	6.0

interwire gap. One question is why the high-wire number case does not show any reduction in pulse width whereas the original high-wire number experiments with tungsten showed a 30% reduction in pulse width and corresponding power increase. This difference is likely due to the variations in the initiation of the wires into plasmas, plus the differences in the radiative properties of these materials, and this will be the subject of future investigation.

Figure 1 shows a comparison of the measured magnesium and aluminum He-alpha and Ly-alpha lines for the low-wire number arrays with the Mg dopant on the inside and the outside. The various intensity ratios are listed in Table II, along with those for the high-wire number shots. When the Mg dopant is in the outer array, strong Mg emissions are observed and the Ly- to He-alpha line ratio is greater than one, indicating a high electron temperature. The magnesium alpha lines radiated approximately 8% of the energy of the aluminum alpha lines even though the Mg ions account for 3.3% of the total stagnated plasma mass. In Z pinches, where the overall opacities are very high, (optical depths of 20 to 50) it has been observed in many experiments that a more optically thin dopant can radiate a disproportionate amount of energy due to the opacity plus collisional quenching limiting the K-shell emissions from the majority constituent [15]. Now when the Mg dopant is in the inner array (1.7% of the total mass) almost no magnesium emissions are observed. In fact, the Mg alpha lines radiate less than 2% of the emissions that the aluminum lines emit. Additionally, the ratio of the magnesium Ly-alpha to He-alpha fell below one. This indicates that the electron temperature at the location of the magnesium ions has decreased. In the high-wire number cases, the change is less dramatic, however, when the magnesium is in the inner array, there is a definite reduction in the Mg Ly-alpha to He-alpha ratio.

To determine quantitatively the location of the Mg at stagnation, we have analyzed the spectral results (see Table II) using collisional radiative equilibrium calculations that assume a fixed ion density and electron temperature profile plus different locations for the Mg component. Our analysis focuses on temperature sensitive diagnostic line ratios such as the ratio of the Ly-alpha to

He-alpha lines in an individual element, plus a more opacity and mass fraction sensitive ratio which is given by the ratio of the sum of the Mg Ly-alpha and He-alpha to the Al Ly-alpha and He-alpha. Based on the previous analyses of temperature and density gradients [15], a generic temperature and density gradients were postulated, see Fig. 2. These gradients would produce spectra that matched the observed aluminum K-shell powers and aluminum line ratios. A validation of the assumed profiles

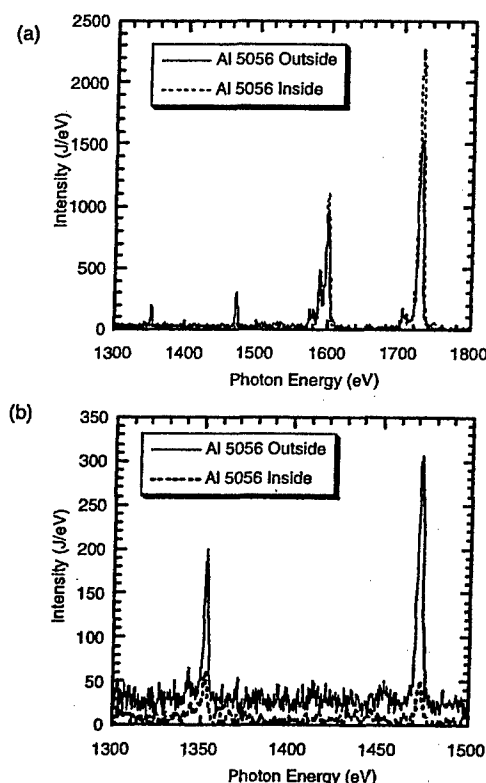


FIG. 1. (a) A comparison of the measured magnesium and aluminum H- and He-like emissions when Mg-bearing alloy (Al 5056) was placed in the outer (solid curve) or inner array (dotted curve) for a 40 mm diameter, 28 onto 14 wire nested implosions. (b) The same data with the range selected to highlight the Mg emissions.

TABLE II Spectral measurements

Shot	Outer wire No.	Outer wire material	Mg Frac. (%)	Mg/Al Alpha Ratio (%)	Mg Ly $\alpha$ /He $\alpha$	Al Ly $\alpha$ /He $\alpha$	Al Ly $\alpha$ /He $\beta$
2832	116	5056	5.0	$11.0 \pm 1.0$	$1.6 \pm 0.2$	$1.2 \pm 0.1$	$1.0 \pm 0.1$
2833	116	5056	3.3	$5.5 \pm 0.5$	$2.2 \pm 0.2$	$1.6 \pm 0.1$	$1.3 \pm 0.1$
2838	116	1100	1.7	$3.5 \pm 0.5$	$0.7 \pm 0.2$	$1.3 \pm 0.1$	$0.9 \pm 0.1$
2834	28	5056	3.3	$8.0 \pm 0.3$	$1.9 \pm 0.2$	$1.4 \pm 0.1$	$1.3 \pm 0.1$
2835	28	1100	1.7	$1.3 \pm 0.4$	$0.8 \pm 0.2$	$1.7 \pm 0.2$	$1.4 \pm 0.1$
2823	28	5056	3.3	$8.5 \pm 0.3$	$1.7 \pm 0.2$	$1.3 \pm 0.1$	$1.1 \pm 0.1$

is provided by shot 2032, which had Al 5056 in both arrays. In this case, the plasma should have a uniform mixture of 5% Mg throughout the pinch. The predicted Mg Ly-alpha to He-alpha ratio is 1.6. The corresponding Mg to Al ratio would be 0.14. The measured values were  $1.6 \pm 0.2$  and  $0.11 \pm 0.01$ , respectively, indicating a reasonable match. For the other shots with Mg in just one array, the predicted magnesium to aluminum alpha ratios are 0.06 and 0.11 for the 1.7% and 3.3% Mg uniformly distributed mass fractions, respectively. These are too high compared to the measured ratios in Table II indicating that a uniform mixing of the materials cannot explain our data.

Since the Mg Ly-alpha to He-alpha ratios and those of the Mg alpha lines to the Al alpha lines cannot be replicated if it is assumed that the Mg is uniformly distributed in the pinch, we next estimate the location of the Mg by ascertaining the Mg location within the assumed profiles that are consistent with the line ratios in Table II. In Figs. 3(a) and 3(b) the Mg Ly-alpha to He-alpha ratio and the total Mg alpha lines to Al alpha lines are plotted as a function of the location of the Mg. Figure 3(a) considers the Mg extending from the axis to some radius in

the pinch, called the outer limit of Mg. Figure 3(b) considers the cases with Mg starting from a varying inner radius (called the inner limit of Mg) to the outer edge of the gradient profile. In both cases, the Mg has a 5% fraction by mass in the regions where it is located in the temperature and density profiles. The measured ratios from the low-wire number experiment where the Mg alloy was on the inner array cannot be fit by any location of Mg

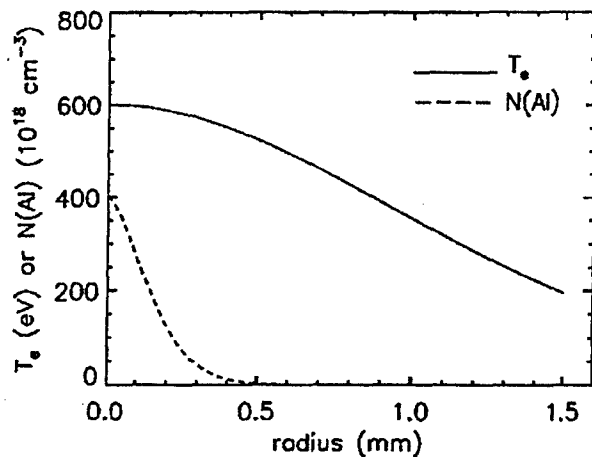


FIG. 2. A generic electron temperature and ion density gradient was developed to match the aluminum line ratios and powers

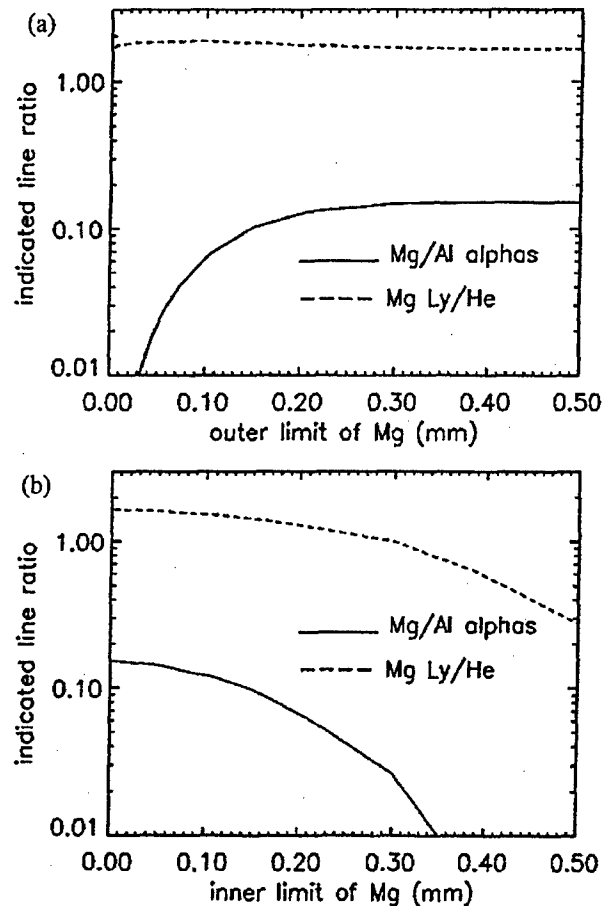


FIG. 3. (a) the outer and (b) inner boundary of the 5% Mg dopant was varied and the resultant variation in Mg to Al alpha ratios and the Mg Ly-alpha to He-alpha ratios are plotted.

if it starts from the hot core, i.e., the data in Fig. 3(a). The same data can be fit using the calculations plotted in Fig. 3(b), and the analysis would indicate Mg could be located from 320  $\mu\text{m}$  radius to the outer limit of the assumed profiles. For the case, where the Mg was located in the outer array, analysis indicates the best fit if the Mg extends from the axis to a radius no more than 120  $\mu\text{m}$  [see Fig. 3(a)]. These gradients are not completely representative of the plasma conditions in the experiment as discussed by Apruzese *et al* [15]. For example, the plasmas can have two- and three-dimensional structure. The one-dimensional gradient analysis, however, does indicate that the most likely explanation for the large variations in the Mg spectra, when the alloys are placed in either the inner or outer array, is that in the former case the Mg-bearing plasma ends up in the outer, cooler regions of the pinch, and in the latter case, the Mg-bearing plasma ends up in the inner, hotter core of the plasma.

In the high-wire number cases, the variations are much less dramatic. However, following the same analyses would suggest that when the Mg dopant is in the outer array, the Mg may extend out to 100  $\mu\text{m}$ , although the Mg Ly-alpha to He-alpha is higher than the assumed gradients would predict. This may be due to differences between the calculated and actual generic gradient conditions. When the Mg is in the inner array, the Mg in the stagnated plasma can not extend further in than 260  $\mu\text{m}$  based on the Mg to Al ratio. The ratio of the Mg Ly-alpha to He-alpha would indicate that the Mg could not extend further in than 330  $\mu\text{m}$ . Again, there is an indication of the outer array sending material through the inner array.

The apparent transparency, somewhat independent of wire number, of the inner array to the material from the outer is substantiated by the early time x-ray emissions. From our data, it is apparent that there is no obvious strike feature at the estimated time of impact, and, moreover, the early time emissions are very similar for both the high and low-wire number cases. This is again indicative that there is no shell-on-shell impact even for the high-wire number implosion, and that the early emissions may be due to snow plowing of precursor material and Ohmic heating in the current sheath.

The low-wire number observations on MAGPIE appear to apply to both our low and high-wire number experiments, i.e., some fraction of the outer wire plasma likely passes through the inner array. With high-wire numbers, the magnetic field is excluded by the outer array so there is probably little coupling of current to the inner array. Using inductive division, we estimate that no more than a few percent could be coupled to the inner array in the high-wire number case, that is, only a few kA per wire. This is a similar situation to the high

inductance inner array [11] where little current was transferred to the inner array, and the wires were observed not to expand so remaining transparent. Unfortunately, we cannot differentiate between a completely transparent interaction, or one in which the outer array material, including the precursor, mixes with the inner array. In addition, since the mass fractions radiating in the K-shell are low ( $<10\%$ ), we cannot rule out that precursor streams carried the Mg to the axis or at least inboard of the inner array, rather than the implosion of the bulk of the mass of the outer array.

Our results indicate for the first time that the outer array material becomes the highest temperature plasma during the implosion of the nested array. Moreover, detailed spectral analyses indicate that the outer array in both high or low-wire number cases is the source of the material that is heated to the highest temperatures. In a one-dimensional analysis, this is the innermost "core" of the stagnated pinch. The authors appreciate useful discussions with M. R. Douglas, P. Coleman, S. Lebedev, Y. Maron, R. Terry, D. Sinars, and J. Chittenden. Sandia is a multiprogram laboratory operated by Sandia Corporation, a Lockheed Martin Company, for the U.S. Department of Energy under Contract No. DE-AC04-94AL85000.

- 
- [1] P.T. Springer *et al*, J. Quant. Spectrosc. Radiat. Transfer **58**, 927 (1997).
  - [2] J. E. Bailey *et al*, Phys. Rev. Lett. **92**, 085002 (2004).
  - [3] M. E. Cuneo *et al*, Phys. Plasmas **8**, 2257 (2001).
  - [4] C. Deeney *et al*, Phys. Rev. Lett. **61**, 1881 (1999).
  - [5] C. Deeney *et al*, Phys. Rev. Lett. **81**, 4883 (1998).
  - [6] R. Baksht, A.V. Fedunin, and A.Yu. Labetsky, IEEE Trans. Plasma Sci. **26**, 1259 (1998).
  - [7] J. Davis, N. A. Gondarenko, and A. L. Velikovich, Appl. Phys. Lett. **70**, 170 (1997).
  - [8] R. E. Terry, J. Davis, C. Deeney, and A. L. Velikovich, Phys. Rev. Lett. **83**, 4305 (1999).
  - [9] Melissa Douglas *et al*, Bull. Am. Phys. Soc. **42**, 1878 (1997).
  - [10] J. P. Chittenden, S. V. Lebedev, S. N. Bland, A. Clardi, and M. G. Haines, Phys. Plasmas **8**, 675 (2001).
  - [11] S. V. Lebedev, R. Aliaga-Rossel, S. N. Bland, J. P. Chittenden, A. E. Dangor, M. Haines, and M. Zakaullah, Phys. Rev. Lett. **84**, 1708 (2000).
  - [12] S. N. Bland, S. V. Lebedev, J. P. Chittenden, C. Jennings, and M. G. Haines, Phys. Plasmas **10**, 1100 (2003).
  - [13] H. Sze *et al*, Phys. Plasmas **7**, 4223 (2001).
  - [14] C. A. Coverdale *et al*, Phys. Rev. Lett. **88**, 065001 (2002).
  - [15] J. P. Apruzese, J. W. Thornhill, K. G. Whitney, C. Deeney, and C. A. Coverdale, Phys. Plasmas **8**, 3799 (2001).



# Characterization of On-Axis Plasma Heating for keV X-Ray Production with Z-Pinches

Alexander S. Chuvatin, Leonid I. Rudakov, Alexander L. Velikovich, Jack Davis, and Vladimir I. Oreshkin

**Abstract**— We discuss a new opportunity of using Z-pinch plasma radiation sources for generating Ar K-shell radiation and harder keV quanta. Our approach to keV x-ray generation is based upon an analogy with laser fusion, where the imploding shell compression heats the low-density inner mass. The suggested design of a Z-pinch load consists then of one or two heavy outer shell(s) with a lower mass on-axis fill (i. e., central gas jet) producing most of the radiation. The outer shell is not supposed to radiate and thus does not need to have high specific energy characterized by the large  $\eta$  parameter [J. Appl. Phys. 67, 1725 (1990)]. Thus, the heavy outer shell does not need to have a very large initial diameter for its implosion to be matched to the long-pulse current driver. Rather, we want to have a large amount of energy from the driver coupled to this shell by the moment when the shell collides with the low-density fill and eventually converts much of this energy to the thermal energy of the on-axis plasma. This configuration is investigated numerically in the framework of a one-dimensional radiation-magnetohydrodynamics model for the case of Ar K-shell radiators. It is demonstrated that the Ar fill is heated in two stages. The first stage corresponds to the shock heating and thermal conduction in an initially low-density fill, and it allows preheating the fill while avoiding significant losses in soft radiation. The fill radiator is then compressed quasi-adiabatically and is heated up to the temperature optimum for K-shell quanta generation. Diffusion of the driving magnetic field is shown to always suppress the conductive heat losses from the hot on-axis plasma to the cold outer shell. Absorption of the K-lines emitted near the axis in the surrounding plasma could be avoided by filling the outer shell with a different gas (like N-on-Ar), which allows a substantial increase in the observed keV x-ray radiation yields.

**Index Terms**— Magnetohydrodynamics, pulse power systems, K-shell radiation production

## I. INTRODUCTION

Z-pinch plasmas are known as efficient radiators both in sub- [1] and multi-keV spectral regions [2]. In particular, at pulse power driver currents  $I_0 > 15$  MA and short current rise times,  $t_0 \leq 100$  ns, an efficient hot x-ray emitter is realized with the argon K-shell yield (photon energies around 3 keV) approaching 300 kJ [2].

The regular way of obtaining such keV x-ray radiators with z-pinches consists in imploding an annular cylindrical plasma shell by the pressure of a pulsed magnetic field. A smooth density distribution produced by a multi-shell nozzle also evolves into a thin shell (a plasma shell) during the run-in phase. The accumulated kinetic energy is converted into the plasma internal energy when this shell stagnates and forms a pinch at the axis. At this pinching moment, the kinetic energy is first converted into the ion thermal energy. The ions must then heat the electrons, so that the ions could be ionized to He- and H-like states to make the plasma radiating in the K-shell during a short inertial/magnetic confinement time [3].

Assuming the primary energy reservoir in this K-shell emitter is the kinetic energy, this approach requires the maximum shell kinetic energy to exceed  $\eta$  times the minimum energy, necessary to ionize the pinch plasma into the K shell upon stagnation [3]. This automatically implies  $\eta \geq 1$  for the shell (or high enough shell velocity) even when the radiative losses accompanying heating and ionization are neglected.

However, the pinch plasma is intensively cooled by soft x-ray emission from the lower than He- and H-like ionization stages. Indeed, the plasma radiative cooling rate is known to be a non-monotonic function of the plasma electron temperature [4, 5]. For attaining the K-shell ionization states during the plasma heating to some optimum temperature [3],  $T_e = T_k$ , where the hot x-ray photons dominate, one must overcome a radiative threshold corresponding to the other emission maximum at  $T_e < T_k$ , which is related to softer (e.g. L- and M-shell) transitions. Otherwise, the abundant soft emission may prevent the plasma from being heated enough to get into the K-shell, which may effectively increase the minimum  $\eta$  numbers necessary for high keV x-ray yields. As the radiation constantly controls the ionization dynamics in plasmas, the value of  $T_k$  depends on the concrete radiative transport conditions or the model used. Therefore, more realistic evaluation of the  $\eta$  parameter demands at least one-dimensional (1D) magnetohydrodynamic calculations accounting for ionization kinetics, radiation production and absorption in the pinch plasma. These calculations show that values of  $\eta$  in the range between 2 and 6 are needed for achieving efficient K-shell emission with available load energies [3].

Then, the electron temperature is known to be highly inhomogeneous at stagnation, the pinch plasma being typically composed of a hot, harder radiation spectrum core surrounded by a colder, softer spectrum exterior [6, 7]. In terms of the optimum temperature, only a fraction of the total load mass can be heated up to  $T_k$  and efficiently produce hot x-rays, the other parts are either under- or over-heated, the latter ones with  $T_e > T_k$  correspond to stripping the plasma to the nucleus. High efficiency of the kinetic-to-keV-radiation energy conversion signifies that this K-shell radiating mass,  $m_k$ , approaches the total available plasma mass. However, even in 1D simulations ensuring the formation of this fraction at the moment of stagnation of the shell is difficult in practice.

The above-mentioned features, or rather difficulties of the plasma heating for multi-keV radiation production, are only aggravated for long-implosion plasma radiation sources, e.g.  $t_0 > 200$  ns [8]. Longer implosion times,  $t_e$  ( $t_e \approx t_0$ ), reduce the risks associated with electric power flow, but may also lead to deterioration of the simple annular shell scheme efficiency in

multi-keV x-rays. Indeed, achieving the high  $\eta$  numbers, or high final velocities prior to thermalization,  $u_{\max}$ , requires larger initial external load radii,  $r_s$  ( $u_{\max} \propto r_s/t_c$ ). Then, as the accelerated plasma shell is Rayleigh-Taylor unstable, larger initial radii lead to higher instability amplitude, decreased homogeneity of the final pinch and thus to further reduction of the radiating mass  $m_t < m_s$ .

All these earlier observations suggest revision of the plasma heating schemes for achieving higher performance for the keV radiation sources, especially in long-implosion regimes. Our starting point will be still that all the available energy is primarily kinetic. We do not consider possible additional plasma heating at stagnation due to enhanced or anomalous dissipation [9]. Let this kinetic energy correspond to a magnetically accelerated plasma shell but not necessarily at high velocity. In other words, we allow  $\eta \sim 1$  or less and consider a heavy plasma shell(s) load matched to a long-rise-time current generator. We no longer rely upon the very efficient plasma ionization when the shell stagnates at the axis because the electrons of the lower- $\eta$  shell are heated slower, from lower-temperature ions.

Instead, when the substantial part of the energy in the system is already kinetic, the inward motion of the shell can be used to compress the plasma inside it. Consider a thin, heavy, high density converging shell filled with a lower density plasma. In this configurations, one may expect direct conversion of the accumulated kinetic energy of the shell into the electron thermal energy of the fill through adiabatic compression, as it happens in typical laser fusion targets [10]. Using this analogy, the shell represents a “pusher”, while the fill acts now similarly to the “thermonuclear fuel”.

This logic brings us to more detailed consideration of shell-on-fill z-pinch configurations in this article. In such configuration, the roles of the external plasma shell and of the on-axis fill are different. The shell serves primarily to ensure efficient magnetic-to-kinetic energy conversion. The fill plasma represents the principal radiator (e.g. argon), which we want to heat up to the temperature optimum for multi-keV x-ray production. In this plasma, we hope to relax all the above-listed difficulties arising during the plasma heating, i.e. to pass the radiative threshold at low  $\eta$ , to provide more homogeneous heating to  $T_e = T_i$  thus increasing the  $m_t$  value, and to achieve all this in a long implosion regime.

The present paper investigates physical mechanisms responsible for this heating in 1D numerical study and it is structured as follows. In Section II our model problem is formulated, as well as the initial and boundary conditions. Section III contains description of the physical model used. Sections IV and V present the results and comparative analysis for annular shell and shell-on-fill implosions accordingly. Finally, all the obtained results are summarized and discussed in Section VI.

## II. PROBLEM FORMULATION

Argon will be considered here as the material for heating and generation of multi-keV x-rays. Our main objective is to identify physical mechanisms responsible for the 1D Z-pinch

ChuvatinPaperArgonEdited2.doc

plasma heating when the initial plasma density distribution changes. We do not look for detailed comparison with existing experimental data and use simplifications both in the problem formulation and in the initial conditions. Existing uncertainties in true experimental conditions (e.g. initial gas conditions, or multi-dimensional effects during implosion) support this simplified approach if the problem is considered in 1D.

We examine two initial density distributions presented in Fig. 1 in cylindrical one-dimensional geometry. The first distribution, Fig. 1(a), is used mainly as a starting point referring to the typical implosion of an annular Ar plasma shell with the initial radius  $r_s = 4$  cm, thickness  $\Delta_s = 3$  mm, uniform density  $\rho_s$  and the mass  $m_s$ . This shell is accelerated by the magnetic field applied at the right boundary. We assume an additional distance of 1 cm between this boundary, which represents the current return in experiments and the shell. The constant density  $\rho_0$  in the figure corresponds to the mass  $m_0 = 1/8$  of the total mass ( $m_s + m_0$ ) [11] and it reflects a simplified view on some residual plasma between the shell and the axis. The shell implosion results will be used for calibration of our model presented in the next Section and they will be compared to the results obtained for the second configuration shown in Fig. 1(b). This configuration represents a shell (of argon or other material) with the same parameters as above imploded onto an Ar on-axis fill with the initial radius  $r_f = 1$  cm, uniform density  $\rho_f$  and the mass  $m_f$ . The residual plasma between the shell and the fill is argon with the initial density always equal to  $\rho_0 = 5 \times 10^{-7}$  g/cm<sup>3</sup>. The initial electron and ion temperatures for all the plasmas in Fig. 1 are equal to 1 eV.

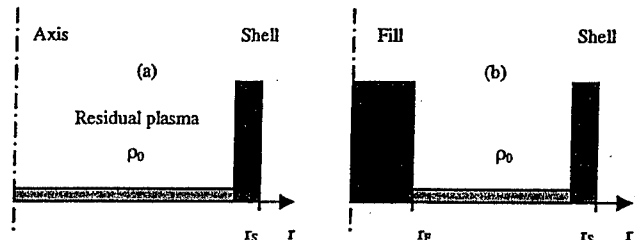


Fig. 1. Two initial density distributions used in the modeling: (a) compression of an annular Ar shell, (b) compression of a shell onto an Ar fill.

An ideal current generator is then taken as the magnetic field source. The current rises in time as  $I(t) = I_0 \sin(\pi/2t_0)$ . The current amplitude,  $I_0 = 8$  MA, and the quarter period,  $t_0 = 250$  ns, roughly correspond to the parameters of an existing long-implosion pulse-power generator Decade Quad [8].

## III. PHYSICAL MODEL

The hydro model we use corresponds to the already widely applied 2-temperature MHD model [12] with the radiation loss term and it is also described elsewhere [13, 14]. We do not look for fitting existing experiments and use classical, rather than enhanced transport coefficients [9].

The magnetohydrodynamic equations below are written in 1D cylindrical geometry and include only the azimuthal component of the magnetic field,  $B_\phi$ . The kinetic coefficients

for the electron thermal conduction and electro-conductivity are thus depending on this azimuthal field ( $\kappa_\perp$ ,  $\sigma_\perp$ ) and they become non-magnetized ( $\kappa_\parallel$ ,  $\sigma_\parallel$ ) at  $B_\phi = 0$  [12]. We start with the equation of continuity,

$$\frac{d\rho}{dt} + \frac{\rho}{r} \frac{\partial}{\partial r}(ru) = 0 \quad (1)$$

and the equation of motion,

$$\rho \frac{du}{dt} = -\frac{\partial}{\partial r} \left( P_e + P + \frac{B_\phi^2}{8\pi} \right) - \frac{B_\phi^2}{4\pi r} \quad (2)$$

$$P = P_i + \mu \frac{\partial u}{\partial r} + q \quad (3)$$

All the notations of physical variables here and below are those conventionally used ( $\rho$  is the mass density,  $u$  is radial velocity,  $T$  is temperature,  $P$  is pressure,  $e$  and  $i$  subscripts denote electrons and ions accordingly, etc). Here  $\mu$  is the physical ion viscosity and  $q$  is the artificial viscosity term, discussed and defined in the next Section.

We proceed with the equations of energy conservation

$$\rho \frac{d\epsilon_i}{dt} = -\frac{P}{r} \frac{\partial}{\partial r}(ru) + \frac{1}{r} \frac{\partial}{\partial r} \left( r \kappa_{i\perp} \frac{\partial T_i}{\partial r} \right) - Q_{ei} \quad (4)$$

$$\rho \frac{d\epsilon_e}{dt} = -\frac{P_e}{r} \frac{\partial}{\partial r}(ru) + \frac{1}{r} \frac{\partial}{\partial r} \left( r \kappa_{e\perp} \frac{\partial T_e}{\partial r} \right) + \frac{1}{\sigma_\perp} \left( \frac{c}{4\pi r} \frac{\partial}{\partial r} (r B_\phi) \right)^2 - \frac{1}{r} \frac{\partial}{\partial r} (r S_r) + Q_{ei} \quad (5)$$

Here  $S_r$  is the radial component of the radiation flux, see below, and  $Q_{ei}$  is the energy exchange term between electrons and ions. The ion-electron equilibration rate is taken from [12]:

$$Q_{ei} = \rho \langle Z \rangle \frac{3m_e T_i - T_e}{m_i^2 \tau_{ei}} \quad (6)$$

where  $\langle Z \rangle$  is the mean charge and  $\tau_{ei}$  is the electron-ion collision time.

The dependencies of the specific internal energies (per ion) and of the pressures on the density and temperature are those classical for an ideal mono-atomic plasma [12], but the specific energy of the electron component includes also the energy spent on ionization,  $I_i$  [13, 14]:

$$\begin{aligned} \epsilon_i &= \frac{3 k_B T_i}{2 m_i} & \epsilon_e &= \frac{3 \langle Z \rangle k_B T_e}{2 m_i} + \frac{I_i}{m_i} \\ P_i &= \frac{k_B \rho T_i}{m_i} & P_e &= \frac{\langle Z \rangle k_B \rho T_e}{m_i} \end{aligned} \quad (7)$$

Finally, the system is completed by the equation for the azimuthal magnetic field

$$\rho \frac{d}{dt} \left( \frac{B_\phi}{r \rho} \right) = \frac{c^2}{4\pi r} \frac{\partial}{\partial r} \left[ \frac{1}{\sigma_\perp} \frac{1}{r} \frac{\partial}{\partial r} (r B_\phi) \right] \quad (8)$$

The radial radiation flux

$$S_r(r) = \int_0^\pi d\theta \int_0^{2\pi} d\phi \sin^2 \theta \cos \phi \int I_\nu(r) d\nu, \quad (9)$$

is calculated from the stationary radiative transport equation solved along the characteristics,  $s$ , which are traced from the spatial points  $r$  [14, 15]:

$$\frac{dI_\nu}{ds} = j_\nu - \kappa_\nu I_\nu \quad (10)$$

Here, as usual in cylindrical geometry,  $\phi$  is the angle between the characteristic projection and the radius-vector and  $\theta$  is the angle between the characteristic and the  $z$  axis.

The radiation-dependent plasma properties, which are  $\langle Z \rangle$ , the plasma opacity,  $\kappa_\nu$ , and the emissivity,  $j_\nu$ , for a given material are tabulated in the same *off-line* fashion as usually are the equations of state [16, 17, 18]. The  $\{\langle Z \rangle, \kappa_\nu, \text{ and } j_\nu\}$  set is thus pre-processed as the function of thermodynamic plasma state (temperature and density,  $T$  and  $\rho$ ) and of the parameter, characterizing the radiation field. It was previously shown that this approach is computer-time efficient in simulations of the radiation-dependent plasma states, which are out of the local thermodynamic equilibrium (LTE). The last parameter may represent the averaged probability-of-escape in [18] or the local radiation intensity in [16, 17]. It is then determined *on-line* in hydro simulations through multi-angle calculations along characteristics either for the mean photon path [18] or for the radiation intensity change along characteristics (Eqs. (9, 10) above) [16, 17].

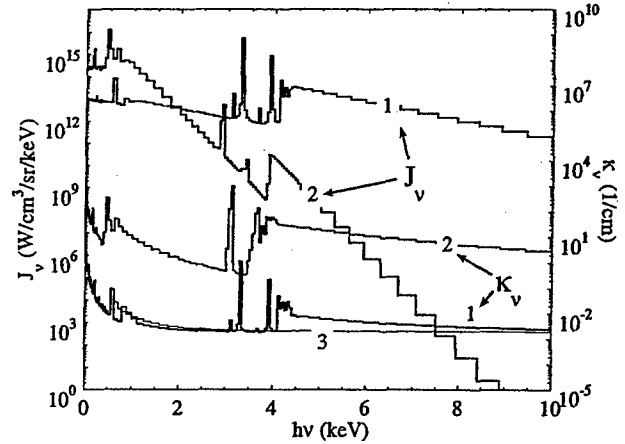


Fig. 2. Example of multi-group LTE emissivity,  $j_\nu$ , and opacity,  $\kappa_\nu$ , used in the simulations. (1) Argon,  $T = 1$  keV,  $\rho = 10^{-2}$  g/cm<sup>3</sup>. (2) Argon,  $T = 200$  eV,  $\rho = 5 \times 10^{-2}$  g/cm<sup>3</sup>. (3) Opacity for nitrogen,  $T = 500$  eV,  $\rho = 10^{-2}$  g/cm<sup>3</sup>. About  $N = 100$  spectral groups were used.

In our physical model, the values of  $j_\nu$  and  $\kappa_\nu$ , as well as the mean charge,  $\langle Z \rangle$ , represent the intensity-dependent on-line corrected non-LTE values through the procedure described in [16]. This allows accessing the  $(T, \rho)$ -tabulated set of  $\{\langle Z \rangle, \kappa_\nu, j_\nu\}$  in the most sophisticated available LTE databases with further detailed consideration of the radiative transfer equation and with correction of the LTE  $\{\langle Z \rangle, \kappa_\nu, j_\nu\}$  table in each spatial cell. Remarkably, comparisons of this LTE-correction algorithm results with those obtained in complete collisional-radiative modeling indicate that both the charge distribution and the detailed  $\kappa_\nu$  and  $j_\nu$  spectra can be fairly well reproduced [16, 19].

The values of  $\kappa_\nu$  and  $j_\nu$  are also photon energy-dependent. As we do not look for detailed comparison of experimental

and synthetic spectra [13] we consider these spectral values to be constant inside each of the  $N$  spectral groups, i.e. inside each of the spectral interval  $[\nu_n, \nu_n + \Delta\nu_n]$ , where  $n$  varies from 1 to  $N$  (the so-called multi-group approximation [20]), Fig. 2. Besides, the quasi-steady-state hypothesis (collisional-radiative processes are much faster than the hydro ones) [21] is also assumed in our model.

Using Eq. (9), the radiation characteristics will be presented by two sets of values integrated over the photon energies. The first set,  $S_{rad}$ ,  $W_{rad}$  and  $E_{rad}$  characterizes the total, spectrally-integrated local flux, power and energy of radiation respectively. The radiation power,  $W_{rad}$ , is obtained from Eq. (9) as  $W_{rad} = 2\pi r_{ex} S_{rad}(r_{ex})$ , where  $r_{ex}(t)$  is the external radius of the plasma shell at each time moment. The radiation energy (total yield),  $E_{rad}$ , represents the time integral of the power  $W_{rad}(t)$ . The second set,  $S_k$ ,  $W_k$  and  $Y_k$  comes from integration only for the spectral groups with  $h\nu > 2.5$  keV and it is the radiation flux, power and the yield from argon in multi-keV x-rays accordingly.

Finally, the system of equations (1-8) written in Lagrangian time derivatives is integrated over each radial zone and then followed in a Lagrangian fashion. About a hundred mass zones were typically used for discretization of each load component in Fig. 1 (i.e. separately for the shell, fill and residual gas) that was sufficient for stable numerical solution of the system (1-8).

#### IV. RESULTS FOR AN ANNULAR SHELL IMPLOSION

We begin with applying the above physical model to a representative example of a conventional plasma shell implosion scheme shown in Fig. 1(a). The model problem is entirely introduced by Sections II and III, except there are two unknowns that we should define, namely the shell mass and the artificial viscosity coefficient  $q$  in Eq. (3).

The latter represents initially a supplementary intrinsic parameter used for numerical treatment of discontinuities [22]. In our calculations this term is chosen as a combination of linear and quadratic artificial viscosities:  $q = \rho (-\mu_1 C_s \Delta u + \mu_2 \Delta u^2)$  if  $\Delta u < 0$  (compression), and  $q = 0$  for  $\Delta u > 0$  (rarefaction) [23]. Here  $C_s$  is the local sound speed,  $\Delta u$  is the radial velocity difference for two neighboring mass zones,  $\mu_1$  and  $\mu_2$  are dimensionless coefficients. Usually, the quadratic viscosity (also called the Neumann viscosity) coefficient,  $\mu_2$ , is responsible for the shock smoothing onto several mass zones, while the linear term is added in order to suppress numerical oscillations behind the shock front [24]. In addition, the choice of  $\mu$  parameters must satisfy  $q < P_t + P_e$  in any mass zone during a simulation. In this case the artificial viscosity value does not influence the numerical solution [24]. The practical values of the Neumann viscosity may lay in the range  $\mu_2 = 0.05$ -2.0 [25]; test modeling of the shock wave and of the Riemann problem [14] have determined  $\mu_1 = 0.05$  and  $\mu_2 = 0.1$  to be sufficient.

At the same time, the artificial term  $q$  represents frequently a free parameter in 1D simulations of z-pinches [13]. Indeed, larger  $\mu_1$  and  $\mu_2$  coefficient values are usually used with respect to the values just necessary for stability of numerical

algorithms. Such a viscous enhancement allows preventing the radiative collapse, improves the agreement between experimental and calculated results [9] and is assumed to emulate the 2- and 3-D effects that limit radial compression in a real situation [26]. In the present study, we also followed this logic by performing calculations with different values of  $\mu_2 > 0.1$  ( $\mu_1 = 0.05$  was fixed).

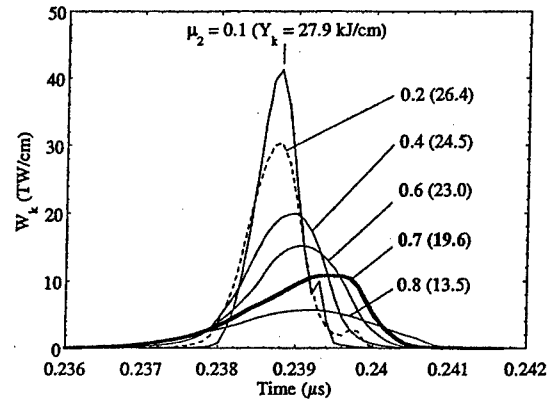


Fig. 3. Multi-keV radiation power,  $W_k$  ( $h\nu > 2.5$  keV), calculated for the shell implosion, Fig. 1(a), with  $r_s = 4$  cm,  $m_s = 420$   $\mu\text{g/cm}$  and for different Neumann viscosity coefficients,  $\mu_2$ . The numbers in parentheses are the x-ray yields,  $Y_k$ , in kJ/cm.

The shell mass, in turn, was chosen to provide the compression time of  $t_c \approx 240$  ns; i.e.  $t_c \approx t_0$ , where  $t_0 = 250$  ns is the quarter-period of the generator current, Section II. The compression time is defined here and below as that between the start of the generator current and the moment of maximum radiation. Numerical "shots" were thus performed for different values of the Neumann viscosity coefficient with varying shell masses. For the initial shell radius fixed at  $r_s = 4$  cm, the optimum mass was found to be  $m_s = 420$   $\mu\text{g/cm}$  and this value was found to be weakly dependent on  $\mu_2$ .

Further criterion for the coefficient  $\mu_2$  was defined in numerical runs with this shell mass and this shell radius. The criterion was based on the simulated multi-keV x-ray radiation power signal,  $W_k$  (see the previous section for definition). Namely, we required the full width at half maximum (FWHM) of the  $W_k(t)$  pulse to be at least 2 ns, that corresponded to some minimum value of  $\mu_2$ . Fig. 3 illustrates the result of these numerical experiments and suggests  $\mu_2 = 0.7$ . We found in simulations that the higher was the value of this coefficient, the wider was the  $W_k(t)$  signal, the lower was the  $Y_k$  yield (Fig. 3) and the larger was the final pinch radius (not presented).

For  $r_s = 4$  cm,  $m_s = 420$   $\mu\text{g/cm}$  and  $\mu_2 = 0.7$ , the calculated K-shell yield was  $Y_k = 19.6$  kJ/cm, Fig. 3. We note that variation of both the shell initial radius and its mass by keeping  $\mu_2 = 0.7$  and constant compression time (i.e. respecting the scaling  $m_s r_s^2 = \text{const}$ ) resulted in lower  $Y_k$  values. Therefore, the above plasma shell parameters correspond here to some optimum, at which, with the chosen pulse-power source, physical model, numerical model and

initial conditions, implosion of an annular plasma shell yields maximum to the energy radiated in keV x-rays.

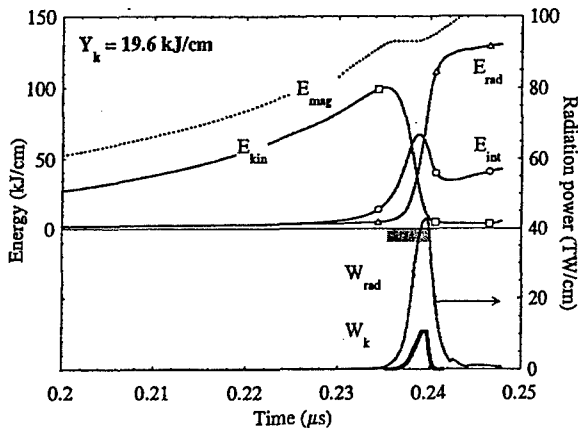


Fig. 4. Energies and radiation power for numerical shot with Ar shell, Fig. 1(a),  $r_s = 4$  cm,  $m_{tot} = 420$   $\mu\text{g/cm}$ . The energies are magnetic (dotted), kinetic (squares), internal (ions + electrons, circles) and total radiated (spectrum-integrated, triangles). The radiation powers are spectrum-integrated,  $W_{rad}$ , and in hot x-rays,  $W_k$ . The gray box indicates approximate duration of the kinetic energy thermalization.

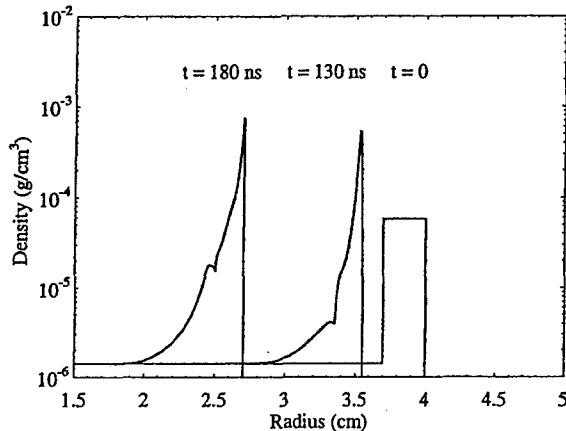


Fig. 5. Ar shell compression, numerical shot of Fig. 4. Spatial distributions of the mass density,  $\rho$ , in the beginning of implosion.

Starting from this point, we keep the Neumann viscosity coefficient fixed at  $\mu_2 = 0.7$ ; all the calculations below have been performed with this default value. Fig. 4 illustrates the energy conversion staging in the scheme with the chosen set of parameters, Fig. 4. Implosion of an annular plasma shell realizes here the regular way of obtaining K-shell hot x-rays with z-pinch already discussed in Section I. Indeed, the magnetic energy is first converted into the kinetic energy during the run-in phase,  $t < 235$  ns. Approximately 100 kJ/cm of the kinetic energy is coupled to the load that corresponds to  $\eta = 2.5$  for our argon shell (minimum energy per Ar ion is taken from [9] in this estimate). When the stagnation begins with a shock reflection from the axis, this kinetic energy starts to be converted into the internal one and the pinch begins to radiate both in soft,  $W_{rad}$ , and in multi-keV x-rays,  $W_k$ , Fig. 3. Presence of the keV x-ray emission indicates that at least

some part,  $m_k$ , of the argon mass is heated to the optimum temperature,  $T_k$ , which was discussed in Section I.

At the beginning of the implosion, the shell is compressed and accelerated by the magnetic field pressure, Fig. 5. Already when the shell traveled the distance comparable to its initial thickness ( $\Delta_s = 3$  mm, see Fig. 1) the established density profile becomes close to that predicted theoretically [27]. The Ohmic heating of the shell is compensated by radiative cooling of the argon plasma. Thus, during the run-in phase, the radiating Ar shell is thin, its thickness is controlled only by the magnetic field skin depth, so that the half of the shell mass is concentrated in the interval of 0.3 mm, as it can be seen in Fig. 5 for  $t = 180$  ns.

Radial distributions appearing in the pinch at implosion,  $t_c = 239.5$  ns, are presented in Fig. 6. The chosen physical values are the plasma density,  $\rho$ , the electron and ion temperatures,  $T_e$ ,  $T_i$ , and the hot radiation flux,  $S_k$ , calculated for the photon energies  $h\nu > 2.5$  keV (see Section III).

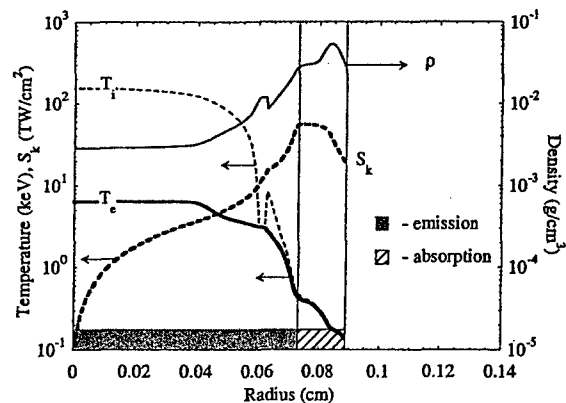


Fig. 6. Ar shell compression, numerical shot of Fig. 4. Spatial distributions of the mass density,  $\rho$ , electron temperature,  $T_e$ , and ion temperature,  $T_i$ , at the moment of peak radiation power,  $t_c = 239.5$  ns. Gray box denotes the hot x-ray production region, hatched box corresponds to the absorption region.

As it can be seen in Fig. 6, the one-dimensional pinch consists of a hot, lower density core surrounded by a colder, higher density exterior. This distribution is typical in 1D modeling of annular shell compressions, where the multi-dimensional convective mixing is not present [7, 13]. The final pinch radius at the moment of maximum radiation power is  $r_{ext} = 0.88$  mm.

The pinch regions, which mostly emit hot x-rays can be characterized by the maximum local radiation power density, simply proportional to  $\rho^2 f(T_e)$  at  $T_e = T_k$  (Section I), where  $f(T_e)$  is the product of the ion mean charge and the cooling rate per free electron per ion [4, 5]. Therefore, the K-shell yield will be proportional to  $\rho m_i f(T_k)$  and the plasma region(s) at some optimum temperature,  $T_k$ , should have the highest density possible and the highest fraction of the total mass possible. Already this logic, which does not take into account the self-absorption of radiation, prompts that highly non-homogeneous density/temperature distributions of Fig. 6 may result in reduced production of hot x-rays. The real situation may be even less advantageous. Indeed, as it was previously

observed [6], a part of the K-shell photons generated by an interior plasma source at  $T_e = T_k$  can be absorbed in colder exterior regions.

In order to quantify these effects, let us recall the physical model described in Section III. The plasma regions, which are intensively cooled by radiation correspond to maximum positive values of the  $[d(rS_r)/dr]/r$  term in Eq. (5). Accordingly, those region where the optimum conditions for K-shell emission are realized correspond to the maximum value of  $[d(rS_r)/dr]/r$ . We found that radial dependencies of  $dS_k/dr$  and  $[d(rS_r)/dr]/r$  were closely proportional to each other, so that comprehensive presentation of the keV x-ray transport could be provided by  $S_k(r)$  spatial distributions.

The pinch region emitting x-rays with  $h\nu > 2.5$  keV, i.e. where  $dS_k/dr > 0$  is denoted by a gray box in Fig. 6. This region has the radius of 0.73 mm and the mass of  $130 \mu\text{g/cm}$ . Less than 30 % of the total argon mass thus produces multi-keV x-rays, the rest of the mass corresponds to the absorption region, where  $dS_k/dr < 0$  (hatched box in Fig. 6). The FWHM of the  $dS_k/dr$  dependence, characterizing the maximum of this function (as well as that of  $[d(rS_r)/dr]/r$ ) is extremely thin (between  $r = 0.69$  mm and  $r = 0.72$  mm) and it corresponds to the plasma temperature range  $T_k = 0.6\text{--}1.1$  keV. In other words, the most intensive argon K-shell emission occurs at these temperatures under thermodynamic and radiation transport conditions realized in this numerical run.

Therefore, three spatial regions could be conventionally defined in Fig. 6. The low-density plasma interior is hot,  $T_e > T_k$ , so that the plasma has burned through the H- and He-like stages and the continuum radiation dominates. However, a plasma layer exists, where the ionization conditions are optimum for K-shell production,  $T_e = T_k$ . This layer is narrow, self-organized at stagnation and its density and mass,  $m_k$ , may apparently be poorly controlled in shell implosion scheme. On the contrary, this K-shell emitting region is surrounded by a colder and denser argon plasma. This plasma exterior has the temperatures  $T_e < T_k$ , at which lower than H- and He-like ionization states dominate and the incoming K-shell photons are absorbed by photoionization.

Finally, the discussed plasma shell run is characterized by  $\eta = 2.5$  for the argon shell,  $Y_k = 19.6$  kJ/cm. The pinch radius at implosion is  $r_{\text{ext}} = 0.88$  mm, the optimum temperatures  $T_k = 0.6\text{--}1.1$  keV exist at the argon plasma densities  $\rho = (1\text{--}3) \times 10^{-2}$  g/cm<sup>3</sup>, so that the hot x-rays emitting mass is  $m_k = 130 \mu\text{g/cm}$  or less. We keep in mind all these characteristics and proceed with the scheme of Fig. 1(b).

## V. RESULTS FOR SHELL-ON-FILL IMPLOSION

The results obtained in the previous section will serve us for comparison with those obtained for the on-axis plasma heating scheme presented in Fig. 1(b). To begin with, we consider the shell and the fill materials both to be argon (Ar/Ar). For this scheme, we already assumed in Section II the same initial shell radius,  $r_s = 4$  cm and we fixed the initial plasma fill radius to  $r_F = 1$  cm. We should choose then the shell and fill masses in order to proceed with detailed analysis for some optimized numerical run. The optimization will be based on

the same principles as for the annular shell, i.e. the compression time has to be close to  $t_c = 240$  ns and the keV x-ray yield,  $Y_k$ , should be maximum in the chosen shot.

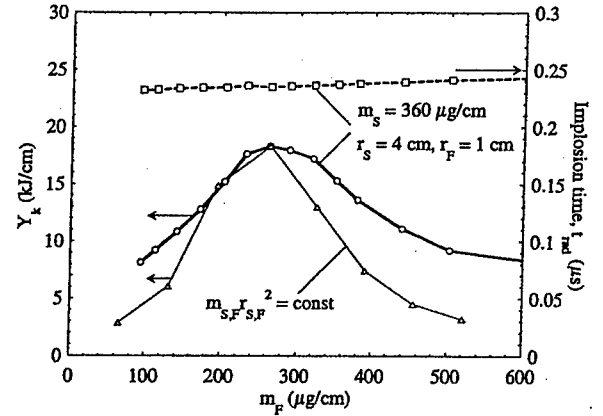


Fig. 7. K-shell yield,  $Y_k$ , and implosion time,  $t_{\text{rad}}$ , dependencies on the fill mass for two cases. Squares and circles correspond to fixed  $m_s$ ,  $r_s$ ,  $r_F$  (see Fig. 1) and varying  $m_F$ . Triangles correspond to  $m r^2 = \text{const}$  scaling for both the shell and the fill.

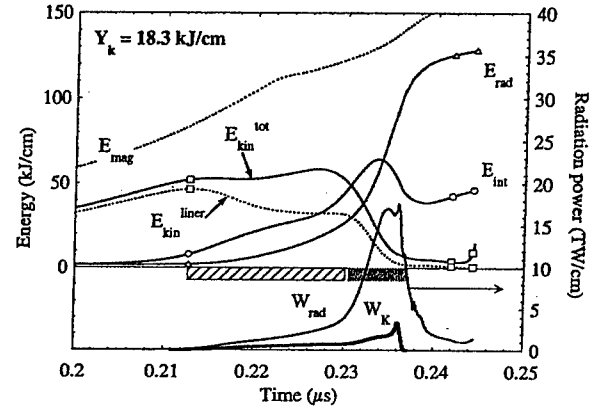


Fig. 8. Energies and radiation power for numerical shot with Ar shell and Ar fill (Ar/Ar), Fig. 1(b),  $r_s = 4$  cm,  $m_s = 360 \mu\text{g/cm}$ ,  $r_F = 1$  cm,  $m_F = 260 \mu\text{g/cm}$ . The energies are magnetic (dotted), total kinetic ( $E_{\text{kin}}^{\text{tot}}$ , squares), shell kinetic ( $E_{\text{kin}}^{\text{shell}}$ , squares), internal (ion + electron, circles) and total radiated (spectrum-integrated, triangles). The radiation powers are spectrum-integrated ( $W_{\text{rad}}$ ) and in hot x-rays ( $W_k$ ). The hatched and gray boxes denote approximate durations of shock-wave and quasi-adiabatic heating processes accordingly.

Fig. 7 summarizes a number of numerical runs performed in the shell-on-fill configuration. We first pay attention to the case when the shell and fill initial radii are fixed (curves with squares and circles). It can be seen that the implosion time is controlled almost exclusively by the shell mass, so that  $m_s = 360 \mu\text{g/cm}$  is the value we can use. In its turn, the choice of the fill mass is  $m_F = 260 \mu\text{g/cm}$  as this value yields maximum to the energy radiated in keV x-rays,  $Y_k = 18.3$  kJ/cm. We immediately notice that the K-shell yield for this optimized fills mass is about the same as that obtained in optimization of the single shell implosion (19.6 kJ). However, we continue with the detailed characterization of the fill heating and radiation production.

Similarly to Fig. 4, Fig. 8 illustrates dynamics of the energy conversion for the above chosen shell-on-fill numerical run conditions. Again, the magnetic energy is first converted into the kinetic one during the run-in phase,  $t < 212$  ns.  $E_{kin}^{shell}$ , which is the kinetic energy calculated for 100 mass zones of the plasma shell, reaches the maximum value of 46 kJ/cm that corresponds to  $\eta = 1.3$  for the argon shell.

The plasma heating and radiation production can be conventionally divided into two phases in Fig. 8. The K-shell photons start to be emitted already after the shell strikes the fill. This multi-keV x-ray prepulse is then followed by the main  $W_k$  peak corresponding to the final thermalization of the shell kinetic energy. Time-dependent spatial distributions of the physical values selected in Section IV will help us in analysis of this staged plasma heating.

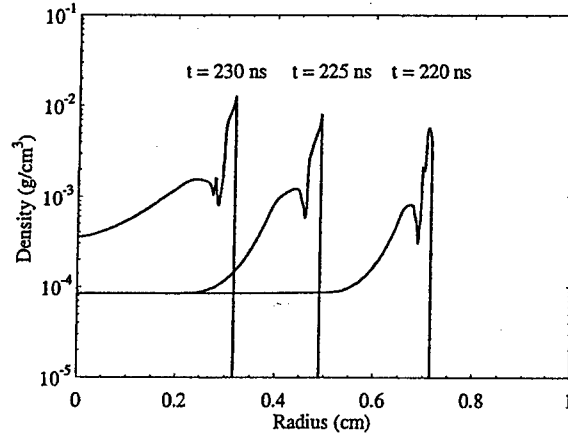


Fig. 9. Shock-wave in argon fill, Ar/Ar numerical shot of Fig. 4. Spatial profiles of the mass density,  $\rho$ , at three consecutive moments of time.

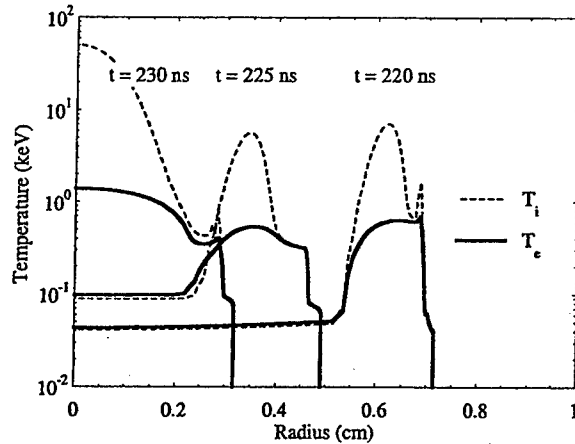


Fig. 10. Ion heating at the shock, Ar/Ar numerical shot of Fig. 4. Spatial profiles of the ion,  $T_i$ , and electron,  $T_e$ , temperatures at three consecutive moments of time.

In the beginning of compression the profiles reproduce those of Fig. 5 and we do not present them here. Figs. 9 and 10 show spatial distributions of the plasma density and temperature already after the shell hit the fill, i.e.  $r_{ext}(t) < 1$  cm. As one can see in Fig. 9, a shock wave is generated in the

fill by the shell pusher. This leads first to heating of the ions at the shock front. Then the ions transfer their internal energy to electrons due to the exchange terms in Eqs. (4-5), Fig. 10.

Therefore, the argon fill plasma is preheated (in terms of electron temperature) already at this stage. Electron thermal conduction leads to formation of an inward-propagating heat wave ahead of the viscous density jump in the shock front [28], Fig. 10. A non-negligible amount of K-shell radiation, corresponding to the  $W_k$  prepulse in Fig. 8 indicates that the radiative threshold discussed in Section I is passed in the heated fill plasma portions.

As the electron temperature governs to a great extent the K-shell production process, let us perform an estimate of this parameter at the shock-wave plasma heating stage. The shock heats first the ions at the front, the heating being determined by the compression term, first term in the right-hand side of Eq. (4). The kinetic energy per ion is thermalized at the viscous jump, so that

$$T_i = \frac{m_i u^2}{3} \quad (11)$$

We further neglect the radiation losses in Eq. (5). Conventional accounting of these losses, as well as the energy spent on ionization is frequently performed by correction of the adiabatic coefficient  $\gamma$  (specific heats ratio) [28]. We consider the non-magnetized plasma in front of the shock and also neglect the Joule heating term in this equation.

We rewrite Eq. (5) in the reference frame moving with the shock and, for simplicity, in plane geometry. Eq. (5) then becomes

$$\begin{aligned} n_e \frac{dT_e}{dt} &= -(\gamma - 1) n_e T_e \frac{\partial u}{\partial x} \\ &+ (\gamma - 1) n_e \frac{3m_e T_i - T_e}{m_i \tau_{ei}} + \frac{\partial}{\partial x} \left( \kappa_e^I \frac{\partial T_e}{\partial x} \right), \end{aligned} \quad (12)$$

$$\kappa_e^I = \gamma'_0 \frac{n_e T_e \tau_{ei}}{m_e},$$

where  $\kappa_e^I$  is the electron thermal conduction coefficient in non-magnetized plasmas,  $\gamma'_0$  is a coefficient depending of the mean ion charge [12] and  $\tau_{ei}$  is the electron-ion collision time

$$\tau_{ei} = C \frac{T_e^{3/2}}{n_i \langle Z \rangle^2} \quad (13)$$

with  $C = 3.5 \cdot 10^4$ ,  $T_e$  in eV and  $n_i$  in  $\text{cm}^{-3}$  [12].

We consider  $T_i \gg T_e$ ,  $T_i$  is defined by Eq. (11) and introduce some characteristic space-,  $\delta$ , and time scale,  $\tau$ , of the electron temperature variation,  $\partial \tau \sim u$ , where  $u$  is approximately equal to the shell velocity. Eq. (12) provides then the following estimate for the electron temperature change rate

$$\frac{dT_e}{dt} \approx (\gamma - 1) \left( T_e \frac{u}{\delta} + \frac{m_e u^2}{\tau_{ei}} \right) - \frac{\kappa_e^I}{n_e} \frac{T_e}{\delta^2} \quad (14)$$

The compression work done on the electrons, as well as their heating from the ions are positive contributions to the right-hand side of Eq. (14), while the heat conduction decreases the temperature at the shock front by transmitting it

to the unperturbed inward plasma, so that the corresponding term in (14) is negative. As Fig. 9 suggests, competition of these processes leads to a rapid establishment of a quasi-stationary value of the electron temperature,  $dT_e/dt \approx 0$ . In order to evaluate this value, we introduce a dimensionless parameter

$$\chi = \frac{\tau}{\tau_{el}} \left( \frac{u}{u_{Te}} \right)^2 \quad (15)$$

where  $u_{Te} = (T_e/m_e)^{1/2}$  is the electron thermal velocity. Substitution of this parameter in Eq. (14) shows that the balance between the compression/heating and the thermal conduction is controlled by the value of  $\chi$ :

$$(\gamma-1)(1+\chi) - \frac{\gamma_0}{\chi} = 0 \quad (16)$$

For  $\gamma_0 \approx 8$  (see [12] for the case  $\langle Z \rangle \gg 1$ ) the last equation yields

$$\chi \approx \sqrt{\frac{\gamma_0}{\gamma-1}} \quad (17)$$

The electron temperature can be estimated from Eq. (15):

$$T_e = \left( \frac{m_e n_e \delta u \langle Z \rangle^2}{C \chi} \right)^{2/5} \quad (18)$$

The last equation can be rewritten in dimensional units:

$$T_e = \left( 10^4 \frac{\delta \rho_F u \langle Z \rangle^2}{\chi A} \right)^{2/5} \quad (19)$$

where  $T_e$  is in eV,  $\delta$  is the heat wave front width in cm,  $\rho_F$  is the fill density in g/cm<sup>3</sup>,  $u$  is the shell velocity in cm/s. Assuming for the parameters of our numerical run  $\delta \sim r_F/10$  (Fig. 10),  $\rho_F \approx (1-3) \times 10^{-4}$  g/cm<sup>3</sup>,  $u \approx 6 \times 10^7$  cm/s,  $\langle Z \rangle = 16$ ,  $A = 40$ , and  $\chi = 3$  (for  $\gamma = 5/3$ ) we obtain  $T_e \approx 0.7$  to 1 keV.

Somewhat smaller  $T_e$  values (500 to 700 eV) appearing at the shock front in Fig. 10 can be explained by the fact that a part of the electron thermal energy goes to ionization and radiation. This effect can be taken into account in Eq. (19) by effective reduction of the adiabatic coefficient [28] and corresponding increase of the  $\chi$  value, see Eq. (17). Using smaller  $\gamma$ ,  $\gamma^* = 1.2-1.3$ , allows matching the theoretical estimate with the numerical result. The impact of these energy channels is more pronounced for higher fill densities and limits in fact the electron temperature rise with  $\rho_F$  in the scaling (19).

This scaling also suggests that the shell velocity should not be too high. Indeed, imagine that the fill is heated to the electron temperature, which is optimum for hot radiation production already at the shock wave stage (one may assume  $T_e = T_k \sim 1$  keV for argon, see Fig. 6 in Section IV). In this case, the shocked fill could radiate the K-shell from still relatively low density, while the final compression would lead to overheating the argon and to the burning through the H- and He-like ionization states. Rather, at the optimum shown in Fig. 7, we hypothesize that the fill is preheated by shock just sufficiently for passing the radiative threshold in argon at low densities, so that not too much radiation energy is lost in soft

transitions. On the contrary, the later compression of the fill, which starts at  $t = 230$  ns in Fig. 10 must do the main job for heating the argon to  $T_e = T_k$  at higher densities. We further consider this second stage of heating.

Similarly to Fig. 6, we present here the spatial distribution of the physical parameters at maximum radiation,  $t_c = 236$  ns. External plasma radius at final implosion:  $r_{ext} = 1.25$  mm. The FWHM of the  $dS_k/dr$  profile (as well as that of  $[d(rS_k)/dr]/r$ ) is much wider than for the annular-shell run of Fig. 6. It is denoted by a dark gray box in Fig. 11 and corresponds to the plasma temperature range  $T_k = 0.7-1.5$  keV. As for the case of the annular shell implosion, these temperatures could be considered as optimum for the Ar K-shell radiation production in the conditions realized here.

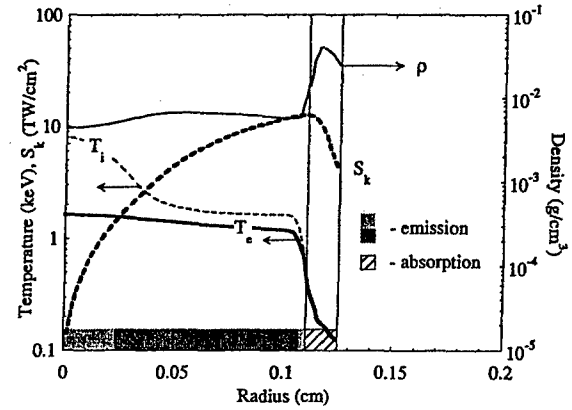


Fig. 11. Ar/Ar compression shot of Fig. 8. Spatial distributions of the mass density,  $\rho$ , electron temperature,  $T_e$ , ion temperature,  $T_i$ , and hot radiation flux,  $S_k$ , at the moment of peak radiation power,  $t_c = 236$  ns. Gray boxes denote the hot x-ray production regions, hatched box corresponds to the absorption region.

The picture, presented in Fig. 11 could be interpreted in the following way. The electron component is first preheated by the shock wave in the fill plasma, its temperature is estimated by Eq. (19) (with corrected  $\gamma^* = 1.2-1.3$ ) and it is equal to  $T_1 = 500-700$  eV. When the temperature front reaches the axis, Fig. 10, the fill compression starts. This compression, from the radius  $r_1 \approx 0.3$  cm (Fig. 10) to the final external radius  $r_2 \approx 0.1$  cm (Fig. 11) can be considered as quasi-adiabatic during the time interval, when the compression increases the internal energy faster than it is lost through radiation, see Fig. 8. In this case, not only do we increase the density of the argon plasma during this second stage, but also increase directly the electron temperature:

$$T_2 = T_1 \left( \frac{r_1}{r_2} \right)^{2(\gamma^*-1)} \quad (20)$$

Again, using the adiabatic coefficient corrected to radiation,  $\gamma^* = 1.2-1.3$ , yields the values of the final electron temperature,  $T_2 = 0.7-1.3$  keV, quite close to those in numerical simulation of Fig. 11.

It may seem surprising in Fig. 11 that these high temperatures are confined to the fill plasma, i.e. that the fill is not rapidly cooled down by the much colder and denser surrounding plasma of the shell. In order to understand why it



happens, we refer to the plasma density profiles presented in Fig. 5. As it was mentioned in Section IV, those profiles are self-similar and they are formed at the early stage of the shell acceleration. As the argon shell intensively radiates, its temperature is low and the plasma shell thickness is shown to be determined only by the magnetic field skin depth [27]. Therefore, this magnetic field must exist in the shell plasma also at the shock wave and quasi-adiabatic compression stages. In this case, the heat flux, the second term in the right-hand side of Eq. (5), can be limited by the effective decrease of the electron heat conductivity coefficient,  $\kappa_e^{-1}$ .

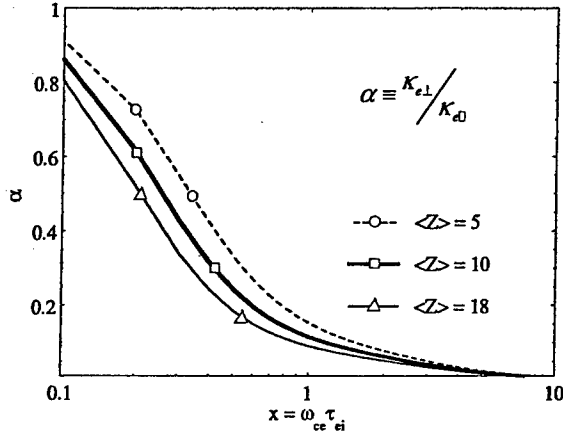


Fig. 12. Ratio,  $\alpha$ , of the magnetized-to-unmagnetized electron heat conduction coefficients as a function of the value  $x = \omega_{ce} \tau_{ei}$  for different mean charge values, [12].

Fig. 12 shows the ratio of the magnetized electron heat conductivity coefficient to the unmagnetized one in the physical model used [12]. This ratio is roughly inversely proportional to  $x^2$ , where  $x = \omega_{ce} \tau_{ei}$  ( $\omega_{ce}$  is the electron gyrofrequency) and it weakly changes with the ion mean charge. As it can be seen, the heat flux suppression is possible already at moderate values of  $x$ : the heat conduction coefficient decreases 2-3 times already at  $x = 0.5$ .

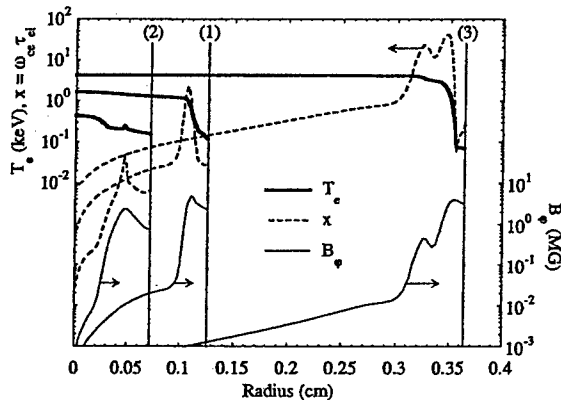


Fig. 13. Temperature spatial profiles at  $t = t_e$  for three numerical shots corresponding to the  $m^2 = \text{const}$  scaling in Fig. 7. (1) optimum shell and fill masses,  $m_s/m_F = 360 \mu\text{g}/260 \mu\text{g}$ ,  $Y_k = 18.3 \text{ kJ}$  (Fig. 8). (2)  $m_s/m_F = 720/520$ ,  $Y_k =$

3.2 kJ. (3)  $m_s/m_F = 180/130$ ,  $Y_k = 6 \text{ kJ}$ . Shell and fill initial radii change in each case, being inversely proportional to the square root of the corresponding mass.

We can see how efficient this magnetic heat confinement is in the following way. Let us vary simultaneously the shell and the fill initial radii and masses while keeping  $m_s r_s^2 = \text{const}$  and  $m_F r_F^2 = \text{const}$ . As a result, we do not change noticeably the implosion time, but perform numerical runs with either more or less heated fill material than in the optimum case of Fig. 8. As, for example, for a lower fill mass we also get higher implosion velocities, or *vice versa*, one can assume over- or underheating of the fill material at stagnation.

Indeed, Fig. 13 shows the resulting profiles for the electron temperature, for the magnetization parameter  $x = \omega_{ce} \tau_{ei}$  and for the magnetic field. All the profiles are obtained in numerical runs with either the optimum masses (Fig. 8), or with two times increased masses (the shell and fill radii were decreased  $\sqrt{2}$  times), or with two times decreased masses (radii increased  $\sqrt{2}$  times). In the latter case, the argon fill temperature is as high as 4 keV but the magnetic heat confinement is very efficient ( $x = 40$  corresponds to  $\alpha = 3 \times 10^{-4}$ ) and maintains high electron temperature gradient between the hot fill and the cold shell. For an overmassed (underheated) fill this effect is moderate, but still visible as a local maximum of  $x(r)$ . Each time, a frozen-in magnetic field of small but sufficient magnitude is present. Since  $x \propto B_\phi T_e^{3/2} / n_e \langle Z \rangle$ , we have here a self-adjusting magnetization, which is just sufficient for thermal insulation.

As we repeatedly state in this paper, over- or underheating of the fill material result in decreased K-shell yields. This can be seen in Fig. 7 which represents the calculated yield in different numerical shots with  $m_s r_s^2 = \text{const}$  and  $m_F r_F^2 = \text{const}$ . The left part of the  $Y_k$  curve (triangles) corresponds to smaller amounts of the fill material and higher implosion velocities. At stagnation, we have high fill temperatures (case 3 in Fig. 13) so that the argon ions are stripped to the nucleus. The overmassed loads yield low temperatures (case 2 in Fig. 13), intense soft radiation, and further increase of the fill mass above  $m_F > 520 \mu\text{g}/\text{cm}$  finally results in radiative collapse [26].

Let us come back to the discussion of the optimized shot of Fig. 11. The entire radiating region (light gray box) has the radius of 1.14 mm and the mass of  $290 \mu\text{g}/\text{cm}$ . Therefore, the entire fill mass, or about a half of the total argon mass is heated to the optimum temperature,  $T_k \sim 1 \text{ keV}$ , and participates in the K-shell radiation production. This mass is at least two times higher than that estimated in Section IV for the single shell implosion. This mass can be apparently better controlled because from the very beginning we designated the fill to be the principal radiator and we succeeded in achieving a more homogeneous heating of argon in it. However, this mass appears to be at lower density  $\rho_F = (5-9) \times 10^{-3} \text{ g/cm}^3$  (instead of  $\rho_S = (1-3) \times 10^{-2} \text{ g/cm}^3$  in Fig. 6) and that is more deceiving, the same effect of radiation self-absorption in the outer denser/colder plasma layer is present both in the annular shell, Fig. 6, and in the shell-on-fill configurations, Fig. 10.

The effect of self-absorption seems to partially cancel the advantages of homogeneous heating and better controlled radiating mass. One of the possible ways to decrease the opacity impact was proposed and tested in [29, 30] and it consists of using mixtures of materials instead of pure radiator material. Usage of two elements with similar atomic numbers was shown to increase the hot radiation power in the optically thick case. However, one could also suggest another concept, when the radiator and absorber materials are very different and separated in space. For example, we already came to the conclusion in Section I that the roles of the shell and the fill are different in principle in the discussed load design. The shell is supposed to be used only as a reservoir of the kinetic energy, then as a pusher. It can serve in this capacity as well if a different material than argon is used. Therefore, a lower-atomic-number shell material having lower opacity in the radiator K-shell photon energy range could provide reduced absorption by photoionization and thus could lead to increased number of K-shell photons escaping the pinch. For example, as one can see in Fig. 2, using nitrogen instead of argon decreases the opacity by an order of magnitude in the shell exterior (compare opacities 2 and 3 in Fig. 2 in the photon energy range under interest).

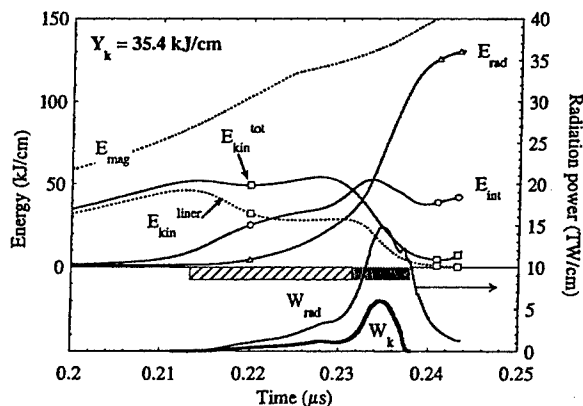


Fig. 14. Energies and radiation power for numerical shot with N shell and Ar fill (N/Ar), Fig. 1(b),  $r_s = 4$  cm,  $m_s = 360$   $\mu\text{g/cm}$ ,  $r_f = 1$  cm,  $m_f = 260$   $\mu\text{g/cm}$ . All the notation is the same as in Fig. 8.

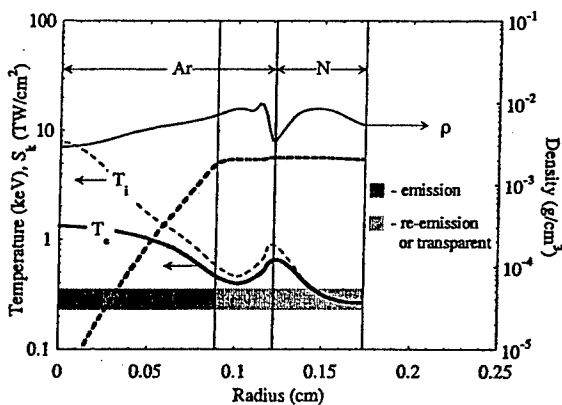


Fig. 15. N/Ar compression shot of Fig. 14. Spatial distributions of the mass density,  $\rho$ , electron temperature,  $T_e$ , ion temperature,  $T_i$ , and hot radiation flux,  $S_k$ .

ChuvatinPaperArgonEdited2.doc

at the moment of peak radiation power,  $t_c = 234.5$  ns. The dark gray box denote the hot x-ray production region.

The next numerical run that we present here was performed for the same conditions as that of Fig. 8, except the shell material was nitrogen. Fig. 14 shows that most of the energy balance features does not change with respect to the similar Ar/Ar simulation. The radiation pulse includes again a relatively long prepulse denoted by the hatched box in the figure, followed by the main radiation peak (gray box) with the maximum at  $t_c = 234.5$  ns. Analysis of the spatial profiles at different moments of time confirmed these two parts of radiation to be generated during the shock heating of the fill and at the final quasi-adiabatic compression accordingly. The electron temperature of the fill at the preheating stage appeared to be approximately the same as both in Fig. 9 and in the estimate of Eq. (19).

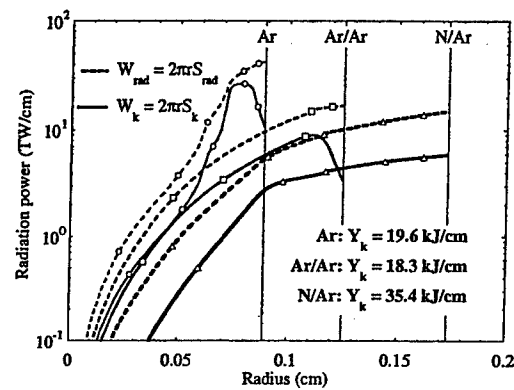


Fig. 16. Comparison of the K-shell local radiation power distributions for the discussed numerical shots: annular Ar shell (circles), Ar shell on Ar fill (squares) and N shell on Ar fill (triangles), see Figs. 4, 8 and 14.

However, the photon energy repartition in the output radiation in Fig. 14 indicates that the efficiency of the hot-radiation production is improved. Indeed, the most important difference between the numerical run of Fig. 14 and the Ar/Ar run of Fig. 8 is in considerably increased K-shell radiation yield,  $Y_k = 35.4$  kJ/cm (instead of  $Y_k = 18.3$  kJ/cm in the Ar/Ar case). Fig. 15 shows that the main physical effect, which is responsible for this increase is the reduced radiation self-absorption in the pinch exterior.

The plasma shell in Fig. 15 is thicker, of lower density and hotter than the external argon part in Fig. 11 that can be explained by less intensive radiative cooling of nitrogen compared to argon. The pinch external radius at stagnation becomes thus larger and reaches  $r_{ext} = 1.73$  mm. The entire fill mass (260  $\mu\text{g/cm}$ ) either produces or transports the K-shell photons without decreasing the  $S_k$  flux value. The Ar K-shell emission region,  $dS_k/dr > 0$ , corresponds to the electron temperature range  $T_e = 0.5\text{--}1.3$  keV and to the argon fill densities  $\rho_F = (3\text{--}7) \times 10^{-3}$  g/cm³, i.e. almost reproduces the values of the Ar/Ar result in Fig. 11. Thus, usage of a lower-atomic-number material for the shell allows one to keep the general advantages of the shell-on-fill heating scheme, decreasing at the same time the K-shell photon trapping in the

cold outer plasma layers, as it may occur in conventional annular shell compression schemes [6].

Radiative properties of all three discussed configurations, i.e. annular Ar shell, Ar shell on Ar fill and N shell on Ar fill are summarized in Fig. 16 and 17. Self-absorption of the hot x-rays, present both in Ar and Ar/Ar simulations is absent in the N/Ar run, Fig. 16. The N/Ar configuration yields the largest-diameter pinch and the longest FWHM of the radiation pulse. Synthetic spectrum calculated for this configuration, Fig. 17, is shifted to softer photon energies, presumably because of lower nitrogen opacity in the shell plasma, Fig. 2, allows more soft radiation to escape from the argon fill. On the contrary, relative contribution of the abundant L-shell transitions in argon at low temperatures (photon energies below about 1 keV) is reduced, because the entire argon mass is now heated, see Fig. 15.

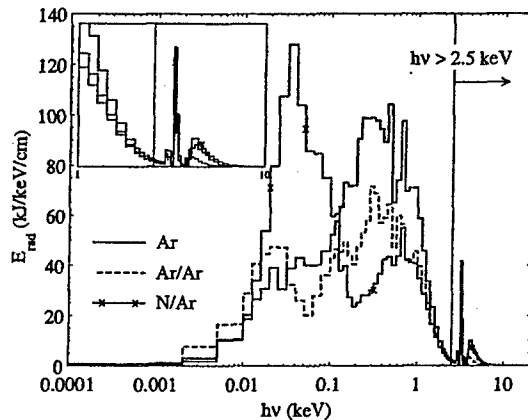


Fig. 17. Time-integrated multi-group synthetic spectra for the discussed numerical shots, Figs. 4, 8 and 14.

## VI. SUMMARY AND DISCUSSION

In summary, we propose to design a structured Z-pinch load with one or two heavy outer plasma shell(s) with low-density on-axis mass (e. g., central gas jet) producing most of the radiation. We further analyze the physical mechanisms responsible for the heating of this on-axis plasma fill to high electron temperatures. As a representative example, we have considered argon as the material to be heated in view of possible optimization of the argon K-shell photons production especially in the long-implosion-time regimes. The proposed initial density distribution with a solid fill compressed by an accelerated plasma shell was simulated numerically in the framework of a 1D radiation magnetohydrodynamic model.

We were not aiming at detailed comparisons with existing experimental data and used several simplified assumptions both in the physical model and in the problem statement. The initial distributions of Fig. 1 with the shell mass assigned to a narrow radial size may certainly differ from those measured for the real gas-puffs. For example, more radially dispersed annular gas flows were already used in the experiment and they were shown to provide higher K-shell yields (e.g., see [2] and the references therein). At the same time, the difference in initial radial density profiles is known to make little effect on

the K-shell yield predicted by 1D radiation-hydro models. Indeed, a distributed fuzzy shell transforms itself into a thin shell during a 1D simulation of implosion [27], producing essentially the same K-shell yield. The effect of the influence of initial conditions can be reasonably explained by a higher 2D stability of implosion in the more filled-in part of the gas flow [2]. Since we are concerned with 1D considerations, the choice of a thin shell in Fig. 1 as a baseline example for comparison is thus legitimate.

We have also used an ideal current generator instead of considering examples of different existing generators having limited impedance. The current waveform introduced in Section II thus differs from those appearing in the experiment. However, the primary energy used for plasma heating in both schemes of Fig. 1 was the kinetic energy. This energy is converted from the magnetic energy and the realistic current pulse shape only changes the ratio of this conversion, still keeping it around the factor of 0.5 [11]. Control numerical shots that we do not present here confirmed that the discussed implosion physics is independent, and the absolute yield values are weakly dependent on the current wave form when the total delivered magnetic energy remains unchanged.

However, even with all these idealizations of the problem the most important and practically interesting parameter characterizing any K-shell radiator scheme must be the yield in multi-keV x-rays. In order to quantify this yield parameter for the new load design with our radiation coupling model, which uses a number of simplifications (such as quasi-stationarity of ionization and multi-group spectral approach) the results were systematically compared, or "calibrated" with those obtained for a conventional annular shell(s) implosion scheme.

With this purpose, we started a comparative study by modeling first the implosion of a typical z-pinch configuration, which is regularly used for generation of the K-shell and harder x-rays in experiments. In this configuration, the main energy source in the on-axis plasma at stagnation is the ion thermal energy, which must be rapidly transferred to the electrons, simultaneously with the intensive radiative cooling in soft quanta. Fast ion-to-electron thermal energy transfer during the short time of inertial and magnetic pinch confinement can be then insured only by achieving high  $\eta$  values (high velocities) of the shell. This last requirement can be difficult to fulfill in the long-implosion-time regimes, as it implies larger initial diameter for a lighter, presumably more 2D unstable shell.

Our results for the annular shell implosion showed that only a part of the argon shell mass was heated to the temperature,  $T_e = T_i$ , which is optimum for efficient hot x-ray emission. This mass portion (less than 30% of the argon mass) was arbitrarily forming at final implosion and could hardly be controlled even in the 1D case. The main argon mass was radiatively cooled by the softer than the K-shell transitions and was not hot enough to get into the He- and H-like ionization state. In addition, the K-shell emission region appeared to be surrounded by a colder radiation absorbing

exterior, similarly to what was previously observed and discussed (see e.g. [6]).

The alternative shell-on-fill configuration introduced and analyzed in the present paper challenges using additional energy transfer channels for electron heating than just the ion-to-electron exchange term, Eq. (6). This load design is based on the analogy with the laser fusion targets that consist of heavy "pusher(s)" and of a low-density "thermonuclear fuel". The shell is a "pusher", transferring the accumulated kinetic energy directly into the electron thermal energy of the fill through quasi-adiabatic compression. The fill plays the role of a "fuel", which should be homogeneously heated to the optimum electron temperature  $T_e$ . Therefore, the fill plasma is supposed to be the main radiator, and not the shell.

First results for this concept showed that a two-stage fill heating could be realized. At the first stage the on-axis radiator material is preheated by shock wave and electron thermal conduction. At some optimum conditions, this preheating allows to overcome the radiative threshold in argon at still low density, so that not too much energy is radiated in soft quanta. When the electron heat wave reaches the axis, the further quasi-adiabatic compression permits direct heating of the electron component on the background of increasing plasma density. In the numerical shots providing the highest K-shell yield almost the entire fill plasma could be homogeneously heated to the temperature  $T_e = T_k$  during this second stage. Therefore, the entire radiator mass participated to the keV emission production. It was demonstrated that the heat flux from the hot fill was suppressed by the magnetic field frozen into the cold shell plasma. The heat insulation was shown to be self-adjusting, so that even higher-than-optimum temperatures were still confined.

However, if the shell and fill materials are both argon, the compressed denser and colder shell plasma absorbed a considerable amount of hot x-rays at stagnation. If a lower-atomic-number material is used for the shell (the example of nitrogen was presented), the K-shell self-absorption was shown to be reduced and a higher multi-keV yield from the argon fill could be obtained. At the same time, nitrogen is still a good soft x-rays radiator (if compared to helium or hydrogen, for example) to form a compact magnetized plasma shell during the run-in phase. This low-internal-energy and sufficiently thin shell is less dependent on the initial conditions (e.g., the initial shell thickness) and can still provide a hard enough collision with the on-axis fill target.

Analytical estimates suggest that the maximum shell velocity should not be too high in order to avoid overheating of the argon fill already in the converging shock wave. The shell can be heavy, and not necessarily at large initial radius, thus making the suggested load design potentially more robust.

To conclude, the shell-on-fill configuration may be beneficial in comparison with the conventional annular plasma shells. The identified advantages consist in relaxing the high- $\eta$  requirement for the whole load mass, staged heating that permits passing the radiative threshold without too much losses in soft quanta, more homogeneous heating of the

radiator material, and increasing the mass participation in the K-shell radiation production. All these advantages are particularly important in the long-implosion-time regimes.

We should note that some recently performed experiments [31, 32] appear to confirm that the presence of a noticeable-mass axial plasma column inside the annular imploding shell(s) increases the K-shell emission. Further work should thus include simulations of more realistic initial density distributions. Then, some initial parameters were fixed almost arbitrary in our study, inside a reasonable margin of values (e.g., initial shell and fill radii), so that a more systematic optimization of the initial conditions is needed. Our concept and conclusions should also be verified with more detailed physical and numerical models, especially in more realistic multi-dimensional simulations and/or including non-stationary ionization model and radiative transfer in spectral lines.

## REFERENCES

- [1] K. Matzen, "Z pinches as intense x-ray sources for high-energy density physics applications", *Phys. Plasmas*, Vol. 4, No. 5, pp. 1519-1527, 1997.
- [2] H. Sze, P. L. Coleman, J. Banister, B. H. Failor, A. Fisher, J. S. Levine, Y. Song, E. M. Waisman, J. P. Apruzese, R. W. Clark, J. Davis, D. Mosher, J. W. Thornhill, A. L. Velikovich, B. V. Weber, C. A. Coverdale, C. Deeney, T. L. Gilliland, J. McGurn, R. B. Spielman, K. W. Struve, W. A. Stygar, and D. Bell, "Efficient argon K-shell radiation from a Z pinch at currents >15 MA", *Phys. Plasmas*, Vol. 8, No. 7, pp. 3135-3138, 2001.
- [3] K. G. Whitney, J. W. Thornhill, J. P. Apruzese, and J. Davis, "Basic considerations for scaling Z-pinch x-ray emission with atomic number", *J. Appl. Phys.*, Vol. 67, No. 4, pp. 1725-1735, 1990.
- [4] D. E. Post, R. V. Jensen, C. B. Tarter, W. H. Grasberger, and W. A. Lokke, "Steady-state radiative cooling rates for low-density, high-temperature plasmas", *At. Data Nucl. Data Tables*, Vol. 20, No. 5, pp. 397-439, 1977. See p. 410 for the Ar cooling rate.
- [5] V. I. Gervids, A. G. Zhidkov, V. S. Marchenko, and S. I. Yakovlenko, "The kinetics of radiation by multiply charged ions in thermonuclear plasmas," in *Reviews of Plasma Physics*, vol. 12, M. A. Leontovich and B. B. Kadomtsev, Ed. New York: Consultants Bureau, 1987, pp. 207-272.
- [6] J. W. Thornhill, K. G. Whitney, J. Davis, and J. P. Apruzese, "Investigation of K-shell emission from moderate-Z, low- $\eta$  (-velocity), Z-pinch implosions", *J. Appl. Phys.*, Vol. 80, No. 2, pp. 710-718, 1996.
- [7] K. G. Whitney and J. W. Thornhill, "The influence of temperature gradients on the distribution of axial current in large current Z-pinch implosion, *IEEE Trans. Plasma Sci.*, Vol. 26, No. 4, 1168-1178, 1998.
- [8] J. Davis, B. V. Weber, J. P. Apruzese, J. W. Thornhill, A. Velikovich, M. Krishnan, P. Coleman, H. Sze, J. Levine, Y. Maron, and I. Vitkovitsky, "Recent progress in DoD's program to develop Ar K-Shell X-ray radiation source", in *Proc. 14<sup>th</sup> IEEE Int. Pulsed Power Conf.*, June 15-18, 2003, Dallas, TX, IEEE Catalog Number 03CH37472C, Editors M. Giesselmann and A. Neuber, pp. 37-41.
- [9] L. I. Rudakov, A. L. Velikovich, J. Davis, J. W. Thornhill, J. L. Giuliani, Jr., and C. Deeney "Buoyant magnetic flux tubes enhance radiation in Z pinches," *Phys. Rev. Lett.* V. 84, No. 15, pp. 3326-3329 (2000); J. Thornhill, K. Whitney, C. Deeney, and P. LePell, "Phenomenological modeling of turbulence in Z-pinch implosions," *Phys. Plasmas*, Vol. 1, No. 2, pp. 321-330, 1994.
- [10] J. Lindl, "Development of the indirect-drive approach to inertial confinement fusion and the target physics basis for ignition and gain", *Phys. Plasmas*, Vol. 2, No. 11, pp. 3933-4024, 1995.
- [11] A. L. Velikovich, J. Davis, V. I. Oreshkin, J. P. Apruzese, R. W. Clark, J. W. Thornhill, and L. I. Rudakov, "High energy photon radiation from a Z-pinch plasma", *Phys. Plasmas*, Vol. 8, No. 10, pp. 4509-4517, 2001.
- [12] S. I. Braginskii, "Transport processes in a plasma," in *Reviews of Plasma Physics*, vol. 1, M. A. Leontovich, Ed. New York: Consultants Bureau, 1965, pp. 205-311.
- [13] J. Davis, R. W. Clark, J. L. Giuliani, J. W. Thornhill and C. Deeney, "Radiative Characteristics of Pulsed Power Driven Z-Pinch Aluminum Plasmas", *IEEE Trans. Plasma Sci.*, Vol. 26, No. 4, pp. 1192-1201, 1998.
- [14] V. A. Gasilov, A. S. Chuvatin, A. Yu. Krukovskii, L. E. Kartasheva, O. G. Olkhovskaya, A. S. Boldarev, D. S. Tarasov, N. V. Serova, S. V. Dyachenko, and O. V. Fryazinov, "MARPLE, a complex of numerical codes

- for simulation of magnetically accelerated plasmas in high-current pulsed power systems," *Mathematical Modeling*, Vol. 15, p. 107, 2003 (in Russian).
- [15] B. N. Chetverushkin, *Mathematical modeling of radiating gas dynamics problems*, Moscow, Nauka, 1985, 304 pp. (in Russian).
- [16] M. Busquet, "Radiation-dependent ionization model for laser produced plasmas", *Phys. Fluids B*, Vol. 5, No. 11, pp. 4191-4205, 1993.
- [17] V. G. Novikov and A. D. Solomyannaya, "Spectral characteristics of plasma consistent with radiation", *High Temperature*, Vol. 36, No. 6, pp. 835-841, 1998 (translated from *Teplofizika Vysokikh Temperatur*, Vol. 36, No. 6, pp. 858-864, 1998, in Russian).
- [18] J. W. Thornhill, J. P. Apruzese, J. Davis, R. W. Clark, A. L. Velikovich, J. L. Giuliani, Jr., Y. K. Chong, K. G. Whitney, C. Deeney, C. A. Coverdale, and F. L. Cochran, "An efficient tabulated collisional radiative equilibrium radiation transport model suitable for multidimensional hydrodynamic calculations", *Phys. Plasmas*, Vol. 8, No. 7, pp. 3480-3489, 2001.
- [19] M. Klapisch, A. Bar-Shalom, and J. Oreg, "Non-local-thermodynamic-equilibrium effects in the simulations of laser-produced plasmas", *Phys. Plasmas*, Vol. 5, No. 5, pp. 1919-1925, 1998.
- [20] H. L. Wilson, *Progress in High Temperature Physics and Chemistry* (Pergamon, Oxford, 1972), Vol. 5, p. 125.
- [21] D. R. Bates, A. E. Kingston, R. W. P. McWhirter, *Proc. R. Soc. A*, Vol. 270, p. 155, 1962.
- [22] W. Schultz, *Methods in Computational Physics*, Vol. 3, B. Alder, S. Fernbach, and M. Rotenberg, Eds., New York, Academic, 1964, p. 1.
- [23] A. A. Samarskii and Yu. P. Popov, *Finite-Difference Schemes for Gas Dynamics* (Nauka, Moscow, 1992) (in Russian); A. A. Samarskii, *The Theory of Difference Schemes*, Monographs and Textbooks in Pure and Applied Mathematics (Marcel Dekker, New York, 2001), Vol. 20.
- [24] V. A. Gasilov, private communication.
- [25] D. Potter, *Computational Physics*, John Wiley and Sons, New York (1973).
- [26] J. Shearer, "Contraction of Z-pinches actuated by radiation losses", *Phys. Fluids*, Vol. 19, No. 9, pp. 1426-1428, 1976.
- [27] L. Rudakov, A. Chuvatin, A. L. Velikovich, and J. Davis, "Confinement and Compression of Magnetic Flux by Plasma Shells", *Phys. Plasmas*, Vol. 10, No. 5, pp. 4435-4447, 2003.
- [28] Ya. B. Zeldovich and Yu. P. Raizer, *Physics of Shock Waves and High Temperature Hydrodynamics Phenomena*, edited by W. D. Hayes and R. F. Probstein (Academic, New York, 1967).
- [29] J. P. Apruzese and J. Davis, "Radiative properties of puffed-gas mixtures: The case of optically thick plasmas composed of two elements with similar atomic numbers", *J. Appl. Phys.*, Vol. 57, No. 9, pp. 4349-4353, 1985.
- [30] C. Deeney, P. D. LePell, B. H. Failor, S. L. Wong, J. P. Apruzese, K. G. Whitney, J. W. Thornhill, J. Davis, E. Yadlowsky, R. C. Hazelton, J. J. Moschella, T. Nash, and N. Loter, "Increased kilo-electron-volt x-ray yields from Z-pinch plasma by mixing elements of similar atomic numbers", *Phys. Rev. E*, Vol. 51, No. 5, pp. 4823-4832, 1995.
- [31] P. L. Coleman, B. H. Failor, J. S. Levine, J. C. Riordan, Y. Song, H. Sze, E. M. Waisman, "A review of recent z-pinch research at Maxwell Physics International", *Laser and Particle Beams*, Vol. 21, No. 3, pp. 409-441, 2001.
- [32] P. Coleman, A. Bixler, A. Gerhan, M. Krishnan, J. Thompson, and K. Wilson, "Continued Development of a 12 cm Diameter Nozzle for Argon Z-pinches", *IEEE Conference Record - Abstracts, 31<sup>st</sup> IEEE Int. Conf. on Plasma Science*, June 28 - July 1, 2004, Baltimore, MD, IEEE Catalog Number 04CH37537, p. 362; P. D. LePell, C. A. Coverdale, C. Deeney, and Y. Maron, "Structure in Mixed Element Plasmas on Z-Accelerator at Sandia National Laboratories", *ibid.*, p. 187; A. V. Shishlov, R. B. Baksht, S. A. Chaikovsky, A. V. Fedunin, F. I. Fursov, V. I. Kokshenev, N. E. Kurmaev, A. Yu. Labetsky, V. I. Oreshkin, A. G. Russkikh, "First Microsecond K-Shell PRS Experiments on the GIT-12 Generator", *ibid.*, p. 407.

#### AFFILIATIONS:

A. Chuvatin: *Laboratoire de Physique et Technologie des Plasmas, Ecole Polytechnique, 91128 Palaiseau, France.*

L. Rudakov: *Berkeley Scholars, Inc., Springfield, VA 22150, USA.*

A. Velikovich and J. Davis: *Plasma Physics Division, Naval Research Laboratory, Washington, DC 20375, USA.*

V. Oreshkin: *High Current Electronics Institute, 634055 Tomsk, Russian Federation.*

# Interferometric Measurement of Physical Phenomena During the Implosion Phase of a Puff-On-Puff Z-Pinch Load on Double-EAGLE

Robert C. Hazelton, Edward J. Yadlowsky, John J. Moschella, E. P. Carlson, C. Vidoli, J. Niemel, B. H. Failor, P. L. Coleman, J. S. Levine, Y. Song, H. M. Sze, and J. W. Thornhill

**Abstract**—Theoretical studies have predicted that the disruptive role of the Rayleigh–Taylor (R–T) instability on the current conduction and implosion characteristics of annular Z-pinch loads will be mitigated by mass accretion if uniform fill or multiple annular shell loads are used. Holographic interferometry was used to study these physical processes during the implosion phase of puff-on-puff loads on a terawatt accelerator. Both axial ( $r$ - $z$ ) density perturbation and azimuthal ( $r$  -  $\theta$ ) filamentation modes of the R–T instability were observed. Significant ionization ( $Z \approx 3 - 10$ ) of the inner gas puff atoms was observed below the anode grid before the outer puff had imploded to this radial position. Radiation hydrodynamic calculations indicate that photoionization by radiation from the outer current carrying shell could not account for this ionization. Current flowing on the inner gas puff could be the source of this ionization. The effect of these physical processes on the radiation yield from z-pinch warrants further investigation.

**Index Terms**—Holographic interferometry, phase-step reconstruction, Rayleigh–Taylor (R–T) instability, z-pinch.

## I. INTRODUCTION

**H**OLOGRAPHIC interferometry was used to study the run-in phase of a puff-on-puff z-pinch implosion on the Double-EAGLE accelerator at Titan Systems Company, San Leandro, CA. Interest in this early time behavior derives from the important role that the Rayleigh–Taylor (R–T) instability has been predicted to play in disrupting the current conduction and implosion processes of thin annular shells. Magnetohydrodynamics models, which calculate the nonlinear evolution of the R–T instability from an assumed initial density perturbation, have been used to predict the implosion of the load and its subsequent K-shell emission. (See [1]–[6] and references therein.) They have found that the calculated characteristics of the radiation pulse can be fitted to the observed values by adjusting the initial density perturbation level. The instability growth rate, which is largest with thin-current shells,

is predicted to decrease through a mass accretion mechanism when uniform gas fill or multiple annular shell loads are used [7]. The puff-on-puff load geometry studied here attempts to capitalize on this mass accretion.

Axially varying intensity distributions of the pinched plasma, recorded with X-ray pinhole cameras, is often cited as evidence for the observation of the R–T instability [8], [9]. The two-dimensional (2-D) plasma-density distribution in the imploding shell must be measured early in the implosion phase to understand how the R–T instability grows and saturates. Interferometry is a measurement technique with the required sensitivity and time response that can be used for this purpose.

Interferometric studies of gas puff z-pinchs have been reported by Shiloh *et al.* [10] using a Mach–Zender interferometer and by Qi *et al.* [11] using a laser shearing interferometer. The work described herein utilizes a two-reference beam holographic system to record a transient plasma event [12]. The hologram can then be analyzed during reconstruction employing a real time phase-stepping technique used commercially to evaluate the quality of optical components [13], [14]. The phase stepping technique reduces the task of determining the phase at each point in the plasma to a series of intensity measurements with a digital camera. This allows 2-D electron density distributions to be made with spatial resolution determined by the number of pixels in digital cameras (typically  $10^6$  or more) and the magnification employed during reconstruction.

The results clearly show both axial and azimuthal variations in the imploding shell 50–70 ns before X-ray emission. The results also reveal a significant ionization of the injected gas downstream from the anode grid plane before the current shell has imploded to this diameter.

## II. EXPERIMENTAL SYSTEM

The holographic interferometry studies were conducted on the Double-EAGLE generator, which provided a 3.5-MA current pulse rising to peak amplitude in 160–180 ns for a short circuit load in the long-pulse mode. The double-annular nozzle system used to produce the puff-on-puff load is shown in Fig. 1. The radii of the inner shell are 1 and 2 cm while those of the outer shell are 3 and 4 cm. The  $105 \mu\text{g/cm}$  linear mass loading was equally divided between the two shells for the shots considered here. A 12-wire grid was used to define the cathode plane while a 24-wire version defined the anode.

Manuscript received March 28, 2003; revised September 9, 2003. This work was supported in part by the Defense Threat Reduction Agency.

R. C. Hazelton, E. J. Yadlowsky, J. J. Moschella, E. P. Carlson, C. Vidoli, and J. Niemel are with HY-Tech Research Corporation, Radford, VA, 24141 USA (e-mail: bhazelton@hytechresearch.com).

B. H. Failor, J. S. Levine, Y. Song, and H. M. Sze are with Titan Systems Company, San Leandro, CA 94577 USA.

P. L. Coleman is with Titan Systems Company, San Leandro, CA 94577 USA, and is also with Alameda Applied Science Corporation, San Leandro, CA 94577 USA.

J. W. Thornhill is with the Naval Research Laboratory, Washington, DC 20375-1705 USA.

Digital Object Identifier 10.1109/TPS.2003.821582

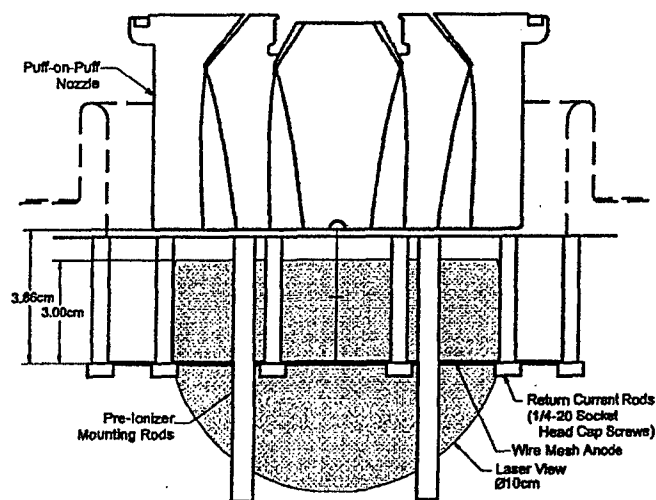


Fig. 1. Approximate position of the laser scene beam passing through Double-EAGLE load region.

A 30-cm-diameter flashboard, concentric with the load and positioned  $\sim 14$  cm below it, was fired  $3.4 \mu\text{s}$  before the main current pulse to pre-ionize the gas. The suite of instruments used to characterize the simulator operation included B-dot loops, calorimeters, zipper array detectors, gated and open shutter pinhole cameras, and X-ray spectrometers. This suite of diagnostics measured the characteristics of the imploded pinch and provided a temporal reference for the holographic measurements. All of the shots in this study were good, producing 12.5–13.4 kJ of Ar K-shell radiation with radiation pulse widths of 15–21 ns.

The frequency doubled 532-nm output from an injection seeded neodymium yttrium aluminum garnet (Nd: YAG) laser created the two reference beam holograms used to study the electron density distribution in the load. The 7-ns output pulse was first compressed to 400 ps using a stimulated Brillouin scattering (SBS) cell. The beam was spatially filtered and 20% of the beam was split off to form the reference beams while the remainder expanded to form the 9.5-cm-diameter scene beam. Periscopes and turning mirrors directed this scene beam through the chamber to the holographic construction table shown in Fig. 2. A 6-in-diameter lens, just outside the vacuum chamber, together with the lens in the beam line of Fig. 2 imaged the pinch region onto the holographic plate. These lenses were used to correct for the refractive bending of the scene beam by density gradients in the pinch.

The reference portion of the beam was expanded to a 3.8-cm diameter. Beam splitters and mirrors form two independent reference beams which were directed to the holographic plate. A double exposure procedure was used to record two holograms using shutters to first record a hologram without plasma and then uncovering the other beam to record a second hologram on the same plate with plasma. After exposure the plate was removed, developed, and bleached to produce a phase hologram.

A continuous-wave (CW) YAG laser was used to reconstruct the two holograms with the same optical system that created them. The interference pattern of the reconstructed holograms was recorded by the digital camera shown in Fig. 2. A phase stepping technique was used to infer the total phase shift through

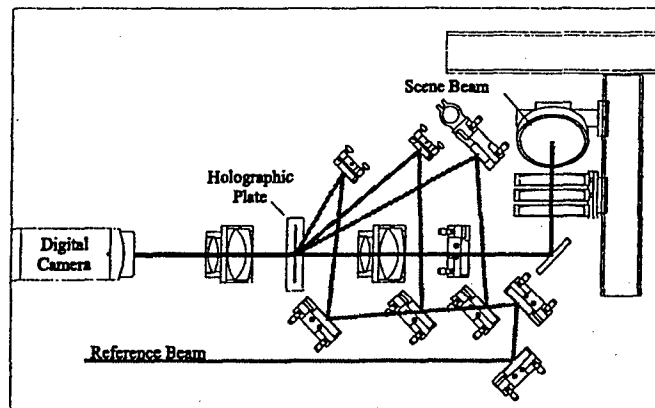


Fig. 2. Schematic of holographic construction/reconstruction table.

the plasma along a chordal line-of-sight by recording intensity patterns of the interferograms instead of trying to measure fringe shifts [13], [14]. This was accomplished by mounting one of the reference beam mirrors on a piezoelectric driver which steps the phase,  $\delta_n$ , of one reference beam relative to the other in increments of  $\pi/2$ . The intensity of the interference pattern of the reconstructed holograms for each phase step is then given by the expression

$$I_n(x, y) = I_o(x, y) + I'(x, y) \cos[\Delta\Phi(x, y) + \delta_n]$$

$$\delta_n = \frac{n\pi}{2}, \quad \text{for } n = 1, 2, 3, 4, 5. \quad (1)$$

Five frames are sequentially recorded by a digital camera for the five values of the phase  $\delta_n$ . The phase difference,  $\Delta\Phi(x, y)$  modulo  $2\pi$ , between the background and plasma holograms can then be inferred from the expression

$$\Delta\Phi(x, y) = \arctan \left( \frac{2(I_2(x, y) - I_4(x, y))}{2I_3(x, y) - I_5(x, y) - I_1(x, y)} \right). \quad (2)$$

A phase unwrap algorithm is used to remove the ambiguities of  $2\pi$  in the values of the phase that have been calculated using (2) [15]. The result is a 2-D map of the chordally integrated phase at each of the  $7 \times 10^5$  pixel locations of the digital camera used in this study. The spatial resolution that can be obtained with this procedure depends on pixel size and the image magnification. The reconstructed image can be magnified and the digital camera panned to view different regions of interest. In this way, a higher local resolution can be obtained while still preserving the entire field of view.

The initial distribution of neutral atoms in the load was measured off-line in a separate test chamber using a laser-induced-fluorescence (LIF) technique [16]. For these measurements, a trace amount of acetone (5%) was added to the Ar in the plenum. The acetone was fluoresced with a frequency-quadrupled YAG laser beam propagating along a diameter through the gas. A digital camera recorded the intensity distribution of fluorescent radiation emitted perpendicular to the laser beam. The fluorescence intensity was related to the neutral atom density by measuring the dependence of the LIF intensity on the static fill pressure in the test chamber. Measurements were made at the same time delay after firing the gas valve as were used in the radiation experiments to allow



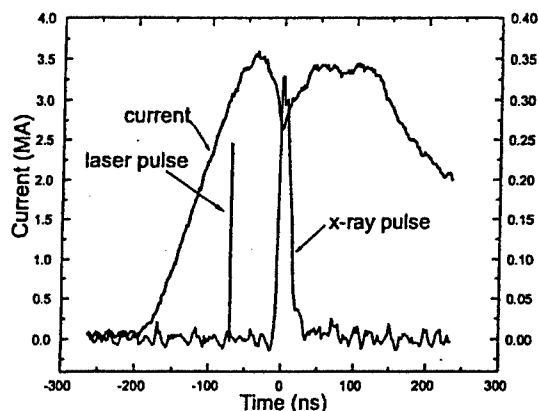


Fig. 3. Timing reference for hologram analyzed here ( $-70$  ns) relative to current waveform and normalized K-shell emission pulse.

a direct comparison of the neutral gas density distribution with the electron density distribution from which ionization levels can be inferred.

### III. RESULTS

A typical current waveform, showing the inductive notch when the load implodes and emits X-rays, is shown in Fig. 3. Holographic measurements were made 70, 50, and 30 ns before X-ray emission and 13 ns after. Holograms recorded with plasma were much dimmer than those without because electromagnetic noise from the generator degraded the laser output. Phase noise associated with the weak holograms complicated the phase unwrap procedure in areas of steep density gradients, such as the limb of the imploding sheath or the pinched plasma. Consequently, quantitative analyses of the current sheath 30 ns before X-ray emission and 13 ns after, are not reliable and will not be addressed. Since the plasma characteristics 50 and 70 ns before X-ray emission are similar, detailed analyses of the hologram taken 70 ns before X-ray emission (shot 4766) are presented here. The only exception is the shadowgram of the current sheath which was captured between the return current rod and the flashboard support on shot 4765 (50 ns before X-ray emission) in Fig. 4. All axial distances are given relative to the cathode. Since the phase maps are not Abel inverted, the transverse position of a chordal line of sight is referenced to the nozzle axis. The shaded area in Fig. 1 shows the load area viewed by the holographic system. Gross features of the density perturbations in the outside surface of the imploding shell can be studied using shadowgraphic techniques, even though quantitative analysis of the steep density gradients in these dim holograms are not reliable. A shadowgram is generated by placing a small aperture at the focal point of the final lens in Fig. 2 to limit the angular divergence of rays imaged onto the digital camera. In this case, only that hologram which was recorded with plasma in the scene beam is reconstructed. The aperture excludes the rays that are highly refracted by density (index) gradients in the sheath forming shadows of the plasma edge, as seen in Fig. 4. The sheath was observed to implode farther near the cathode consistent with zipper array measurements which show X-ray emission to proceed from cathode to anode. The 2-D contours of the phase and

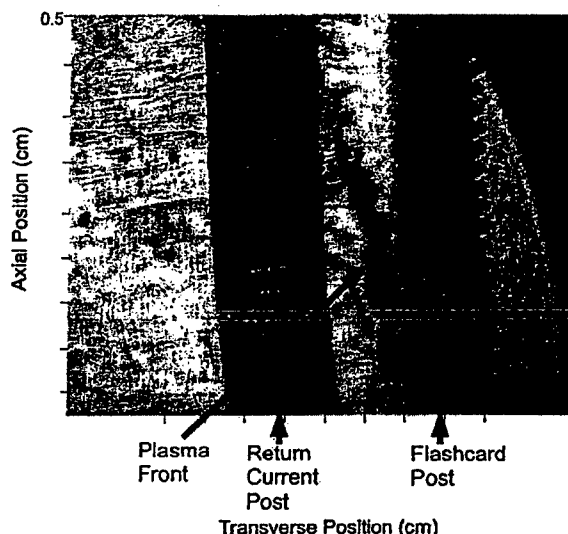


Fig. 4. Shadowgram of the plasma front 50 ns before peak X-ray emission. The view is between the return current post in the center of the figure and the threaded flashboard support at the right of the figure. Here, one can see perturbations on the exterior of the shell. In addition, the shell is seen to be further imploded nearer the cathode (top).

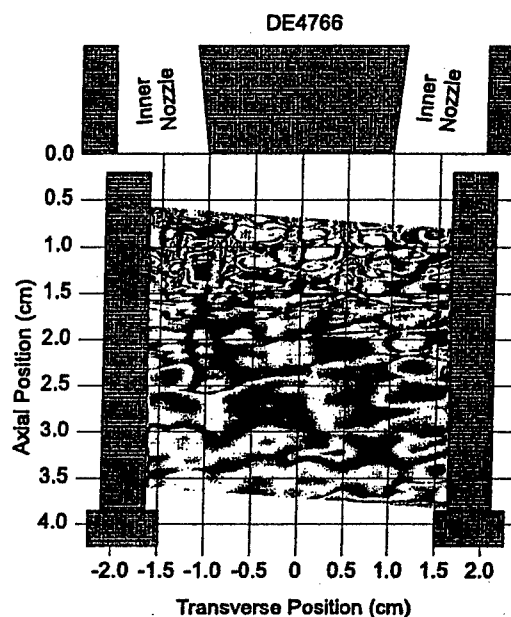


Fig. 5. Distribution of phase  $\Delta\Phi(x, y)$  modulo  $2\pi$  obtained with phase stepping analysis of interferogram taken 70 ns before peak X-ray emission. The two preionizer support rods are just outside the return current rods (bolts). (Grayscale light to dark  $\Rightarrow 0^\circ$ – $180^\circ$ ).

line integrated electron densities obtained with the phase step reconstruction technique for shot 4766 are shown in the next three Figs. 5–7. The very high electron-density surface plasmas that are generated adjacent to the anode have been allowed to go off scale (shown white in Figs. 6 and 7) to emphasis electron density variations associated with the injected gas puff. The image was cropped to view the region bounded by the electrodes and return current rods in Figs. 5 and 6. The constant phase contour map, modulo  $2\pi$ , obtained by applying (2) to every pixel sampled by the camera, is shown in Fig. 5 with the phase difference between adjacent light and dark regions being



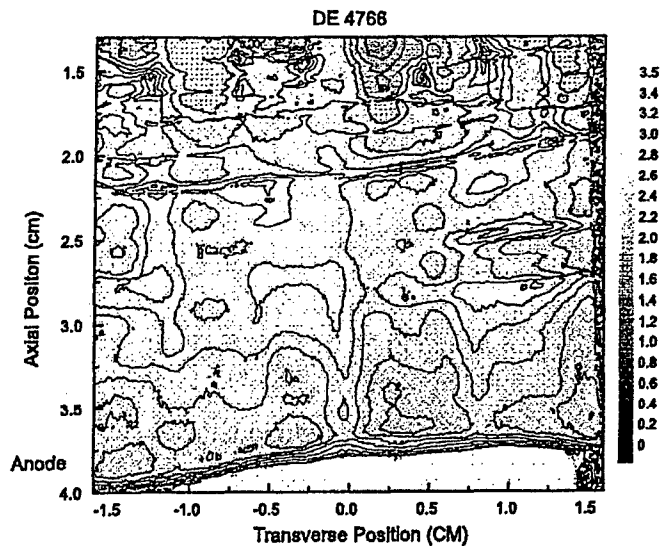


Fig. 6. Contour plot of line-integrated electron density 70 ns before X-ray emission. Here, the contour levels have been adjusted to highlight the variation in plasma density in the A-K gap. The high-density plasma at the anode appears white. The gray scale bar varies linearly from 0 at the bottom to  $3.5 \times 10^{18} \text{ cm}^{-2}$  at the top.

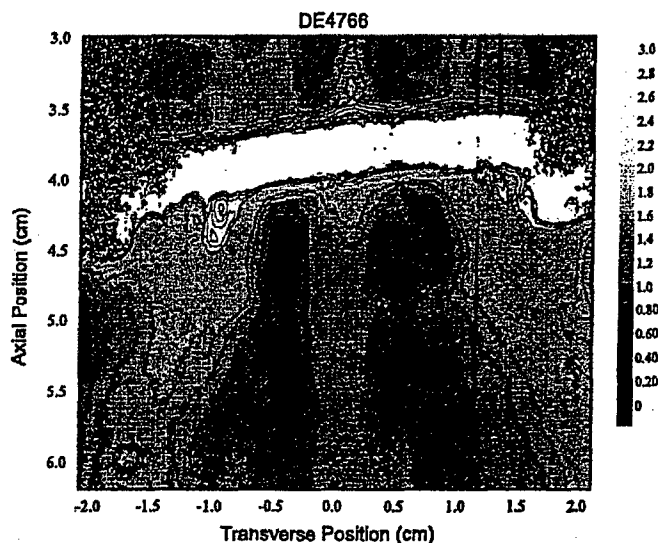


Fig. 7. Contour plot of line integrated electron density showing regions in the anode-cathode (A-K) gap and below the anode. Here, the contour levels have been selected to highlight the density variations in the region below the anode which appears white because of the high-density surface plasma there. The grayscale bar varies linearly from 0 at the bottom to  $3 \times 10^{18} / \text{cm}^2$  at the top.

$\pi$  radians. A contour plot of the line integrated electron density obtained by applying the phase unwrap to the data in Fig. 5 is shown in Fig. 6. The reconstruction camera was translated to obtain the line integrated electron density contours in Fig. 7 that straddle the anode plane. All electron densities within the anode-cathode gap are relative with a constant off set probable, since there is no unobstructed path to a no-plasma reference region. This reference region is available below the anode grid wires and the electron densities here are absolute values. The constant phase surfaces in Fig. 5 reveal a periodic structure both in axial position and in the transverse direction (which

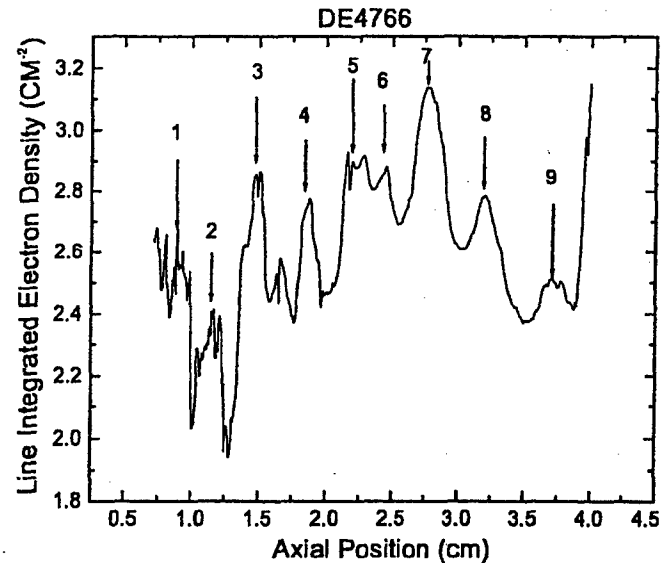


Fig. 8. Axial scan of density distribution shown in Fig. 6 made at transverse position =  $-1.3 \text{ cm}$ . Each peak amplitude has been numbered sequentially. Their axial positions are shown in Fig. 9.

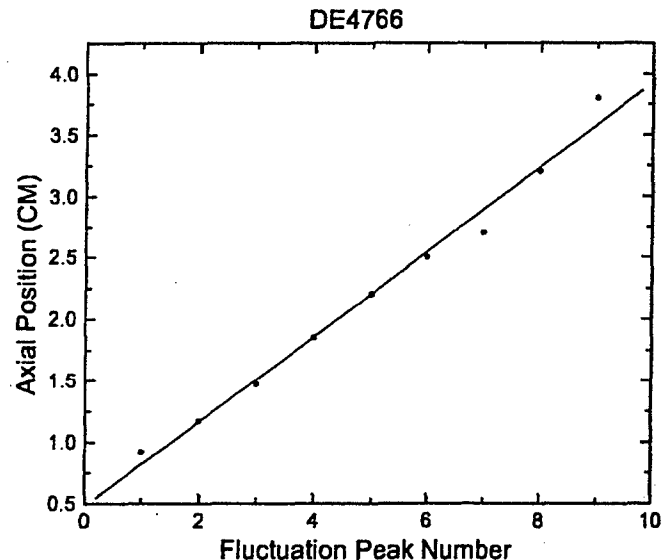


Fig. 9. Axial position of sequentially numbered density peaks in Fig. 8.

corresponds to the azimuthal position on a thin shell). The axial variation is more quantitatively revealed in the axial scan of the electron density shown in Fig. 8. The axial positions of the density peaks, labeled numerically in Fig. 8, are presented in Fig. 9 as a function of the peak number. The straight line fit to the data emphasizes the periodic nature of the fluctuations. The slope of the line yields a value of 3.1 mm for the perturbation wavelength, which lengthens slightly as the anode is approached. A pronounced perturbation is also observed in the azimuthal direction. A transverse scan 1.5 cm from the cathode in Fig. 5 is characterized by a wavelength of 5.2 mm.

The density contours below the wire grid anode in Fig. 7 reveal a plasma shell which is radially centered on the inner shell injection nozzle. This shell is more evident in the transverse density scan, shown in Fig. 10, where an on-axis peak is also evident. The continuation of this on-axis peak above the wire

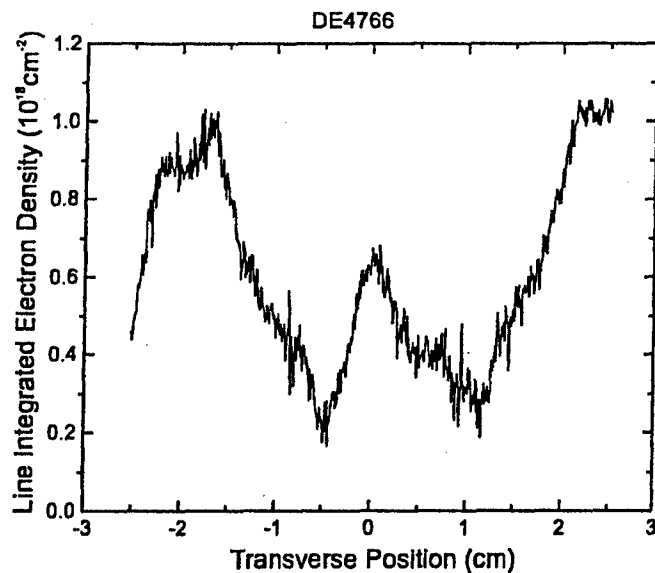


Fig. 10. Line-of-sight density distribution 1.5 cm below anode grid plane (taken from Fig. 7).

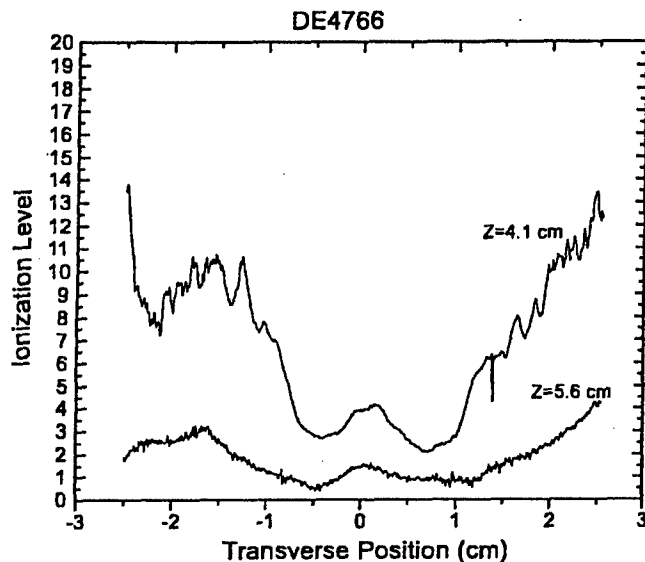


Fig. 11. Ratio of electron line-of-sight densities at axial distances 4.1 and 5.6 cm from the cathode to the Ar neutral line-of-sight densities at 3.5 cm as a function of transverse position.

anode grid is also evident in Fig. 10 even though the axial and azimuthal perturbation mask any other inner shell structure in the A-K gap. Since the absolute electron density is known below the anode grid, the line-of-sight electron density can be compared with the line-of-sight density of Ar atoms measured with LIF to determine the distribution of ionization levels shown in Fig. 11. This was obtained by assuming that the line-of-sight neutral density distribution 3.5 cm from the cathode, shown in Fig. 12, approximates the distributions 4.1 and 5.6 cm from the cathode. This is a reasonable assumption since variation between the line-of-sight densities observed with the LIF technique at 3.0 and 3.5 cm is too small to measure.

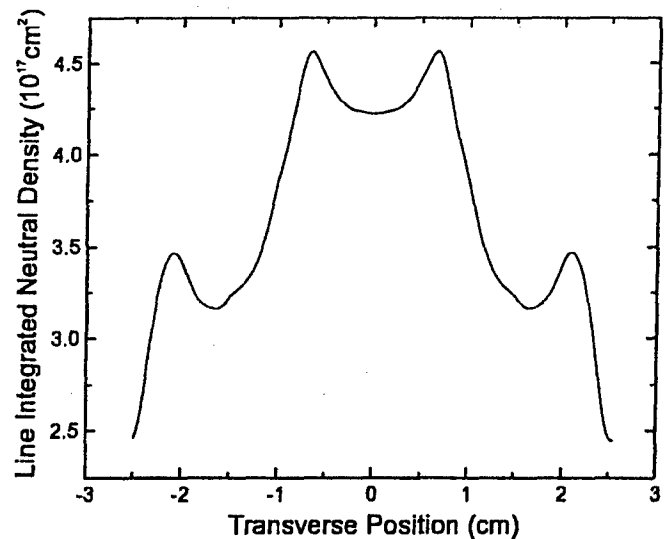


Fig. 12. Integrated line-of-sight density distribution of neutral Ar atoms inferred from LIF measurements 3.5 cm from cathode.

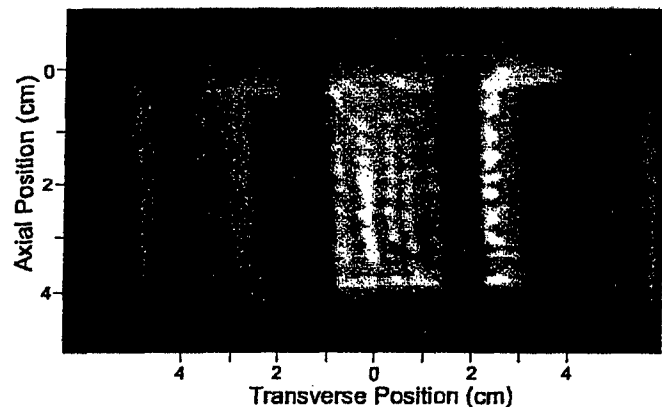


Fig. 13. Image of imploding gas puff on DM-2 39 ns before peak X-ray emission viewed through return current rods and recorded with framing camera. Axis of 4-cm long pinch is vertical with near return current rods dark and those on far side illuminated by radiation from pinch.

#### IV. DISCUSSION OF RESULTS

Evidence for axial and azimuthal density fluctuations during the implosion phase of the pinch are clearly evident in Figs. 4-7. The axial density perturbations have an average axial scale length of  $\lambda_o \sim 3.1$  mm while azimuthal perturbations, 1.5 cm from the cathode, have a scale length 5.2 mm. This latter scale length can be up to twice as large if nonregistration of the perturbations locates nodes on one side of the shell opposite to maxima on the other side. The periodicity of the perturbation, which is shown in Fig. 9 for the axial modes, implies an external seeding process. A similar periodicity was observed in optical framing camera photographs taken under similar conditions to this campaign and in other studies. Fig. 13 shows an exceptional example of this periodic filamentary structure taken on the DM-2 simulator when imploding a 5-cm-thin shell Ar gas puff [17]. In general, the number of filaments that are observed, about 20, does not correspond directly to the 24 wires that constitute the anode wire grid or to the 18 holes in the gas feed lines upstream of the nozzles that could be perturbing

the gas flow. Similar filamentation were not observed by the authors on the ACE 4 accelerator at Maxwell Technologies where mesh grids were used instead of radial grids to define the anode and cathode planes [17]. The relatively close match between the wire number and filamentation number observed in optical emission photographs suggests that the wire arrangement can be generating an azimuthally asymmetric current flow. This azimuthal perturbation in the axial currents can be responsible for the azimuthal density perturbations observed in this study. The question of whether these perturbations grow unstably under the action of the self-generated magnetic fields requires further study. The analysis by Kleev and Velikovich [18] predict that  $r - \theta$  modes of the R-T instability will have a filamentary structure similar to that observed here. Although these modes have a lower growth rate than the  $r - z$  modes, the current asymmetry may provide a strong initial perturbation. Sanford *et al.* [19] have shown that  $r - \theta$  modes of the R-T instability will preserve the azimuthal asymmetry of an external seed perturbation.

The very high ionization level ( $Z \sim 10$ ) that is observed in the plasma shell below the anode grid is a feature that has not been reported before. The peak density of this shell is approximately centered on the inner shell injection nozzle, 1.5 cm from the pinch axis, and well inside the current carrying outer shell, which is 2.9 cm from the axis at the anode end. The absence of optical emission from the inner shell location in axial images of the pinch taken under similar conditions may not be inconsistent with the present results. The framing camera may not have had adequate dynamic range to detect this low-level emission when axially viewing the very bright emission from the cathode.

The existence of this plasma shell cannot be attributed to the UV or plasma flux from the flashboard preionizer. Measurements [20]–[22] have shown that a preionization level of 1%–10% is expected from the UV radiation and that the plasma electrons from the flashboard would arrive at least  $0.5 \mu\text{s}$  after X-ray emission. This UV ionization level is much lower than the values of  $Z \sim 10$  that are measured in this study and the flashboard plasma arrives after the holograms are recorded.

A radiation hydrodynamic code has been used to simulate the implosion of a puff-on-puff load for conditions corresponding to the present experiment too see if radiation from the outer shell could photoionize the inner shell [23]. The initial gas density distribution for the one-dimensional (1-D) model calculations is given by the profile labeled  $-140 \text{ ns}$  in Fig. 14. The predicted radial distribution of ions and average ionization state is shown in Fig. 14 and 15, respectively. A close examination of these figures reveals no ionization in regions where the initial gas density has not been perturbed. This implies that within the scope of this model all heating and ionization occurs as a result of compressing the gas and no significant photoionization takes place upstream of the front, in particular, below the grid anode. This conclusion is tentative until the L-shell radiation physics in the model has been benchmarked by experiments.

If photoionization and ionization process associated with the flashboard preionizer have been correctly dismissed, the present results suggest that electrons associated with currents flowing on the inner gas puff may be ionizing the inner shell gas atoms located below the anode grid. Baksht *et al.* [24] have used Ro-

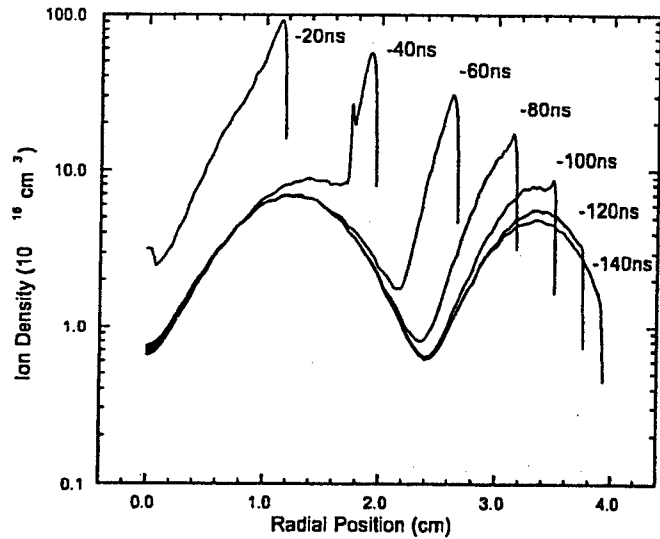


Fig. 14. Radiation hydrodynamic model prediction of the radial ion plus neutral density distributions at different times before peak X-ray emission. The distribution at  $t = -140 \text{ ns}$  (excluding the spike at maximum radius) is the initial gas density distribution.

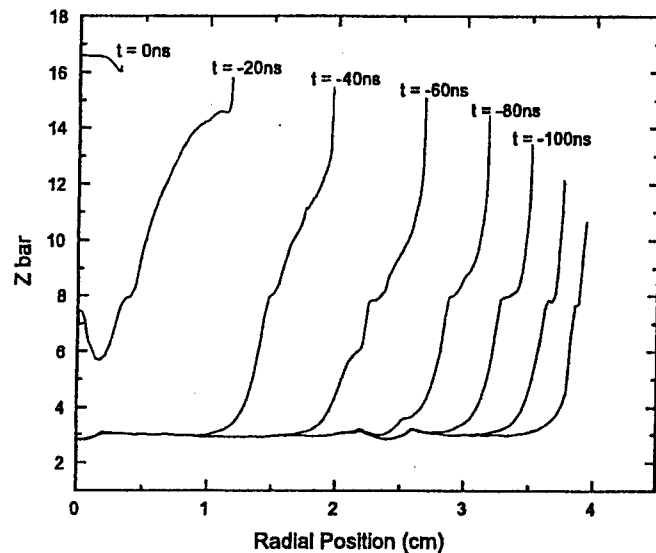


Fig. 15. Radial distribution of average ionization levels corresponding to the density distributions in Fig. 14.

gowsky coils located below the anode grid to separately measure currents flowing on the inner and outer gas puff of a multiple gas puff load. They have observed the generator current to be shared between these two gas shells if no preionization was used and have attributed insufficient preionization to explain the current sharing that was observed in 64% of the cases when preionization was used. Since Baksht *et al.* measured these inner shell currents downstream of the anode grid, they could account for the plasma density observed there in the present study. Furthermore, the presence of this plasma could be an indication that insufficient preionization was provided by UV radiation from the flashcard, in at least some cases. The important aspect of the present work is that the high ionization levels observed early in the implosion, well inside the current carrying outer shell, may represent an important physical process not currently considered in simulations of Z-pinch implosions.

## V. CONCLUSION AND FUTURE WORK

Holographic interferometry has been used successfully on a terawatt class simulator to study the implosion dynamics of a puff-on-puff gas load. Both axial and azimuthal density perturbations have been observed having scale lengths of 3.1 and 5.2 mm, respectively. The azimuthal perturbations are very similar to the axial striations or streamers observed with an optical framing camera and have the general features attributed to the  $r - \theta$  Rayleigh Taylor modes first discussed by Kleev and Velikovich [18] and recently studied by Sanford *et al.* [19].

A plasma shell is observed below the grid anode which is centered on the inner gas puff nozzle. This shell is well inside the current carrying outer shell at this time and the ionization level ( $Z \leq 10$ ) cannot be attributed to photo-ionization by radiation from the outer shell or by the flashboard preionizer. Electrons associated with current flow on the inner gas puff is suggested as a source of the ionization. The presence of such electrons could have an effect on modeling the radiation characteristics of Z-pinch. Additional measurements are required to determine if currents are flowing on the inner gas puff before a firm conclusion can be reached about the origin of the ionization.

Although these measurements revealed qualitative features of interesting physical phenomena occurring during the implosion phase of a PRS, they also point out the shortcomings of the technique. A zero-density reference plane is required within the A-K gap to measure absolute density fluctuations there. A multibeam heterodyne interferometer system is planned to measure the absolute phase at three locations in the A-K gap for this purpose. The presence of azimuthal perturbations complicates the task of inferring radial electron density distributions. Straightforward Abel inversion techniques cannot be used and tomographic techniques are required to obtain the 3-D density distribution. A perturbation expansion analysis may be used to infer a zero order radial profile from spatially averaged phase measurements provided the perturbations are a small fraction of the average density. These measurements would have to be augmented by spectroscopic measurements and collisional radiative equilibrium (CRE) modeling to determine the ion mass fluctuation levels. The identification of the observed density fluctuation as the R-T instability requires time-resolved measurements of their growth and saturation which can be compared with theoretical predictions. A two-time holographic interferometer system that HY-Tech has built and tested [24] would be suitable for this purpose. Finally, Rogowsky coils should be added downstream of the anode grid to measure currents that might be flowing on the inner gas puff.

## ACKNOWLEDGMENT

The authors would like to acknowledge the assistance of the Double-EAGLE operating crew in conducting the experiment and J. Banister for designing the periscope used to direct the laser beam through the plasma. They would also like to thank J. P. Apruzese, A. L. Velikovich, J. Davis, and K. G. Whitney for their useful discussions, and acknowledge the encouragement by D. Bell.

## REFERENCES

- [1] T. W. Hussey, N. F. Roderick, and D. A. Kloc, "Sealing of (MHD) instabilities in imploding plasma lenses," *J. Appl. Phys.*, vol. 51, pp. 1452-1463, 1980.
- [2] N. F. Roderick and T. W. Hussey, "A model for the saturation of the hydromagnetic Rayleigh-Taylor instability," *J. Appl. Phys.*, vol. 56, pp. 1387-1390, 1984.
- [3] N. F. Roderick, R. E. Peterkin Jr., T. W. Hussey, R. B. Spielman, M. R. Douglas, and C. Deeney, "Hydrodynamic Rayleigh-Taylor instabilities in high-velocity gas puff implosions," *Phys. Plasmas*, vol. 5, pp. 1477-1484, 1998.
- [4] D. L. Petersen, R. L. Bowers, W. Matuska, K. D. McLenithan, G. A. Chandler, C. Deeney, M. S. Derzon, M. Douglas, M. K. Matzen, T. J. Nash, R. B. Spielman, K. W. Struve, W. A. Stygar, and N. F. Roderick, "Insights and applications of two-dimensional simulations to Z-pinch experiments," *Phys. Plasmas*, vol. 6, pp. 2178-2184, 1999.
- [5] T. W. L. Sanford, R. C. Mock, R. B. Spielman, M. G. Haines, J. P. Chittenden, K. G. Whitney, J. P. Apruzese, D. L. Petersen, J. B. Greenly, D. B. Sinar, D. B. Reesman, and D. Mosher, "Wire array Z-pinch insights for enhanced X-ray production," *Phys. Plasmas*, vol. 6, pp. 2030-2040, 1999.
- [6] T. J. Nash, M. S. Derzon, G. A. Chandler, R. Leeper, D. Fehl, J. Lash, C. Ruiz, G. Cooper, J. F. Seaman, J. McGurn, S. Lazier, J. Torres, D. Jobe, T. Gilliland, M. Hurst, R. Mock, P. Ryan, D. Nielsen, J. Armijo, J. McKenney, R. Hawn, D. Hebron, J. J. MacFarlane, D. Petersen, R. Bowers, W. Matuska, and D. D. Ryutov, "High-temperature dynamic hohlraums on the pulsed power driver Z," *Phys. Plasmas*, vol. 6, pp. 2023-2029, 1999.
- [7] S. M. Gol'berg and A. L. Velikovich, "Suppression of Rayleigh-Taylor instability by the snowplow mechanism," *Phys. Fluids*, vol. B5, pp. 1164-1172, 1993.
- [8] J. S. Pearlman and J. C. Riordan, "Interferometry of a gas-puff Z-pinch," *Proc. SPIE*, vol. 537, pp. 102-107, 1985.
- [9] R. J. Dukart, T. W. Hussey, and N. F. Roderick, *Megagauss Technology and Pulsed Power Applications*, C. M. Fowler, R. S. Caird, and D. J. Erickson, Eds. New York: Plenum, 1987, pp. 183-189.
- [10] J. Shiloh, A. Fisher, and E. Bar-Avraham, "Interferometry of a gas-puff Z-pinch," *Appl. Phys. Lett.*, vol. 35, pp. 390-392, 1979.
- [11] N. Qi, J. Schein, J. Thompson, P. Coleman, M. McFarland, R. R. Prasad, M. Krishnan, B. V. Weber, B. G. Moosman, J. W. Schumer, D. Mosher, R. J. Comisso, and D. Bell, "Z pinch imploding plasma density profile measurements using a two-frame laser shearing interferometer," *IEEE Trans. Plasma Sci.*, vol. 30, pp. 227-238, Feb. 2002.
- [12] P. Hariharan, *Optical Holography Principles, Techniques, and Applications*, 2nd ed. Cambridge, U.K.: Cambridge Univ. Press, 1996, pp. 245-270.
- [13] K. Creath, "Phase-measurement interferometry techniques," in *Progress in Optics*. Amsterdam, The Netherlands: North-Holland, 1988, vol. 26, pp. 349-393.
- [14] J. E. Grievekamp and J. H. Bruning, "Phase shifting interferometry," in *Optical Shop Testing*, D. Malacara, Ed. New York: Wiley, pp. 501-598.
- [15] D. C. Ghiglia and M. D. Pritt, *Two-Dimensional Phase Unwrapping Theory, Algorithms, and Software*. New York: Wiley, 1998.
- [16] B. H. Failor, S. Chantrenne, P. L. Coleman, J. S. Levine, Y. Song, and H. M. Sze, "Proof-of-principle laser-induced fluorescence measurements of gas distributions from super sonic nozzles," *Rev. Sci. Instrum.*, vol. 74, pp. 1070-1076, 2003.
- [17] P. Coleman, private communication.
- [18] A. I. Kleev and A. L. Velikovich, "Filamentation instabilities of dynamic Z-pinch and theta pinches," *Plasma Phys. Control. Fusion*, vol. 32, pp. 763-777, 1990.
- [19] T. W. L. Sanford, N. F. Roderick, R. C. Mock, K. W. Strive, and D. L. Peterson, "Azimuthal structure in wire-array Z-pinch experiments," *IEEE Trans. Plasma Sci.*, vol. 30, pp. 538-546, Apr. 2002.
- [20] Y. Song, P. Coleman, B. H. Failor, A. Fisher, R. Ingermanson, J. S. Levine, H. Sze, E. Waisman, R. J. Comisso, T. Cochran, J. Davis, B. Moosman, A. L. Velikovich, B. V. Weber, D. Bell, and R. Schneider, "Valve and nozzle design for injecting a shell-on-shell gas puff load into a Z-pinch," *Rev. Sci. Instrum.*, vol. 71, pp. 3080-3084, 2000.
- [21] P. L. Coleman, B. H. Failor, J. S. Levine, J. C. Riordan, Y. Song, H. Sze, and E. M. Waisman, "Review of recent z-pinch research at Maxwell physics international," *Laser Part. Beams*, vol. 19, pp. 409-441, 2001.
- [22] B. G. Moosman, B. V. Weber, S. J. Stephanakis, R. J. Comisso, and A. Fisher, "Measurement of gas preionization for plasma radiation sources," *Rev. Sci. Instrum.*, vol. 70, pp. 672-676, 1999.

- [23] J. W. Thornhill, K. G. Whitney, and J. Davis, "Transition from  $I^4$  to  $I^2$  scaling of K-shell emission in aluminum array implosions," *J. Quant. Spectrosc. Radiat. Transf.*, vol. 44, pp. 251–259, 1990.
- [24] R. B. Baksht, A. G. Russkikh, and A. A. Chagin, "Study of the effect of preionization on current sharing between sheaths of a double-cascade gas puff," *Plasma Phys. Rep.*, vol. 23, pp. 175–182, 1997.
- [25] B. V. Weber, B. G. Moosman, S. J. Stephanakis, D. D. Hinshelwood, D. Mosher, J. W. Schumer, D. R. Welch, B. V. Oliver, and D. V. Rose, "Plasma evolution from rod-pinch diodes," in *Proc. 29th IEEE Int. Conf. Plasma Science*, Banff, AB, Canada, May 26–30, 2002, p. 249.

**Robert C. Hazelton** was born in Billings, MT, in 1948. He received B.S. degrees in electrical engineering and physics from Montana State University, Bozeman, in 1971, and the M.S. and Ph.D. degrees in electrical engineering from Colorado State University, Fort Collins, in 1976 and 1978, respectively.

While with the Kollmorgan Corporation, Radford, VA, he obtained patents for the laser machining of dc motor armatures and pioneered development of ReFeB magnets. Since co-founding HY-Tech Research Corporation, Radford, he has been involved in developing resonant laser diagnostic techniques for plasma opening switches, relativistic electron beam channels, low-pressure discharges, and applying interferometry to studying Z-pinch plasmas.

**Edward J. Yadlowsky** was born in Johnson City, NY, in 1940. He received the B.S. degree in physics from the University of Rochester, Rochester, NY, in 1962, and the Ph.D. degree in physics from the University of Maryland, College Park, in 1970.

After a National Research Council Postdoctoral appointment at the National Oceanic and Atmospheric Administration, he joined the Faculty of Colorado State University, Fort Collins, where, in addition to teaching, he used electron beams and lasers to study discharges and laser-produced plasmas. Since 1983, he has been President and Co-Founder of HY-Tech Research Corporation, Radford, VA, and has been involved in studies of surface breakdowns on insulators, radiation-induced conductivity in insulators, plasma opening-switch physics, and Z-pinches.

**John J. Moschella** received the Ph.D. degree in plasma physics from Cornell University, Ithaca, NY, in 1991.

He is currently a Staff Scientist at HY-Tech Research Corporation, Radford, VA. While with HY-Tech, he has studied Marshall gun sources for plasma opening switches and developed a two-reference-beam holographic interferometer to measure POS plasma densities.

**E. P. Carlson**, photograph and biography not available at the time of publication.

**C. Vidoli**, photograph and biography not available at the time of publication.

**J. Niemel**, photograph and biography not available at the time of publication.

**B. H. Failor**, photograph and biography not available at the time of publication.

**P. L. Coleman**, photograph and biography not available at the time of publication.

**J. S. Levine**, photograph and biography not available at the time of publication.

**Y. Song**, photograph and biography not available at the time of publication.

**H. M. Sze**, photograph and biography not available at the time of publication.

**J. W. Thornhill**, photograph and biography not available at the time of publication.

## Design of a Multilayer Mirror Monochromatic X-ray Imager for the Z Accelerator

B. Jones<sup>a)</sup>, C. Deeney

*Sandia National Laboratories, Albuquerque, New Mexico 87185*

A. Pirela, C. Meyer

*Ktech Corp., Albuquerque, New Mexico 87123*

D. Petmecky, P. Gard

*Technical Manufacturing Industries (TMI), Inc., Albuquerque, New Mexico 87123*

R. Clark, J. Davis

*Naval Research Laboratory, Washington, DC 20375*

A time-resolved pinhole camera is being developed for monochromatic soft x-ray imaging of z-pinch plasmas on the Z accelerator [R. B. Spielman *et al.*, Phys. Plasmas **5**, 2105 (1998)] at Sandia National Laboratories. Pinhole images will reflect from a planar multilayer mirror onto a microchannel plate detector. A W/Si or Cr/C multilayer reflects a narrow energy range (full width at half maximum  $< 10$  eV) centered at 277 eV with peak reflectivity up to 20%. This choice of energy will allow final implosion imaging of any wire-array z-pinch fielded on Z, as well as bench testing using a carbon K- $\alpha$  source. Aluminized parylene filters will eliminate optical and second harmonic reflection, and the 34 degree multilayer grazing angle will allow detector shielding from high energy x-rays. The beamline will also include a standard in-line pinhole camera, which can be filtered to obtain simultaneous higher-photon-energy images. Future instruments could use multiple mirrors to image at several energies, or operate at low grazing angle to image 1-10 keV K-shell emission.

<sup>a)</sup> Electronic mail: [bmjones@sandia.gov](mailto:bmjones@sandia.gov)

## I. INTRODUCTION

The Z accelerator [1] at Sandia National Laboratories is capable of driving 20 MA z-pinchs with a rise time of 100 ns, producing >250 TW, 1.8 MJ soft x-ray yields. The machine's core diagnostic set [2] includes several x-ray pinhole cameras that can be filtered for a variety of wide-band photon energies. By using a thin filter, low-energy emission can be detected along with contributions from higher-energy emission, but monochromatic imaging of low-energy photons is not possible with filtering alone.

One approach to developing an imaging monochromator is to combine filtered pinhole imaging with grazing incidence reflection. The grazing incidence streak camera system currently operating on Z does this by combining a 2  $\mu\text{m}$  Ti filter with a 2° grazing angle reflection from a quartz mirror, giving a net bandpass of 406-454 eV (full width at half maximum) with a small additional contribution at ~1-2 keV [3]. In this paper, we discuss the design of a pinhole camera system that instead uses reflection from a planar multilayer mirror in order to obtain < 10 eV bandwidth at a photon energy of 277 eV. The diagnostic will also incorporate a standard in-line pinhole camera in the same beamline, enabling simultaneous imaging at 277 eV and at higher photon energies (i.e. K-shell photons, for low-Z wire array z-pinchs such as Al or stainless steel). It has been suggested that some of the structure in the K-shell emission is due to reabsorption in clouds of non-uniform cold plasma surrounding the hot core [4,5], and this multilayer-based diagnostic may address these physics issues. In addition, a streak camera could be combined with this system to radially or axially resolve the final implosion phase.

In Sec. II, we present the pinhole camera hardware for this diagnostic, which is presently being manufactured. In Sec. III, the design considerations that determine the multilayer and filter arrangement are discussed.

## II. PINHOLE CAMERA INSTRUMENT LAYOUT

Figure 1 shows the hardware design for the instrument, intended for a Z side-on  $12^\circ$  line-of-sight. The instrument includes cartridge slot modules (1-6) in two locations shown in Fig. 1(a), which can house a variety of components. In the initial configuration, copper baffles in the first slot (1) will protect the instrument from debris generated in the load region. The pinholes (2) are located 3.56 m from the z-pinch source, a distance chosen to put them as close to the source as practical while remaining outside the four-port flange shown, which is at the wall of the Z vacuum chamber. The camera magnification is 0.5, chosen for enhanced signal and wide field of view (15 mm). Magnification could be increased in the future with the addition of an independent in-vacuum pinhole mount stage. Conical pinholes in 1 mm thick Au/Pt disks will be demountable, and combined with a 6 mm tin-alloy plate to absorb hard x-rays. Pinhole diameters of  $114\text{ }\mu\text{m}$  give the optimal spatial resolution of  $483\text{ }\mu\text{m}$ , limited by diffraction at 277 eV for this configuration [6]. Following the pinhole unit is a tungsten baffle cartridge (3), and then optional filter cartridges (4, 5). The tube with rectangular cross-section can be modified to accommodate a wide-aperture fast valve. Choice of filter material will be discussed in Sec. III.

All of these cartridge units must be positioned accurately in order to properly align the camera. As the Z load region flexes upon vacuum pump-down, the instrument is designed to facilitate alignment under vacuum. The alignment telescope shown in Fig. 1(a) views the load region



through cross-hairs with the aid of an alignment mirror that rotates into position against a precision-machined surface. The ball gimble pivots the instrument into alignment with the source, and XY translators on each cartridge unit then allow the unit to be positioned by aligning cross-hairs on the back of the cartridge (Fig. 1(b)) with the telescope cross-hairs. During this process, an LED unit (Fig. 1(a), position (6)) illuminates the beamline. Upon completion of alignment, the LED unit and the alignment mirror are retracted. The multilayer mirror is rigidly fixed at the proper grazing incidence angle relative to the telescope. Any pipe sag or load movement is compensated for during the alignment under vacuum. The multilayer is mounted on a precision-machined substrate, clamped in place, and easily demountable.

The gate valve on the front end of the camera allows differential pumping in advance of the main Z vacuum chamber pump-down, as well as vacuum isolation in the event of leaks. All vacuum seals including cap plates covering cartridge slots and the multilayer box are of o-ring type, which historically produce fewer vacuum leaks on Z. The exception to this is a plastic conflat flange that mounts the microchannel plate detector to the device. The instrument has several pump-out ports to facilitate differential pumping on either side of filter units if required.

The detector box at the end of the assembly will initially house one multilayer mirror, reflecting with a grazing angle of  $34^\circ$ . The second multilayer mount location may eventually be used to mount a second mirror designed to look at higher photon energy, or with a streak camera detector. Each detector location includes a filter mount as shown in Fig. 1(c). The filter at the off-axis detector location will be aluminized to shield the detector from optical fluorescence that may occur at the multilayer mirror surface. The detector box will also mount a 0.5 inch thick lead shield to screen the off-axis detector from direct line-of-sight hard x-ray exposure.

### III. MULTILAYER MIRROR AND FILTER DESIGN

Multilayer mirrors can reflect  $\sim 0.1$ -10 keV photons efficiently. In the initial version of this diagnostic, the energy 277 eV was chosen for several reasons. First, any z-pinch load on Z will radiate prodigiously at this energy, and the instrument can be fielded on a variety of shots. Second, the large corresponding grazing angle allows for robust shielding of the detector. As will be discussed, dispersion is not an issue at this grazing angle and alignment is less critical. Also, a carbon K- $\alpha$  Manson source can be used to calibrate the instrument, and the carbon edge of plastic filters can be used to eliminate  $< 100$  eV and second harmonic reflected photons. Finally, off-the-shelf multilayers are available that meet the design requirements for this system.

As a design tool, a set of IDL routines were written use that tabulated atomic scattering factors [7] with Fresnel reflection coefficients and a recursion relation to calculate multilayer reflectivity [8], including a Debye-Waller model of surface roughness [9]. Both W/Si and Cr/C multilayers of nominally 40 Å period were purchased from Osmic, Inc., with Cu K- $\alpha$  reflectivity measured versus grazing angle by the vendor and shown in Fig. 2 (solid line) for a W/Si mirror. With the layer materials and number of layers (120) known, a least-squares fit was performed on several free parameters characterizing the multilayer performance. Angles less than  $0.1^\circ$  were excluded as the source image was falling off the mirror, and above  $3.3^\circ$  were excluded as the measurements were dominated by noise. The resulting best-fit parameters (41.22 Å bi-layer period, 0.2389 W/Si layer thickness ratio, and 3.514 Å surface roughness for this multilayer) were obtained with a reported fit accuracy of the order of a part in  $10^4$ . The best-fit reflectivity curve is shown in Fig. 2 (dotted line), and matches low-grazing-angle reflectivity rise, and also the first (Fig. 2(b)) and second (Fig. 2(c)) harmonic reflection peaks. Similar fit results are

obtained for Cr/C multilayers, although the calculated peaks are narrower than the measurements, likely because of interdiffusion between layers that is not properly accounted for in the model. Calculations presented here assume unpolarized x-rays; note that the calculated W/Si multilayer reflection of s-polarized radiation exceeds p-polarized reflection by a factor of six in the  $34^\circ$  grazing angle configuration discussed.

With the multilayer mirror parameters determined as discussed above, a grazing angle can be designed in order to reflect photons at 277 eV. Figure 3(a) shows calculated reflectivity curves for the W/Si mirror discussed above (dotted line,  $33.67^\circ$  grazing angle, 2.0% peak reflectivity) and a 40.15 Å period, 75 bi-layer Cr/C multilayer (solid line,  $34.31^\circ$  grazing angle, 20.6% peak reflectivity), which have been normalized to compare the shape of the first harmonic peak. The addition of a 2 µm parylene-N filter coated with 1000Å Al (Fig. 3(b)) eliminates low-energy and second harmonic reflection. Figure 3(c) shows the calculated multilayer reflectivity multiplied by the filter transmission and a 1D radiation-hydrodynamic modeled emission spectrum for a stainless steel array on Z (55 mm diameter, 140 x Ø10.42 µm wires). The signal contributing to the image at the microchannel plate detector is mainly from low-energy continuum emission, with contributions from several M-shell lines. There are no contributions at photon energies outside the range shown in Fig. 3. The Cr/C gives a factor of ~5 greater signal than the W/Si mirror. Using this rad-hydro model spectrum and referencing filtered pinhole camera data collected for stainless steel loads on Z using the same style Burle 8-frame, 8 mm half-strip microchannel plate that will be fielded in this diagnostic, it is estimated that a 200 V forward DC bias on the microchannel plate (driven with 2 ns, 2 kV pulser with 9-way splitter) will compensate for the loss in signal due to the narrow bandpass of the instrument. Planckian tungsten z-pinchs should provide greater signal than stainless steel.

Also shown in Fig. 3(a) are the W/Si reflectivity curves resulting from perturbing the grazing angle by  $\pm 0.1^\circ$  (dashed curves). This is the level of variation across the mirror for a given image due to the geometry of the ray paths, and is the alignment accuracy desired of the instrument. In the case of the 0.5 magnification,  $34^\circ$  grazing angle, 277 eV photon energy configuration of this diagnostic, this perturbation to the bandpass as a result of dispersion at the mirror is a negligible effect. The signal is dominated by continuum emission and this slight shift in the energy of peak reflectivity will not alter the essential information provided by the images. Reconfiguring the instrument for low grazing angle operation in order to image higher energy photons (according to Bragg's law) would introduce greater dispersion into the images.

It is possible to take advantage of the dispersion across a multilayer mirror at low grazing angle in order to gain spectral information about the plasma source. Monochromatic imaging by grazing incidence reflection of pinhole array images from a flat crystal [10] or multilayer mirror [11] has been performed previously for imploded capsules driven by intense lasers. In this technique, the pinhole array is tilted so that adjacent images are displaced along the axis of dispersion. Significant dispersion exists across each image, but a composite monochromatic image of the source can be created from the data set [11]. A future modification to the instrument discussed here could allow this same technique to be applied to dense z-pinch. The in-line pinhole camera could be replaced with a 20 Å W/Si mirror at  $2.75^\circ$  grazing angle, reflecting 6.7 keV Fe K-shell photons with 40% efficiency. With a tilted pinhole array located at the present pinhole cartridge location, a 5 mm height of the pinch could be imaged, with dispersion across each image covering a range of energies from the Fe K- $\alpha$  line to the Fe He- $\alpha$  line (typically the brightest Fe K-shell line in stainless steel pinches on Z). Imaging of the Fe K- $\alpha$  line on a Manson source would allow verification of the mirror alignment, and the multiple

images of a z-pinch plasma could allow reconstruction of monochromatic Fe K-shell line or continuum images which could be used to infer 2D electron temperature profiles [12]. Two multilayers oriented for orthogonal polarizations could allow imaging spectropolarimetry [13].

#### ACKNOWLEDGEMENTS

The authors would like to thank D. Nielsen (Ktech Corp.), T. J. Nash (Sandia), J. Wood (Osmic, Inc.), and J. P. Apruzese (NRL) for valuable contributions to the design of this diagnostic. Sandia is a multi-program laboratory operated by Sandia Corporation, a Lockheed Martin Company, for the United States Department of Energy under Contract DE-AC04-94AL85000.

- [1] R. B. Spielman, C. Deeney, G. A. Chandler *et al.*, Phys. Plasmas **5**, 2105 (1998).
- [2] T. J. Nash, M. S. Derzon, G. A. Chandler *et al.*, Rev. Sci. Instrum. **72**, 1167 (2001).
- [3] D. F. Wenger *et al.*, these proceedings (High-Temperature Plasma Diagnostics Conference 2004).
- [4] C. Deeney, T. J. Nash, P. D. LePell *et al.*, Bull. Am. Phys. Soc. **48**, 237 (2003).
- [5] P. D. LePell, C. A. Coverdale, C. Deeney, and Y. Maron, Bull. Am. Phys. Soc. **48**, 237 (2003).
- [6] D. B. Sinars, G. R. Bennett, D. F. Wenger *et al.*, Appl. Opt. **42**, 4059 (2003).
- [7] <http://www-cxro.lbl.gov>
- [8] J. H. Underwood and T. W. Barbee, Jr., Appl. Opt. **20**, 3027 (1981).
- [9] E. Spiller, **Soft X-ray Optics**, 1st ed. (SPIE Press, Bellingham, WA, 1994), pp. 112, 132.
- [10] B. Yaakobi, F. J. Marshall, and D. K. Bradley, Appl. Opt. **37**, 8074 (1998).
- [11] L. A. Welser, R. C. Mancini, J. A. Koch *et al.*, Rev. Sci. Instrum. **74**, 1951 (2003).
- [12] J. P. Apruzese, K. G. Whitney, J. Davis, and P. C. Kepple, J. Quant. Spectrosc. Radiat. Transfer **57**, 41 (1997).
- [13] A. S. Shlyaptseva, S. B. Hansen, V. L. Kantsyrev *et al.*, Rev. Sci. Instrum. **72**, 1241 (2001).

FIG. 1. (a) The hardware design layout for the multilayer mirror pinhole camera diagnostic. Cartridge modules (1-6) can mount baffles, pinholes, filters, and alignment LEDs. (b) A pinhole cartridge unit, with cross-hair used for alignment with telescope. (c) The interior of the multilayer mirror box.

FIG. 2. (a) Measured W/Si multilayer reflectivity versus Cu K- $\alpha$  grazing angle (solid), compared to a calculated best-fit curve (dotted). Excellent agreement is seen for the first (b) and second (c) harmonic reflection peaks.

FIG. 3. (a) Calculated reflectivity (R) at  $\sim 34^\circ$  grazing angle for  $\sim 40$  Å period W/Si (dotted line) and Cr/C (solid line) multilayers, normalized to unity peak reflectivity. Perturbing the grazing angle of the W/Si mirror by  $\pm 0.1^\circ$  (dashed curves) shifts the energy at peak only slightly. (b) The transmission (T) of a 2  $\mu\text{m}$  parylene-N + 1000 Å Al filter which blocks low-energy photons and second harmonic reflection from the multilayer. (c) Rad-hydro-modeled emission intensity (I) from a stainless steel pinch on Z. (d) The product of R, T, and I, which is the signal incident on the detector. The dotted vertical line shows the carbon K- $\alpha$  line energy.

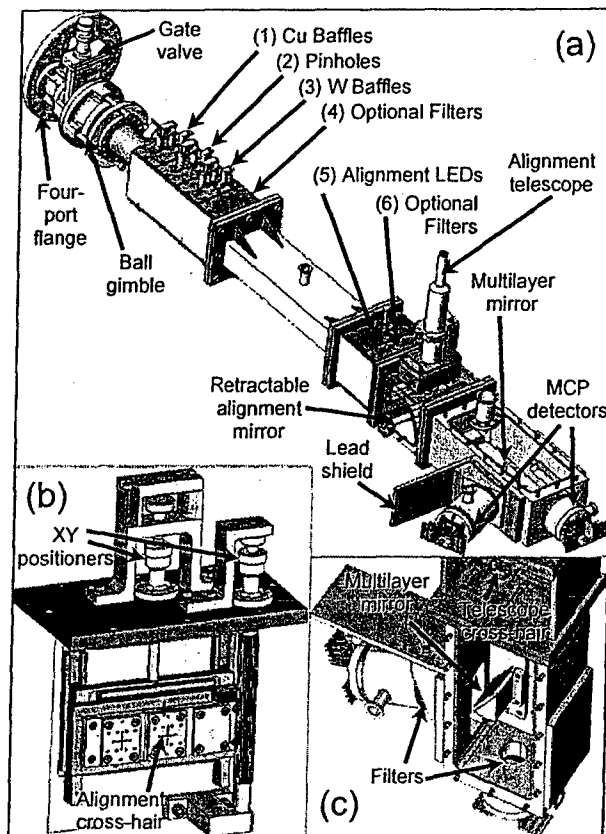


FIGURE 1, B. Jones



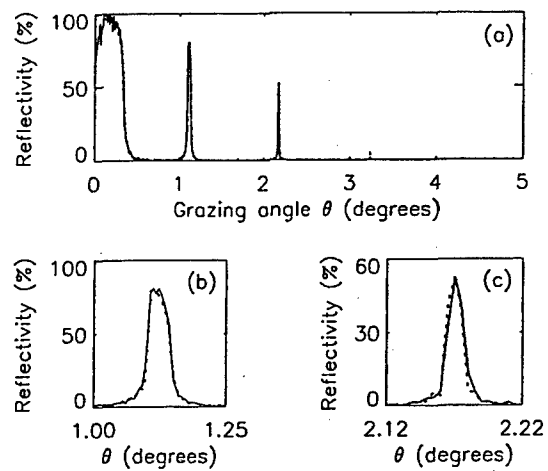


FIGURE 2, B. Jones

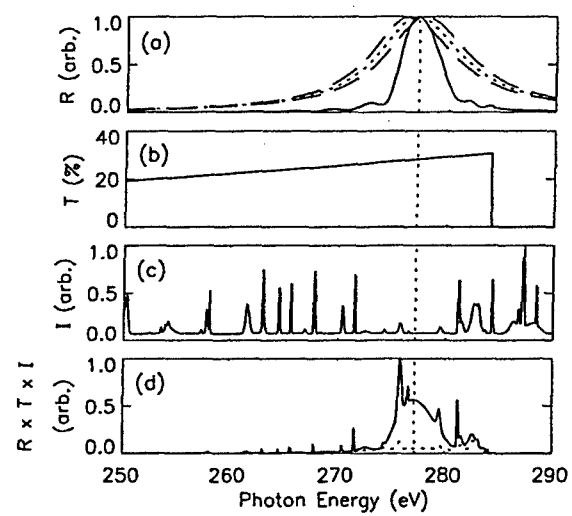


FIGURE 3, B. Jones